Climate variability of Svalbard in the first decade of the 21st century and its impact on Vestfonna ice cap, Nordaustlandet

–

An analysis based on field observations, remote sensing and numerical modeling

vorgelegt von

Dipl. Ing. Roman Finkelnburg

aus Berlin

Von der Fakultät VI - Planen Bauen Umwelt

der Technischen Universität Berlin

zur Erlangung des akademischen Grades

Doktor der Naturwissenschaften

- Dr.rer.nat. -

genehmigte Dissertation

Promotionsausschuss:

Vorsitzender:	Prof. Dr. Gerd Wessolek
Gutachter:	Prof. Dr. Dieter Scherer
Gutachter:	Prof. Dr. Christoph Schneider

Tag der wissenschaftlichen Aussprache: 03.05.2013

Berlin 2013

D 83

Table of contents

List of papers

The dissertation is presented in cumulative form and consists of five individual manuscripts, which are referred to by their corresponding Roman numerals in the text. All manuscripts are completely reproduced in Appendix A-E. Three manuscripts are published. Two manuscripts are prepared for submission.

I. Möller, M., Möller, R., Beaudon, E., Mattila, O.-P. , Finkelnburg, R., Braun, M., Grabiec, M. Jonsell, U., Luks, B., Puczko, D., Scherer, D. and Schneider C., 2011. Snowpack characteristics of Vestfonna and De Geerfonna (Nordaustlandet, Svalbard) – a spatiotemporal analysis based on multiyear snow-pit data. *Geografiska Annaler: Series A*, 93 (4), 273-285. doi:10.1111/j.1468-0459.2011.00440.x. [*]

II. Möller, M., Finkelnburg, R., Braun, M., Hock, R., Jonsell, U., Pohjola, V. A., Scherer, D. and Schneider, C., 2011. Climatic mass balance of the ice cap Vestfonna, Svalbard: A spatially distributed assessment using ERA-Interim and MODIS data. *Journal of Geophysical Research – Earth Surface*, 116. doi: 10.1029/2010JF001905. [**]

III. Finkelnburg, R., Maussion, F. and Scherer, D., 2013. Seasonality and variability of the climate in Svalbard as resolved by the European Arctic Reanalysis (EAR) for the glacier mass-balance years 2001 to 2011. To be submitted to the *Journal of Climate*.

IV. Sauter, T., Möller, M., Finkelnburg, R., Grabiecz, M., Scherer, D. and Schneider, C., 2013. Snowdrift modelling for Vestfonna ice cap, northeastern Svalbard. *The Cryosphere Discuss*., 7, 709-741, doi: 10.5194/tcd-7-709-2013.

V. Finkelnburg, R., Scherer, D., Möller, M., Hock, R., Jonsell, U., Braun, M. and Schneider, C., 2013. On elevational gradients of air temperature on Vestfonna, Svalbard. To be submitted to *The Cryosphere*.

[*]The paper is reprinted with permission of the *Geografiska Annaler*.

[**]The paper is reprinted with permission of the *Journal Geophysical Research*.

Acknowledgements

First of all, I would like to express my gratitude to my supervisor, Prof. Dieter Scherer, who provided a truly unconstrained working atmosphere, giving me all possible freedom to develop and define the topic of my thesis and to pursue any emerging ideas, including field work in Svalbard and the attendance of various conferences. I also thank Prof. Christoph Schneider with his open-minded attitude for examining this thesis.

I would like to thank all my colleagues in Berlin for the warm and fuzzy atmosphere at work, all the cake and coffee and their valuable professional and interpersonal support. Special thanks to Hartmut Küster and Ingo Suchland who helped substantially to set up measurement equipment and gave logistical support. I am deeply grateful to Fabien Maussion who was a priceless companion over the years in science and programming, (Sv)Albert Polze who gave various support not only during field work and Anselm Arndt, Dr. Fred Meier, Dr. Thomas Mölg and Marco Otto for reviewing my manuscripts, listening and discussing all my ideas.

I am thankful to all the colleagues from other institutions who made the various field campaigns successful and an enriching and instructive time. Special thanks go to Prof. Matthias Braun, Dr. Marco Möller, Rebecca Möller, Dr. Tobias Sauter and Lars Schneider.

Finally, I would like to thank my family and all my friends for their infinite support.

This work was funded by grants no. BR 2105/6-1, SCHE 750/3-1, SCHE 750/3-2, SCHN 680/2-1, SCHN 680/2-2 of the German Research Foundation (DFG) and grants no. 03F0623A and 03F0623B of the German Federal Ministry of Education and Research (BMBF). The Geografiska Annaler and Journal Geophysical Research are acknowledged for granting the reprint of previously published material in this thesis.

Roman Finkelnburg

Berlin, March 2013

Summary

The Arctic is an important element in the global climate. Circulations of the atmosphere and the ocean transport energy from the equator to high-latitudes. In the northern hemisphere this is mainly done by transient disturbances of the atmospheric circulation (cyclones and anticyclones, low- and high-pressure regions) at mid-latitudes and the North Atlantic Current. Svalbard, an archipelago in the North Atlantic and Arctic Ocean, is strongly influenced by the activity of the North Atlantic cyclone track transporting moisture and moist static energy into the region. Furthermore, strong climate gradients with interannual and intra annual variability are generated by the interaction of the West Spitsbergen Current transporting warm Atlantic water northward and the fluctuating sea ice margin. The climate of Svalbard is characterized by close couplings between atmosphere, ocean and land.

Two of the largest ice masses of the European Arctic (Vest- and Austfonna) and several smaller ice bodies (e.g. De Geerfonna) are located in the north-east of Svalbard, on Nordaustlandet. Little is known about the current state and variability of the surface energy balance (SEB) and surface mass balance (SMB) of these ice masses and their sensitivity to large-scale atmospheric forcing. The central goal of this work is to improve the understanding of atmosphere-cryosphere interactions on Arctic glaciers and in particular to investigate seasonality and variability of the climate in Svalbard and its impact on Vestfonna ice cap. A methodology combining field observations, remote sensing and numerical modeling is employed to provide detailed information about the state and sensitivity of SEB and SMB on Vestfonna, what meso-scale processes generate the changes and how these processes link the synoptic to the local process space during the first decade of the 21st century. This thesis also demonstrates how difficult it is to obtain field observational data and to reliably assess the current state and future development in the Arctic region.

The SEB and SMB on Vestfonna show the highest sensitivity of surface ablation rates to changes in radiation conditions. Surface albedo is identified as a key factor for ablation rate estimations on Vestfonna. The SMB on Vestfonna also shows high dependency on snowdrift, causing considerable mass loss in accumulation rates. An annual SMB rate on Vestfonna of $+0.02 \pm 0.22$ m w.e. yr^{-1} is calculated from a regional reanalysis, i.e. the

European Arctic Reanalysis (EAR), and an annual SMB rate of -0.02 ± 0.20 m w.e. yr^{-1} is calculated by an empirical approach for the mass balance years 2001 to 2009. The estimate derived from the EAR is assumed to be too high since snow drift is not considered in the accumulation rates, and a constant high surface albedo could have caused underestimations in ablation rates. On the other hand the empirical approach shows uncertainty in estimating the air-temperature fields and refreezing rates. Thus, combining results derived from both approaches, the "pessimistic" annual SMB rate on Vestfonna of about -0.09 ± 0.19 m w.e. yr^{-1} for the mass balance years 2001 to 2009 is estimated by using the higher ablation rates derived from EAR calculations and the lower accumulations rates derived from the empirical study.

The activity of the North Atlantic cyclone track shows strong influence on accumulation and ablation rates on Vestfonna. Since the North Atlantic Oscillation (NAO) is one of the most important indices of variability in the northern hemisphere atmospheric circulation, it also shows strong correlations with accumulation and ablation rates on Vestfonna. During winter, the NAO index significantly correlates with the frequency of cyclones from the North Atlantic sector through precipitation, air-temperature and wind speed. The moisture transported by the cyclones into the region during the winter season mainly determines the annual accumulation rates on Vestfonna. During summer, the NAO index significantly anti-correlates with local cyclogenesis and summer precipitation, generating variability in ablation rates on Vestfonna by complex feedback mechanisms between surface albedo, surface absorption of solar radiation and air-temperature.

All results indicate that the annual SMB rate was almost balanced on Vestfonna during the first decade of the 21st century. However, especially changes in the rain-snow ratio due to changes in air-temperature are assumed to have great potential to generate strong changes in the SMB rates on Vestfonna in the future.

Zusammenfassung

Die Arktis ist ein wichtiges Element des globalen Klimasystems. Zirkulationen der Atmosphäre und des Ozeans transportieren Energie vom Äquator in die hohen Breiten. In der Nordhemisphäre geschieht dies hauptsächlich durch Störungen der atmosphärischen Zirkulation (Zyklone und Antizyklone) in den mittleren Breiten und durch den Nordatlantikstrom. Die Inselgruppe Svalbard ist durch ihre Lage stark durch Sturmtiefs beeinflusst, die Feuchte und feuchtstatische Energie aus dem Nordatlantik in den Arktischen Ozean transportieren. Darüber hinaus erzeugen der Westspitzbergenstrom, der warmes Atlantikwasser nordwärts transportiert, und die fluktuierenden Eiskante des Nordpolarmeeres starke Klimagradienten mit inter- und intraannueller Variabilität, wobei die enge Kopplung von Atmosphäre, Ozean und Land maßgeblich das Klima Svalbards prägt.

Zwei der größten Eismassen der europäischen Arktis (Vest- und Austfonna) und etliche kleinere Eismasse (z.B. De Geerfonna) befinden sich im Nordosten Svalbards auf der Insel Nordaustlandet. Wenig ist über den momentanen Zustand, die Variabilität und die Sensitivität der Oberflächenenergiebilanz (SEB) und Oberflächenmassenbilanz (SMB) dieser Eismassen und den großräumigen Antrieb bekannt. Die zentrale Zielsetzung dieser Arbeit ist, das Verständnis der Wechselbeziehungen zwischen der Atmosphäre und der Kryosphäre bezogen auf Arktische Gletschersysteme zu verbessern. Im Speziellen sollen die Saisonalität und Variabilität des Klimas Svalbards und der damit verbundene Einfluss auf die Vestfonna-Eiskappe untersucht werden. Die angewandte Methodik kombiniert Felduntersuchungen, Fernerkundung und numerische Modellierung, um den Zustand und die Sensitivität der SEB und der SMB des Vestfonna, die steuernden mesoskaligen Prozesse und die Art und Weise, wie diese Prozesse den synoptischen und lokalen Prozessraum verbinden, für die erste Dekade des 21. Jahrhunderts zu untersuchen. Diese Arbeit zeigt auch, wie schwierig es ist, Felddaten in der Arktis zu erheben und zuverlässig den momentanen und zukünftigen Zustand in der Arktis abzuschätzen.

Die Oberflächenablationsraten des Vestfonna sind stark durch die Strahlung gesteuert, wodurch die Oberflächenalbedo als ein entscheidendes Schlüsselelement zur Abschätzung der Ablationraten identifiziert wurde. Darüber hinaus beeinflusst der Masseverlust durch windgesteuerte Schneeverfrachtung erheblich die Akkumulationsraten und stellt damit ein

weiteres wichtiges Element der SMB des Vestfonna dar. Aus einer regionalen Reanalyse, der European Arctic Reanalysis (EAR), wurde eine jährliche SMB von +0.02 ± 0.22 m w.e. yr^{-1} und aus einem empirischen Ansatz eine jährliche SMB von −0.02 ± 0.20 m w.e. yr^{-1} für den Vestfonna als Mittelwert der Massenbilanzjahre 2001 bis 2009 berechnet. Da das für die EAR verwendete Modell keinen Masseverlust durch Schneeverwehungen berechnet und zusätzlich zu hohe Oberflächenalbeden annimmt, sind die Akkumulationraten bei diesem Ansatz wahrscheinlich über- und die Ablationsraten unterschätzt worden. Der empirische Ansatz zeigt hingegen starke Unsicherheiten in der Abschätzung des Temperaturfeldes und der Wiedergefrierraten. Eine Kombination der höheren Ablationsraten der EAR und der niedrigeren Akkumulationsraten des empirischen Ansatzes ergeben eine jährliche SMB des Vestfonna von −0.09 ± 0.19 m w.e. yr^{-1} als Mittelwert der Massenbilanzjahre 2001 bis 2009.

Sturmtiefs aus dem Nordatlantik zeigten starken Einfluss auf die Akkumulations- und Ablationsraten des Vestfonna. Da die Nordatlantische Oszillation (NAO) einer der wichtigsten Indizes für den Modus der atmosphärischen Zirkulation der Nordhemisphäre ist, zeigte dieser Index auch Korrelationen mit den Ablations- und Akkumulationsraten des Vestfonna. Im Winter korrelierte der NAO-Index signifikant mit der Häufigkeit der eintreffenden Sturmtiefs aus dem Nordatlantik, welche stark auf Niederschlag, Lufttemperatur und Windgeschwindigkeit wirkten. Dabei wurde die jährliche Akkumulationsrate des Vestfonna hauptsächlich durch den mit den Sturmtiefs verbundene Feuchtetransport im Winter geprägt. Im Sommer anti-korrelierte der NAO-Index signifikant mit der lokalen Zyklogenese und den damit verbundenen Niederschlägen. Die Analysen induzieren, dass die Ablationsraten des Vestfonna hierbei durch komplexe Rückkopplungen zwischen Niederschlag, Oberflächenalbedo, Absorption solarer Strahlung und Lufttemperatur gesteuert wurden.

Alle Ergebnisse zeigen eine fast ausgeglichene SMB des Vestfonna für die erste Dekade des 21. Jahrhunderts. Dennoch birgt die enge Kopplung der Ablationsraten an das Regen-Schnee-Verhältnisses über die Lufttemperatur ein großes Potential für zukünftige Änderungen der SMB des Vestfonna.

List of figures

List of tables

1 Introduction

1.1 Motivation

Warming of the global climate system is indisputable since the IPCC Fourth Assessment Report (IPCC, 2007). Observations in all continents document the impact of regional climate change on natural systems while Polar regions experience the strongest regional warming on Earth. Nevertheless, great regional differences are observable (e.g. ACIA, 2005; AMAP, 2012).

The Arctic is an important element in the global climate. It works in concert with the Antarctic to set up the large-scale circulation patterns and teleconnections that make our planet habitable (e.g. Barber et al., 2008). Circulations of the atmosphere and the ocean transport energy from the equator to high-latitudes. In the northern hemisphere this is mainly done by transient disturbances of the atmospheric circulation (cyclones and anticyclones, low- and high-pressure regions) at mid-latitudes and the North Atlantic Current (e.g. Tsukernik et al., 2007; Sorteberg and Walsh, 2008; Walczowski and Piechura, 2011; Rudels, 2012). Property changes in the Arctic such as snow or ice cover therefore influence the energy balance of the whole Earth and its seasonality and vice versa.

Meanwhile great changes in the Arctic environment are observable (e.g. Gardner et al., 2011; Berthier et al., 2010; Moholdt et al., 2012). Arctic glaciers and ice caps are assumed to be major contributors to global sea level rise (e.g. Arendt et al., 2002; Berthier et al., 2010; Wu et al., 2010). Kaser et al. (2006) estimate Arctic glaciers (without Greenland) to be responsible for one fourth of the sea level rise since 1960 and other studies (e.g. Raper and Braithwaite, 2006; Meier et al., 2007; Bahr et al., 2009) indicate a future increase since most Arctic glaciers are located in the region of the greatest predicted temperature increase during the next decades (e.g. Rinke and Dethloff, 2008).

However models used in current climate projections show the largest differences between individual results in the Polar regions (e.g. Stroeve et al., 2007). Results of remote sensing studies like Jacob et al. (2012) stay in contrast to traditional mass balance estimates (e.g. Bamber, 2012). In this context Mölg and Kaser (2011) point out problems of traditional multiscale mass balance studies since they often bypassed the mesoscale process space by

statistical transfer functions or subgrid parameterizations and included simplified glacier mass balance models. Furthermore, other studies (e.g. New et al., 2002; Førland and Hanssen-Bauer, 2003; Kristjánsson et al., 2011) point out that the knowledge of the Arctic climate system suffers from a prominent lack of observational data compared to other regions. This indicates great uncertainty about the current state and future development in the Arctic region.

Thus, the central goal of this work is to improve the understanding of atmosphere-cryosphere interactions on Arctic glaciers. Little is known about the current state and variability of the surface energy balance (SEB) and surface mass balance (SMB) of two of the largest ice masses of the European Arctic, i.e. Vest- and Austfonna ice caps. Therefore, this work adds new data on current state and variability of SEB and SMB components of Vestfonna ice cap and their sensitivity to large-scale atmospheric forcing in the first decade of the 21st century. An overview of the general research concept is presented in Figure 1.1.

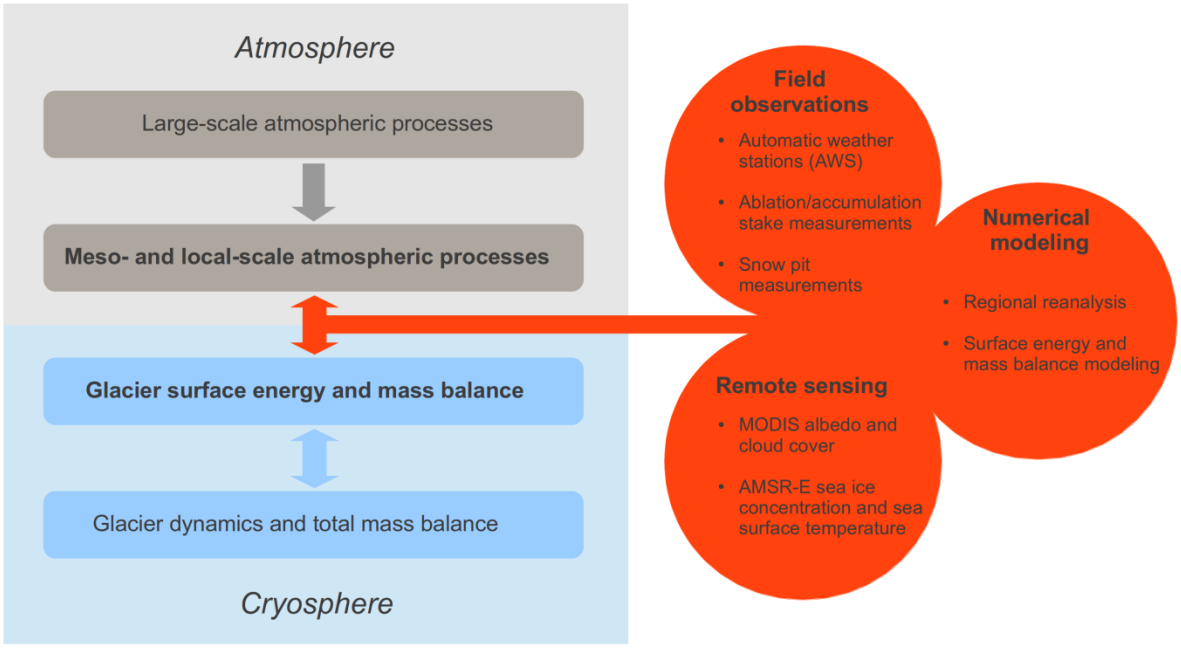

Figure 1.1 *General research concept.*

The research strategy comprises methods of field observation, remote sensing and numerical modeling to investigate the cryosphere-atmosphere interactions by complementary approaches. Field observational data is used to analyse the involved

processes, to calibrate and optimize the SEB/SMB and meso-scale atmospheric modeling (regional reanalysis). Complementary data sets derived from remote sensing, global tropospheric analyses and reanalyses are used in the analyses and for model forcing providing data on large-scale climate variability. Thus, numerical modeling forms a key element in this study by linking the large-scale variability to the local-scale at the cryosphere-atmosphere interface and provides distributed data sets on high spatiotemporal resolution for further analyses. Specific objectives of this work are defined in Section 1.3.

This thesis is part of the research projects “Dynamic Response of Surface Energy and Mass Balance of Vest- and Austfonna (Nordaustlandet, Svalbard) on Climate Change” funded by grants no. BR 2105/6-1, SCHE 750/3-1, SCHE 750/3-2, SCHN 680/2-1, SCHN 680/2-2 of the German Research Foundation (DFG) and “Sensitivity of Vestfonna to climate change” funded by grants no. 03F0623A and 03F0623B of the German Federal Ministry of Education and Research (BMBF). Both projects are part of the international project frameworks “GlacioDyn”, “IPY – Kinnvika” and “ESF - SvalGlac”. The origin and relation of these project frameworks are briefly summarized in the following paragraphs.

1.2 “GlacioDyn”, “IPY – Kinnvika” and “ESF – SvalGlac”

Coordinated international science programmes like the International Polar Year (IPY) 2007/2008 or the European Polar Board programme PolarCLIMATE of the European Science Foundation (ESF) have been established to improve the knowledge about the Polar regions.

Six scientific themes have been defined within the IPY framework.

- **Status**: to determine the present environmental status of the Polar regions;
- **Change**: to quantify and understand past and present natural environmental and social change in the Polar regions and to improve projections of future change;
- **Global linkages**: to advance understanding on all scales of the links and interactions between Polar regions and the rest of the globe and of the processes controlling these;
- **New frontiers**: to investigate the frontiers of science in the Polar regions;
- **Vantage point**: to use the unique vantage point of the Polar regions to develop and enhance observatories from the interior of the Earth to the sun and the cosmos beyond;

- **The human dimension**: to investigate the cultural, historical and social processes that shape the sustainability of circumpolar human societies and to identify their unique contributions to global cultural diversity and citizenship.

The IPY efforts to organize and implement structures and strategies for science frameworks, data management, outreach, communication and education have led to the formation of large international scientific consortia for research on the response of Arctic glaciers to climate change. Among others two fully endorsed IPY core activities, namely "GlacioDyn" and "IPY - Kinnvika", have been established aiming on the dynamics of a key set of Arctic glaciers, using observational techniques and models for data aggregation and analysis. Herein "IPY – Kinnvika" particularly focuses on the northernmost terrain of the European Arctic: Nordaustlandet, Svalbard. Several investigations have been started and a field infrastructure has been established. Most of these efforts have been continued by the subsequent "ESF – SvalGlac" project within the European Polar Board programme "PolarClimate".

1.3 Aims and outlines of this thesis

This work addresses the topics (1) field observations (2) glacier surface energy and mass balance and (3) linking the synoptic to local process space by asking the following research questions.

I. Which expedition procedures and which methods for measuring surface energy and mass balance components and atmospheric variables are practical and applicable in the region of Vestfonna ice cap?
II. What is the current state and sensitivity of the surface energy and mass balance of Vestfonna ice cap?
III. Which large-scale processes produce changes in surface energy and mass balance components on Vestfonna ice cap and how do these process chains link the synoptic to the local process space?

A large part of this work was to set the basis for the analyses. Field campaigns, using automatic and manual measurements, had to be conducted in the region of Vestfonna ice cap and a powerful computational modeling and analysis infrastructure had to be established. These efforts will be briefly presented in addition to the applied analytical work.

Research question I is mainly addressed by analyzing field work. Research question II and III are addressed by modeling approaches, though field work was crucial to obtain the calibration and validation data.

This thesis is organized into four main parts excluding, the introduction. Chapter 2 introduces the study region. A methodical overview is given in Chapter 3. The results are discussed and analyzed in Chapter 4 and conclusions are drawn in Chapter 5.

2 Study region

2.1 Overview

The study region of this work is Svalbard, an archipelago in the North Atlantic and Arctic Ocean far north of the Arctic Circle (see Figure 2.1). The Svalbard archipelago comprises a land area of about 63,000 km^2 (Hisdal, 1976) consisting of various islands, islets and rock stacks. The biggest island Spitsbergen (~39,000 km^2) is separated by the Hinlopen Strait from the second largest island Nordaustlandet (~14,600 km^2) and by Storfjorden from the third largest island Edgeøya (~5,000 km^2). Most of the archipelago is covered by glaciers, ice fields and ice caps. Svalbard comprises about 13 % (~36,600 km^2) of the ice-covered land areas (~272,700 km^2) of the whole Arctic (Dowdeswell et al., 1997).

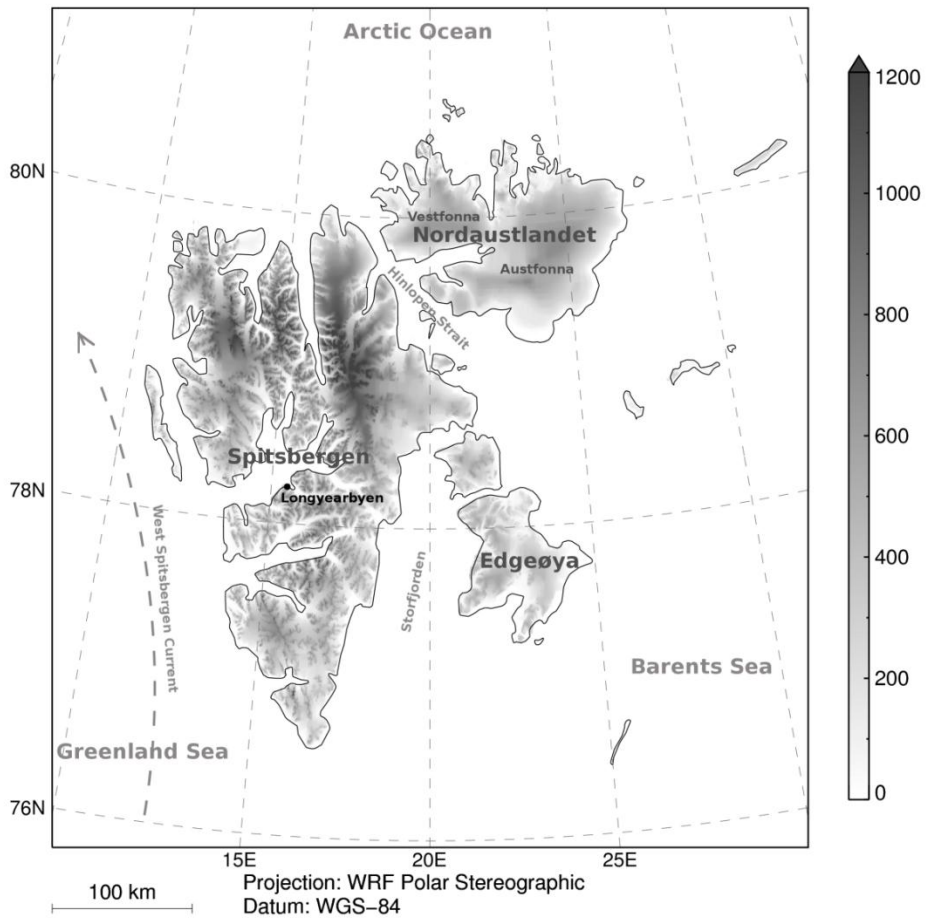

Figure 2.1 *Overview of the Svalbard study region. Shading indicates the terrain height.*

Two of the largest ice masses of the European Arctic (Vest- and Austfonna) and several smaller ice bodies (e.g. De Geerfonna) are located in the north-east on Nordaustlandet. Austfonna is the largest (8,120 km^2) and Vestfonna the second largest (2,340 km^2) single ice body of Svalbard (Hagen et al., 2003; Braun et al., 2011). The field observational data was gathered and surface energy balance (SEB) and surface mass balance (SMB) studies conducted in the region of Vestfonna (see Figure 2.2), a polythermal ice cap approximately 1,100 km south of the North Pole. Vestfonna has a dome-like shape with altitudes up to 647 m a.s.l. (see Figure 2.2). Two large ridges form the highest points of Vestfonna stretching across the central parts in east-west and north-south directions. Vestfonna drains through several outlet glaciers most of them terminating in the ocean.

The climate of Svalbard is characterized by close couplings between atmosphere, ocean and land. Svalbard lies in the border zone of cold Arctic air from the Polar Basin and mild maritime air over the oceans towards the south (e.g. Hisdal, 1976). Svalbard is strongly influenced by the activity of the North Atlantic cyclone track transporting moisture and moist static energy (sensible heat, latent heat and geopotential) into the region (e.g. Tsukernik et al., 2007; Sorteberg and Walsh, 2008). This and the North Atlantic Current (i.e. the West Spitsbergen Current) generate a maritime climate characterized by cooler summers and warmer winters than generally found at comparable latitudes. Furthermore, strong climate gradients with interannual and intra annual variability are generated by the interaction of the West Spitsbergen Current transporting warm Atlantic water northward and the fluctuating sea ice margin (e.g. Walczowski and Piechura, 2011). The warm ocean current can reach Nordaustlandet only by circling around the northern top of Spitsbergen (see Figure 2.1) due to the complex Barents Sea bathymetry, while sea ice formation and southward transportation is generally stronger in the eastern sea regions of Svalbard (e.g. Nghiem et al., 2005). This makes Nordaustlandet one of the coldest regions of Svalbard. Furthermore, the high latitudinal position makes the annual rotation of polar day and polar night an important amplifier of seasonal features in Svalbard and in the Vestfonna region.

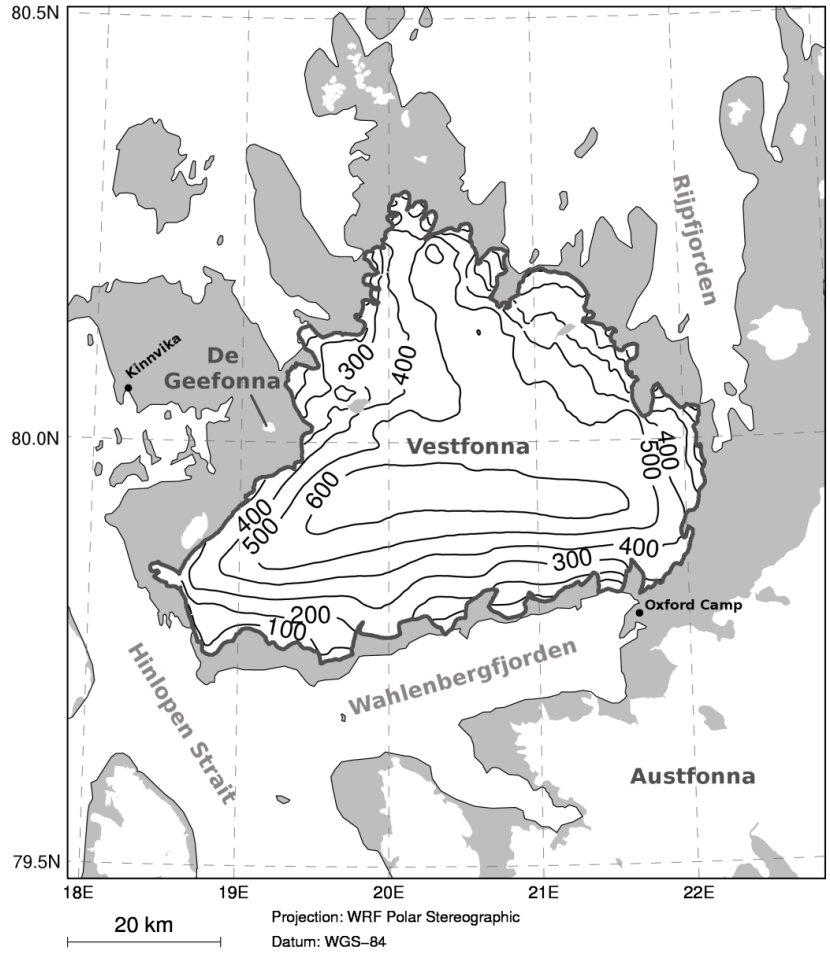

Figure 2.2 *Overview of the Vestfonna study region. Contours indicate terrain height on Vestfonna.*

2.2 Previous work in the region of Vestfonna

2.2.1 Weather and climate observations

The first reported scientific expedition on Nordaustlandet (Torell and Nordenskjöld) was in 1861 (Chydenius, 1865). Herein, only some generalised weather observations were mentioned. In 1873 an expedition by Nordenskiöld produced some general data on air pressure and air-temperature (Barr, 1988; Ahlmann, 1933). Between 1899 and 1902 the expedition for measuring an arc of meridian on Svalbard took place (De Geer, 1923). It is likely that some measurements were carried out besides the survey of Nordaustlandet. The first comprehensive description of various atmospheric variables (air pressure, air-temperature, humidity, clouds, sun, wind and precipitation) covering nearly a month was

obtained by “The Oxford University Arctic Expedition” in 1924 led by F.G. Binney (Tymms, 1925; Sandford, 1926). Seven years later H.W. Ahlmann led “The Swedish-Norwegian Artic Expedition” (Ahlmann, 1933; Angström, 1933; Eriksson, 1933). Data sets of differing temporal resolution (general, daily and hourly observations) for several locations were published for the period 29th June to 10th August 1931. Observations on humidity, air pressure, clouds, fog, visibility, precipitation, air-temperature, wind speed and direction, radiation and the general weather situation were provided. “The Oxford University Arctic Expedition” led by A.R. Glen in 1935-36 brought the first winter data (Glen, 1937 and 1939). Several sites were observed between September 1935 and August 1936. Monthly and daily data sets have been found for observations on snow, wind speed and wind direction, air pressure, air-temperature, sun hours, clouds and rain. At the end of the Second World War the German weather station “Haudegen” was operating near Rijpfjorden district (see Figure 2.2) between 13th September 1944 and 5th September 1945 (Dege, 1960). Observations on air pressure, air-temperature, humidity, visibility, weather situation, wind speed and direction, clouds and precipitation were carried out every three hours. Daily radiosonde data and general observations are also available. In Thompson (1953) weather observations are mentioned for the Oxford expeditions led by Hartog in 1949 and 1951. Also an Oxford expedition to Nordaustlandet in 1955 was mentioned in Donner and West (1957), but no data could be found. During the International Geophysical Year (IGY) in 1956-58 the Kinnvika research station was build (see Figure 2.2). Weather measurements have only been found in Swedish for 1957-58 at Kinnvika (Liljequist, 1959; Schytt, 1964; Ekman, 1971; Palosuo, 1987a). Monthly means and general observations of air pressure, air-temperature, wind speed and wind direction, precipitation, clouds and sun hours were found. So far no weather data could be found for the Swedish expedition (Stockholm University) led by V. Schytt in 1966 (Schytt, 1967; Schytt et al., 1968). Martma (pers. com.) mentioned weather observations for Kinnvika and a drill site on Vestfonna covering a few weeks in 1981. In Arkhipov et al. (1987) general and daily observations of air pressure, air-temperature, wind and precipitation were published, which covered a few weeks in 1985 at a drill site at Austfonna. Another ice core drilling took place in 1987 but it is unclear if weather observations were carried out. Blake (2006) mentioned a Nordaustlandet-90 expedition which could not be proven through further references. In 1995 the Japanese Arctic Glaciological Expedition (JAGE) observed air-temperature, air pressure, weather situation,

visibility, wind and clouds twice a day at a drilling site at Vestfonna between 19th May and 11th June (Motoyama et al., 2001; Motoyama, pers. com.). Another JAGE produced hourly observations on air-temperature, wind speed and humidity for a drilling site at Austfonna between 9th March and 19th April 1998 (Watanabe et al., 2000; Motoyama et al., 2001; Kameda, pers. com.). The JAGE 1999 observed the same variables as JAGE 1995 at another drilling site at Austfonna between 26th April and 30th May 1999 (Motoyama et al., 2001; Motoyama, pers. com.). Continuous automatic weather station (AWS) measurements started on Nordaustlandet in April 2004, when two AWSes were installed on Austfonna (Schuler et al., 2007). In 2007 an additional AWS was set up by The University Center in Svalbard (UNIS) at the coast line of Rijpfjorden.

The weather observations before 2004 were mostly manually measured and consist of disconnected time series. Only three data sets (1935-36, 1944-45 and 1957-58) provide continuous observations for nearly a whole year. All other data sets cover a few weeks up to a few months. Most expeditions were highly influenced by weather or sea ice conditions. So most data was found for periods between May and August while other months, i.e. the winter season, are barely covered.

2.2.2 Glaciological studies

Although earlier explorations in the region of Vestfonna were carried out The Oxford University Arctic Expedition in 1924 was the first exploration of inner parts of Vestfonna. Sandford (1925) described the general shape and morphology of the ice cap including its drainage characteristics on crevasses and moraines. The first overview of the glaciological conditions on Vestfonna was given by Sandford (1929). The Swedish-Norgwegian Arctic Expedition in 1931 carried out detailed analyses of the general snow-pack evolution during the ablation season including the transient snow-line altitude of the glaciated areas on Nordaustlandet (Ahlmann, 1933). Fjeldstad (1933) described the snow and firn stratification in the accumulation area of Vestfonna and published several snow and firn-temperature profiles. The Oxford University Arctic Expedition in 1934/35 studied Vestfonna for a 14-month-period (Glen, 1939). Moss (1938) presented detailed measurements of the snow and firn-temperature. He also discussed the impact of wind drift in connection with observed accumulation processes on Vestfonna. The first comprehensive overview on Vestfonna ice

cap and all glaciated areas on Nordaustlandet was given by Glen (1939 and 1941). Further glaciological studies were carried out during the International Geophysical Year 1957/58 (Schytt, 1964). Palosuo (1987a and 1987b) presented first studies of refreezing of melt water on Vestfonna and point energy balance studies including descriptions of the temperature distribution and evolution in the upper 10 m of a glacier. Ice cores were drilled at Ahlmann Summit in 1981 and at the second peak further east in 1995 (Vaykmyae et al., 1985; Punning et al., 1986; Sinkevich, 1991; Pinglot et al., 1999; Kotlyakov et al., 2004). The ice core studies provided the first data on paleoclimate reconstructions in the region of Vestfonna and Svalbard-wide accumulation patterns. First data of snow chemistry resulted from field work within the "IPY-Kinnvika" core project (Beaudon and Moore, 2009).

3 Materials and methods

3.1 Field observations

The study area was Nordaustlandet, Svalbard, where the two ice caps Vest- and Austfonna form the largest ice masses of the European Arctic (see Figure 2.2). The field measurements comprised meteorological-climatological investigations by AWSes installed on or close to Vestfonna as well as mass-balance observations on Vestfonna and De Geerfonna.

3.1.1 Field work

Nine field campaigns have been conducted between May 2008 and June 2012 in the region of Vestfonna (see Figure 2.2). In May 2008 a measurement network comprising six AWSes and 24 ablation stakes were installed and the first manual measurements were conducted (see Figure 3.1). During the following campaigns the measurement systems were maintained and further manual observations were gathered. The measurement methods are described in the following sections. In 2009 four AWSes and nine ablation stakes were removed. In 2012 the last two AWSes and the remaining 15 ablation stakes were removed.

Except for the dismounting campaign in 2012 all field work was scheduled so that one field campaign took place before and one after the ablation season. Depending on weather conditions and scheduled tasks a campaign took one to three weeks of field work. In spring only transportation by helicopter from Lonyearbyen to Nordaustlandet was possible due to the sea ice situation. Snowmobiles could be used during four spring campaigns for field work on Nordaustlandet. All other campaigns were conducted by foot operations. Two summer campaigns were completely based on ship logistics. During the other two summer campaigns the team was dropped by helicopter in the field and brought back to Longyearbyen by ship.

During spring campaigns the use of snowmobiles and the old Kinnvika research station (see Section 2.3.1) as a logistical base was possible until it was prohibited in the end of 2009 by the Governor of Svalbard due to cultural heritage issues. For the last two spring campaigns the use of snowmobiles and a fortified camp at Oxfordhalvøya of Norwegian project partners (PI Hagen) doing research on Austfonna was granted (see Figure 2.2). During

campaigns without skidoo logistics these sites could not be used as bases since mobility in the field was strongly limited due to foot operations.

Temporary camps comprising a kitchen tent and sleeping tents were established during field work close to the measurement sites. The only exceptions were the two campaigns where a ship was used as the logistical base and day trips by foot to the respective measurements sites were carried out. During all other campaigns the team stayed most of the time in the temporary tent camps on the glacier.

The team comprised three to four members. Shifting night watches and bear fences were established at the camp sites during each campaign. For bear defence two firearms and signal pistols with flares were always available. Beside the risk of polar bear attacks also storms, crevasses and slush flows endangered the field work. Therefore the team was in addition to the rifles and signal pistols equipped with four GPS systems, two satellite phones, an emergency beacon and a comprehensive medical pack. Some examples of the logistics and equipment are presented in Appendix F.

Funding of the field work was granted by the DFG and BMBF within the projects “Dynamic Response of Surface Energy and Mass Balance of Vest- and Austfonna (Nordaustlandet, Svalbard) on Climate Change” and “Sensitivity of Vestfonna to climate change”. Logistical support was given by Alfred Wegener Institut (AWI), Norsk Polarinstitutt (NPI), the Swedish Polar Research Secretary (SPRS) and the Polish Research Vessel Horyzont II (Akademia Morska, Gdynia).

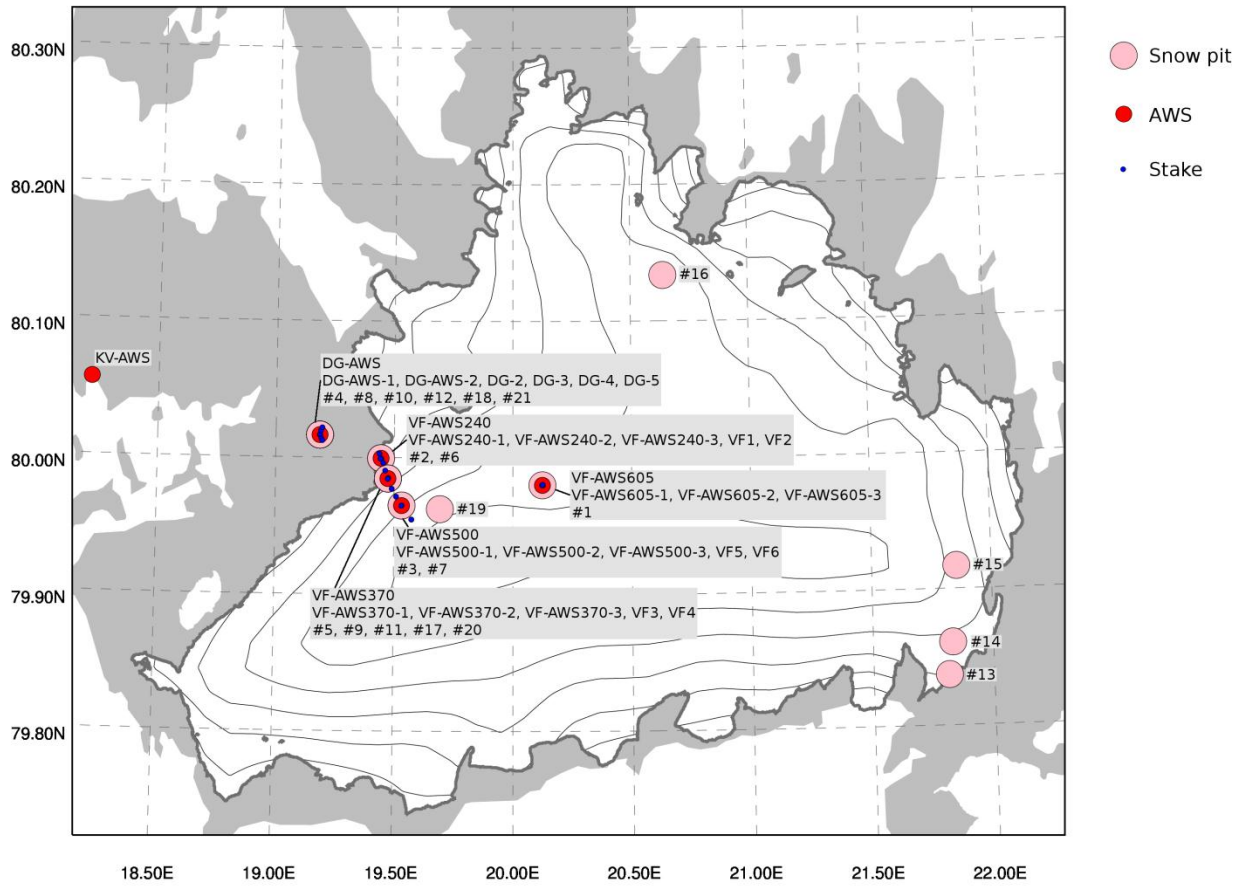

Figure 3.1 *Overview on measurements in the Vestfonna region. Contours indicate terrain height on Vestfonna. Pink dots are snow pit sites, red dots are AWS sites and blue dots are ablation/accumulation stakes locations. At sites of multiple measurements labels AWS names are indicated in the first line, ablation/accumulation stake name in the second line and snow pit number in the third line.*

3.1.2 Automatic measurement systems

Six AWSes were installed in the region of Vestfonna in May 2008 (see Figure 3.1). A small and a large AWS setup was used (see Figure 3.2 and Table G.1) at different measurement sites. Except for KV-AWS the aluminium tube constructions were set up on snow and ice surfaces. Each mast of the AWS was drilled 2 m into the ice and wired with three anchor stakes which were also drilled 2 m into the ice. At KV-AWS the anchors and masts were fixed by heavy stones on solid ground. Solar panels were used to recharge the batteries when solar radiation was available. During yearly field campaigns at the beginning and the end of

the ablation season the measurement systems were maintained and recorded data was gathered.

Small AWS setup *Large AWS setup*

Figure 3.2 *Automatic weather station (AWS) setups.*

All stations recorded air-temperature, relative humidity, short-wave radiation fluxes, net radiation, vertical profiles of soil and ice temperature and surface displacement. The AWS inclination was recorded (VTI Technologies, SCA111T) and radiation shields for the air-temperature sensors were ventilated by connecting the fans directly to solar panels, thus minimizing radiation errors. Some stations also measured long-wave radiation fluxes, wind speed and direction, atmospheric CO_2 and water vapor concentration, three-dimensional wind components and virtual acoustic air-temperature, soil and ice heat flux and water content. CR800 and CR1000 (Campbell Sci.) loggers were used. For wind variables aggregation methods were used. All other variables were measured and stored as instantaneous samples. Storage rates changed over time. (See Tables in Appendix G for further details.)

Precipitation values are one of the most serious uncertainties in the Arctic due to severe measuring problems (e.g. Førland and Hanssen-Bauer, 2003). Manual measurements of snow water equivalent (SWE) require a considerable effort, which is why several automatic methods for single-point SWE estimates have been developed. Egli et al. (2009) compared different automatic methods for estimating snow water equivalent. In their assessment the snowpillow technique performed best followed by techniques measuring the snow depth

and estimating bulk snow densities. Gauges and laser-based optical systems performed worst. Even if the snowpillow had performed better its installation and maintenance require a considerable effort. Thus, a sonic ranger (e.g. Goodisen et al., 1988) measuring of the snow depth was used in this study and the bulk snow densities were determined from snow pit observations.

3.1.3 Manual measurements

A network consisting of 24 ablation/accumulation-stakes has been installed in the region of Vestfonna in May 2008 (see Figure 3.1). Manual measurements of snow depth and ice surface height changes were carried out at the ablation/accumulation-stakes. A total of 88 successful repeat readings were retrieved during the field campaigns between May 2008 and June 2012 (see Table J.8). Additionally manual measurements of snow water equivalent and bulk snow densities as well as profiles of snow temperature, snow density, grain size, grain type and snow stratigraphy were carried out in 21 snow pits (see Table J.9) during these campaigns. Locations of snow pits were distributed across the ice cap (see Figure 3.1). Examples of an ablation/accumulation-stake and a snow pit measurement are shown in Figure 3.3.

Ablation/accumulation-stake

Snow pit

Figure 3.3 *Examples of ablation/accumulation-stake and a snow pit.*

Snow pit locations were chosen where they were undisturbed by snowmobile or foot tracks. Each pit was excavated at least down to the respective previous end-of-summer surface. North facing walls were chosen for snow sampling to diminish disturbance by sunshine.

Excavated snow was placed aside of the pit, avoiding influences on the edge of the sampling wall. Access to the deeper parts of the pits was assured by construction of several steps opposite to the test walls. The stratigraphic records acquired from the test walls comprise layering, hardness, density and/or temperature of the snowpack. Layering was determined according to snow-hardness classifications along the profile and visual inspection of the test wall regarding varying grain characteristics. Snow hardness itself was classified using the hand hardness test. Measurements of snow density were performed using different metal tube density samplers. Ice layers and wind or melt crusts within the snow pack that could not be measured separately were treated in different ways. A density of 800 kg m^{-3} was assigned to ice layers. Crusts created by strong wind drift or temporal melt events were not treated separately but were sampled together with the over and/or underlying snow layers. They were thus not allocated a specific density. Snow temperature was measured using handheld thermometers with attachable metal probes.

The ablation/accumulation-stakes have been metered by measuring the distance between the snow surface and a fixed reference mark above the snow surface on the stake using a measuring tape.

3.2 Modeling and analysis framework

3.2.1 Hardware

A complex computational infrastructure has been established to set the basis for the applied modeling and analyses in this thesis. The infrastructure comprises 26 computing nodes, two controlling nodes and a 138 TB pool of network attached storage (NAS) distributed over three separate locations (see Figure 3.4) and wired by a Gigabit LAN network. Specifications of the hardware can be found in Tables in Appendix H. Extensive testing of hardware, customised software installation and development was carried out. The computing infrastructure can be distinguished into two subsequent frameworks: a framework exclusively for modeling tasks and an additional framework for data analyses, product generation, data storage and backup tasks (see Figure 3.5).

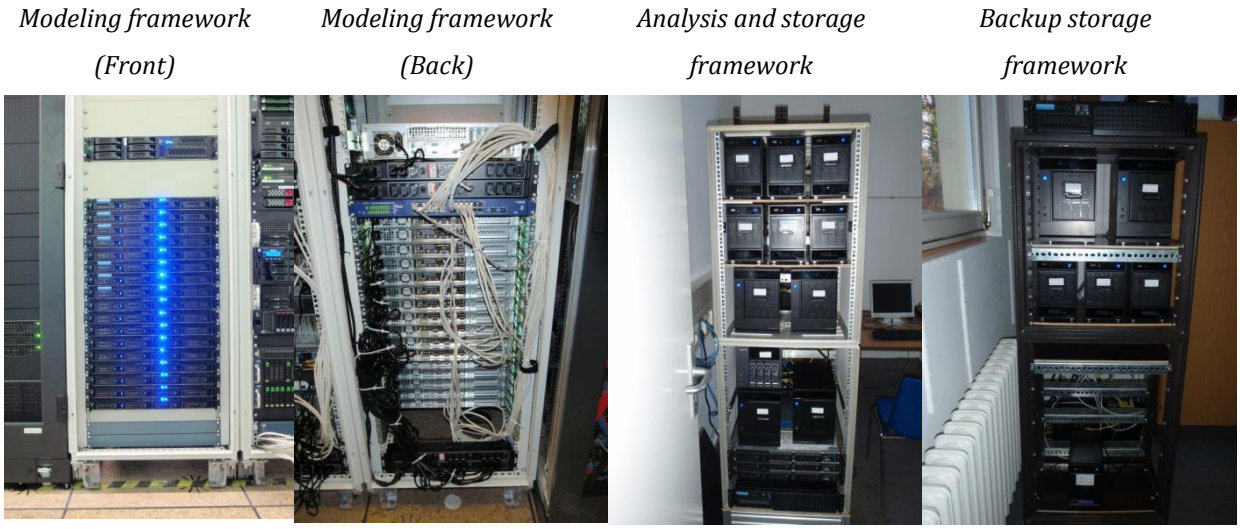

Figure 3.4 *Computer infrastructure.*

3.2.2 Software

Software addressing various tasks had to be developed to achieve the results of this thesis. Data sets had to be pre-processed, distributed, gathered, post-processed, stored, analyzed and backed up. Processing of data and modeling had to be controlled and logged, and tools for detailed data analysis had to be developed and adjusted. Key areas of this software development work are outlined schematically for an exemplary data processing chain in Figure 3.5.

Debian GNU/Linux 6.0.1 was used as the operating system in all the computing systems. As pointed out earlier the developed data processing software can be separated into two main frameworks, i.e. the modeling software framework and the analysis and storage software framework (see Figure 3.5). Both frameworks are separated by software and by location, i.e. the modeling framework is located in the IT-Service-Center of the Technische Universität Berlin (tubIT) and the analysis and storage framework is located in two rooms of the Department of Ecology of the Technische Universität Berlin (see Figure 3.4).

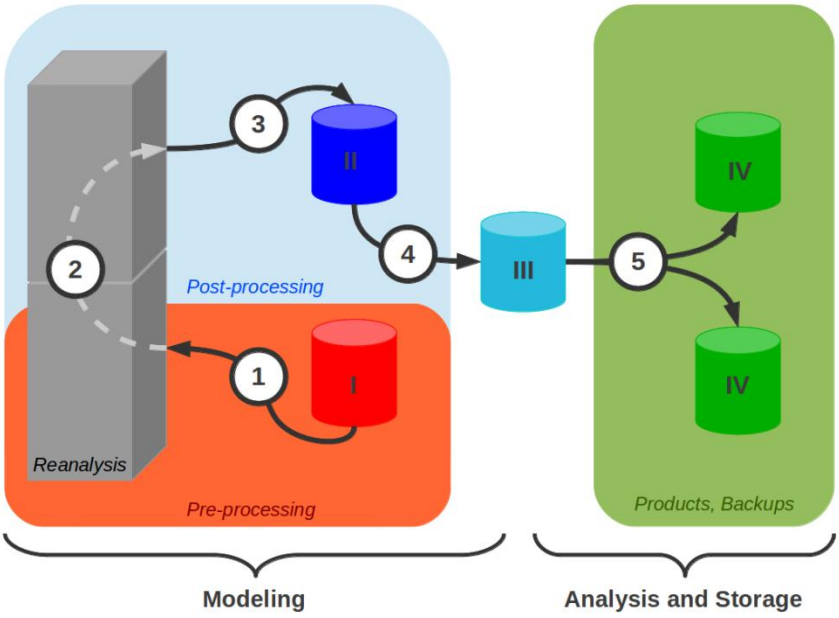

Figure 3.5 *Areas of software development within the established data processing chain. Roman numerals indicate states of data processing: Input data (I), raw model output (II), post-processed model output (III), products and analyses from post-processed model output (IV). Arabic numerals indicate section of software development: Input data pre-processing (1), job distributing, controlling and logging within the modeling cluster (2), gathering of model results and garbage collection within the modeling cluster (3), post-processing of raw model output (4), product generation, analyses and data backup (5).*

The modeling software framework is mainly based on the open source batch-queuing system Sun Grid Engine (SGE), developed and supported by Sun Microsystems. This software was installed on all nodes of the modeling framework. On this basis Apache Ant, a software tool for automating software build processes, was used to develop, define and run modules of data processing chains on the individual computing nodes. These modules integrate various binaries and scripts written in JAVA, C, C++, Fortran, Shell scripting, Perl, NCL and CDO for pre-processing, modeling and post-processing tasks. In addition an interface for automated recording of all important metadata of the conducted data processing or modeling in a MySQL data base was developed and integrated. The model used in this thesis and data sets for the regional reanalysis within this framework are described in detail in Section 3.3.3.

The programming language IDL (Interactive Data Language) was mainly used for data analysis. The developed programs are partly based on preexisting IDL libraries (TNT and WAVE) at the Chair of Climatology. A major task is to produce “easy to use” products for

project partners and own analyses from the regional reanalysis data. Furthermore, IDL was used to do individual data analyses and plots also part of this thesis. Beside this a backup concept was developed and realized by Perl and Shell scripts. Herein the rsync software application and the cron daemon, a time-based job scheduler in Unix-like computer operating systems, were used to handle all data storage and backup tasks automatically.

3.3 Analytical methods

3.3.1 Measurement quality assessment

The quality of automatic measurements is assessed by the availability of valid data. Thus, a strict filtering method was developed and applied to identify invalid data in the records. The first filtering method was a cross checking of values of different variables at the considered AWS to reveal malfunctions or other problems. The tilt sensor was used to identify station overturn (exceeding of 20° difference from perpendicular) and to correct radiation and surface displacement measurements by the measured angle. For upward facing radiation sensors the short wave albedo was used to reveal and mask periods of coverage and shading (i.e. riming, snow and ice coverage). For combined air-temperature and humidity sensors both variables had to be in a valid range. At ultra-sonic anemometers measurements of all three directions in space (u, v and w) and of the acoustic temperature had to be valid. The second filtering level included a range checking of the remaining values. Range limits for the diverse variables are presented in Tab 3.1. In the case of surface displacement an upper limit was set to the distance of the ice or soil surface, where it had been manually measured. Also a difference of more than 0.2 m from daily mean was filtered out. Finally, extremes and periods of known malfunction were masked manually in the data.

Table 3.1 *Validity ranges for measured variables.*

Variable	Range
Air temperature	-50 °C to 30 °C
Relative humidity	0 % to 100 %
Up and Down-welling short-wave radiation	0 Wm^{-2} to 1367 Wm^{-2}
Downwelling long-wave radiation	100 Wm^{-2} to 500 Wm^{-2}
Upwelling long-wave radiation	100 Wm^{-2} to 400 Wm^{-2}
Net radiation	300 Wm^{-2} to 800 Wm^{-2}
Wind speed	0 ms^{-1} to 80 ms^{-1}
Wind direction	0° to 360°
Air pressure	800 hPa to 1100 hPa
Surface displacement	> 0.4 m

The resulting filtered data was used to calculate the percentage of monthly valid data. The number of records representing 100 % was calculated from the storage intervals. In months comprising less than 50 % of valid data the cause of error or failure was tried to be determined. Besides no and unknown failures five additional failure categories have been defined as described in Table 3.2. The respective categories have been used at each AWS and sensor to assess the measurement quality and general problems.

Table 3.2 *Categories of measurement failures.*

Category	Description
N	No failure. Data availability is greater or equal to 50 %.
C	Failure of the physical AWS setup due to climate conditions, e.g. station fell over due to strong wind, riming or ablation.
E	Failure in the electric system, e.g. AWS ran out of power or short-circuited due to melt water.
A	Failure caused by animals, e.g. cables damaged by polar foxes or polar bears.
S	Sensor failure, e.g. corrosion of the sensor head.
P	Failure due to bug in logger program.
U	Unknown cause.

Concerning the manual measurements, i.e. ablation/accumulation stake readings and snow pits measurements, the spatiotemporal distribution and availability is briefly discussed.

Some of the data derived from snow pit measurements are also analyzed in Paper I. Furthermore, the availability of manual measurement data is strongly connected to the general success of a certain field campaign. Therefore, general problems of field work are also discussed.

3.3.2 Climatic mass balance analysis

A glacier mass balance may consider mass changes of a whole glacier or only within parts of it over a certain period. Thus, SMB, internal mass balance and basal mass balance are often distinguished. The surface layer is defined as the part between the current glacier-atmosphere interface and the last summer surface. The SMB respectively comprises all mass changes only within this layer. All mass changes within the interior of the glacier are summarized by the internal mass balance. Nevertheless, changes of the internal mass balance are strongly connected to processes at the glacier surface, e.g. percolation of melt water and subsequent refreezing. Thus, the SMB and the internal mass balance are summarized by the climatic mass balance (Cogley et al., 2011). The basal mass balance is often neglected in mass balance studies since it is difficult to measure and changes are small compared to the other parts.

The model used in Paper II was mainly developed by Marco Möller. The climatic mass balance of Vestfonna is computed by summing up results of surface accumulation, surface ablation and refreezing calculations. The model is calibrated by point climatic mass balance observations at the ablation/accumulation stake network, through snow pit observations and AWS measurement data. Input data sets of suitable resolution for the modeling were obtained by applying statistical methods for downscaling and spatial distribution of reanalysis and remote sensing data.

The ablation is calculated by an enhanced version of the temperature-radiation-index model of Pellicciotti et al. (2005), considering air-temperature and absorbed short-wave radiation as influencing factors.

$$\boldsymbol{a} = \boldsymbol{f_t T} + \boldsymbol{f_r R_A} \qquad for \boldsymbol{T} > \boldsymbol{0^{\circ}C} \qquad (1)$$

$$\boldsymbol{a} = \boldsymbol{0} \qquad for \boldsymbol{T} \leq \boldsymbol{0^{\circ}C} \qquad (2)$$

where a is ablation, f_t and f_r are empirical coefficients, T is air-temperature and R_A is absorbed short-wave radiation. The values f_t = 1.394 mm w.e. K^{-1} day^{-1} and f_r = 0.098 mm w.e. W^{-1} m^2 day^{-1} have been determined for Vestfonna. Refreezing is estimated using the P_{max} approach (Reeh, 1991). As done by Schuler et al. (2007) for Austfonna, P_{max} is set to 0.6. Hence, melt and rainwater are retained by refreezing processes until 60% of the current year's winter accumulation is reached. Surface accumulation is assumed to be exclusively formed by snowfall. All precipitation occurring at air-temperatures below 0 °C is assumed to fall as snow, while rain is assumed for all precipitation at temperatures above 2 °C. Between 0 and 2 °C, a mixture of snow and rain is assumed and the amount of snowfall is scaled between 100 % (0 °C) and 0 % (2 °C) using a hyperbolic function (Möller et al., 2007).

Modeling is done for the 9-year period from September 2000 until August 2009 with a daily resolution on a 250 m grid. Input data are derived from ERA-Interim daily air-temperature and total precipitation of a grid point south of Vestfonna and MODIS-based cloud cover (MOD06_L2) and albedo (MOD10A1) data using statistical transfer functions for downscaling, distribution and variance inflation. Terrain information is based on the elevation data set of the ASTER Global Digital Elevation Model (GDEM).

(Further details are described in Paper II.)

3.3.3 European Arctic Reanalysis (EAR)

Observational data is not available for most Arctic regions and available data sets often comprise only single point measurements of short periods. This substantially complicates the analysis of atmospheric processes and atmosphere-cryosphere interactions at a regional scale. Available data sets of global circulation models or from remote sensing are not at the resolution needed for local climate impact studies. A successful downscaling of climate signals present in coarse observational data sets allows to reconstruct atmospheric variables at local scales where the data is needed.

Various techniques have been developed to bridge the gap between scales. Two kinds of approaches can be distinguished. One is the statistical downscaling which uses observed relationships of variables to large scale patterns to generate data of higher spatiotemporal

resolution from the coarser data sets. Although frequently used and often quite successful in reconstructing regional climate the estimated relationships might not hold true in a changing climate or for other regions. The other type of downscaling technique relies on high-resolution modeling to dynamically downscale the atmospheric flow to a regional scale. This method is physically based and coherent but is computationally expensive and subject to error due to imperfect parameterizations, land-surface conditions and numerics. However, a successful numerical modeling of the regional circulation is a valuable tool for subsequent meteorological and climatological studies since it provides homogenous distributed data sets of high resolution for detailed process analyses at different scales.

Numerical models suitable for dynamical downscaling purposes have been developed and used since the late 1970s as a tool in meteorology for weather forecasting purposes. Most of Numerical Weather Prediction (NWP) modeling is done by national and international organizations that manage large data sets from various heterogeneous sources. Data from satellites, weather stations, radio-soundings and radar are combined with models through complex data assimilation methods to obtain the best estimate of the state of the atmosphere every six hours. Realistic initialization data of atmospheric and boundary conditions play a fundamental role for atmospheric modeling and forecasting at both the global and regional scales. At the regional scale the importance of soil conditions increases since they may affect especially near surface variables at short time scales. This sensitivity is generally larger for NWP models that include detailed schemes of soil–vegetation–atmosphere interactions.

Operational analysis data sets generally suffer from inconsistencies over time since operational analysis systems are frequently being improved. Therefore, the technique of reanalysis uses modern analysis systems to reprocess long-term observational data. Using high-resolution limited area models (LAM) for this purpose is called regional reanalysis. The NCEP North American Regional Reanalysis (NARR) or the Arctic System Reanalysis (ASR) projects are examples of providing regional reanalysis data sets of 30 km horizontal resolution for limited areas. Nevertheless, the term regional reanalysis can also be used for reprocessing observational data sets together using a LAM on a regional scale without a temporal assimilation. This approach keeps observational data sets unmodified but uses state-of-the-art LAMs for analyzing the atmospheric flow on regional scales. This does not

allow trend analyses but maintains the goal of avoiding over-interpretation in cases where observations have been insufficient.

In Paper III such a regional reanalysis has been done for the European Arctic, i.e. European Arctic Reanalysis (EAR), using version 3.1.1 of a polar-optimized LAM known as Polar WRF. Polar WRF (http://polarmet.osu.edu/PolarMet/pwrf.html) is being developed at Ohio State University on the basis of the Weather Research and Forecasting (WRF) Model (http://www.wrf-model.org/index.php), a next-generation mesoscale numerical weather prediction system designed to serve both operational forecasting and atmospheric research needs. The reanalysis was initialized by data from the Operational Model Global Tropospheric Analyses (Final Analyses, FNL; data set ds083.2), published by the CISL Data Support Section at the U.S. National Center for Atmospheric Research, Boulder, CO; performed by the U.S. National Centers for Environmental Prediction (NCEP)) (1°, 6 h) and NCEP's Real-time, global, sea surface temperature (RTG_SST) analysis (0.5°, daily). Static geographical fields are initialized by the United States Geological Survey (USGS) geographical data sets. Additionally we used daily sea ice concentrations from Advanced Microwave Scanning Radiometer for Earth Observing System (AMSR-E) observations at 12.5 km horizontal resolution. Since data of daily sea surface temperature are not available before 12th February 2001 and daily sea ice concentration are not available before 20th June 2002 we did the reanalysis before these dates without the respective data set. We filled missing values in the sea ice dataset with values of the nearest valid neighbor and generated 6 h data sets from the daily data of SST and sea ice by linear interpolation. Thus, the reanalysis was driven providing data of lateral boundary conditions at 6 h intervals.

Three two-way nesting levels of 30 km, 10 km and 2 km horizontal resolution are defined with a polar stereographic projection (see Figure 3.6). The first-level EAR domain called the European Arctic domain (99 x 99 grid points, 30 km) is centered at 80.0 °N, 20.0 °E. The second-level Svalbard domain (49 x 52 grid points, 10 km) covers the archipelago of Svalbard. Six third-level domains of 2 km horizontal resolution cover areas of Svalbard of special interest. These are areas where we have access to data of field observations like AWS observations or synoptic observations by the Norwegian Meteorological Institute, i.e. Nordaustlandet domain (106 x 86 grid points, 2 km), North-West Spitsbergen domain (46 x 66 grid points, 2 km), Lomonosovfonna domain (31 x 31 grid points, 2 km), Longyearbyen

domain (26 x 26 grid points, 2 km), Hornsund domain (46 x 31 grid points, 2 km) and Hopen domain (21 x 26 grid points, 2 km).

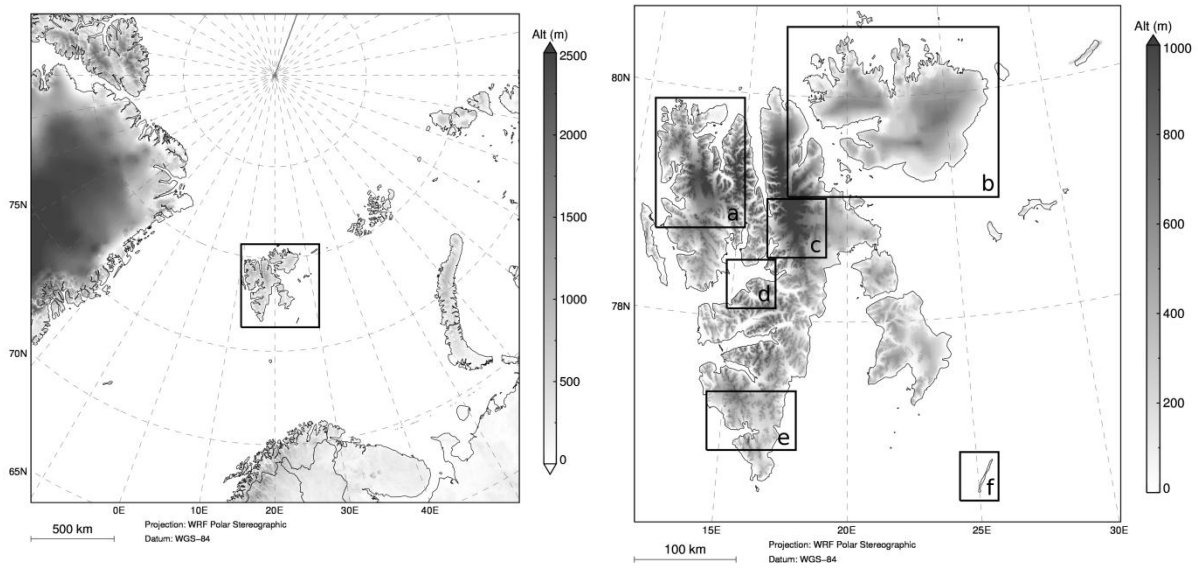

Figure 3.6 *Terrain height and location of the parent European Arctic domain (left) and the second-level Svalbard domain (right) .part of the European Arctic Reanalysis (EAR). Black squares show the location of the nested Svalbard domain (left) and of the six third-level domains (right): a) Northwest Spitsbergen, b) Nordaustlandet, c) Lomonosovfonna, d) Longyearbyen, e) Hornsund and f) Hopen.*

All domains are resolved by 28 vertical levels with the top set to 50 hPa. The first nine levels approximately represent the bottom 1500 m of the boundary layer. We set the surface parameterization options to use time-varying sea surface temperature and fractional sea ice cover. The Runge-Kutta time step is set to 120 s for the European Arctic domain, to 40 s for the Svalbard domain and to 8 s for the third-level domains. The choice for the physical parameterization schemes as summarized in Paper III is based on the studies of Hines and Bromwich (2008), Hines et al. (2011) and diverse sensitivity studies.

A cascading approach was used for the reanalysis of the different domain levels. In a first step all three domain levels were processed using a two-way telescope nesting obtaining reanalysis data for the third-level domains. In a second step the reanalysis of the Svalbard domain was processed by discarding all third-level domains from the recalculation to obtain unaffected results, i.e. we found out the two-way nesting produces artifacts in the region of

nesting in the data of the parent domain (Maussion et al., 2011). In a last step the reanalysis of the European Arctic domain was done without any nesting of other domains.

Individual simulation runs comprising 36 h were produced by daily reinitialization (simulation started at 1200 UTC daily). A continuous time series comprising a period of 1st September 2000 to 31st August 2011 for each domain analog to the strategy of Maussion et al. (2011) was produced by assembling individual simulation runs comprising 36 h each, whereof the first 12 h were discarded to avoid spin-up effects and the next 24 h were stored. Output was written at 3-hourly intervals for the European Arctic domain and at hourly intervals for all other domains.

After production the EAR data sets have been analyzed with synoptic observations of the Norwegian Meteorological Institute provided by the National Climate Data Center (NCDC) and field observations of AWS measurements in the region of Vestfonna.

(Further details are described in Paper III.)

3.3.4 Snowdrift analysis

Field observations indicate that a considerable part of solid precipitation is redistributed by wind drift in the region of Vestfonna. The redistribution of snow mass by wind drift can have an important impact on the balance of glaciers. Thus, an assessment study of the intensity of the redistribution process has been conducted in Paper IV. The snowdrift model used in this thesis was developed by Tobias Sauter.

Blowing and drifting of snow is considered to be a dilute two-phase flow consisting of solid snow particles in a fluid phase. Within a thin surface layer (i.e. saltation layer) the ejected particles follow a ballistic trajectory under the influence of gravity. Snow particles in suspension are balanced by the particle-fluid drag force and the counteracting gravity force. Transport- and exchange processes in such two-phase flows are created by turbulent fluid motion, which in turn is affected by the presence of the particles. The model neglects interactions between particles and snow particles are treated as a continuous phase solely interacting with the background flow.

The rate of snow mass change is described by the continuum equation for conservation of mass. Therefore, the Reynolds averaged Navier-Stokes equation is solved using the k-ω

turbulence model. The snow mass flux at the boundaries for the saltation layer is given by the formulation of Pomeroy and Gray (1990)

$$\boldsymbol{q_{salt} = \frac{0.68\rho}{u_* g} u_{th}(u_*^2 - u_{th}^2)} \qquad (3)$$

where q_{salt} is snow mass flux in the saltation layer, ρ is air density, u_* is the friction velocity, g is gravity acceleration and u_{th} is friction velocity threshold. The inlet snow density profile for the suspension layer is given by Pomeroy and Male (1992)

$$\boldsymbol{\phi_s(u_*, z) = 0.8 \cdot exp[-1.55\left(4.784 {u_*}^{-0.544} - z^{-0.544}\right)]} \qquad (4)$$

where ϕ_s is snow mass in saltation layer, u_* is the friction velocity and z height above ground. Sublimation of suspended snow particles has been approximated as a function of the mean particle size, solar radiation, saturation deficit and conductive and advective energy and moisture transfer.

The spatiotemporal estimate of snowdrift was applied to the southwestern part of Vestfonna ice cap for the accumulation period 2008/2009 since radio-echo sounding measurements (Grabiec et al., 2011) are available for this region only for May 2009. The domain top was set to 3000 m consisting of five vertical layers in the near surface layer (5 m) and further 40 vertical layers above. The model was forced by 2 km atmospheric fields from the EAR (see Section 3.3.3) and resolves processes on a spatial resolution of 250 m. Terrain information is based on the elevation data set of the ASTER Global Digital Elevation Model (GDEM). Besides radio-echo sounding measurements results have also been compared to onsite snow-pit data.

(Further details are described in Paper IV.)

3.3.5 Analysis of elevational gradients of air-temperature

The climatic mass balance modeling study in Paper II used a constant elevational gradient of air-temperature (i.e., $\frac{\partial T}{\partial h}$ = −7 K/km) and a digital elevation model (i.e., ASTER GDEM) to extrapolate air-temperature data across the entire Vestfonna ice cap. Other studies have shown considerable seasonal or even daily variations in $\frac{\partial T}{\partial h}$ (e.g. Braun and Hock, 2004; Marshall et al. 2007; Gardner and Sharp, 2009; Gardner et al., 2009; Petersen and Pellicciotti, 2011) indicating that modeling results may be sensitive to the assumptions on $\frac{\partial T}{\partial h}$. Thus, $\frac{\partial T}{\partial h}$ and its temporal variability on Vestfonna is investigated in Paper V with the ultimate goal to improve the spatial representation of air-temperature in mass balance modeling.

Since all time series of air-temperature measurements show considerable data gaps due to measurement failures a direct analysis of these data is not constructive. Data obtained from a statistical reconstruction method and from the EAR are analyzed instead for the period 2001 to 2011. The reconstruction method uses data at Svalbard-Lufthavn, Longyearbyen (WMO-Nr. 010080, 15.4667°E 78.2500°N, 28 m a.s.l.) operated by the Norwegian Meteorological Institute to reconstruct daily temperatures of each AWS by linear regressions. In addition, gridded 2 m air-temperature data of the Vestfonna region of 2 km horizontal resolution obtained from the EAR are used.

Daily $\frac{\partial T}{\partial h}$ are computed from day by day least-squares regression. In the regression analysis altitude is used as the predictor and air-temperature is used as the predictand. The slope of the resulting regression function defines $\frac{\partial T}{\partial h}$. Results are compared to $\frac{\partial T}{\partial h}$ derived from measurements where available. When measurement data only comprises elevational differences less than 150 m results are discarded since the difference in the near-surface air-temperatures at two different altitudes is likely to be smaller than the measurement error of the sensors. Since the EAR provides gridded data sets a comparison of results obtained from distributed and single-point data is implicitly done.

In addition net radiation data obtained from AWS measurements on Vestfonna, AMSR-E sea ice concentration data and vertical profiles of air temperature measured by radio soundings

in 1944/1945 at Haudegen station (Dege, 1960) is used to explore and discuss the origin of interannual and intra annual variability of $\frac{\partial T}{\partial h}$.

(Further details are described in Paper V.)

3.3.6 Analysis of the impact and origin of cyclones, the North Atlantic Oscillation (NAO) and the Arctic Oscillation (AO)

Data sets of Northern Hemisphere Cyclone Locations and Characteristics from NCEP/NCAR Reanalysis Data provided by the National Snow and Ice Data Center (http://nsidc.org/data/docs/daac/nsidc0423_cyclone/) and indices of the North Atlantic Oscillation (NAO) and the Arctic Oscillation (AO) provided by the NOAA Climate Prediction Center (http://www.cpc.ncep.noaa.gov) are analyzed by linear regression analyses to investigate the impact of modes of northern hemisphere atmospheric circulation on the local climate.

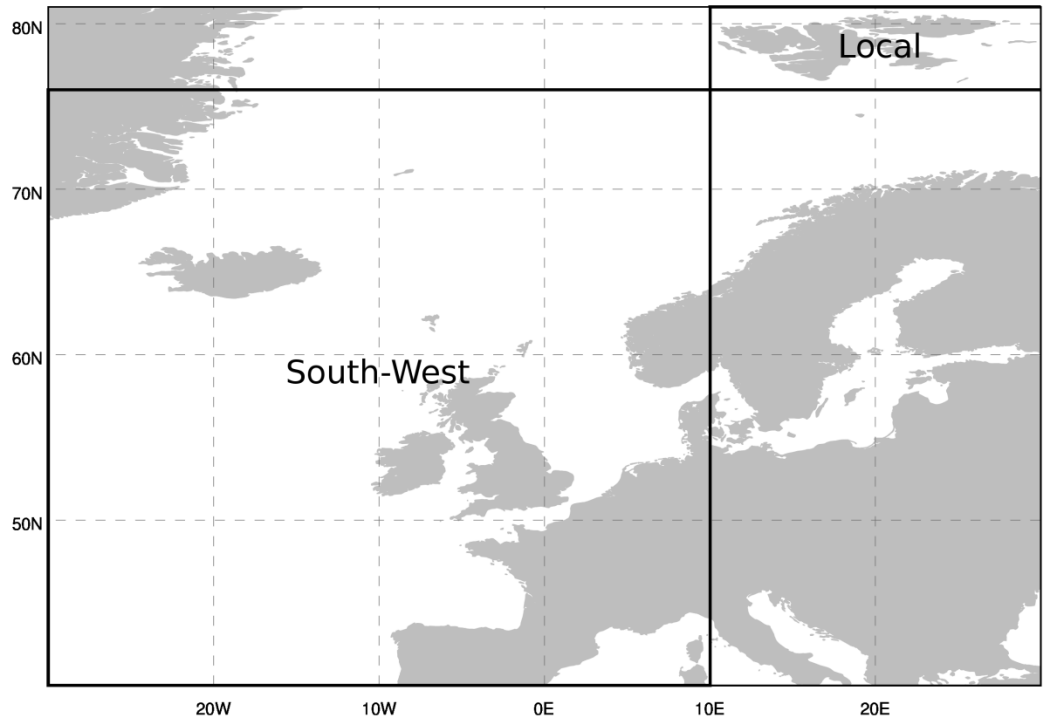

Figure 3.7 *Areas of cyclogenesis.*

In a first step cyclones are detected within a monitoring sector comprising the main islands of Svalbard (76°N 10°E to 81°N 30°E) in the cyclone data set. In a second step for each of the detected cyclones the location of first detection within the data set is identified. If this location lies within the areas “South-West” (40°N 30°W to 76°N 10°E) or “Local” (76°N 20°W to 81°N 10°E) shown in Figure 3.7 the cyclone is added to the respective area category. If the cyclone origin lies not in one of these areas the cyclone is added to the category “Other”.

The frequency of cyclones of a specific area category and variations in the NAO and AO are finally analyzed by seasonal linear regressions with anomalies in air-temperature, precipitation and wind speed on Vestfonna and in Svalbard as resolved by the EAR.

4 Results and synthesis

4.1 Which expedition procedures and which methods for measuring surface energy and mass balance components and atmospheric variables are practical and applicable in the region of Vestfonna ice cap?

4.1.1 Expedition procedures

A team of three to four members performed well during the nine field campaigns. All scheduled tasks, except during the summer campaign 2008, could be achieved with this team size. For daily recovery four bear watches of two and a half hours length each provided seven and a half hours sleep for each team member. Thus, periods for recovery could be kept short and efficient.

During summer campaigns only by foot operations were possible due to insufficient snow cover around the ice cap. Therefore, the mobility during summer campaigns was strongly limited. Besides the gathering of data on a very local scale only minor maintenance at the AWSes was possible since the transportation of heavy tools and spare parts was not possible. The summer campaign 2008 made clear that it would be more trouble than it is worth to reach measurement sites by foot operations far inside the ice cap, like Ahlmann Summit where VF-AWS605 was located. The team reached its performance limit while doing by foot operations of 15 km per day and carrying equipment of 30 kg per person. During spring the use of snowmobiles with sledges or pulkas during by foot operations was possible due to a broadly available snow cover. This strongly improved the capability of the team to transport heavy equipment. Nevertheless, the mobility was still very limited during spring campaigns if no usage of snowmobiles was possible.

The team had five contacts with polar bears. In two situations a polar bear had to be scared away by firing flares at it from a signal pistol. Once a maximum of five flares had to be used to succeed. Nevertheless, the set of two rifles with ten bullets each and two signal pistols with ten flares each provided enough resources for self-defense. The used bear watch strategy enabled early warning of all team members so that the team could act adequately and no polar bear was killed or injured. Also the temporary field camps were structured so

that the toilet place and food storages, which could attract polar bears by their smell, were far away from the sleeping tents.

The use of helicopter transport required the allocation of about three day time slots for each flight in the planning schedule since weather conditions like icing or decreased visibility due to white out strongly complicated the transfers in the region of Svalbard. In two cases a helicopter flight had to be aborted due to bad flying condition. The cargo (passengers plus equipment) was limited to 600 kg per flight. Thus, if more or heavier equipment was required (e.g. snowmobiles, heavy or bulky spare parts, etc.) it had to be transported by additional flights or stored in the field beforehand. In summer campaigns ship transport was used in addition to helicopter transport, enabling large amounts of cargo. Nevertheless, the transport in the field during summer campaigns was very limited since all terrain vehicles (ATV) were forbidden by environmental laws in this region and no snow cover for snowmobile logistics was available. In two summer campaigns the ship anchored in the bay closest to the measurement sites, what enabled the possibility to use the ship as the base. That strongly improved the efficiency of the team since recovery was better onboard and a large set of equipment was available.

To sum it up, spring campaigns using helicopter transport with snowmobiles logistics were indispensable for installation, dismounting and major maintenance of the measurement network. Without the logistical support from other groups (especially snowmobiles) the field work would have been hardly successful. Maintenance work generally strongly competed with work for manual measurements, i.e. excavating snow pits. Summer campaign using ship transport and by foot operations are suitable for gathering data close to the fringe of the ice cap. Major maintenance of the stations and reaching areas far inside the ice cap is not possible during summer campaigns due to logistical constraints. However summer campaigns provided valuable data on ablation from ablation/accumulation stakes metering and snow pit measurements. A brief summary of the conducted field work is presented in Appendix J.

4.1.2 Automatic measurements

In the following paragraphs the performance of AWS measurements will be assessed. VF-AWS605 fell over due to extensive riming in June 2008 and was subsequently buried by

snow. Also VF-AWS500 was bent over in July 2008 but fixed in August. The event destroyed the solar-radiation sensor of the VF-AWS500. At VF-AWS500, VF-AWS370 and VF-AWS240 an Ultrasonic Anemometer (Thies, USA 4.3830.22.300) was installed until May 2009. No valid data could be acquired due to a bug in the manufacturer software. Nevertheless, the high power consumption of the heating of these sensors caused low battery power at these AWSes in January 2009. At DG-AWS a lot of measurement failures were observed during 2008/2009 until battery power was low in April 2009. The nature of the failures strongly indicated problems in the electric system of the logger box. Thus, we completely replaced the logger box in May 2009. At KV-AWS polar foxes destroyed the power cables in December 2008. The damaged electricity caused short circuits which broke the logger at KV-AWS and no valid data could be acquired after December 2008. Bugs in the logger program caused some data loss at VF-AWS605 and KV-AWS. At VF-AWS500, VF-AWS370 and DG-AWS the sonic ranger sensors showed severe problems with airborne sea salt corroding the sensor head and causing sensor failures. The sensor head was replaced at VF-AWS370 and DG-AWS in May 2011. Due to the variety of technical and logistical problems VF-AWS240, VF-AWS500 and VF-AWS605 were removed in spring 2009. In summer 2009 KV-AWS had to be removed since Kinnvika station was closed by the governor and only DG-AWS and VF-AWS370 remained operating.

At VF-AWS370 a polar bear destroyed all cable connections of the sensors installed above ground in August 2009. The AWS was fixed in May 2010. Low battery power in March 2010, i.e. after winter, at DG-AWS caused data loss. During a complete inspection of the electricity in June 2010 the team found large amounts of condense water behind an access cover in the logger box. At this point the electric contacts of multiple sensors had been corroded causing short circuits in the whole system. The station inclinometer was broken but all other problems could be fixed. The team started in May 2011 to put large amounts of drying agents into the logger boxes of DG-AWS and VF-AWS370 to absorb the emerging condense water. At VF-AWS370 the power cable was cut in October 2011. No evidence that the damage was caused by animals was found this time. It is very likely that extensive ablation at the end of summer stretched and exposed the cables and subsequent extensive riming and strong winds during October caused the final fail. Furthermore, an Ultrasonic Anemometer (Gill Instr. WindMaster) at VF-AWS370 also started to fail due to rime at the

sensor heads in July 2011 and the whole DG-AWS fell over due to extensive riming and strong winds in October 2011.

The following sensors have not been considered in this assessment since no valid data could be obtained at all. At VF-AWS605, DG-AWS and KV-AWS a cup anemometer (Schildknecht) was installed but the needle bearings were destroyed after a few days due to riming. Also a laser precipitation monitor (Thies, 5.4110.01.000) was initially installed at KV-AWS. The sensor completely failed due to heating and power consumption problems. At VF-AWS605, VF-AWS500, VF-AWS370 and VF-AWS240 a precision infrared temperature sensor (Campbell Sci., IRTS-P) was installed. This sensor revealed to not be suitable for measuring thermal surface radiation at the measurement sites. The former mentioned Ultrasonic Anemometer (Thies, USA 4.3830.22.300) installed at VF-AWS500, VF-AWS370 and VF-AWS240 was removed as well from the assessment since no valid data could be acquired. For the remaining sensors the various failures fall into the categories described in Section 3.3.1. Results are presented in Table 4.1. Detailed assessment results for each AWS can be found in Appendix J.

Table 4.1 *Results of the measurement quality assessment. Used categories are described in Table 3.2.*

N	C	E	A	S	P	U
56%	14%	12%	11%	3%	1%	3%

As indicated before most measurement failures were caused by the rough climatic conditions (14 %), electrical problems (12 %) or animals (11 %). Minor data loss was produced by internal sensor errors (3 %) or bugs in the logger program (1 %). Nevertheless, gaps of distinct variables (e.g. snow depth) at individual AWSes (e.g. VF-AWS605) were enormous. A remaining part of 3 % unknown measurement failures is strongly assumed to be related to electrical problems and internal sensor errors. In average 56 % of measurements were successful. Four of six AWSes had to be removed after a year since the additional benefit did not make up for logistical costs. Especially AWSes above the equilibrium line altitude (ELA) of about 400 m a.s.l. quickly showed strong physical problems due to extensive riming and snowfall. However at lower altitudes special events like the

once in October 2011 caused equal problems. The long polar night prevented recharging by solar panels and cold temperatures further lowered the capacity of the emptying batteries. A wind generator failed at VF-AWS370 since it was destroyed due to rotor unbalance caused by riming and icing. These energy constraints are less frequent during polar day. Nevertheless, sensors with high energy consumption may prevent batteries from completely recharging also during this season. In lower altitudes and coastal regions data loss due to damage by animals can be enormous.

4.1.3 Manual measurements

Assessing conducted manual measurements the most limiting factors were logistical constraints, manpower and climatic conditions. A strong elevation dependency can be observed in repeat readings of the ablation/accumulation stake network (see Table J.8). On the one hand this is due to the inability to reach the Ahlmann measurement site during summer campaigns or without snowmobile logistics and on the other hand most of the ablation stakes above 400 m a.s.l. were destroyed by riming. Thus, nine ablation/accumulation stakes have been removed in spring 2009 since they were broken or not reachable during the previous campaigns. One of the biggest problem during spring campaigns was to find the ablation/accumulation stakes after extensive snow fall. Thus, except in 2009, the number of repeat readings is higher during summer campaigns than during spring campaigns. During summer 2009 long lasting whiteout conditions strongly decreased the ability to find the AWSes and ablation/accumulation stakes by foot operations due to limited visibility. Also the snow pit data shows elevation dependency (see Table J.9). Nine snow pits are available below 300 m a.s.l., eight between 300 m a.s.l. and 500 m a.s.l. and four above 500 m a.s.l.. Only four snow pits (see Table J.10) have been excavated during summer campaigns since nearly no snow cover was available at altitudes reachable by foot operations or other fieldwork (mainly maintenance of the AWSes) consumed most of the time and manpower during the other campaigns. Some of these factors were also observable during spring campaigns. During campaigns of intense work on other tasks like dismounting of AWSes (e.g. spring 2009 and spring 2012) or limited mobility (spring 2010) the number of conducted snow pit measurements is reduced to one or two each campaign (see Table J.10). Besides the temporal and elevational bias a general

distribution bias to western areas and to the glacier fringe is observable in all field observations of this study due to the logistical constraints (see Figure 3.1).

4.1.4 Surface energy and mass balance measurements

In the following paragraphs sensor performance is assessed focusing on individual components of the SEB and SMB. Concerning net radiation measurements the CNR-1 (Kipp&Zonen) sensor performed best. All individual fluxes of the net radiation are measured which is an important benefit compared to the NR-LITE (Campbell Sci.) sensor which further requires wind speed correction. For measurements of individual radiation fluxes CS300 (Campbell Sci.) sensors showed good performance measuring short-wave fluxes and CGR3 (Kipp&Zonen) showed good performance measuring long-wave fluxes. Direct measurements of turbulent heat fluxes using ultra sonic anemometers and infrared gas analyzers failed due to severe energy problems. However this is more a problem of being unable to provide enough energy at remote locations than with the measurement systems themselves. Thus, since sufficient energy could not be provided bulk approaches using measurements of wind speed, air-temperatures and relative humidity remained the only way for turbulent heat fluxes estimations. Wind speed measurements failed using cup anemometer (Schildknecht) but other sensors (Young, 05103-45) performed well. Air-temperature and relative humidity measurements performed well using CS215 (Campbell Sci.) sensors with ventilated radiation shields. Also CS107 (Campbell Sci.) temperature probes performed well measuring soil and ice temperature profiles and therefore providing data on ground heat flux. The SR50A (Campbell Sci.) sonic ranger sensors were the only sensors installed for automated indirect SMB measurements. They showed severe problems with airborne sea salt corroding the sensor heads. This caused large data loss at DG-AWS and VF-AWS370 (see Appendix J). At VF-AWS500 the sonic ranger was damaged after the station fell over due to extensive riming. The sensor seems generally suitable but needs a lot of maintenance by replacing sensor heads after at least a year in the region of Vestfonna. A problem is the inability of the sensor to directly measure snow water equivalents or to detect liquid precipitation. This and the large data loss made manual measurements (ablation/accumulation stakes and snow pits) indispensable for SMB estimates in this study. Nevertheless, only integral values could be achieved since these methods require considerable logistical effort and manpower.

4.2 What is the current state and sensitivity of the surface energy and mass balance of Vestfonna ice cap?

Results in Paper I reveal mean snow densities of 388 ± 43 kg m^{-3} for the snowpack of Vestfonna with no apparent spatial or interannual variability. A distinctly higher value of more than 457 ± 70 kg m^{-3} is obtained for De Geerfonna. A spatial comparison of snow water equivalents above the previous end-of-summer surface serves for obtaining insights into the spatial distribution of snow accumulation across Vestfonna. Altitude is found to be the only significant spatial parameter for controlling snow accumulation across the ice cap. Furthermore, these data is used to scale snow precipitation by quadratic index functions for the climatic mass balance study of Vestfonna in Paper II. The determination of snow density is also needed for accumulation and ablation calculations from stake readings. The homogeneous snow density that is observed throughout Vestfonna justifies the simplified assumptions of constant snow density in mass balance-modeling.

4.2.1 Climatic mass balance resolved by an empirical method

In Paper II the modeled SMB regime of the Vestfonna ice cap is characterized by long accumulation periods (September to May) and short ablation (June to August). Model results reveal a mean climatic mass balance rate of -0.02 ± 0.20 m w.e. yr^{-1} suggesting roughly balanced conditions for the period September 2000 to August 2009. Year-to-year variability is relatively low (<0.5 m) as indicated by the small standard deviation of annual balances (0.15 m w.e.). The mean annual surface ablation rate is -0.58 ± 0.18 m w.e. yr^{-1}, while annual surface accumulation and refreezing rates amount to $+0.40 \pm 0.07$ m w.e. yr^{-1} and $+0.15 \pm 0.04$ m w.e. yr^{-1}, respectively. Hence, on average, approximately one fourth of the surface ablation refreezes. For individual mass balance years this fraction ranges between 5 % and 48 %. In average the temperature-index module contributes 31 % and the radiation-index module 69 % to total melt. The modeled glacier-wide climatic mass balance of Vestfonna is presented in Figure 4.1.

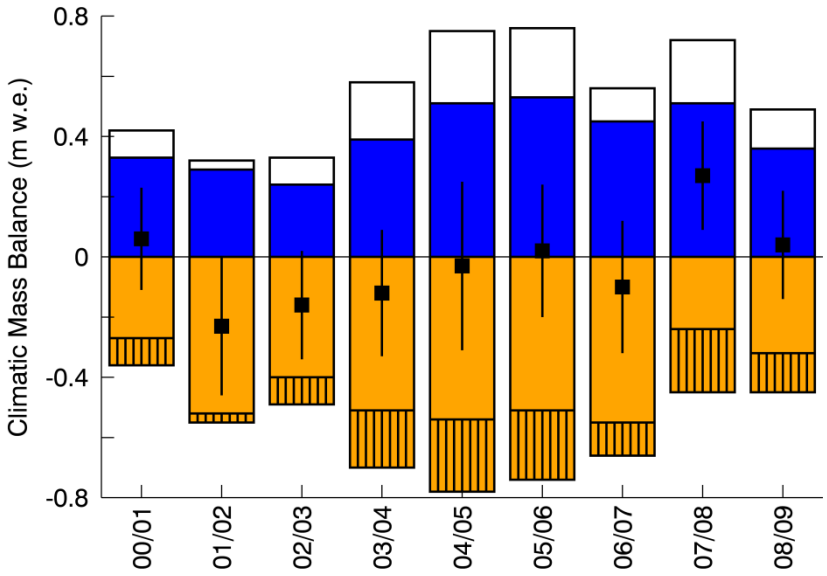

Figure 4.1 *Glacier-wide climatic mass balance of Vestfonna for the mass balance years 2001 to 2009: The bar chart shows annual ablation (orange bars), annual accumulation (blue bars), and annual refreezing (white bars). The refrozen part of ablation is indicated by hatching. Black squares with error bars represent the annual balances. Each mass balance year lasts from 1st September to 31st August.*

4.2.2 Surface energy and mass balance as resolved by the EAR

Analyzing the SEB of Vestfonna for the same period (September 2000 to August 2009) data of the EAR of Paper III is used. The SEB is resolved in the EAR by an optimized version of the unified NOAH LSM (Version 1.0 July 2007) of the Polar WRF 3.1.1 model. The algorithm solving the SEB distinguishes the following fluxes.

$$\boldsymbol{Q_N + Q_H + Q_L + Q_G + Q_M = 0} \qquad (5)$$

where Q_N is net radiation, Q_H is sensible heat flux, Q_L is latent heat flux, Q_G is ground heat flux and Q_M comprises all heat fluxes for melt and refreezing processes within the snowpack. Q_N and Q_M are conglomerates of other variables. Q_N is calculated by

$$\boldsymbol{Q_N = S_{\downarrow}(1-\alpha) + L_{\downarrow} - \varepsilon\sigma T_S^4} \qquad (6)$$

where $S_{\downarrow}$ is downward short wave flux, α is albedo, $L_{\downarrow}$ is downward long wave flux, ε is surface emissivity, σ is Stefan-Boltzmann constant and T_S is surface skin temperature. Q_M comprizes three individual calculated fluxes.

$$\boldsymbol{Q_M = F_1 + F_2 + F_3} \qquad (7)$$

where F_1 is the heat flux from snow surface to newly accumulated precipitation, F_2 is the freezing rain latent heat flux and F_3 is the snow phase change heat flux. Considering Q_M a negative value can be equated with melt and a positive value with refreezing.

Since background albedo is 0.8 for whole Nordaustlandet due to USGS land cover types, snow depth is set back daily to 0.5 m due to reinitialisation of the model, snow albedo is 0.8 and no further input data has been provided α and ε values are constants on Vestfonna in the EAR (α = 0.8 and ε = 0.98 for Vestfonna grid points). Other studies (e.g. Winther et al., 1999; Möller, 2012) and measurements of VF-AWS370 (see Figure K.1) indicate that albedo of fresh snow in Svalbard is about 0.85 but considerably decreases during ablation season. The mean value for the period June to August 2011 at the ELA measured by VF-AWS370 was about 0.7. Thus, it is assumed that the EAR underestimates the surface absorption of solar radiation especially in ablation areas. Nevertheless, SEB of Vestfonna will be analyzed as resolved by the EAR in this study. The SEB of Vestfonna on 2 km horizontal resolution for the period September 2000 to August 2009 is presented in Figure 4.2.

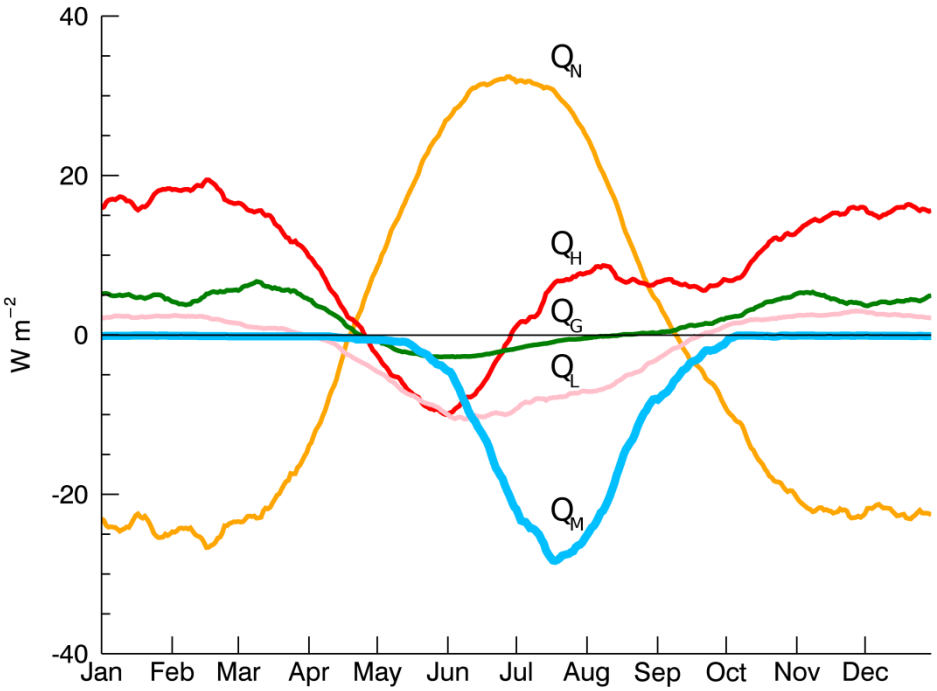

Figure 4.2 *Seasonal course of surface energy balance (SEB) of Vestfonna ice cap as resolved by the European Arctic Reanalysis (EAR) on 2 km horizontal resolution for the mass balance years 2001 to 2009. A 30-day moving window was used to smooth the curves.*

In Paper I an analysis of all spring 2008 temperature profiles reveals that the reduction of the cold content from the previous winter season starts in late April. This is consistent with the starting decrease of Q_M in Figure 4.2. Q_M indicates ablation between beginning of May and end of September. Decrease of Q_M accelerates begin of June. The minimum is reached in the middle of July and Q_M immediately takes a mirror-inverted course. The calculated annual energy budget consumed by Q_M sums up to 164 ± 39 MJ m^{-2} yr^{-1}. Year-to-year variability of Q_M and the following values is indicated by total mean ± one standard deviation. Q_N supplies 74 ± 7 %, Q_H 23 ± 5 % and Q_G 3 ± 2 % to the melt energy budget. The energy budget is equivalent to a mean annual surface ablation rate of −0.49 ± 0.12 m w.e. yr^{-1}. Furthermore, the EAR resolves +0.09 ± 0.02 m w.e. yr^{-1} of liquid precipitation and +0.51 ± 0.13 m w.e. yr^{-1} of solid precipitation within the same period. Energy fluxes from freezing and melting of the liquid precipitation are assumed to equal out. Thus, an additional throughput of 0.09 m w.e. yr^{-1} to the melting and refreezing fluxes of Q_M is assumed. The resulting mean surface mass balance rate of Vestfonna as resolved by the EAR is +0.02 ± 0.22 m w.e. yr^{-1} for the mass balance years 2001 to 2009. The obtained

value is in accordance with the mean climatic mass balance rate of −0.02 ± 0.20 m w.e. yr^{-1} obtained from the empirical study in Paper II. Figure 4.3 shows annual mean values of the SEB and SMB as resolved by the EAR.

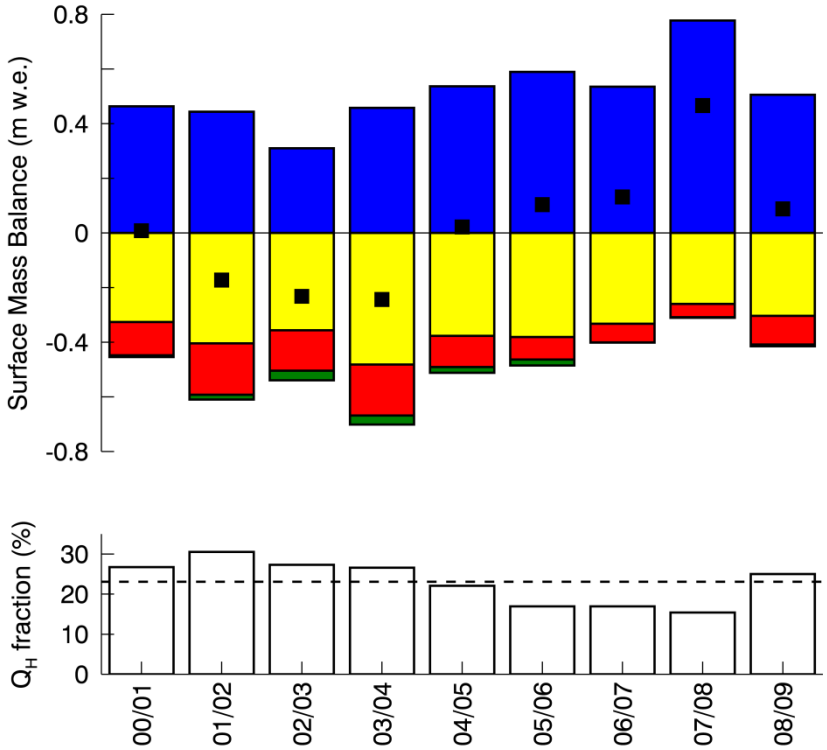

Figure 4.3 *Modeled glacier-wide surface energy and mass balance of Vestfonna as resolved by the European Arctic Reanalysis (EAR) for the mass balance years 2001 to 2009: Bar charts show the contribution of net radiation (yellow), sensible heat flux (red) and ground heat flux (green) to annual ablation and solid precipitation (blue). White bars show the annual fraction and dashed line the mean of sensible heat flux on ablation. Black squares represent the annual balances. Each mass balance year lasts from 1st September to 31st August.*

4.2.3 Comparison and discussion of results derived from the empirical method and the EAR

For comparison annual SMB values are derived from the climatic mass balance modeling of Paper II by neglecting refreezing rates and reducing the ablation rates by the same amount. The resulting ablation rates are indicated in Figure 4.1. Differences between annual SMB obtained from the empirical approach and from the EAR show strong year-to-year variability

(see Figure K.2). A detailed error analysis in Paper II reveals that the largest uncertainty in the empirical approach is produced in ablation rates by air-temperature and albedo estimations. A detailed error analysis of the SEB modeling results has not been conducted so far. Nevertheless, obtained ablation rates are in the error limits but indicate higher ablation most of the years as estimated by the empirical approach. The empirical approach is compared with measured point climatic mass balances at the stakes in the period 2007 to 2009 in Paper II. For this period total ablation calculated from the SEB model of the EAR is only 0.02 m w.e. less than calculated by the empirical approach (see Figure K.2.).

The analysis in Paper I shows that the cold content of the snowpack was completely removed by energy gain throughout warmer episodes of the ablation season. As this development was evident up to at least 500 m a.s.l., it is reasonable to assume that summer melting regularly affects the entire ice cap. This is supported by the firn-core data of Beaudon et al. (2011) and was also reported from in situ observations by Sandford (1925) and Ahlmann (1933). Also analyses in Paper V reveal an increase of elevational gradients of near-surface air temperature ($\frac{\partial T}{\partial h}$) on Vestfonna during summer (see Figure K.3). The summer increase of $\frac{\partial T}{\partial h}$ could be confirmed by AWS measurements. Obtained seasonal mean values of $\frac{\partial T}{\partial h}$ of about -4 K km^{-1} for June to August reaching monthly means of about -3 K km^{-1} in July are strong evidence of prevailing melt conditions all over the ice cap.

In Paper II a constant $\frac{\partial T}{\partial h}$ of -7 K km^{-1} has been used for air-temperature extrapolation over the ice cap since the analysis of Paper V was not available at that time. Unfortunately, the assessment of changes in $\frac{\partial T}{\partial h}$ on ablation using methods of Paper II is not conclusive. Vestfonna shows a quasi-linear relation of altitude and portion of grid points of the used ASTER DEM. The used reference altitude of 370 m a.s.l. at VF-AWS370 for ERA-Interim air-temperature reconstruction is close to the altitude of 396 m a.s.l. at which exactly 50 % of Vestfonna grid points are below and above the altitude (see Figure K.4). Thus, glacier-wide means of air-temperature or temperature based ablation estimates are insensitive to changes in $\frac{\partial T}{\partial h}$ when the reference altitude of 370 m a.s.l. for air-temperature extrapolation is used (see Figure K.5). Nevertheless, changes of glacier-wide ablation rates should result

when air-temperature is assumed to be about 0 °C during ablation at lower altitudes and $\frac{\partial T}{\partial h}$ values are rather −4 K km^{-1} than −7 K km^{-1} as indicated by analyses in Paper V.

Annual accumulation rates obtained from solid precipitation of the EAR exceed estimated accumulation of the empirical approach in all years (see Figure K.2). Also most of the error limits are exceeded. Furthermore, Polar WRF 3.1.1 is not capable of resolving snowdrift processes. Nevertheless, persistent katabatic wind flows throughout the year were observed in Paper III. Moss (1938) reported wind-drift conditions during 119 of 255 days between September 1935 and June 1936 in the region of Vestfonna. Also wind crusts have been found in the snow profiles at various locations in analyses of Paper I, indicating strong wind regimes. Thus, the spatial snowdrift over Vestfonna ice cap during the accumulation season 2008/2009 was analyzed in Paper IV. The analysis revealed that blowing and drifting snow were frequent processes (10 – 25 %), which strongly modified snow accumulation distribution of the entire ice cap. In particular, along the wind exposed zones about 10 - 20 % of the primarily accumulated snow was redistributed to peripheral zones and must be considered a loss term for the ice cap mass balance. Furthermore, the analysis showed that there is a pronounced snowdrift sublimation of about 6 - 12 %. Thus, annual surface accumulation as resolved by the EAR has to be corrected by mass loss due to snowdrift on Vestfonna. Some annual surface accumulation rates for the period September 2000 to August 2009 assuming different annual mean mass losses due to snowdrift are presented in Table K.2. Thus, expecting a mean SMB rate of −0.02 m w.e. yr^{-1} as estimated in Paper II a mass loss of 7 % due to snowdrift would be sufficient in addition to the melt rates derived from SEB modeling of the EAR. A mass loss of 20 % due to snowdrift would generate annual surface accumulation rates into the range of error limits of the accumulation rates of the empirical approach. Nevertheless, the fact that De Geerfonna received up to 20 % additional snow mass in the analysis of Paper IV, which is in accordance with field observations, indicates the importance of detailed wind modeling to resolve the whole complexity of these processes.

4.2.4 Summary

To sum it up, presented approaches show the highest sensitivity of surface ablation rates to changes in radiation conditions. However SMB on Vestfonna is also assumed to be highly

influenced by considerable mass loss due to snowdrift. The SMB rate obtained directly from EAR data of about +0.02 ± 0.22 m w.e. yr^{-1} is assumed to be too high due to the snow drift and albedo problematic. The SMB of −0.02 ± 0.20 m w.e. yr^{-1} derived from Paper II showed great uncertainty in estimating the air-temperature field and probably underestimates ablation in the temperature-index module. For the validation period 2007 to 2009 both approaches produced similar total ablation with only 0.02 m w.e. difference. Thus, more indications for a negative SMB than for a neutral or positive SMB on Vestfonna could be found. Assuming the larger ablation rate of −0.49 ± 0.12 m w.e. yr^{-1} of the SEB as resolved by the EAR and the lower accumulation rates of +0.40 ± 0.07 m w.e. yr^{-1} of the empirical approach in Paper II a negative annual SMB rate of about −0.09 ± 0.19 m w.e. yr^{-1} would result for Vestfonna.

4.3 Which large-scale processes produce changes in surface energy and mass balance components on Vestfonna and how do these process chains link the synoptic to the local process space?

On Vestfonna katabatic winds showed strong impact on accumulation patterns and ablation showed strong sensitivity to surface net radiation and sensible heat flux (see Section 4.2). Incoming long wave radiation and sensible heat flux represent usually the largest energy sources for snow and ice melt and strongly correlate with air-temperature (e.g. Ohmura, 2001). The contribution of sensible heat to ablation is determined by the temperature gradients between the air and the surface and turbulence in the lower atmosphere as the mechanism of vertical air exchange (e.g. Hock, 2005). Other studies (e.g. Oerlemans and Grisogono, 2002) show the sensible heat flux on glacial sites is mostly conditioned by changes in air-temperature and wind speed during ablation seasons. Furthermore, Möller (2012) showed precipitation and air-temperature are the principle governing factors for albedo evolution on Vestfonna. Since sensitivity to radiation is large surface albedo plays a key role in understanding the SEB and SMB of Vestfonna. To sum it up, the climate elements air-temperature, precipitation and wind seem to be the least common denominator for an inexpensive description of the governing conditions of SEB and SMB on Vestfonna. Thus, analyses of the seasonality and variability of air-temperature, precipitation and wind are assumed to capture most of the seasonality and variability of the SEB and SMB on Vestfonna. Since the regional reanalysis method solves the whole mesoscale (e.g. Orlanski,

1975) physical links between energy and mass exchange at the glacier-atmosphere interface and large-scale climate dynamics are analyzed in the following paragraphs.

4.3.1 General patterns of air-temperature, precipitation and wind speed

Air-temperature

Analyses in Paper III of the EAR data for the glacier mass-balance years 2001 to 2011 identify Nordaustlandet as the coldest region of Svalbard (see Figure L.1). December to February (DJF) is the coldest and June to August (JJA) the warmest season for all areas of the Svalbard domain. A pronounced south-west to north-east gradient in air-temperatures is observable. Standard deviation of annual mean air-temperature is larger for lower altitudes and mainly happening in the eastern parts of Svalbard (see Figure L.2). The largest standard deviation is found over sea areas in the east of Svalbard and the lowest standard deviation at sea areas in the south-west or at the highest points of Spitsbergen. Land areas show a generally lower standard deviation than sea areas. A clear seasonality of standard deviation is observable (see Figure L3). In general the DJF season shows the largest standard deviation and JJA shows the lowest standard deviation. Air temperature is very stably spatially distributed and strongly influenced by orography. However, the absolute range of air-temperature within the orographic pattern varies by season. The range of air-temperatures is the largest in DJF and the smallest in JJA while Paper III shows the large range of air-temperature during DJF in Svalbard is mainly generated by differences in sea surface temperature. The West-Spitsbergen-Current (see Figure 2.1) transports warm Atlantic water northwards and the sea ice margin fluctuates in the east. The complex Barents Sea bathymetry forces the warm ocean current along the western coast of Spitsbergen while sea ice formation and southward transportation is generally stronger in the eastern sea regions of Svalbard (e.g. Nghiem et al., 2005). This sets up the large ranges in DJF and the generally pronounced south-west to north-east gradient in air-temperatures. In contrast analyses of $\frac{\partial T}{\partial h}$ on Vestfonna in Paper V show values close to 0 K km^{-1} in DJF (see Figure K.3) indicating small ranges of air-temperature on land areas. The seasonal course of $\frac{\partial T}{\partial h}$ indicates that air-temperature ranges are largest during September to November (SON) and March to May (MAM) and smallest in DJF and JJA over land areas. The two maxima of $\frac{\partial T}{\partial h}$ on Vestfonna are

mainly caused by processes of radiative cooling in winter and melt in summer. Nevertheless, considerable year-to-year variability was observed especially during winter.

Wind

The eleven-year mean wind field as resolved by the EAR in Figure L.1 shows a strong south-west component on synoptic scale with wind speeds of about 6 m s^{-1}. Over sea areas the wind field is generally very uniform due to the lack of disturbing land masses. In valleys and areas surrounded by high mountains or ice caps wind speed is lower due to sheltering effects and reaches values of 3-4 m s^{-1}. In contrast highest wind speeds of about 8 m s^{-1} are reached at high elevations (ridges). Prevalent katabatic wind fields are observable especially at large ice caps like Vestfonna or Austfonna on Nordaustlandet. Also analyses of the vertical wind field revealed strong down winds (often exceed 0.4 m s^{-1} in the eleven-year mean) especially over mountain tops and ice caps which have strong katabatic wind systems. In contrast to that the surrounding sheltered areas which show low wind speeds experience pronounced up winds. The up and down wind columns reach heights of about 1500 m above ground while the horizontal extent between the opposed columns is in the scale of 50 km. This is consistent with observations of Sandvik and Furevik (2002) or Barstad and Adakudlu (2011). DJF is the windiest season at most places reaching values of 10 m s^{-1} whereas JJA is the calmest season. Areas of higher relative standard deviations of about 16 % are mainly limited to areas of generally low wind speed (see Figure L.2). These areas are orographically sheltered from the north-east which is the main wind direction and show strong up winds. In contrast the relative standard deviation is lower at ridges where the highest wind speeds and strong down winds are present. A clear seasonality of standard deviation is observable (see Figure L.3). Largest values are found in DJF and lowest values are found in JJA. In contrast to that the relative standard deviation of wind speed is largest (smallest) in MAM (SON) indicating that the seasonal coefficient of variation of year-to-year variability is greatest (smallest) in MAM (SON).

Precipitation

A distinct orographic dependency of precipitation as resolved by the EAR is observable in Figure L.1 while the absolute amount of precipitation decreases with latitude and maxima tend to be located eastwards. A strong relation of snow water equivalent (SWE) to elevation

is also found in field observations. Analyses in Paper I and Paper II of SWE and elevation across Vestfonna revealed a highly significant correlation (r^2 = 0.92, 0.01 significance level) and a weak positive partial correlation of SWE with both easterly and northerly directions, which is consistent with results of the EAR. Paper IV furthermore shows local accumulation patterns on Vestfonna and De Geerfonna are consistent when snowdrift is considered. Field observations of Winther et al. (1998) showed elevation, south-north and west-east precipitation gradients on Spitsbergen. The precipitation distribution in Figure L.1 derived from the EAR shows consistent patterns and amounts. Precipitation over sea areas is small compared to land areas due to the lack of orography. SON is the wettest and JJA the driest season. A distinct decrease of precipitation is observable between SON and JJA. Svalbard is in average wetter than the Nordaustlandet region. South Spitsbergen is the wettest region of Svalbard with the highest values of about 1139 mm/year of accumulated annual precipitation. Within the Nordaustlandet domain accumulated annual precipitation reaches values of about 844 mm/year. Spatial mean of accumulated annual precipitation of all land based grid points reaches 602 mm/year within the Svalbard domain and 545 mm/year within the Nordaustlandet domain. This is due to large dry regions in the center and north-west of Spitsbergen. The largest relative standard deviation of annual mean precipitation of about 37 % is found in the eastern parts on land with a prominent decrease from north to south (see Figure L.2). The spatial distribution is not consistent with the spatial distribution of precipitation in general. For instance Vestfonna and Austfonna in the Nordaustlandet domain show areas of the same annual precipitation amount but the relative standard deviation of the north-eastern areas on Austfonna is nearly doubled compared to the other areas. SON shows the largest and JJA the lowest standard deviation (see Figure L.3). Nevertheless, as well as found for wind speed the relative standard deviation of precipitation is largest (smallest) in MAM (SON) indicating that the seasonal coefficient of variation of year-to-year variability is greatest (smallest) in MAM (SON).

4.3.2 Analysis of seasonal correlations

One phenomenon observed during field work is that perseverative solid precipitation can considerably dampen the albedo decrease during ablation seasons. This further dampens ablation rates due to the strong sensitivity to net radiation. For instance SMB studies in

Section 4.2 show the lowest ablation rates for the mass balance year 2008 (see Figures 4.1 and 4.3). Field observations on Vestfonna confirm perseverative snow fall events during May to August 2008. Furthermore, the EAR data shows the highest amount of solid precipitation and the lowest rain-snow ration, i.e. fraction of liquid to solid precipitation, during ablation season 2008 compared to the other mass-balance years between 2001 to 2011 (see Figures L.4 and L.5).

The correlation analysis of EAR data in Table L.1 indicates that the rain-snow ration is strongly controlled by air-temperature during spring and summer (correlations significant on 0.05 significance level). During the other seasons air-temperature and rain-snow ratio showed no significant correlation on 0.05 significance level. Studies of Möller (2012) and in Paper II also documented this relation during ablation season. A direct correlation of air-temperature and precipitation shows only 77 % probability in JJA. However, precipitation shows significant correlations (on 0.05 significance level) with wind speed during ablation season (see JJA in Table L.1). This relation is also significant on 0.05 significance level in SON and DJF. Furthermore, during high winter (DJF) correlations between all three variables are significant on 0.05 significance level. The correlations during winter are assumed to be caused by relations of cyclone frequency from southern directions advecting warm wet air to Svalbard (see below).

Only weak variability in air-temperature is observable between ablation seasons compared to accumulation seasons in the EAR data (see Figure L.4). The lack of variability strongly influences correlations of air-temperature with other variables during ablation season (see Table L.1). Dampening effects on air-temperature by existing antagonistic processes during ablation season are assumed to be the cause. On the one hand warm air advection reduces the heating effect of the solar rays but increases thermal radiation due to related overcast skies (e.g. Hisdal, 1976). On the other hand the existence of concurring processes of melt and refreezing dampens the variability of air-temperature and fixes it at about 0 °C (e.g. Ohmura, 2001). Since the dampening effect of melt and refreezing processes vanishes during accumulation season air-temperature shows more variance in these seasons (see Figures L.3 and L.4). Analyses in Paper V showed strong impact of surface thermal net radiation which is strongly controlled by clouds during the polar night on the seasonal variability of $\frac{\partial T}{\partial h}$. This supplies an explanation for the observed strong correlation between

air-temperature and precipitation anomalies during accumulation periods on Vestfonna (see Table L.1) since precipitation is connected to overcast skies. Furthermore, this is consistent with significant correlations (see Table L.2) of year-to-year variations of DJF means of sea ice, precipitation, air-temperature and $\frac{\partial T}{\partial h}$. Less sea ice correlates with precipitation (more clouds) and air-temperature while more sea ice correlates with increases in $\frac{\partial T}{\partial h}$ due to less clouds and increased radiative cooling.

4.3.3 Analysis of the impact and origin of cyclones

A clear seasonality of standard deviation of seasonal mean air-temperature, precipitation and wind speed on Nordaustlandet and in Svalbard between years is observable in the EAR data (see Figure L.3). All variables show a decrease of interannual variability between DJF to JJA. Interannual variability of precipitation is also increased in SON, showing even higher values than in DJF on Nordaustlandet while the interannual variability of air-temperature and wind speed in SON shows intermediate values. Further analyses of the seasonal impact of cyclones of different origin on anomalies of air-temperature, precipitation and wind speed on Vestfonna (see Section 3.3.6) reveal significant correlations (on 0.05 significance level) with local cyclogenesis in summer and cyclogenesis in the North Atlantic in winter (see Table L.3). Significant correlations (on 0.05 significance level) with frequency of cyclones from the south-west sector affecting Svalbard are observable in SON with precipitation anomalies, in DJF with anomalies in precipitation, air-temperature and wind speed and in MAM with wind speed anomalies. The local cyclogenesis anti-correlates significantly (on 0.05 significance level) with precipitation anomalies in DJF. In JJA the frequency of cyclones from the south-west affecting Svalbard significantly anti-correlates (on 0.05 significance level) with anomalies in wind speed and sea ice while local cyclogenesis significantly correlates (on 0.05 significance level) with precipitation anomalies.

Other studies (e.g. Tsukernik et al., 2007; Sorteberg and Walsh, 2008) point out that Svalbard is strongly influenced by the activity of the North Atlantic cyclone track transporting moisture and moist static energy (sensible heat, latent heat and geopotential) into the region by cyclones of 200 to 500 km in diameter (e.g. Kristjansson et al., 2011). Thus precipitation and air-temperature anomalies during winter are strongly connected to advection of moisture and sensible heat from the south. The cyclones further affect the sea

ice margin and thus generate additional changes in precipitation, air-temperature and $\frac{\partial T}{\partial h}$ during winter due to the exposure of warm sea water and associated cloud formation. Thus, during winters with less sea ice or late recovering of sea ice (e.g. winter 2005/2006, 2006/2007 and 2007/2008, see Figure L.6) $\frac{\partial T}{\partial h}$ shows low values (see Figure K.3) since air-temperatures at low altitudes are increased, radiative cooling is decreased due to clouds and turbulent mixing is increased by the cyclones. In contrast, during winters with positive sea ice anomaly or early recovering of sea ice (e.g. 2003/2004, 2010/2011) $\frac{\partial T}{\partial h}$ shows the highest values due to excessive radiative cooling. The differences are especially noticeable when comparing extreme years, e.g. the winters of 2003/2004 and 2007/2008.

During summer the activity of the North Atlantic cyclone track is generally decreased and precipitation anomalies as resolved by the EAR show strong correlations with local cyclogenesis (see Table L.3). Also sea ice anomalies show correlations (with 88 % probability) with precipitation in JJA (see Table L.2), i.e. more sea ice generates more precipitation. Other studies (e.g. Inoue and Hori, 2011) observed frontal cyclogenesis at marginal sea ice zones in the Arctic and discuss the thermal contrast between ocean and ice surfaces as likely favorable to cyclogenesis. Thus, the position of the sea ice margin in conjunction with the activity of the North Atlantic cyclone track is supposed to mainly control the precipitation anomalies during summer and affect ablation rates by complex feedback mechanisms of surface albedo, surface absorption of solar radiation and air-temperature. On the other hand the correlation of warm air advection by cyclones from southern directions with air-temperatures is assumed to be strongly distorted during summer due to the dampening effect of melt and refreezing processes. However, further analyses of events of cold air advection during JJA (not shown) revealed strong correlations with negative air temperature anomalies.

4.3.4 Correlations with the North Atlantic Oscillation (NAO) and the Arctic Oscillation (AO)

The NAO is one of the most important indices of variability in the northern hemisphere atmospheric circulation (e.g. Wanner et al., 2001) and a measure of the strength of the westerly flow which mainly controls storm tracks across the North Atlantic. Thus, the

frequency of cyclones originated in the North Atlantic sector affecting Svalbard, the local cyclogenesis in the Svalbard sector and seasonal variability of air-temperature, precipitation and wind speed on Vestfonna as resolved by the EAR are analyzed with the NAO Index in the following paragraphs. The AO Index was also analyzed but showed only weak correlations with seasonal variability of air-temperature, precipitation and wind speed (see Table L.4).

Table L.3 shows significant correlations (on 0.05 significance level) of the frequency of cyclones originated in the south-west sector affecting Svalbard with the NAO Index in DJF. In contrast significant anti-correlation (on 0.05 significance level) is observed between the NAO Index with local cyclogenesis in JJA. Also seasonal anomalies of air-temperature, precipitation and wind speed on Vestfonna show correlations with NAO Index (see Table L.4). The NAO Index shows significant correlations (on 0.05 significance level) with wind speed anomalies in SON and with precipitation and wind speed in DJF. In JJA air-temperature anomalies correlate on 0.05 significance level with the NAO Index. Furthermore, Other studies reported correlations of positive NAO conditions with less sea ice in the Barents Sea (Yamamoto et al., 2006), increased precipitation over Svalbard (Rogers et al., 2001) and anti-correlation of sea ice anomalies in the Barents Sea with air-temperature anomalies over Svalbard (Koenigk et al., 2009). Nevertheless, a significant correlation on 0.05 significance of NAO Index and the sea ice anomalies in the smaller Nordaustlandet domain was not observed in this study.

Since the activity of the North Atlantic cyclone track shows correlations with the NAO Index and its impact on Svalbard is strongly assumed to generate most of the variability in SEB and SMB rates of Vestfonna also analyses in Paper II showed dependencies of the mass balance variability on the NAO Index. Modeled winter balances correlate significantly (r^2 = 0.44, 0.1 significance level) with the mean winter NAO Index (DJF). The summer balances in turn anti-correlate significantly (r^2 = 0.46, 0.05 significance level) with the mean summer NAO Index (JJA).

4.3.5 Summary

To sum it up, correlation analyses showed the activity of the North Atlantic cyclone track strongly influences the variability of SEB and SMB on Vestfonna. Since the activity of the North Atlantic cyclone track correlates with NAO also correlations are observed with this

index. Increased frequency of cyclones from the south-west during winter (summer) shows positive (negative) impact on SMB rates on Vestfonna. The cyclones of meso-α-scale advect moist and warm air and influence the sea ice margin. During winter accumulation rates correlate with the activity of the North Atlantic cyclone track, i.e. moisture transport by cyclones from the south during September to February. During summer precipitation anti-correlates with the activity of the North Atlantic cyclone track but correlates with local cyclogenesis and sea ice anomalies. Furthermore, the summer precipitation is assumed to control ablation rates by complex feedback mechanisms of surface albedo, surface absorption of solar radiation and air-temperature while most of the variability of the ablation rates is generated in the higher parts of Vestfonna. The activity of the North Atlantic cyclone track and NAO index anti-correlate with ablation rates and correlates with accumulation rates on Vestfonna. Variability in air-temperature and precipitation shows strong orographic dependency, i.e. the highest elevations experience the highest variability in precipitation and summer air-temperature and the lowest elevations experience the highest variability in winter air-temperature. Maximum variability of precipitation is dislocated to north-eastern directions.

Since most of the variability is generated on meso-α-scale the statistical transfer functions of Paper II show good performance. Nevertheless, the identification of complex snowdrift processes on micro-α-scale, local differences in dampening of air-temperatures by melt and refreezing processes, cyclogenesis in the region of Svalbard during summer and associated precipitation-ablation feedbacks and a general dislocation of maximum variability of precipitation to north-eastern directions indicate large uncertainty and error proneness of the statistical transfer functions in a changing climate.

5 Concluding remarks and outlook

At the beginning of this work, the goal was to improve our understanding of the atmosphere-cryosphere interactions on Arctic glaciers and in particular to investigate seasonality and variability of the climate in Svalbard and its impact on Vestfonna ice cap. Now, five years later, nine field campaigns have been conducted, a powerful computational modeling and analysis infrastructure has been implemented and huge data sets of field observational data and regional reanalysis data are available. The results of this thesis provide detailed information about the state and sensitivity of SEB and SMB on Vestfonna, what meso-scale processes generate the changes and how these processes link the synoptic to the local process space during the first decade of the 21st century. This thesis also demonstrates how difficult it is to obtain field observational data and to reliably assess the current state and future development in the Arctic region. The mechanisms of impacts and interactions in the region of Svalbard are complex and could only partly be analyzed in this work. Nevertheless, the answered questions may contribute to further close the large gap in knowledge that exists for the Arctic.

The SEB and SMB on Vestfonna show the highest sensitivity of surface ablation rates to changes in radiation conditions. Surface albedo is identified as a key factor for ablation rate estimations on Vestfonna. The SMB on Vestfonna also shows high dependency on snowdrift causing considerable mass loss in accumulation rates. An annual SMB rate on Vestfonna of $+0.02 \pm 0.22$ m w.e. yr^{-1} is calculated from the EAR data and an annual SMB rate of -0.02 ± 0.20 m w.e. yr^{-1} is calculated by an empirical approach for the mass balance years 2001 to 2009. The estimate derived from the EAR is assumed to be too high since snow drift is not considered in the accumulation rates and the constant surface albedo of 0.8 could have caused underestimations in ablation rates. The empirical approach shows uncertainty in estimating the air-temperature fields. Furthermore, uncertainty about estimated refreezing rates used to calculate SMB rates from climatic mass balance estimates exists. However, combining results derived from both approaches, the “pessimistic” annual SMB rate on Vestfonna of about -0.09 ± 0.19 m w.e. yr^{-1} for the mass balance years 2001 to 2009 is estimated by using the higher ablation rates derived from EAR calculations and the lower accumulations rates derived from the empirical study.

All results indicate that the annual SMB rate was almost balanced during the last decade on Vestfonna. However, especially changes in the rain-snow ratio due to changes in air-temperature are assumed to have great potential to generate strong changes in the SMB rates on Vestfonna in the future. Since this thesis concentrates only on SEB and SMB changes of the ice cap, changes in glacier dynamics have not been investigated. Nevertheless, other studies suggest calving to be a non-negligible term of Vestfonna's overall budget while several outlet glaciers seem to be of surge type (e.g. Braun et al., 2011; Pettersson et al., 2011; Schäfer et al., 2012). However, since reliable estimates of the calving rates and glacier dynamics are lacking, a considerable uncertainty about the overall budget of Vestfonna still remains. Furthermore, detailed analyses of refreezing rates on Vestfonna remain one of the crucial research topics for the future.

The activity of the North Atlantic cyclone track shows strong influence on accumulation and ablation rates on Vestfonna. Since the NAO is one of the most important indices of variability in the northern hemisphere atmospheric circulation, and a measure of the strength of the westerly flow which mainly controls storm tracks across the North Atlantic, it also shows strong correlations with accumulation and ablation rates on Vestfonna. During winter, the NAO index significantly correlates with the frequency of cyclones from the North Atlantic sector through precipitation, air-temperature and wind speed since moisture and moist static energy is transported by the cyclones into the region. During summer, the NAO index significantly anti-correlates with local cyclogenesis and summer precipitation, generating variability in ablation rates on Vestfonna by complex feedback mechanisms between surface albedo, surface absorption of solar radiation and air-temperature.

Variability in air-temperature and precipitation show strong orographic dependency in general, and most of the seasonal variability is generated on meso-α-scale. This is why statistical transfer functions showed good performance in the empirical study. Nevertheless, especially snow drift and summer precipitation show considerable year-to-year variability on smaller scales indicating large uncertainty and error potential of the employed statistical transfer functions in a changing climate.

The regional reanalysis method shows great potential for process-based analyses of the atmosphere-cryosphere interface. Since this approach is based on physical laws rather than statistical transfer functions, it is supposed to better reproduce relations between the

atmosphere and cryosphere also under a changing climate. Nevertheless, this study also demonstrates great possibilities of future optimization of the EAR. One of the crucial prerequisites is to provide a highly accurate DEM for future regional reanalyses as well as for other modeling, since most of the analyzed variables show strong orographic dependency. In addition, detailed datasets of land surface categories and related properties are required. Especially errors in the surface energy balance modeling could be decreased by using additional remote sensing products of snow depth and surface albedo in the reanalysis. A subsequent implementation of high resolution snow drift modeling is further required to reproduce accurate accumulation patterns from reanalysis data.

References

ACIA, Arctic Climate Impact Assessment, Cambridge University Press, 2005, http://www.amap.no/acia/.

Ahlmann, H.W., 1933. Scientific results of the Swedish-Norwegian Arctic Expedition in the summer of 1931. *Geografiska Annaler*, 15, 47-68, 161-216 and 261-295.

AMAP. 2012. Arctic monitoring and Assessment Programme (AMAP), 2012.

Angström, A., 1933. Scientific results of the Swedish-Norwegian Arctic Expedition in the summer of 1931. Part VII - On the total Radiation from Sun and Sky at Sveanor (79°56.5'N, 18°18'E). *Geografiska Annaler*, 15, 151-159.

Arendt, A., Echelmeyer, K., Harrison, W., Lingle, C. and Valentine, V., 2002. Rapid wastage of Alaska glaciers and their contribution to rising sea level. *Science*, 297, 382-386.

Arkhipov, S.M., Vaykmyae, R.A., Vasilenko, Ye.V., Zagorodnov, V.S., Zinger, Ye.M., Martma, T.A., Macheret, Yu.Ya., Punning, Y.-M.K., Samoylov, O.Yu., Sin'kevich, S.A., Toots, M.D. and Troitskiy, L.S., 1987. Soviet glaciological investigations on Austfonna , Nordaustlandet, Svalbard in 1984-1985. *Polar Geography and Geology*, 11(1), 25-49.

Bahr, D. B., Dyurgerov, M. and Meier, M. F., 2009. Sea-level rise from glaciers and ice caps: A lower bound. *Geophysical Research Letters*, 36.

Bamber, J., 2012. CLIMATE CHANGE Shrinking glaciers under scrutiny. *Nature*, 482, 482-483.

Barber, D. G., Lukovich, J. V., Keogak, J., Baryluk, S., Fortier, L. and Henry, G. H. R., 2008. The Changing Climate of the Arctic. *Arctic*, 61, 7-26.

Barr, W., 1988. The Helgoland expedition to Svalbard: Die Deutsche Expedition in das Nördliche Eismeer, 1898. *Arctic Institute of North America, Arctic*, 41(3), 203-214.

Beaudon, E. and Moore, J., 2009. Frost flower chemical signature in winter snow on Vestfonna ice cap, Nordaustlandet, Svalbard. *The Cryosphere*, 3, 147-154.

Berthier, E., Schiefer, E., Clarke, G. K. C., Menounos, B. and Remy, F., 2010. Contribution of Alaskan glaciers to sea-level rise derived from satellite imagery. *Nature Geoscience*, 3, 92-95.

Blake, W., 2006. Occurrence of the Mytilus edulis complex on Nordaustlandet, Svalbard: radiocarbon ages and climatic implications. *Polar Reasearch*, 25(2), 123-137.

Braun, M. and Hock, R. 2004. Spatially distributed surface energy balance and ablation modelling on the ice cap of King George Island, Antarctica. *Global and Planetary Change*, 42(1–4), 45–58.

Braun, M., Pohjola, V. A., Pettersson, R., Moeller, M., Finkelnburg, R., Falk, U., Scherer, D. and Schneider, C., 2011. Changes of Glacier Frontal Positions of Vestfonna (Nordaustlandet, Svalbard). *Geografiska Annaler*, Series A: Physical Geography, 93, 301-310.

Chydenius, K., 1865. Svenska expedition till Spetsbergen ar 1861 under ledning af Otto Torell [The Swedish Expedition to Svalbard in 1861, led by Otto Torell]. *P.A. Norstedt & Söner*, Stockholm.

Cogley, J.G., Arendt, A.A., Bauder, A., Braithwaite, R.J., Hock, R., Jansson, P., Kaser, G., Möller, M., Nicholson, L., Rasmussen, L.A. and Zemp, M., 2011. Glossary of Glacier Mass Balance and Related Terms. *IHP-VII Technical Documents in Hydrology No. 86, IACS Contribution No. 2*, UNESCO-IHP, Paris.

Dege, W., 1960. Wissenschaftliche Beobachtungen auf dem Nordostland von Spitzbergen 1944-1945. *Berichte des Deutschen Wetterdienstes*, 72, 99 p.

De Geer, G., 1923. Mesure d'un arc de méridien au Spitzberg 1899 - 1902. Mission suédoise. 1: 200 000. Feuille 1. Cap Nord. Feuille 2. Hinlopen.

Donner, J. J. and West, R. G., 1957. The Quaternary geology of Brageneset, Nordaustlandet, Spitsbergen. *Norsk Polarinstitutt*, 109, 1-29.

Dowdeswell, J., Hagen, J., Bjornsson, H., Glazovsky, A., Harrison, W., Holmlund, P., Jania, J., Koerner, R., Lefauconnier, B., Ommanney, C. and Thomas, R., 1997. The mass balance of circum-Arctic glaciers and recent climate change. *Quaternary Research*, 48, 1-14.

Egli, L., Jonas, T. and Meister, R., 2009. Comparison of different automatic methods for estimating snow water equivalent. *Cold Regions Science and Technology*, 57, 107-115.

Ekman, S.R., 1971. Seismic investigations on the Nordaustlandet ice caps. *Geografiska Annaler*, Series A: Physical Geography, 53, 1-13.

Eriksson, B.E., 1933. Scientific results of the Swedish-Norwegian Arctic Expedition in the summer of 1931. Part VI - Climatology and Meteorology. *Geografiska Annaler*, 15, 117-150.

Fjeldstad, J.E., 1933. Scientific results of the Swedish-Norwegian Arctic Expedition in the summer of 1931. Part IX – Snow and ice temperatures. *Geografiska Annaler*, 15, 296-315.

Førland , E. and Hanssen-Bauer, I., 2003. Past and future climate variations in the Norwegian Arctic: overview and novel analyses. *Polar Research*, 22, 113-124.

Gardner, A. S., Moholdt, G., Wouters, B., Wolken, G. J., Burgess, D. O., Sharp, M. J., Cogley, J. G., Braun, C. and Labine, C., 2011. Sharply increased mass loss from glaciers and ice caps in the Canadian Arctic Archipelago. *Nature*, 473, 357-360.

Gardner, A. S. and Sharp, M., 2009. Sensitivity of net mass-balance estimates to near-surface temperature lapse rates when employing the degree-day method to estimate glacier melt. *Annals of Glaciology*, 50, 80-86.

Gardner, A. S., Sharp, M. J., Koerner, R. M., Labine, C., Boon, S., Marshall, S. J., Burgess, D. O. and Lewis, D., 2009. Near-Surface Temperature Lapse Rates over Arctic Glaciers and Their Implications for Temperature Downscaling. *Journal of Climate*, 22, 4281-4298.

Glen, A.R., 1937. The Oxford University Arctic Expedition, North East Land, 1935-36. *The Geographical Journal*, 90(3), 193-222.

Glen, A.R., 1939. The glaciology of North East Land. Geografiska Annaler, 21, 1-38.

Glen, A.R., 1941. A sub-arctic glacier cap: The West Ice of North East Land. *The Geographical Journal*, 98(2), 65-76.

Goodisen, B., Metcalfe, J., Wilson, R. and Jones, K., 1988. The Canadian automatic snow depth sensor: a performance update. *Proceedings of the 56th Annual Western Snow Conference*.

Grabiec, M., Puczko, D., Budzik, T., and Gajek, G., 2011. Snow distribution patterns on Svalbard glaciers derived from radio-echo soundings. *Polish Polar Research*, 32, 393–421.

Hagen, J., Melvold, K., Pinglot, F. and Dowdeswell, J., 2003. On the net mass balance of the glaciers and ice caps in Svalbard, Norwegian Arctic. *Arctic, Antarctic, and Alpine Research*, 35, 264-270.

Hines, K. M. and Bromwich, D. H., 2008. Development and testing of Polar Weather Research and Forecasting (WRF) Model. Part I: Greenland ice sheet meteorology. *Monthly Weather Review*, 136, 1971-1989.

Hines, K. M., Bromwich, D. H., Bai, L.-S., Barlage, M. and Slater, A. G., 2011. Development and Testing of Polar WRF. Part III: Arctic Land. *Journal of Climate*, 24, 26-48.

Hisdal, V., 1976. Geography of Svalbard: a short survey. *Norsk Polarinstitutt*, 75.

Hock, R., 2005. Glacier melt: a review of processes and their modelling. *Progress in Physical Geography*, 29, 362-391.

Inoue, J. and Hori, M. E., 2011. Arctic cyclogenesis at the marginal ice zone: A contributory mechanism for the temperature amplification?. *Geophysical Research Letters*, 38.

IPCC, 2007. Cambridge University Press, Cambridge, United Kingdom and New York, NY, USA.

Jacob, T., Wahr, J., Pfeffer, W. T. and Swenson, S., 2012. Recent contributions of glaciers and ice caps to sea level rise. *Nature*, 482, 514-518.

Kaser, G., Cogley, J. G., Dyurgerov, M. B., Meier, M. F. and Ohmura, A., 2006. Mass balance of glaciers and ice caps: Consensus estimates for 1961-2004. *Geophysical Research Letters*, 33.

Koenigk, T., Mikolajewicz, U., Jungclaus, J. H. and Kroll, A., 2009. Sea ice in the Barents Sea: Seasonal to interannual variability and climate feedbacks in a global coupled model. *Climate Dynamics*, 32, 1119–1138

Kotlyakov, V.M., Arkhipov, S.M., Henderson, K.A. and Nagornov, O.V., 2004. Deep drilling of glaciers in Eurasian Arctic as a source of paleoclimatic records. *Quaternary Science Reviews*, 23(11-13), 1371-1390.

Kristjansson, J. E., Barstad, I., Aspelien, T., Fore, I., Godoy, O., Hov, O., Irvine, E., Iversen, T., Kolstad, E., Nordeng, T. E., McInnes, H., Randriamampianina, R., Reuder, J., Saetra, O., Shapiro, M., Spengler, T. and Olafsson, H., 2011. The Norwegian IPY-THORPEX Polar Lows and Arctic Fronts during the 2008 Ancloya Campaign. *Bulletin of the American Meteorological Society*, 92, 1443-1466.

Liljequist, G.H., 1959. Murchison Bay. Den svensk-finsk-schweiziska expedition till Nordaustlandet 1957-58. *Ymer*, 79, 81-139.

Marshall, S. J., Sharp, M. J., Burgess, D. O. and Anslow, F. S., 2007. Near-surface-temperature lapse rates on the Prince of Wales Icefield, Ellesmere Island, Canada: implications for regional downscaling of temperature. *International Journal of Climatology*, 27, 385-398.

Maussion, F., Scherer, D., Finkelnburg, R., Richters, J., Yang, W. and Yao, T., 2011. WRF simulation of a precipitation event over the Tibetan Plateau, China - an assessment using remote sensing and ground observations. *Hydrology and Earth System Science*, 15, 1795-1817.

Meier, M. F., Dyurgerov, M. B., Rick, U. K., O'Neel, S., Pfeffer, W. T., Anderson, R. S., Anderson, S. P. and Glazovsky, A. F., 2007. Glaciers dominate Eustatic sea-level rise in the 21st century. *Science*, 317, 1064-1067.

Moholdt, G., Wouters, B. and Gardner, A. S., 2012. Recent mass changes of glaciers in the Russian High Arctic. *Geophysical Research Letters*, 39.

Mölg, T. and Kaser, G., 2011. A new approach to resolving climate-cryosphere relations: Downscaling climate dynamics to glacier-scale mass and energy balance without statistical scale linking. *Journal of Geophysical Research – Atmospheres*, 116.

Möller, M., 2012. A minimal, statistical model for the surface albedo of Vestfonna ice cap, Svalbard. *The Cryosphere*, 6, 1049-1061.

Möller, M., Schneider, C. and Kilian, R. ,2007. Glacier change and climate forcing in recent decades at Gran Campo Nevado, southernmost Patagonia. *Annals of Glaciology*, 46, 136–144.

Moss, R., 1938. The physics of an ice-cap. *The Geographical Journal*, 92(3), 211-231.

Motoyama, H., Watanabe, O., Goto-Azuma, K., Igarashi, M., Miyahara, H., Nagasaki, T., Karlof, L. and Isaksson, E., 2001. Activities of the Japanese Arctic Glaciological Expedition in 1999 (JAGE 1999). *Memoirs of National Institute of Polar Research*, 54, 253-60.

New, M., Lister, D., Hulme, M. and Makin, I., 2002. A high-resolution data set of surface climate over global land areas. *Climate Research*, 21, 1-25.

Nghiem, S., Van Woert, M. and Neumann, G., 2005. Rapid formation of a sea ice barrier east of Svalbard. *Journal of Geophysical Research - Oceans*, 110.

Oerlemans, J. and Grisogono, B., 2002. Glacier winds and parameterisation of the related surface heat fluxes. *Tellus Series A - Dynamic Meteorology and Oceanography*, 54, 440-452.

Ohmura, A., 2001. Physical basis for the temperature-based melt-index method. *Journal of Applied Meteorology*, 40, 753-761.

Orlanski, I., 1975. A rational subdivision of scales for atmospheric processes. *Bulletin of the American Meteorological Society*, 56, 527-530.

Palosuo, E., 1987a. A study of snow and ice temperatures on Vestfonna, Svalbard, 1956, 1957 and 1958. *Geografiska Annaler*, 69A(3-4), 431-437.

Palosuo, E., 1987b. Ice layers and superimposition of ice on the summit and slope of Vestfonna, Svalbard. *Geografiska Annaler*, 69A(2), 289-296.

Pellicciotti, F., Brock, B., Strasser, U., Burlando, P., Funk, M. and Corripio, J., 2005. An enhanced temperature-index glacier melt model including the shortwave radiation balance: Development and testing for Haut Glacier d'Arolla, Switzerland. *Journal of Glaciology*, 51(175), 573–587.

Petersen, L. and Pellicciotti, F., 2011. Spatial and temporal variability of air temperature on a melting glacier: Atmospheric controls, extrapolation methods and their effect on melt modeling, Juncal Norte Glacier, Chile. *Journal of Geophysical Research - Atmosphere*, 116.

Pettersson, R., Christoffersen, P., Dowdeswell, J. A., Pohjola, V. A., Hubbard, A. and Strozzi, T., 2011. Ice Thickness and Basal Conditions of Vestfonna Ice Cap, Eastern Svalbard. *Geografiska Annaler*, Series A: Physical Geography, 93A, 311-322.

Pinglot, J., Pourchet, M., Lefauconnier, B., Hagen, J., Isaksson, E., Vaikmae, R. and Kamiyama, K., 1999. Accumulation in Svalbard glaciers deduced from ice cores with nuclear tests and Chernobyl reference layers. *Polar Research*, 18, 315-321.

Pomeroy, J. and Gray, D., 1990. Saltation of Snow. *Water Resources Research*, 26, 1583–1594.

Pomeroy, J. and Male, D., 1992. Steady-state suspension of snow. *Journal of Hydrology*, 136, 275–301.

Punning, Ya.-M.K., Martma, T.A., Tuygu, K.E., Vaikmäe, R.A., Pourchet, M. and Pinglot, J.F., 1986. Stratification in an ice core from Vestfonna, Nordaustlandet. *Polar Geography and Geology*, 10(1), 39-43.

Raper, S. and Braithwaite, R., 2006. Low sea level rise projections from mountain glaciers and icecaps under global warming. *Nature*, 439, 311-313.

Reeh, N., 1991. Parameterization of melt rate and surface temperature on the Greenland ice sheet. *Polarforschung*, 59(3), 113–128.

Rinke, A. and Dethloff, K., 2008. Simulated circum-Arctic climate changes by the end of the 21st century. *Global and Planetary Change*, 62, 173-186.

Rogers, A. N., Bromwich, D. H., Sinclair, E. N. and Cullather, R. I., 2001. The atmospheric hydrologic cycle over the Arctic Basin from reanalysis. Part II: Interannual variability. *Journal of Climate*, 14(11), 2414–2429.

Rudels, B., 2012. Arctic Ocean circulation and variability - advection and external forcing encounter constraints and local processes. *Ocean Science*, 8, 261-286.

Schäfer, M., Zwinger, T., Christoffersen, P., Gillet-Chaulet, F., Laakso, K., Pettersson, R., Pohjola, V. A., Strozzi, T. and Moore, J.C., 2012. Sensitivity of basal conditions in an inverse model: Vestfonna ice cap, Nordaustlandet/Svalbard. *The Cryosphere*, 6, 771-783.

Sandford, K.S., 1925. The Oxford University Arctic Expedition 1924. II – Geology and glaciology. *The Geographical Journal*, 66(2), 114-120.

Sandford, K.S., 1926. Summer in North-East Land, 1924: The climate and surface changes. *The Geographical Journal*, 68(3), 200-225.

Sandford, K.S., 1929. The glacial conditions and quaternary history of North-East Land. *The Geographical Journal*, 68(3), 200-225.

Schuler, T.V., Loe, E., Taurisano, A., Eiken, T., Hagen, J.O. and Kohler, J., 2007. Calibrating a surface mass-balance model for Austfonna ice cap, Svalbard. Annals of Glaciology, 46, 241-248.

Schytt, V., 1964. Scientific results of the Swedish Glaciological Expedition to Nordaustlandet, Spitsbergen, 1957 and 1958. *Geografiska Annaler*, Series A: Physical Geography, 46(3), 243-281.

Schytt, V., 1967. A study of "ablation gradient". *Geografiska Annaler*, 49A(2-4), 327-332.

Schytt, V., Hoppe, G., Blake, W., Jr., and Grosswald, M.G., 1968. The extent of the Würm glaciation in the European Arctic: A preliminary report about the Stockholm University Svalbard Ex-pedition 1966. *International Association of Scientific Hydrology*, 79, 207-216.

Sinkevich, S., 1991. Climate warming in the twentieth century as reflected in Svalbard ice cores. *IAHS Publications*, 208, 258-267.

Sorteberg, A., Kvamstø, N. G. and Byrkjedal, Ø., 2005. Wintertime Nordic Seas cyclone variability and its impact on oceanic volume transport into the Nordic Seas*. The Nordic Seas: An integrated Perspective*, AGU Geophysical Monograph Series, 158.

Sorteberg, A. and Walsh, J. E., 2008. Seasonal cyclone variability at 70 degrees N and its impact on moisture transport into the Arctic. *Tellus Series A - Dynamic Meteorology and Oceanography*, 60, 570-586.

Stroeve, J., Holland, M. M., Meier, W., Scambos, T. and Serreze, M., 2007. Arctic sea ice decline: Faster than forecast. *Geophysical Research Letters*, 34.

Thompson, H.R., 1953. Geology and Geomorphology in Southern Nordaustlandet (Nort-East Land), Spitsbergen. *Proceedings of Geologists' Association*,64(4), 293-312.

Tsukernik, M., Kindig, D. N. and Serreze, M. C., 2007. Characteristics of winter cyclone activity in the northern North Atlantic: Insights from observations and regional modeling. *Journal of Geophysical Research – Atmospheres*, 112.

Tymms, F., 1925. The Oxford University Arctic Expedition, 1924. III – Meteorology. *The Geographical Journal*, 66(2), 120-126.

Vaykmyae, R.A., Martma, T.A., Punning, Ya.-M.K. and Tyugu, K.R., 1985. Variations in d18O and Cl- in an ice core from Vestfonna Nordaustlandet. *Polar Geography and Geology*, 9(4), 329-333.

Walczowski, W. and Piechura, J., 2011. Influence of the West Spitsbergen Current on the local climate. *International Journal of Climatology*, 31, 1088-1093.

Wanner, H., Bronnimann, S., Casty, C., Gyalistras, D., Luterbacher, J., Schmutz, C., Stephenson, D. and Xoplaki, E., 2001. North Atlantic Oscillation - Concepts and studies. *Surveys in Geophysics*, 22, 321-382.

Watanabe, O., Kamiyama, K., Kameda, T., Takahashi, S., and Isaksson, E., 2000. Activities of the Japanese Arctic Glaciological Expedition in 1998 (JAGE 1998). *Bulletin of Glaciological Research*, 17, 31–35.

Winther, J., Bruland, O., Sand, K., Killingtveit, A. and Marechal, D., 1998. Snow accumulation distribution on Spitsbergen, Svalbard, in 1997. *Polar Research*, 17, 155-164.

Winther, J., Gerland, S., Orbaek, J., Ivanov, B., Blanco, A. and Boike, J., 1999. Spectral reflectance of melting snow in a high Arctic watershed on Svalbard: some implications for optical satellite remote sensing studies. *Hydrological Processes*, 13, 2033-2049.

Wu, X., Heflin, M. B., Schotman, H., Vermeersen, B. L. A., Dong, D., Gross, R. S., Ivins, E. R., Moore, A. and Owen, S. E., 2010. Simultaneous estimation of global present-day water transport and glacial isostatic adjustment. *Nature Geoscience*, 3, 642-646.

Yamamoto, K., Tachibana, Y., Honda, M. and Ukita, J., 2006. Intra-seasonal relationship between the Northern Hemisphere sea ice variability and the North Atlantic Oscillation. *Geophysical Research Letters*, 33, L14711.

Personal communication

Martma, T., Institute of Geology, Tallinn University of Technology, Estonia.

Motoyama, H., National Institute of Polar Research, Tokyo, Japan.

Kameda, T., Kitami Institute of Technology, Hokkaido, Japan.

Appendix A: Snowpack characteristics of Vestfonna and De Geerfonna (Nordaustlandet, Svalbard) – a spatiotemporal analysis based on multiyear snow-pit data

Möller, M., Möller, R., Beaudon, E., Mattila, O.-P. , Finkelnburg, R., Braun, M., Grabiec, M. Jonsell, U., Luks, B., Puczko, D., Scherer, D. and Schneider C., 2011. Snowpack characteristics of Vestfonna and De Geerfonna (Nordaustlandet, Svalbard) – a spatiotemporal analysis based on multiyear snow-pit data. *Geografiska Annaler: Series A*, 93 (4), 273-285. doi:10.1111/j.1468-0459.2011.00440.x.

Status: Published

Own contribution:

- Preparation, conduction and leading of field campaigns
- Acquisition of field observational data
- Processing of field observational data
- Review, comments and improvements of the manuscript

SNOWPACK CHARACTERISTICS OF VESTFONNA AND DE GEERFONNA (NORDAUSTLANDET, SVALBARD) – A SPATIOTEMPORAL ANALYSIS BASED ON MULTIYEAR SNOW-PIT DATA

BY
MARCO MÖLLER[1], REBECCA MÖLLER[2], ÉMILIE BEAUDON[3], OLLI-PEKKA MATTILA[4], ROMAN FINKELNBURG[5], MATTHIAS BRAUN[6,7], MARIUSZ GRABIEC[8], ULF JONSELL[9], BARTŁOMIEJ LUKS[10], DARIUSZ PUCZKO[10], DIETER SCHERER[5] AND CHRISTOPH SCHNEIDER[1]

[1]Department of Geography, RWTH Aachen University, Germany
[2]Geological Institute, RWTH Aachen University, Germany
[3]Arctic Centre, University of Lapland, Rovaniemi, Finland
[4]Department of Physics, University of Helsinki, Finland
[5]Department of Ecology, TU Berlin, Germany
[6]Geophysical Institute, University of Alaska, Fairbanks, USA
[7]Centre for Remote Sensing on Land Applications (ZFL), University of Bonn, Germany
[8]Department of Geomorphology, University of Silesia, Sosnowiec, Poland
[9]Department of Earth Sciences, Uppsala University, Sweden
[10]Institute of Geophysics, Polish Academy of Sciences, Warsaw, Poland

Möller, M., Möller, R., Beaudon, É., Mattila, O.-P., Finkelnburg, R., Braun, M., Grabiec, M., Jonsell, U., Luks, B., Puczko, D., Scherer, D. and Schneider, C., 2011. Snowpack characteristics of Vestfonna and De Geerfonna (Nordaustlandet, Svalbard) – a spatiotemporal analysis based on multiyear snow-pit data. *Geografiska Ann*aler, *Series A: Physical Geography,* ••, ••–••. DOI: 10.1111/j.1468-0459.2011.00440.x

ABSTRACT. Extensive glaciological field measurements were carried out on the ice cap Vestfonna as well as on the minor ice body De Geerfonna (Nordaustlandet, Svalbard) within the framework of IPY Kinnvika. Field campaigns were conducted during the period 2007–2010 in spring (April/May) and summer (August). In this study we compile and present snow cover information obtained from 22 snow pits that were dug on Vestfonna during this period. Locations are along two transects on the northwestern, land terminating slope of the ice cap, on its central summit, Ahlmann Summit, and at a set of several other locations in the eastern and northern part of the ice cap. Snow-cover information acquired from four snow pits on adjacent De Geerfonna is also incorporated in this study. Field data are analysed regarding snow stratigraphy, snow density, snow hardness and snow temperature. Results reveal mean snow densities of around 400 kg m^{-3} for the snowpack of Vestfonna with no apparent spatial or interannual variability. A distinctly higher value of more than 450 kg m^{-3} was obtained for De Geerfonna. A spatial comparison of snow water equivalents above the previous end-of-summer surface serves for obtaining insights into the spatial distribution of snow accumulation across Vestfonna. Altitude was found to be the only significant spatial parameter for controlling snow accumulation across the ice cap.

Key words: accumulation, snow cover, snow profiles, Svalbard

Introduction

In the framework of the IPY (International Polar Year) Kinnvika project (Pohjola *et al*. 2011) and its follow-on activities several field campaigns with focus on snow-cover related fieldwork were carried out during seven individual field campaigns on Nordaustlandet, Svalbard, in the period 2007–2010. Snow cover conditions were investigated on the ice cap Vestfonna as well as the neighbouring minor ice body De Geerfonna. Snow-cover related fieldwork on Vestfonna focused on two transects along the northwestern slope of the ice cap and on its main ridges, including the two highest points, Ahlmann Summit and Japanese Summit, whereas the activities on De Geerfonna were limited to one central study site (Fig. 1, Table 1). In all, 26 snow pits (22 on Vestfonna, 4 on De Geerfonna) were excavated during the various field campaigns.

DOI: 10.1111/j.1468-0459.2011.00440.x

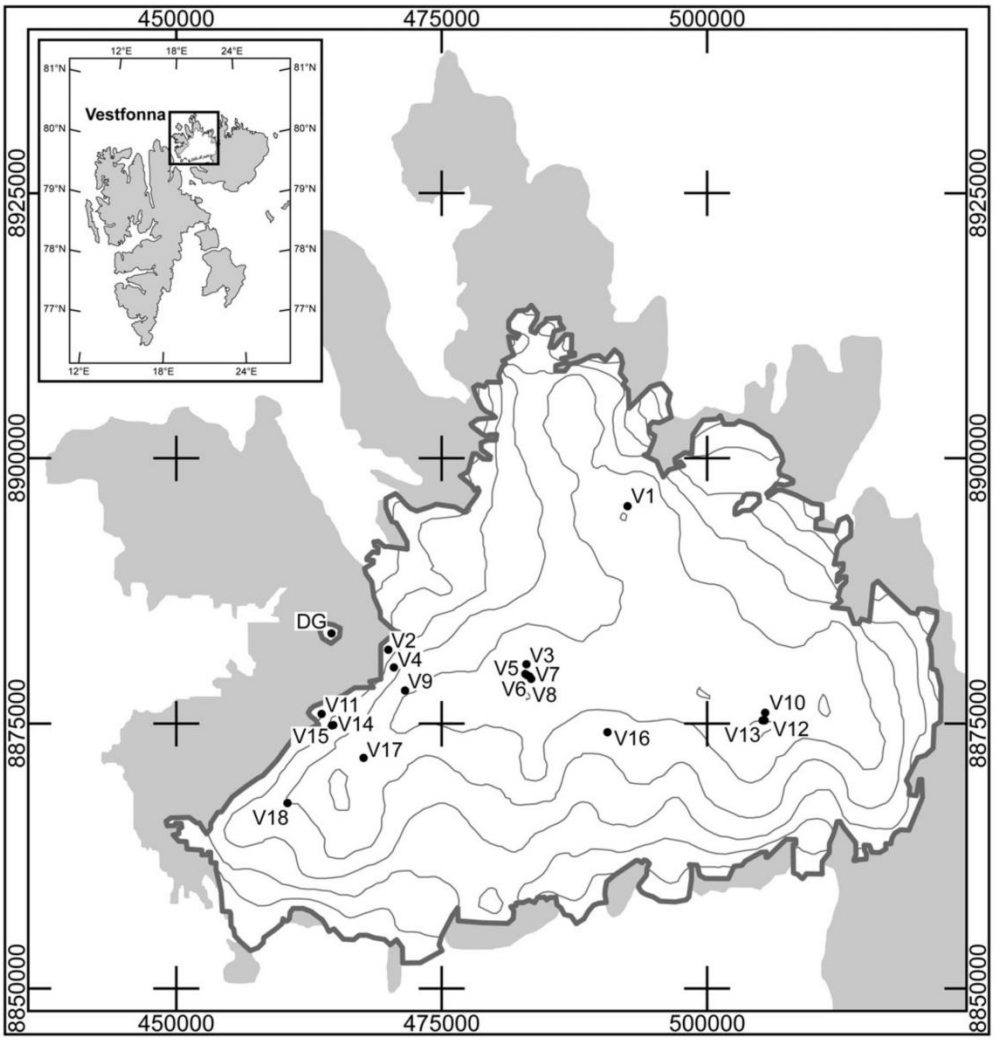

Fig. 1. Location of Vestfonna and De Geerfonna and overview of locations of snow pits. Contour spacing is 100 m. Coordinates correspond to Universal Transverse Mercator (UTM) zone 34N. Inset: Location of the study area within the Svalbard archipelago.

The aim of this study is to present a comprehensive compilation of snow stratigraphy data from recent point-based field investigations. It provides a data basis of in situ information regarding snow accumulation on Vestfonna and western Nordaustlandet. Hence, the more descriptive main part of the study is supplemented by a basic analysis of spatial distribution of accumulation across Vestfonna. Our results serve as a basis for calibration and validation regarding a) mass- and energy-balance modelling of the ice cap (Möller *et al.* 2011) and b) meteorological modelling of atmospheric conditions over Nordaustlandet. Still only limited information on the status of mass balance and its climate forcing is available for this major Arctic ice cap. This study provides valuable information on physical properties and processes within a high Arctic snowpack and thus contributes to closing this gap in the knowledge on Arctic glacier mass balance.

Table 1. Overview on locations of snow pits. IDs correspond to locations given in Fig. 1 and are denoted according to decreasing latitude. Coordinates correspond to UTM Zone 34N, WGS84. Elevation is given in m a.s.l., air temperature in °C. Subgroups are arranged according to field seasons. Snow-pit locations within each subgroup are sorted according to decreasing latitude. The pits on De Geerfonna are presented separately. PSS is depth of the previous end-of-summer surface (m) and SWE is snow water equivalent down to previous end-of-summer surface (m w.e.). Density is given in kg m^{-3}, hardness refers to classes presented in Table 2 and snow temperature is given in °C. For all profile attributes measured mean ± one standard deviation (mean) as well as minimum and maximum (min/max) are presented.

ID	Date	Northing	Easting	Elevation (m a.s.l.)	Air temp. (°C)	PSS (m)	SWE (m w.e.)	Density (kg m^{-3})		Hardness		Temperature (°C)	
								mean	min/max	mean	min/max	mean	min/max
V3	2007/04/28	8880537	482896	556	–19.0	1.57	0.61	388 ± 54	261/442	n.a.	n.a.	n.a.	n.a.
V10	2007/04/29	8875956	505488	531	n.a.	1.57	0.62	393 ± 29	361/432	n.a.	n.a.	n.a.	n.a.
V15	2007/05/03	8874795	464538	335	–6.1	0.98	0.41	413 ± 57	204/492	n.a.	n.a.	n.a.	n.a.
V1	2008/05/09	8895948	492673	500	–10.4	1.47	0.60	410 ± 58	310/490	3.1 ± 0.6	2/4	–11.0 ± 0.7	–12.0/–10.1
V2	2008/05/19	8881934	469841	240	–6.8	2.00	0.89	444 ± 60	316/520	3.9 ± 0.3	3/4	–8.0 ± 0.8	–8.9/–6.9
V4	2008/05/28	8880270	470372	370	–6.3	1.00	0.39	399 ± 57	200/458	3.6 ± 0.9	1/6	–6.9 ± 1.1	–8.5/–5.4
V6	2008/04/24	8879535	482926	600	n.a.	1.86	n.a.	n.a.	n.a.	4.0 ± 0.7	3/5	–15.4 ± 1.8	–17.5/–12.4
V7	2008/05/18	8879498	482989	600	–4.5	1.99	0.77	388 ± 52	143/465	4.0 ± 0.4	1/5	–8.7 ± 2.3	–11.5/–4.5
V9	2008/05/20	8878046	471446	500	–8.2	1.20	0.46	381 ± 22	341/400	3.9 ± 0.5	2/5	–8.9 ± 0.2	–9.1/–8.6
V11	2008/04/30	8875846	463513	200	n.a.	0.43	0.16	366 ± 24	350/400	2.4 ± 0.5	2/3	–9.0 ± 1.3	–10.8/–7.8
V13	2008/05/05	8875197	505365	550	–11.6	1.59	0.62	388 ± 46	250/440	3.3 ± 0.9	1/4	–14.0 ± 1.1	–15.8/–11.8
V14	2008/04/28	8874796	464600	250	n.a.	0.63	0.26	419 ± 28	400/460	2.9 ± 0.8	1/4	–10.2 ± 0.5	–10.8/–9.7
V16	2008/05/01	8874141	490609	450	n.a.	1.65	0.50	301 ± 44	250/350	3.6 ± 0.6	1/4	–11.6 ± 1.8	–13.3/–7.7
V17	2008/04/30	8871690	467511	500	n.a.	1.60	0.49	309 ± 56	150/400	3.3 ± 0.8	1/5	–11.7 ± 0.7	–12.7/–10.3
DG	2008/05/26	8883953	464887	240	–3.5	1.30	0.61	467 ± 82	220/570	3.9 ± 0.5	1/5	–6.6 ± 1.8	–8.9/–3.3
V2	2008/08/05	8881934	469841	240	–2.4	1.07	0.48	477 ± 45	233/526	3.7 ± 0.9	1/6	–1.0 ± 0.2	–1.7/–0.9
V9	2008/08/08	8878046	471446	500	–4.1	1.34	0.56	436 ± 107	188/495	4.0 ± 0.5	1/6	–1.1 ± 0.1	–1.4/–1.0
V5	2009/04/26	8879651	482797	607	–13.0	1.15	0.37	323 ± 20	301/362	n.a.	n.a.	n.a.	n.a.
V8	2009/05/19	8879433	483092	612	n.a.	1.16	0.40	341 ± 40	240/400	3.6 ± 0.7	1/5	n.a.	n.a.
V12	2009/05/08	8875236	505377	613	n.a.	0.90	0.35	385 ± 37	281/422	n.a.	n.a.	n.a.	n.a.
V18	2009/05/13	8867394	460289	403	n.a.	0.80	0.29	362 ± 28	322/402	n.a.	n.a.	n.a.	n.a.
DG	2009/05/23	8883953	464887	240	–1.9	1.20	0.48	397 ± 49	323/456	2.7 ± 1.1	1/4	–6.4 ± 1.7	–9.1/–3.5
V4	2010/05/16	8880270	470372	370	–1.9	0.94	0.38	404 ± 43	336/480	3.4 ± 1.1	2/6	–6.1 ± 1.9	–8.5/–3.3
DG	2010/05/19	8883953	464887	240	+2.3	1.17	0.48	413 ± 62	120/463	3.3 ± 1.0	1/6	–5.1 ± 2.8	–8.4/–0.7
V4	2010/08/20	8880270	470372	370	+1.6	0.18	0.07	411 ± 0	411/411	2.0 ± 0.0	2/2	–0.8 ± 0.0	–0.9/–0.8
DG	2010/08/21	8883953	464887	240	–0.8	0.30	0.17	554 ± 138	417/690	3.3 ± 1.2	2/5	–1.0 ± 0.3	–1.7/–0.9

The comprehensively described results, moreover, provide validation and ground-truth data for various remote sensing applications, as only in situ observations permit the analysis of the validity and accuracy of various satellite obtained snowpack characteristics (e.g. Tong and Velicogna 2010). From multispectral sensors like MODIS, AVHRR, TM or ETM+ snow surface temperatures can be derived (Dozier and Painter 2004). Radar sensors like AMSR-E, in contrast, allow for a determination of water equivalent, density and depth as well as liquid water content of the snowpack (e.g. Kelly *et al*. 2003). This study presents a valuable set of ground-truth data, as in situ observations of these snow-cover properties are generally scarce in remote Arctic regions. However, accuracy-assessment studies of remote sensing data have highly individual requirements regarding ground-truth information. This study, therefore, aims to provide the most comprehensive description of point snowpack observations possible, in order to serve the varying needs of the remote sensing community.

Previous work

The first exploration of Vestfonna, including its interior parts, was done by A.E. Nordenskiöld who crossed the ice cap during an expedition in 1873 (Ahlmann 1933). After that, Vestfonna was investigated in several studies during the twentieth century.

Pioneering scientific work was conducted in the context of the Oxford University Arctic Expedition 1924 (Thompson 1953). Extensive descriptions of spatial distribution and intra-annual evolution of the snow cover were presented by Sandford (1925, 1929). Seven years later, the glacierized areas of Nordaustlandet were studied by the Swedish-Norwegian Arctic Expedition 1931. From this second exploration, a detailed analysis of general snow-pack evolution during the ablation season, including transient snow-line elevations, were achieved (Ahlmann 1933). Moreover, snow and firn stratification in the accumulation area as well as several snow- and firn-temperature profiles were described (Fjeldstad 1933). In 1935–36 Vestfonna was yet again visited by a British expedition from Oxford University (Thompson 1953). A detailed description of observations related to snow and firn temperature measurements and accumulation processes, including considerations of the influence of wind drift, was presented by Moss (1938) and Glen (1939).

Snowpack studies carried out during the International Geophysical Year 1957–58 focused on refreezing of melt water, as well as on snow density and ice temperatures. Related fieldwork was carried out on Ahlmann Summit and on the nearby northwestern slope of the ice cap (Schytt 1964; Palosuo 1987a, 1987b). In the 1980s and 1990s, ice cores were drilled near Ahlmann Summit (1981) as well as on the secondary, eastern peak (1995) of the ice cap (Vaykmyae *et al*. 1985; Punning *et al*. 1986; Sinkevich 1991; Pinglot *et al*. 1999; Matoba *et al*. 2002; Kotlyakov *et al*. 2004). The core data reveal information about long-term accumulation on Vestfonna. In this work we report the next phase in the study of snow characteristics on Vestfonna. Beaudon and Moore (2009) reported preliminary results, and here we publish all data of snow properties that were collected from Vestfonna during IPY.

Study area and climate conditions

The study area comprises two ice bodies in the western part of the island Nordaustlandet (northeastern Svalbard archipelago, Fig. 1) at around 80° N, the polythermal ice cap Vestfonna and a minor ice body called De Geerfonna.

With a surface area of ~2340 km^2 in 2005 (Braun *et al*. 2011), Vestfonna is the second largest single ice mass of Svalbard, and one of the largest ice masses of the European Arctic. The highest parts of the ice cap reach 630 m a.s.l. The dome-like shape of Vestfonna is dominated by two large ridges. The main one is an E-W oriented ridge that extends over the highest points of the ice cap. Ahlmann Summit is located almost in the centre, whereas a slightly higher peak is located in the eastern part of the ice cap. Starting from this eastern peak, a ridge extends northward. It culminates in a secondary peak close to its northernmost edge. Moving away from these central ridges, the surface topography of Vestfonna is mainly formed by the extensive basins of its outlet glaciers.

De Geerfonna is a minor ice body located on Storsteinhalvøya close to the northwestern ice margin of Vestfonna. It is situated on a south-facing slope covering a surface area of 1.6 km^2 in 2005 (Braun *et al*. 2011) and elevations between 200 and 270 m a.s.l. It has a slightly concave, rather uniform topography.

The climate of Svalbard is influenced by cold arctic air masses as well as by comparably warm ocean water originating in the North Atlantic

Current (Loeng 1991; Schuler *et al*. 2007). Due to strongly maritime influence summer seasons on Svalbard are generally cooler than at comparable latitudes while the winter seasons are generally warmer. Air temperatures in the study area were measured since spring 2007. Mean air temperature during the short summer seasons was 0.0°C at around 350 m a.s.l. on the northwestern slope of Vestfonna. Most of the summer days were characterized by mean air temperatures of between −3.5 and +3.2°C (lower and upper 10% percentiles). During winter, air temperatures typically fluctuated between −24.1 and −3.5°C (lower and upper 10% percentiles) but did also show several periods of considerable, short-term warming with air temperatures rising close to melting point. Nordaustlandet is less influenced by westerly weather systems than other parts of the archipelago. Its climate is mainly affected by weather systems originating in the Barents Sea region (Taurisano *et al*. 2007). The major source of moisture is formed by the ice-free areas of the Barents Sea, and the precipitation regime is mostly governed by easterly weather systems (Førland *et al*. 1997). However, the western part of Nordaustlandet is situated in the lee of Austfonna during synoptic conditions of easterly air flow. Therefore, precipitation is less than that at Austfonna (Hagen *et al*. 1993) but absolute amounts are highly variable (Beaudon *et al*. 2011).

Methods

Snow pit locations were chosen such that they are undisturbed by snowmobile or foot tracks. Each pit was excavated at least down to the respective previous end-of-summer surface (PSS). This layer was easily identifiable as the ice surface throughout the lower parts of the ice cap. Throughout the uppermost parts of the ice cap PSS was identifiable as a continuously thick, hard and icy layer mostly overlain by a layer of autumn hoar. The PSS marker horizon thus showed a two-part structure that has been reported before (e.g. Steffen *et al*. 1999). North facing walls were chosen for snow sampling to diminish disturbance by sunshine. Excavated snow was placed aside of the pit avoiding influences on the edge of the sampling wall. Access to the deeper parts of the pits was assured by construction of several steps opposite to the test walls.

The stratigraphic records acquired from the test walls comprise layering, hardness, density and/or temperature of the snowpack. Layering was determined according to snow-hardness classifications along the profile and visual inspection of the test wall regarding varying grain characteristics. Snow hardness itself was classified using the hand hardness test (Table 2). Measurements of snow density were performed using different metal tube density samplers. Ice layers and wind or melt crusts within the snow pack that could not be measured separately were treated in different ways. A density of 800 kg m^{-3} was assigned to ice layers (Parry *et al*. 2007). Crusts created by strong wind-drift or temporal melt events were not treated separately but were sampled together with the over and/or underlying snow layers. They were thus not allocated a specific density. Snow temperature was measured using handheld thermometers with attachable metal probes.

Table 2. Overview on hardness classes of deposited snow. Classes are denoted according to the hand hardness test (Fierz *et al*. 2009).

Term	Hand hardness index	Hand test object
Very soft	1	Fist
Soft	2	4 fingers
Medium	3	1 finger
Hard	4	Pencil
Very hard	5	Knife blade
Ice	6	Ice

Snow water equivalents (SWE) above the PSS were calculated according to measured bulk densities along the respective profiles. If density measurements did not cover the entire profile depth down to the PSS, bulk densities of the respective snow pits were calculated from the sampled parts of the profiles only and are assumed to be constant down to the PSS.

Results and discussion

Snow-profile analysis

Fieldwork In the period 2007–2010 snow profiles from a total of 22 snow pits on Vestfonna and four snow pits on De Geerfonna were analysed. Variability regarding the amount of snow-pit data was high in both space and time due to logistical restrictions. The majority of the snow pits was excavated within the last month of an accumulation season (May). Only four snow profiles were obtained during or close to the end of an ablation season (August). At a limited number of locations (V2, V4, V9 and DG) snow pits were excavated

during several, successive field campaigns. They were denoted by identical coordinates and IDs (Fig. 1, Table 1) even if their actual locations in the field varied within a few tens of metres.

In spring 2007 three snow pits were excavated on Vestfonna (Table 1). Locations (Fig. 1) were on the central ridge close to the drilling sites of the 2007 firn cores described by Beaudon *et al*. (2011) and on the northwestern slope of the ice cap.

During the spring 2008 field season, highest spatial coverage of the ice cap was achieved. Eleven snow pits were excavated in total (Table 1). Locations (Fig. 1) were along two transects on the northwestern slope, along the main E–W ridge and on the northern summit. Snow-pit locations V2, V4 and V9 correspond to the locations of AWS1-3 in Möller *et al*. (2011). In summer 2008 the locations V2 and V9 were revisited and snow profile studies were renewed during the ablation season (Table 1).

During spring 2009 snow pits were dug at the locations of the 2009 firn-coring sites (Beaudon *et al*. 2011), on Ahlmann Summit and on a secondary peak located in the southern slope of the ice cap (Fig. 1, Table 1).

In 2010, snow profiling on Vestfonna was only done at one location on its northwestern slope (Fig. 1) during both the spring and the summer field season (Table 1).

All four snow pits on De Geerfonna were excavated at the same location (Fig. 1). Snow profiles were obtained in the spring seasons 2008 and 2009 as well as in spring and summer of 2010 (Table 1).

Table 1 gives a comprehensive overview of the attributes of all 26 snow profiles expressed by bulk values and internal variability measures.

Snow density and hardness Snow-density data of Vestfonna (Fig. 2) reveal a mean bulk density of 388 ± 43 kg m^{-3} (mean $\pm$ one standard deviation) over all 22 snow profiles, which is in good agreement with values reported for other Arctic ice caps (e.g. Bell *et al*. 2008). Also the former studies on Vestfonna in the 1930s and 1950s reported comparable values (Moss 1938; Schytt 1964). The increase of density during the ablation seasons was found to be rather low. Mean spring density is 379 ± 39 kg m^{-3} (n = 19), whereas mean summer density amounts to 442 ± 33 kg m^{-3} (n = 3).

The small standard deviation of bulk snow density across Vestfonna suggests that snow density is rather homogeneous in both space and time in terms of bulk values. No spatial or altitudinal patterns are observable. Layers characterized by distinctly higher densities are evident in both the spring and the summer snow profiles, indicating no major densification during the ablation seasons. Snow-hardness profiles yield a rather homogeneous, medium range mean bulk value of 3.4 ± 0.6 without significant variations in space or time (Table 1). No spatial, altitudinal or temporal patterns are identifiable, except for very limited formation of thin ice layers during the summer seasons (Fig. 3). However, it has to be borne in mind that the information on changes between spring and summer characteristics is based on scarce data from only two snow-pit locations.

Snow density on De Geerfonna is higher than on Vestfonna. Mean bulk density amounts to 457 ± 70 kg m^{-3} when considering all four snow profiles (Table 1). Regarding snow hardness no significant differences between De Geerfonna and Vestfonna are observable (Table 1, Fig. 2).

These findings point to continuous settling and compaction by wind drift. Wind drift comprises the only frequently present agent that is able to assure continuous rounding of snow grains and thus a densification of the snow cover even during the months without melting. Wind-deposited snow is usually characterized by higher density than undisturbed snow as grains are smaller. Therefore, the snowpack is more compact due to rounding of the snow crystals during drift transport (Goodison *et al*. 1981). Wind crusts, i.e. thin layers of high hardness (5), that were found in the spring snowpack at various locations (Fig. 2) support this hypothesis. Especially, as in the uppermost parts of the ice cap high wind speeds frequently occur. Moss (1938) reported wind-drift conditions during 119 of 255 days between September 1935 and June 1936.

Snow depth on De Geerfonna was found to be distinctly higher than at comparable terrain elevations on Vestfonna (Table 1). This also supports the hypothesis of strong wind-drift influences on the snowpack of the study region, as the observed pattern can be attributed to the periodical deposition of wind-drifted snow in the hollow covered by De Geerfonna. Moreover, the higher snow depths result in a positive feedback regarding density, as bulk snow density tends to increase with snowpack thickness, because of stronger compaction due to the increasing pressure of overlying snow.

Snow temperatures Mean temperature of the snowpack of Vestfonna at the end of the accumulation seasons is -10.1 ± 2.7°C (mean $\pm$ one

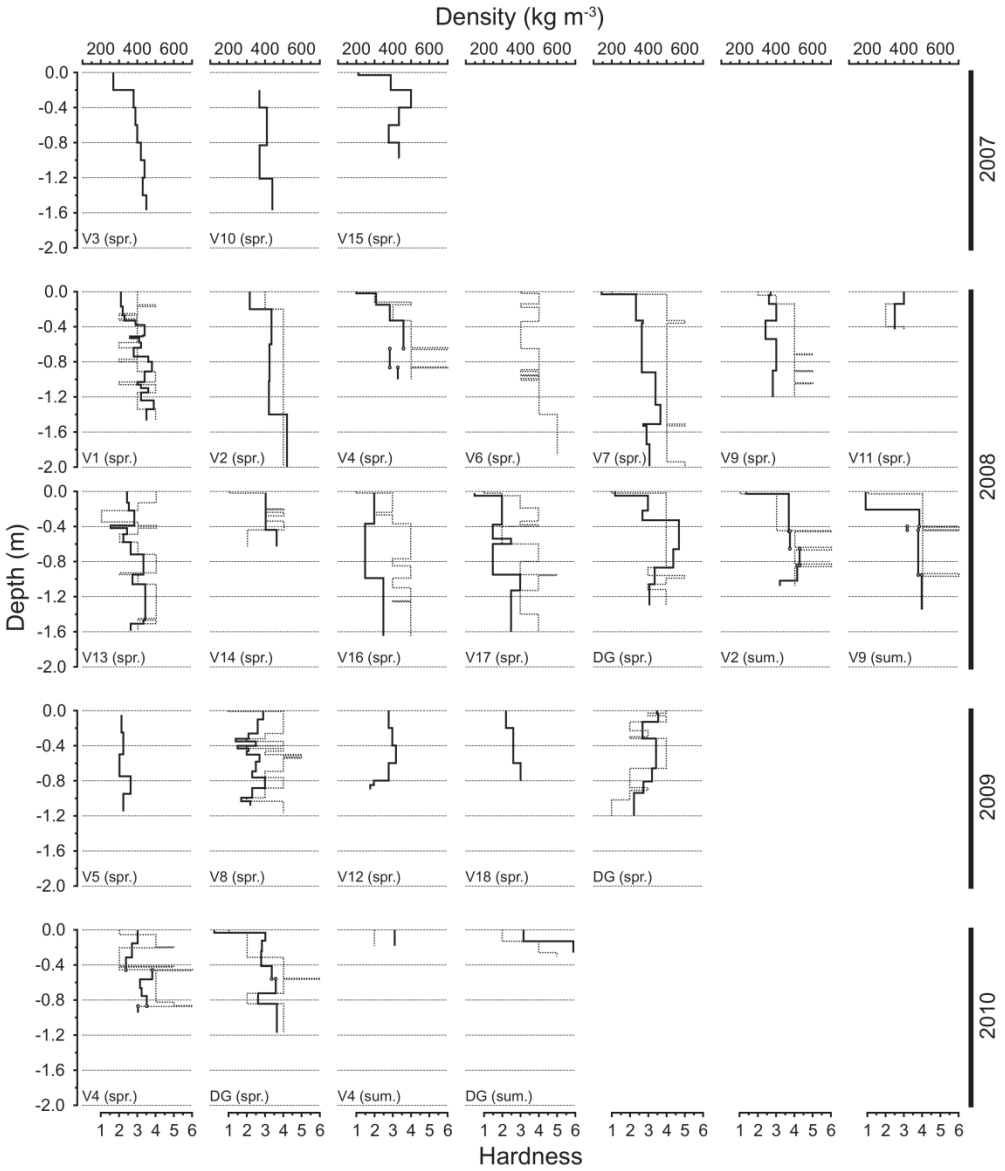

Fig. 2. Profiles of snow density (solid lines) and snow hardness (dashed lines). The snow-pit ID (Table 1) is given in the lower left of each profile graph. The date of snow pit excavation is given by year and season. The year is marked by black bars on the right. The season, either spring (spr.) or summer (sum.), is given after the snow-pit ID.

standard deviation). Temperatures decrease with increasing altitude (Table 1). Accordingly, the snowpack on De Geerfonna was found to be distinctly warmer at the end of the accumulation seasons (–6.0 ± 0.8°C). A direct comparison of spring 2008 data yields –6.6 ± 1.8°C on De Geerfonna against –8.0 ± 0.8°C in comparable altitude (V2, Table 1) on Vestfonna.

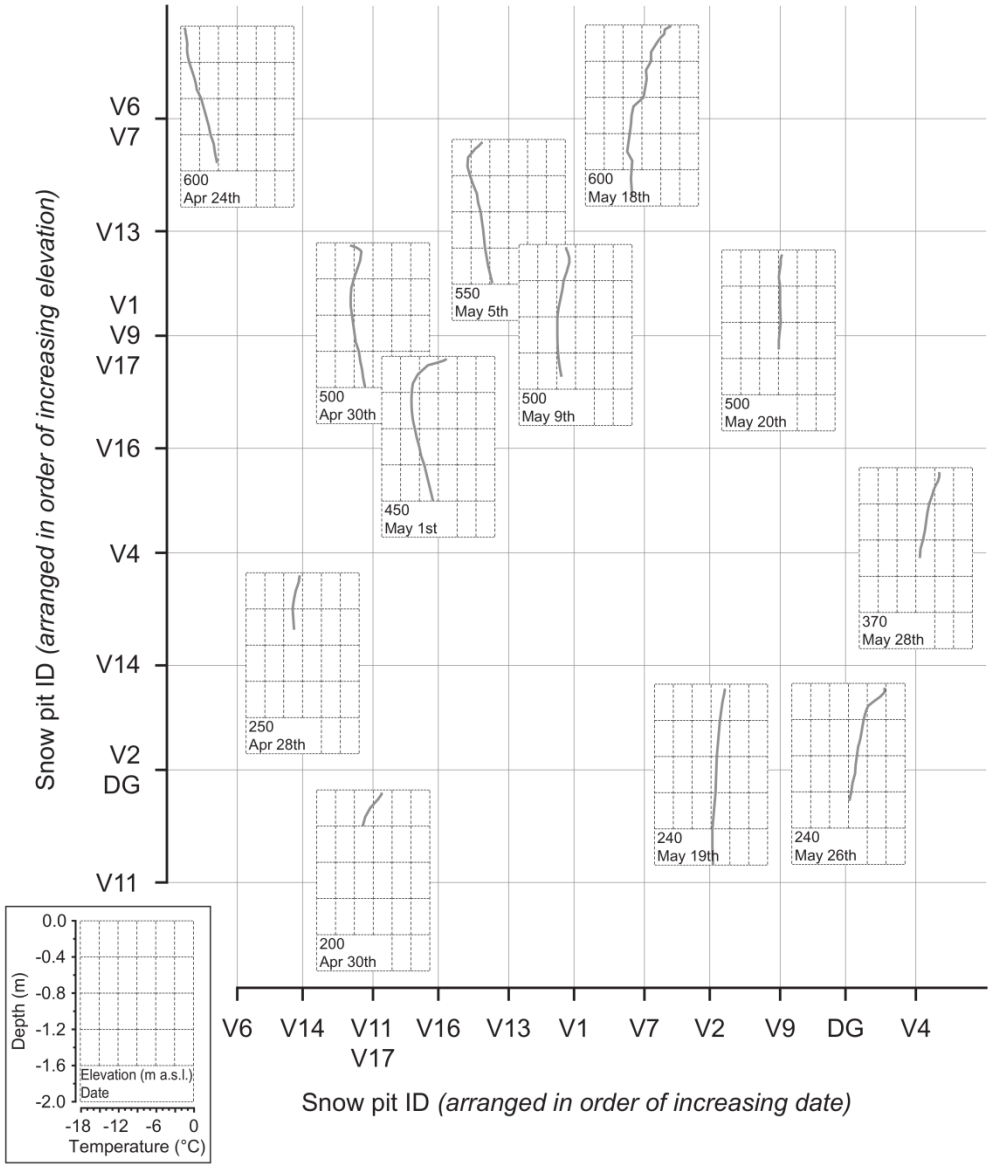

Fig. 3. Snow temperature profiles obtained during spring 2008. Individual profiles are given with elevation and date of excavation (lower left corner of each profile graph) in a coordinate system that represents the spatiotemporal distribution of the corresponding snow pits. The profiles are arranged in order of increasing data (x-axis) and elevation (y-axis). Positioning of the profiles within the coordinate system is done according to their snow-pit ID (cf. second subgroup of Table 1). A legend for all temperature profiles is given in the lower left.

An analysis of all spring 2008 temperature profiles (Fig. 3) revealed a starting of the reduction of the cold content from the previous winter season in late April. At lower altitudes on Vestfonna (cf. V11 in Fig. 3) the seasonal warming signal already penetrated down into the glacier ice, while at higher altitudes, the signal just started to affect the upper parts of the snowpack (cf. V16 and V17 in Fig. 3). Until late May, the entire snowpack of the ice cap was affected by a deeper penetration of the warming signal (e.g. V7 in Fig. 3). The snow temperature profiles give evidence that this development was occasionally interrupted by short-term cooling at the beginning of May (cf. V1 and V17 in Fig. 3). Ahlmann (1933) described the beginning of the summer melt on Vestfonna and thus the complete removal of the cold content for the second half of June. Accordingly, in the summer seasons, all snow pits reveal homogeneous temperature profiles near the melting point (e.g. Fig. 4).

Annual snowpack evolution In 2008, repeat data were obtained at V2 and V9 (Fig. 1, Table 1). The frequent existence of ice layers in the corresponding summer profiles (Fig. 4) indicate refreezing processes within the snowpack. Regarding summer 2008, the various, rather thin (<1 cm) ice layers that were observed at different depths within snow profiles V2 and V9 indicate several strong but short melt events interrupted by periods of snow accumulation. Long-lasting melt events would likely have resulted in thicker layers. This difference was already reported for Vestfonna by Sandford (1929). Snow densification during summer 2008 was thus influenced by frequent snowfall events such that the snow cover outlasted the entire ablation season. However, even in this snow-rich summer the cold content of the snowpack was completely removed by energy gain throughout warmer episodes of the ablation season (Fig. 4). As this development was evident up to at least 500 m a.s.l. (Table 1), it is reasonable to assume that summer melting regularly affects the entire ice cap. This is supported by the firn-core data of Beaudon *et al*. (2011) and was also reported from in situ observations by Sandford (1925) and Ahlmann (1933).

Likewise, the repeat data of 2010 obtained at V4 and DG cannot be regarded as representative. The summer snowpack of V4 (Fig. 2) comprised a single layer of fresh snow under conditions of surface melting. The snowpack at DG (Fig. 2) indeed showed an increase of bulk density of 141 kg m^{-3} (Table 1) between the spring and the summer season, but the distinctly higher bulk density of the summer snowpack (554 ± 0 kg m^{-3}) can be attributed to a thick, water-saturated snow layer.

Spatial distribution of accumulation

Snow water equivalents (SWE) above the PSS were calculated from measurements of snow depth and bulk snow density for each snow pit (Table 1). The absolute variation in SWE found across Vestfonna and De Geerfonna is in the range between 0.16 and 0.89 m w.e. (Fig. 5, Table 1) considering the entire study period. Spatial distribution of accumulation and thus SWE across Vestfonna has been assumed to be predominantly controlled by altitude (Möller *et al*. 2011). This is supported by the results of this analysis (Table 3).

From Fig. 5 a clear distribution of SWE according to elevation becomes obvious for Vestfonna for spring 2008. This is also the case for all other years studied (Table 1). Only one snow pit (V2) forms an outlier from this pattern. It is explainable by an increase of snow depth towards lower elevations at the lowermost parts of the north-western slopes of Vestfonna that originates from deposition of wind-drifted snow in the hollow along the fringe of the ice cap. A band of snow cover regularly outlasts the summer months throughout these areas and can be regarded as evidence for a systematic accumulation pattern. Hence, SWE obtained from V2 was excluded from further analysis.

The strong relation between SWE and elevation across Vestfonna is demonstrated by a highly significant (99% level) correlation of 0.96 (*t*-test; Table 3). A significant (95% level) positive correlation is also evident between SWE and easting (0.71). This coincidence is, however, biased by a likewise significant (90% level) correlation between elevation and easting (0.65). A partial correlation analysis (Table 3) reveals that elevation is by far the most important factor for determining the spatial variability of SWE and thus accumulation on the ice cap. Multiple partial correlation analysis reveals a highly significant (99% level) value of r = 0.93 between SWE and elevation when leaving out easting and northing. Easting and northing only account for insignificant partial correlations with SWE of 0.34 and 0.35, respectively. In summary, this indicates that the spatial distribution of accumulation across Vestfonna is primarily controlled by elevation, at least during the 2007/

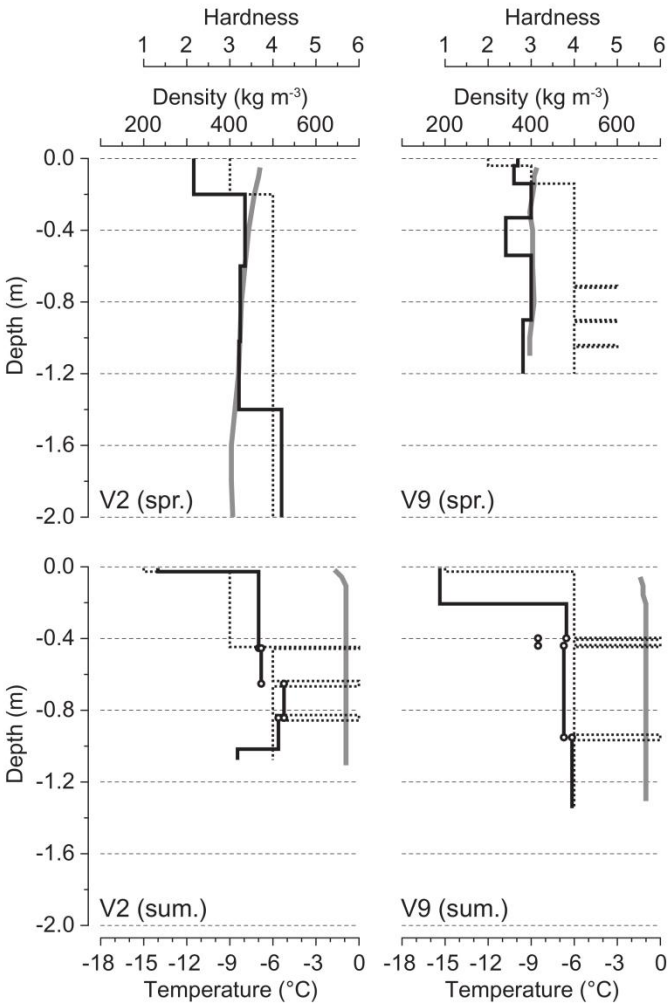

Fig. 4. Snow profiles obtained at the same locations in spring (upper graphs; V2 on May 19, V9 on May 20) and summer (lower graphs; V2 on August 5, V9 on August 8) 2008: snow density (black line), snow hardness (dashed line) and snow temperature (grey line). The snow-pit ID (cf. second and third subgroup of Table 1) is given in the lower left of each profile graph. Ice layers within the stratigraphy are indicated by broken snow density lines (black circles).

2008 accumulation period. The positive, weak partial correlations of SWE with both easting and northing might be interpreted as a slight increase of accumulation towards easterly and northerly directions. This interpretation is also partly supported by ground penetrating radar studies of Grabiec Puczko, Budzik and Gajek (unpublished) in spring 2009.

This conclusion, however, partly contradicts the findings of Hagen *et al*. (1993) who suggested a decrease of precipitation sums throughout the very eastern and northern parts of Vestfonna. Hagen *et al*. (1993) also suggest that the maximum precipitation over the ice cap occurs in the area around its eastern peak, which in this study is represented by snow pits V10, V12 and V13. The seeming increase of SWE with easting indeed fits this pattern, but an increase towards northerly directions is not supported by Hagen *et al*. (1993).

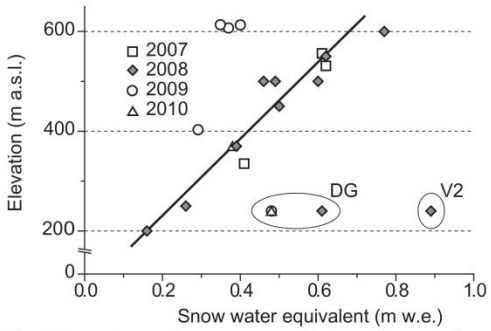

Fig. 5. Dependency of snow water equivalent (above previous summer surface) on elevation. Data are obtained from snow pits excavated during the four spring field seasons in the period 2007–2010. DG marks values obtained on De Geerfonna. The thick black line represents the linear regression ($r^2 = 0.92$, Table 3) for values of spring 2008. It is calculated by leaving out data of snow pit V2 which is located in an area of high, wind-drifted snow accumulation. It is biased towards much higher snow depth when compared to overall Vestfonna.

Table 3. Correlation matrix regarding snow water equivalents (SWE) obtained from snow pits on Vestfonna during the spring 2008 field season and spatial parameters of the snow-pit locations (cf. second subgroup of Table 1). Snow pits V2 and DG are excluded from the analysis. The dependency of SWE on the corresponding spatial parameters is given as both, Pearson correlation (cor.) and partial correlation (p.cor.). Statistically significant values (90% level) are represented by bold characters.

	Easting	Northing	Elevation	SWE	
				cor.	p.cor.
SWE	–	–	–	n.a.	n.a.
Altitude	–	–	n.a.	**0.96**	**0.93**
Northing	–	n.a.	0.20	0.31	0.35
Easting	n.a.	0.32	**0.65**	**0.71**	0.34

A discrepancy appears when comparing our results with the results of the firn-core study of Beaudon *et al*. (2011) in terms of both absolute and relative considerations. In spring 2008, SWE above the 2007 end-of-summer surface was measured to 0.77 m w.e. on Ahlmann Summit (V7, Table 1). The corresponding accumulation rates for the years 2007 and 2008 obtained from a firn core drilled at V5 (about 250 m horizontal distance to V7) in spring 2009 are suggested to be 0.48 and 0.77 m w.e., respectively (Beaudon *et al*. 2011).

This difference might be attributed to temporal aspects related to the two different data sources. The firn core data represent annual sums integrated roughly over an entire calendar year. The snow pit data, on the other hand, represent sums integrated over an accumulation season that lasts roughly from the end of September to the date of the snow pit excavation in April or May. As both inter- and intra-annual variability of snow accumulation is high throughout the study region (Möller *et al*. 2011) the varying time reference can be seen as a likely explanation for the obtained discrepancy.

A discrepancy also appears when comparing our findings regarding zonal accumulation variability on Vestfonna to the findings obtained by Beaudon *et al*. (2011). Two firn cores drilled at Ahlmann Summit and at the eastern peak of Vestfonna in spring 2007, at the same locations where the pits V3 and V10 were dug, revealed distinctly differing mean annual accumulation rates in recent years. While the core taken from Ahlmann Summit (V3) indicated an annual accumulation rate of 0.52 ± 0.15 m w.e. (mean ± one standard deviation), the core extracted from the eastern peak (V10) only suggested an annual accumulation rate of 0.25 ± 0.08 m w.e. and thus roughly half the amount of Ahlmann Summit (Beaudon *et al*. 2011). The spatial analysis of SWE above PSS obtained from the set of spring 2008 snow pits, however, revealed no statistically significant zonal variability of snow accumulation across the ice cap (Table 3).

A look into the inter-annual variability of accumulation differences between the two firn-core sites puts this seeming discrepancy into perspective. Years with almost equal accumulation sums at both sites are frequently found in the firn-core data (Beaudon *et al*. 2011). This suggests that the accumulation season 2007–2008 and therewith our snow-pit data might also represent such a year.

Small-scale accumulation variability due to patchy deposition of wind-drifted snow has to be regarded as another possible source for the discrepancies between snow pit and firn-core data. Formation of large and flat sastrugi is a common feature on Vestfonna and can cause accumulation differences of several decimetres within a radius of some tens of metres. However, this affects both data sources, even though different magnitudes cannot be ruled out. Further studies regarding the relocation of snow across the ice cap by wind drift are needed to contribute to a quantification of potential local- or regional-scale snow-depth differences and to reveal their spatial and/or temporal impact on SWE distribution.

Conclusions

Snow profile data obtained from 22 snow pits on Vestfonna and from four snow pits on De Geerfonna were analysed regarding density, hardness and temperature distribution within the snowpacks. Results reveal homogeneous snow densities across Vestfonna with no distinct spatial or interannual variability being evident (Table 1). Mean bulk snow density was calculated to be ~400 kg m^{-3}. The snowpack of De Geerfonna was found to be considerably denser with a mean bulk density of ~450 kg m^{-3}. This fact was attributed to the influences of periodic deposition of wind-drifted snow in the hollow covered by De Geerfonna that results in both higher snow density and higher snow depth (Fig. 5).

The homogeneous snow density that was observed throughout Vestfonna justifies simplified assumptions of constant snow density in future mass balance-modelling studies.

The amounts of snow accumulation across Vestfonna were found to be predominantly controlled by elevation. Especially, SWE above PSS measured in spring 2008 showed a highly significant partial correlation with elevation (0.93, Table 3). Partial correlations with easting and northing were found to be low. A distinct spatial difference between western and eastern parts of the ice cap as represented in long-term mean accumulation rates derived from the firn-core studies of Beaudon *et al*. (2011) is thus not evident for the accumulation season 2007–2008. This suggests high inter-annual variability of the accumulation pattern on Vestfonna. It stresses the need for further studies on wind-drift based relocation of snow across the ice cap. Also, gains and losses of snow from or to areas beyond the lateral borders of Vestfonna should be investigated in the future. Nevertheless, even the present knowledge on spatial distribution of accumulation already facilitates first calibration and validation applications in regional precipitation modelling studies.

Acknowledgements

This study was funded by grants no. BR 2105/6-1, SCHE 750/3-1 and SCHN 680/2-1 of the German Research Foundation (DFG). Additional funding was provided by the Finnish Academy, the Polish Ministry of Science and Higher Education (grant no. IPY/279/2006) and the Swedish Research Council. Our gratitude is expressed to all people involved in field work during the various field campaigns. The Swedish Polar Research Secretariat (SPRS) and the Alfred Wegener Institut für Polar- und Meeresforschung (AWI) are acknowledged for logistical support.

Marco Möller, Department of Geography, RWTH Aachen University, Templergraben 55, 52056 Aachen, Germany.
E-mail: marco.moeller@geo.rwth-aachen.de

Rebecca Möller, Geological Institute, RWTH Aachen University, Wüllnerstraße 2, 52056 Aachen, Germany.

Emilie Beaudon, Arctic Centre, University of Lapland, Pohjoisranta 4, 96100 Rovaniemi, Finland.

Olli-Pekka Mattila, Department of Physics, University of Helsinki, Gustaf Hällströmin katu 2a, 00560 Helsinki, Finland.

Roman Finkelnburg, Department of Ecology, Technische Universität Berlin, Rothenburgstraße 12, 12165 Berlin, Germany.

Matthias Braun, Geophysical Institute, University of Alaska Fairbanks, 903 Koyukuk Drive Fairbanks, AK99775-7320, USA.

Mariusz Grabiec, Department of Geomorphology, University of Silesia, Będzińska. 60, 41-200 Sosnowiec, Poland.

Ulf Jonsell, Department of Earth Sciences, Uppsala University, Villavägen 16, SE-752 36 Uppsala, Sweden.

Bartłomiej Luks, Institute of Geophysics, Polish Academy of Sciences, Księcia Janusza 64, 01-452 Warsaw, Poland.

Dariusz Puczko, Institute of Geophysics, Polish Academy of Sciences, Księcia Janusza 64, 01-452 Warsaw, Poland.

Dieter Scherer, Department of Ecology, Technische Universität Berlin, Rothenburgstraße 12, 12165 Berlin, Germany.

Christoph Schneider, Department of Geography, RWTH Aachen University, Templergraben 55, 52056 Aachen, Germany.

References

Ahlmann, H.W., 1933. Scientific results of the Swedish-Norwegian Arctic Expedition in the summer of 1931. Part VIII – Glaciology. *Geografiska Annaler*, 15, 161–216.

Beaudon, E. and Moore, J., 2009. Frost flower chemical signature in winter snow on Vestfonna ice cap (Nordaustlandet, Svalbard). *The Cryosphere*, 3 (2), 147–154.

Beaudon, E., Arppe, L., Jonsell, U., Martma, T., Möller, M., Pohjola, V.A., Scherer, D. and Moore, J.C., 2011. Spatial and temporal variability of net accumulation from shallow cores from Vestfonna ice cap (Nordaustlandet, Svalbard). *Geografiska Annaler: Series A, Physical Geography*. doi: 10.1111/j.1468-0459.2011.00439.x.

Bell, C., Mair, D., Burgess, D., Sharp, M., Demuth, M., Cawkwell, F., Bingham, R. and Wadham, J., 2008. Spatial and temporal variability in the snowpack of a High Arctic ice cap: implications for mass-change measurements. *Annals of Glaciology*, 48, 159–170.

Braun, M., Pohjola, V.A., Pettersson, R., Möller, M., Finkelnburg, R., Falk, U., Scherer, D. and Schneider, C., 2011. Changes of glacier frontal positions of Vestfonna (Nordaustlandet, Svalbard). *Geografiska Annaler: Series A, Physical Geography*. doi: 10.1111/j.1468-0459.2011.00437.x.

Dozier, J. and Painter, T.H., 2004. Multispectral and hyperspectral remote sensing of alpine snow properties. *Annual Review of Earth and Planetary Sciences*, 32, 465–494.

Fierz, C., Armstrong, R.L., Durand, Y., Etchevers, P., Greene, E., McClung, D.M., Nishimura, K., Satyawali, P.K. and Sokratov, S.A., 2009. *The International Classification for Seasonal Snow on the Ground*. IHP-VII Technical Documents in Hydrology N°83, IACS Contribution N°1. UNESCO-IHP, Paris.

Fjeldstad, J.E., 1933. Scientific results of the Swedish-Norwegian Arctic Expedition in the summer of 1931. Part IX – snow and ice temperatures. *Geografiska Annaler*, 15, 296–315.

Førland, E.J., Hanssen-Bauer, I. and Nordli, P.Ø., 1997. *Climate Statistics and Longterm Series of Temperatures and Precipitation at Svalbard and Jan Mayen*. Det Norske Meteorologiske Institutt, Oslo.

Glen, A.R., 1939. The glaciology of North East Land. *Geografiska Annaler*, 21, 1–38.

Goodison, B.E., Ferguson, H.L. and McKay, G.A., 1981. Measurement and data analysis. In: *Handbook of Snow*. Pergamon, Toronto. 191–274.

Grabiec, M., Puczko, D., Budzik, T. and Gajek, G., unpublished. The snow distribution patterns on Svalbard glaciers of different types derived from radio-echo soundings. *Polish Polar Research*.

Hagen, J.O., Liestøl, O., Roland, E. and Jørgensen, T., 1993. *Glacier Atlas of Svalbard and Jan Mayen*. Meddelelser Nr. 129. Norsk Polarinstitutt, Oslo.

Kelly, R.E., Chang, A.T., Tsang, L. and Foster, J.L., 2003. A prototype AMSR-E global snow area and snow depth algorithm. *IEEE Transactions on Geoscience and Remote Sensing*, 41 (2), 230–242.

Kotlyakov, V.M., Arkhipov, S.M., Henderson, K.A. and Nagornov, O.V., 2004. Deep drilling of glaciers in Eurasian Arctic as a source of paleoclimatic records. *Quaternary Science Reviews*, 23 (11–13), 1371–1390. doi:10.1016/j.quascirev.2003.12.013.

Loeng, H., 1991. Features of the physical oceanographic conditions of the Barents Sea. *Polar Research*, 10 (1), 5–18. doi:10.1111/j.1751-8369.1991.tb00630.x.

Matoba, S., Narita, H., Motoyama, H., Kamiyama, K. and Watanabe, O., 2002. Ice core chemistry of Vestfonna Ice Cap in Svalbard, Norway. *Journal of Geophysical Research*, 107 (D23), 4721, doi:10.1029/2002JD002205.

Möller, M., Finkelnburg, R., Braun, M., Hock, R., Jonsell, U., Pohjola, V.A., Scherer, D. and Schneider, C., 2011. Climatic mass balance of the ice cap Vestfonna, Svalbard: A spatially distributed assessment using ERA-Interim and MODIS data. *Journal of Geophysical Research*, 116, F03009. doi:10.1029/2010JF001905.

Moss, R., 1938. The physics of an ice-cap. *The Geographical Journal*, 92 (3), 211–231.

Palosuo, E., 1987a. A study of snow and ice temperatures on Vestfonna, Svalbard, 1956, 1957 and 1958. *Geografiska Annaler: Series A, Physical Geography*, 69 (3–4), 431–437.

Palosuo, E., 1987b. Ice layers and superimposition of ice on the summit and slope of Vestfonna, Svalbard. *Geografiska Annaler: Series A, Physical Geography*, 69 (2), 289–296.

Parry, V., Nienow, P., Mair, D., Scott, J., Hubbard, B., Steffen, K. and Wingham, D., 2007. Investigations of meltwater refreezing and density variations in the snowpack and firn within the percolation zone of the Greenland ice sheet. *Annals of Glaciology*, 46, 61–68.

Pinglot, J.F., Pourchet, M., Lefauconnier, B., Hagen, J.O., Isaksson, E., Vaikmäe, R. and Kamiyama, K., 1999. Accumulation in Svalbard glaciers deduced from ice cores with nuclear tests and Chernobyl reference layers. *Polar Research*, 18 (2), 315–321.

Pohjola, V.A., Kankaanpää, P., Moore, J.C. and Pastusiak, T., 2011. The International Polar Year Project 'KINNVIKA' – Arctic warming and impact research at 80° N. *Geografiska Annaler, Series A, Physical Geography*. doi: 10.1111/j.1468-0459.2011.00436.x.

Punning, Ya.-M.K., Martma, T.A., Tuygu, K.E., Vaikmäe, R.A., Pourchet, M. and Pinglot, J.F., 1986. Stratification in an ice core from Vestfonna, Nordaustlandet. *Polar Geography and Geology*, 10 (1), 39–43.

Sandford, K.S., 1925. The Oxford University Arctic Expedition 1924 – II: geology and glaciology. *The Geographical Journal*, 66 (2), 114–120.

Sandford, K.S., 1929. The glacial conditions and quaternary history of North-East Land. *The Geographical Journal*, 68 (3), 200–225.

Schuler, T.V., Loe, E., Taurisano, A., Eiken, T., Hagen, J.O. and Kohler, J., 2007. Calibrating a surface mass-balance model for Austfonna ice cap, Svalbard. *Annals of Glaciology*, 46, 241–248.

Schytt, V., 1964. Scientific results of the Swedish Glaciological Expedition to Nordaustlandet, Spitsbergen, 1957 and 1958. *Geografiska Annaler*, 46 (3), 243–281.

Sinkevich, S.A., 1991. Climate warming in the twentieth century as reflected in Svalbard ice cores. *IAHS Publications*, 208, 257–267.

Steffen, K., Abdalati, W. and Sherjal, I., 1999. Faceted crystal formation in the northeastern Greenland low-accumulation region. *Journal of Glaciology*, 45 (149), 63–68.

Taurisano, A., Schuler, T.V., Hagen, J.O., Eiken, T., Loe, E., Melvold, K. and Kohler, J., 2007. The distribution of snow accumulation across the Austfonna ice cap, Svalbard: direct measurements and modeling. *Polar Research*, 26 (1), 7–13.

Thompson, H.R., 1953. Oxford expeditions to Nordaustlandet (North east land), Spitsbergen. *Arctic*, 6 (3), 213–222.

Tong, J. and Velicogna, I., 2010. A comparison of AMSR-E/Aqua snow products with in situ observations and MODIS snow cover products in the Mackenzie River Basin, Canada. *Remote Sensing*, 2 (10), 2313–2322.

Vaykmyae, R.A., Martma, T.A., Punning, Ya.-M.K. and Tyugu, K.R., 1985. Variations in $d^{18}O$ and Cl- in an ice core from Vestfonna Nordaustlandet. *Polar Geography and Geology*, 9 (4), 329–333.

Manuscript received Jan., 2011, revised and accepted Jul., 2011

Appendix B: Climatic mass balance of the ice cap Vestfonna, Svalbard: A spatially distributed assessment using ERA-Interim and MODIS data

Möller, M., Finkelnburg, R., Braun, M., Hock, R., Jonsell, U., Pohjola, V. A., Scherer, D. and Schneider, C., 2011. Climatic mass balance of the ice cap Vestfonna, Svalbard: A spatially distributed assessment using ERA-Interim and MODIS data. *Journal of Geophysical Research – Earth Surface*, 116. doi: 10.1029/2010JF001905.

Status: Published

Own contribution:

- Preparation, conduction and leading of field campaigns
- Design and implementation of measurement concepts
- Acquisition of field observational data
- Processing, analysis and interpretation of AWS data
- Preparation of manuscript parts concerning AWS data
- Review, comments and improvements of the manuscript

Climatic mass balance of the ice cap Vestfonna, Svalbard: A spatially distributed assessment using ERA-Interim and MODIS data

Marco Möller,[1] Roman Finkelnburg,[2] Matthias Braun,[3,4] Regine Hock,[3,5] Ulf Jonsell,[5,6,7] Veijo A. Pohjola,[5] Dieter Scherer,[2] and Christoph Schneider[1]

Received 19 October 2010; revised 30 March 2011; accepted 22 June 2011; published 18 August 2011.

[1] The ice cap Vestfonna in the northern Svalbard archipelago is one of the largest ice bodies of the European Arctic (~2400 km^2), but little is known about its mass balance. We model the climatic mass balance of the ice cap for the period September 2000 to August 2009 on a daily basis. Ablation is calculated by a spatially distributed temperature-radiation-index melt model. Air temperature forcing is provided by ERA-Interim data that is downscaled using data from an automatic weather station operated on the ice cap. Spatially distributed net shortwave radiation fluxes are obtained from standard trigonometric techniques combined with Moderate Resolution Imaging Spectroradiometer-based cloud cover and surface albedo information. Accumulation is derived from ERA-Interim precipitation data that are bias corrected and spatially distributed as a function of elevation. Refreezing is incorporated using the P_{max} approach. Results indicate that mass balance years are characterized by short ablation seasons (June to August) and correspondingly longer accumulation periods (September to May). The modeled, annual climatic mass balance rate shows an almost balanced mean of -0.02 ± 0.20 m w.e. yr^{-1} (meters water equivalent per year) with an associated equilibrium line altitude of 383 ± 54 m above sea level (mean ± one standard deviation). The mean winter balance is $+0.32 \pm 0.06$ m w.e. yr^{-1}, and the mean summer balance -0.35 ± 0.17 m w.e. yr^{-1}. Roughly one fourth of total surface ablation is retained by refreezing indicating that refreezing is an important component of the mass budget of Vestfonna.

Citation: Möller, M., R. Finkelnburg, M. Braun, R. Hock, U. Jonsell, V. A. Pohjola, D. Scherer, and C. Schneider (2011), Climatic mass balance of the ice cap Vestfonna, Svalbard: A spatially distributed assessment using ERA-Interim and MODIS data, *J. Geophys. Res.*, *116*, F03009, doi:10.1029/2010JF001905.

1. Introduction

[2] The Arctic glaciers outside of Greenland have been found to be a major contributor to present sea level rise [e.g., *Arendt et al.*, 2002; *Berthier et al.*, 2010; *Wu et al.*, 2010]. They account for about one fourth of all glacier (excluding Greenland and Antarctica) sea level rise contributions since 1960 [*Kaser et al.*, 2006]. These contributions are expected to increase in the future [*Raper and Braithwaite*, 2006; *Meier et al.*, 2007; *Bahr et al.*, 2009], as these glaciers are located in the region of highest predicted air temperature increase during the coming decades [*Rinke and Dethloff*, 2008].

[3] During the last four decades the glaciers and ice caps of Svalbard showed a mean geodetic mass balance of -0.36 ± 0.02 m w.e. yr^{-1} (meters water equivalent per year), (excluding Austfonna and Kvitøya) corresponding to a mean sea level rise contribution of 0.026 ± 0.001 mm yr^{-1} [*Nuth et al.*, 2010]. However, their surface mass balance was roughly in equilibrium (-0.014 ± 0.003 m w.e. yr^{-1}) during the last 30 years of the 20th century [*Hagen et al.*, 2003]. Glaciers in western Svalbard have experienced an accelerating thinning during recent decades with changes in surface elevation of −0.47 and −0.62 m w.e. yr^{-1} during the periods 1995–2003 and 2003–2005, respectively [*Kohler et al.*, 2007]. These values are in line with results from the ice caps on Edgeøya, eastern Svalbard, where the thinning rate averaged −0.63 m w.e. yr^{-1} for the period 2002–2004 [*Kääb*, 2008], and results from southern Spitsbergen where mean thinning during 1990–2005 was −0.55 m w.e. yr^{-1} [*Nuth et al.*, 2010]. However, most recent estimates indicate significant changes in the mass balance pattern of the Svalbard archipelago. For the period 2003–2008,

[1]Department of Geography, RWTH Aachen University, Aachen, Germany.
[2]Department of Ecology, Technische Universität Berlin, Berlin, Germany.
[3]Geophysical Institute, University of Alaska Fairbanks, Fairbanks, Alaska, USA.
[4]Center for Remote Sensing of Land Surfaces, University of Bonn, Bonn, Germany.
[5]Department of Earth Sciences, Uppsala University, Uppsala, Sweden.
[6]Escuela Técnica Superior de Ingenieros de Telecomunicación, Universidad Politécnica de Madrid, Madrid, Spain.
[7]Now at Swedish Polar Research Secretariat, Stockholm, Sweden.

0148-0227/11/2010JF001905

Moholdt et al. [2010b] calculated the overall geodetic mass balance to be much less negative at -0.11 ± 0.04 m w.e. yr^{-1}.

[4] Results for Vestfonna are close to the regional mean (-0.14 ± 0.07 m w.e. yr^{-1}), while a much more positive balance of $+0.1 \pm 0.04$ m w.e. yr^{-1} was obtained for Austfonna for the same period [*Moholdt et al.*, 2010b]. Positive mass balances for Austfonna have also been reported for the end of the 20th century [*Bevan et al.*, 2007]. For Vestfonna *Nuth et al.* [2010] obtained a near zero glacier-wide geodetic mass balance of $+0.05 \pm 0.15$ m w.e. yr^{-1} for the period 1990–2005 and a thickening of parts of its accumulation area.

[5] Hence, Vestfonna seems to have shifted from slight mass gain to mass loss. Vestfonna does not experience the typical low-elevation thinning observed throughout the Svalbard archipelago. Rather, it features a complex pattern of ice thickness changes [*Moholdt et al.*, 2010b] due to the relatively complex surface topography of Vestfonna when compared to the smoother surface of Austfonna.

[6] With the exception of Austfonna, the negative mass balance observations agree with the positive trends of air temperature observed in the Arctic and the Svalbard area in particular [*Rigor et al.*, 2000; *Moritz et al.*, 2002]. In general, the archipelago experienced warming during the 20th century [e.g., *Hanssen-Bauer and Førland*, 1998; *Førland and Hanssen-Bauer*, 2003]. During the last decades of the 20th century, the Atlantic sector of the Arctic as a whole showed the strongest warming trend of any part of the northern polar region [*Przybylak*, 2000; 2007]. During the period 2001–2005, the mean annual air temperature in the Atlantic sector of the Arctic was 1.3 K higher than its long-term mean during 1951–1990 [*Przybylak*, 2007]. This development led to a considerable increase of the mean length of annual melt season throughout the Arctic [*Stroeve et al.*, 2006b], and thus possibly initiated a trend toward more negative mass balances.

[7] The aim of this study is to model daily fields of surface accumulation, surface ablation, refreezing, and their sum, the so-called climatic mass balance of Vestfonna for the first decade of the 21st century (September 2000 to August 2009). We apply the spatially distributed temperature-radiation-index ablation model presented by *Pellicciotti et al.* [2005] that is based on air temperature and net shortwave radiation inputs. We enhance the model by including fractional cloud cover and albedo fields derived from daily MODIS (Moderate Resolution Imaging Spectroradiometer) imagery in order to compute net shortwave radiation. The model is forced by statistically downscaled ERA-Interim daily air temperatures. Local reference is provided by records of automatic weather stations (AWS) operated in the study area. Accumulation is modeled as a function of altitude based on ERA-Interim daily total precipitation. Our model approach accounts for the frequent and spatially variable cloud cover in the study area, despite the limited availability of meteorological data at boundary layer level. Model results provide new insight into the spatial and temporal variability of the surface mass balance of Svalbard's second largest ice cap.

2. Study Area

[8] Vestfonna is a polythermal ice cap located on the island Nordaustlandet (northernmost Svalbard archipelago) at around 80°N (Figure 1). It covers ~2400 km^2 making it one of the largest ice masses of the European Arctic. It ranges in altitude from sea level to 630 m above sea level (asl). The ice cap has a main ridge that is oriented east-west, with its second highest point, called Ahlmann Summit, located near the center. Another main ridge extends northward from a slightly higher peak located in the eastern part of the ice cap. Between these ridges, Vestfonna has pronounced, bowl-shaped outlet glacier basins. Some of these outlet glaciers have been suggested to be surge-type glaciers [*Dowdeswell and Collin*, 1990], although this has not yet been proven.

[9] The majority of the ice cap drains southward into Wahlenbergfjorden through large (>5 km wide) calving fronts [*Strozzi et al.*, 2008]. The largest outlet glacier, Franklinbreen, is located on the northwestern side of the ice cap and drains into Lady Franklinfjorden. A few smaller outlet glaciers drain into northeastern fjords.

[10] Svalbard features a maritime climate characterized by cooler summers and warmer winters than generally found at comparable latitudes. Mean monthly air temperatures on Vestfonna during the short summer seasons do not exceed +3°C and in winter they typically range between −10°C and −15°C. Periods of considerable short-term warming with air temperatures rising close to the melting point frequently occur, even during the winter months (Figure 2).

[11] The location of Vestfonna in the northeastern part of Svalbard causes the ice cap to be more directly influenced by weather systems originating in the Barents Sea region than by the westerly weather systems that determine the climate of other parts of the archipelago [*Taurisano et al.*, 2007]. Accordingly, the ice-free areas of the Barents Sea form the major source of moisture for precipitation over Nordaustlandet [*Førland et al.*, 1997]. However, as Vestfonna is situated in the lee of its higher-elevation neighbor, Austfonna, it receives less precipitation and has a smaller horizontal precipitation gradient than Austfonna [*Taurisano et al.*, 2007].

3. Data

[12] The model requires elevation data of the ice-cap surface as well as daily air temperature and precipitation data. Fractional cloud cover, atmospheric turbidity and albedo data are used to compute net shortwave radiation. Mass balance data that are obtained from ablation-stake measurements are used to calibrate the model.

3.1. Glacier Outline and Elevation Data

[13] The glacier outlines were digitized from Terra ASTER (Advanced Spaceborne Thermal Emission and Reflection Radiometer) imagery acquired on 17 August 2000 (EOS Data Gateway Granule ID: SC:ASTL1B 00-08-12:36:0010269001). Terrain information is based on the elevation data set of the ASTER Global Digital Elevation Model (GDEM). Small data gaps in the uppermost parts of the ice cap were filled with values interpolated from surrounding grid cells. Sporadic elevation outliers along the ridges were likewise substituted with interpolated values. The original grid was then bilinearly resampled to a grid-cell resolution of 250 × 250 m to facilitate coregistration with the MODIS data sets.

3.2. Meteorological Data

[14] The model is forced by statistically downscaled daily ERA-Interim 2 m air temperatures and daily ERA-Interim total precipitation (Figure 2). ERA-Interim is the follow-up

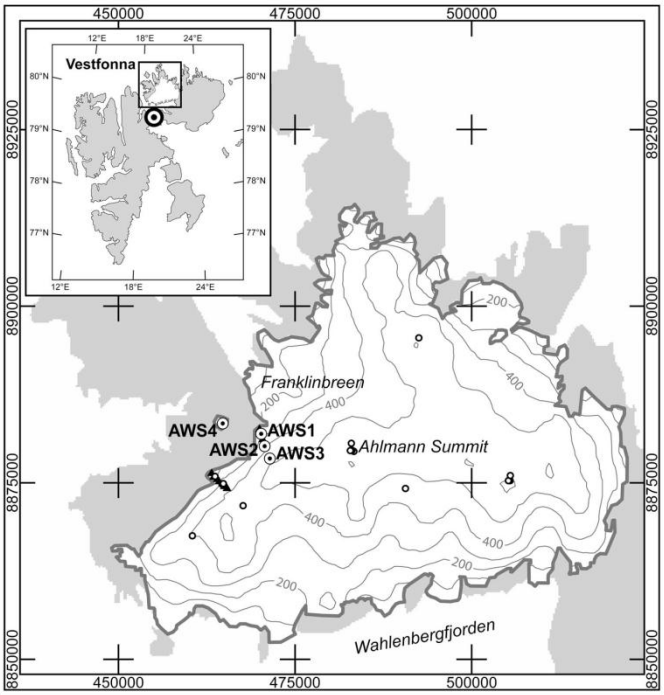

Figure 1. Location of the ice cap Vestfonna and overview on installed measurement network. The four AWSs are marked by large black circles. Locations of stakes are marked by small triangles, and locations of snow pits are marked by small circles. Locations along the transect AWS1-3 are hidden behind the AWSs marks. Contour spacing is 100 m. Coordinates correspond to Universal Transverse Mercator (UTM) zone 34N. Inset: Location of Vestfonna within Svalbard archipelago. Black circle marks the location of the ERA-Interim grid point.

reanalysis product of the well-established ERA-40 data set [*Uppala et al.*, 2005]. Data are supplied by the European Centre for Medium-Range Weather Forecasts (ECMWF). We use data from the grid point located at 79.5°N 19.5°E (Figure 1). The downscaling procedure for air temperature data is detailed in section 4.5.

[15] In addition, data from four automatic weather stations (AWS) operated on the northwestern side of the ice cap and on neighboring De Geerfonna (Figure 1) during the period 27 May 2008 to 30 April 2010 are used to downscale ERA-Interim air temperatures, to derive temperature slope lapse rates, and to calibrate the radiation model (Table 1).

[16] The air temperature records of AWS2 show data gaps in the winter seasons due to power shortage. They were filled by linearly scaled data (R^2 = 0.97) of the AWS on De Geerfonna (AWS4) in order to provide a continuous local reference during air temperature downscaling. However, short gaps without any air temperature data remain in May 2009 and March 2010. The time series is nevertheless considered an adequate local reference for downscaling as in this study air temperature accuracy is by far most important during the summer seasons.

3.3. Albedo

[17] Terra MODIS data were used for retrieval of daily albedo fields of Vestfonna. Albedo information is based on the daily updated MODIS snow product MOD10A1 version 5 [*Hall et al.*, 2002; *Hall and Riggs*, 2007] with a spatial resolution of 500 m. Daily albedo information is based on the scene acquired closest to nadir relating to each individual pixel. Where no MODIS albedo information is available due to cloud cover, the albedo time series at that grid point is interpolated between the temporally closest data values available.

[18] During polar winter, when no MODIS snow cover data are available (25 October to 15 February), the entire ice cap is assumed to be covered with snow having a constant albedo of 0.80. Mean update interval for albedo over the ice cap is 2.9 ± 10.8 days for the period of available MODIS snow cover, with the given range indicating one standard deviation and thus a strongly asymmetric distribution.

[19] On the southern outlet glacier tongues of the ice cap, small areas of permanent data gaps are present in the MODIS snow product (26.25 km^2). Surface albedo throughout these

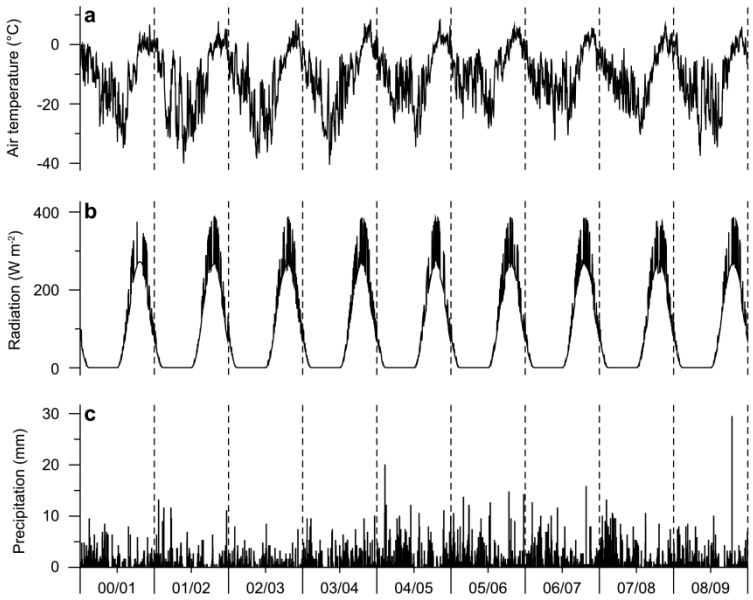

Figure 2. Climate data time series for mass balance years 2000/2001 to 2008/2009: (a) downscaled ERA-Interim air temperature, (b) modeled global radiation, and (c) scaled ERA-Interim precipitation sums. All data are presented at a daily resolution and refer to the location of AWS2 (see Figure 1). Annual subdivisions on the *x* axis start September 1.

areas was extrapolated based on the albedo of neighboring grid cells.

[20] Comparison of remotely sensed surface albedo with the measurement record of AWS2 yield a mean difference of +0.02 over the period May 2008 to July 2009 and a root mean square error (RMSE) of 0.12. This result is in agreement with uncertainties obtained by *Greuell and Oerlemans* [2005] on the Greenland ice sheet and is regarded as an adequate reproduction of in situ conditions, given that the AWS only samples a small point within the much larger MODIS footprint [*Stroeve et al.*, 2006a]. A characteristic annual evolution of the albedo bias depending on solar zenith angle as described by *Wang and Zender* [2010] is not clearly identifiable due to the limited length of the study period. Therefore, a systematic correction of the albedo fields was not feasible, and uncertainty of unknown magnitude is introduced to modeled climatic mass balances.

3.4. Fractional Cloud Cover

[21] Daily fractional cloud cover fields over Vestfonna were created on the basis of the MOD10A1 daily snow product and serve as input for the global radiation computation. Binary cloud cover information is contained by default in this 500 m resolution gridded data set. MODIS cloud cover information has been widely used in several studies and was successfully validated over snow covered ground [e.g., *Berendes et al.*, 2004; *Wang et al.*, 2008].

[22] Preprocessed fractional cloud cover fields are provided by the MODIS cloud product (MOD06_L2), but only on a 5 km spatial resolution. These fields are created by averaging the binary cloud cover information (1 km) of fixed 5 × 5 pixel subsets. We customized this method to obtain fractional cloud cover fields at the same 500 m resolution as the MOD10A1 input data. A running 5 × 5 pixel window is used to calculate fractional cloud cover for the respective central pixel. During polar night, when no MOD10A1 data are available (25 October to 15 February) and incoming shortwave radiation is negligible, fractional cloud cover is assumed to be 0 throughout the entire model domain.

3.5. Atmospheric Turbidity

[23] Atmospheric turbidity data needed for radiation modeling are represented by the Linke turbidity factor [*Linke*, 1961]. The Solar Radiation Database SoDa [*Wald et al.*, 2002] provides mean monthly values of the Linke turbidity factor on a 0.5° global grid. It is a standard tool among solar engineering

Table 1. Metadata of Automatic Weather Stations[a]

Station	Altitude (m asl)	Period
AWS1	240	23 May 2008–30 Apr 2009
AWS2	370	29 May 2008–30 Apr 2010
AWS3	500	22 May 2008–30 Apr 2009
AWS4	240	27 May 2008–30 Apr 2010
Variable at AWS1-4	sensor	accuracy
Air temperature	Campbell CS215	±0.9°C
Shortwave radiation	Campbell CS300	±5%

[a]All four AWS recorded air temperature and incoming and reflected shortwave radiation.

Table 2. Overview of Model Parameters. *dT/dz* Is Air Temperature Slope Lapse Rate

Parameter	Value and Unit	Equation
m, n	0.0000099, 0.0079	1
f_T	1.394 mm w.e. K^{-1} day^{-1}	2
f_R	0.098 mm w.e. W^{-1} m^2 day^{-1}	2
o_1, p_1	−2.73°C, 1.10	3
o_2, p_2	−4.26°C, 0.90	3
o_3, p_3	−1.79°C, 1.05	3
o_4, p_4	−3.34°C, 1.00	3
o_5, p_5	−3.37°C, 1.08	3
o_6, p_6	−2.70°C, 1.30	3
o_7, p_7	−2.30°C, 1.20	3
o_8, p_8	−4.00°C, 2.01	3
o_9, p_9	−2.96°C, 1.26	3
o_{10}, p_{10}	−2.57°C, 1.06	3
o_{11}, p_{11}	−3.10°C, 1.02	3
o_{12}, p_{12}	−2.74°C, 1.02	3
q, r	0.0, 0.364	9, 10
dT/dz	−7.0 K km^{-1}	n.a.

professionals and a widely used data provider for various solar radiation modeling applications [e.g., *Schüttemeyer et al.*, 2007]. Grids of monthly values were downloaded from the database (http://www.soda-is.com) and resampled to the 250 m resolution model domain.

3.6. Mass Balance Data

[24] Measurements of snow depth and ice surface height changes used for calibration of the mass balance model were carried out at a network of ablation/accumulation-stakes consisting of 15 stakes distributed over parts of the ablation area of the ice cap (Figure 1). We do not use stake data from the accumulation area because the amount of refreezing is not measured. A total of 29 successful repeat readings were retrieved during several field campaigns in 2007, 2008, and 2009. Measurement intervals are grouped into two major classes, that is, 70–90 days (between spring and summer campaigns) and 270 days (between summer and spring campaigns).

[25] Measurements of snow water equivalent and bulk snow densities were carried out in 21 snow pits distributed across the ice cap (Figure 1) [*Möller et al.*, 2011]. Data were used for calibration of the accumulation model and for conversion of repeat stake measurements into water equivalent values. A mean bulk snow density of 398 ± 41 kg m^{-3} (mean ± one standard deviation) was obtained from the snow pits. Density showed a low variability in space and time, which is explained by continuous compaction of the snowpack throughout the year due to frequent snowdrift [*Goodison et al.*, 1981]. Accordingly, all snow-related mass balance measurements are converted into water equivalent value using a single snow density (400 kg m^{-3}). Ice density is set to 900 kg m^{-3} [*Paterson*, 1994].

4. Model Description and Calibration

4.1. Mass Balance Model

[26] Our mass balance model computes surface accumulation, surface ablation and refreezing as well as their sum, the so-called climatic mass balance, following the terminology by *Cogley et al.* [2011]. Ablation (defined as negative in case of mass loss) is calculated as a function of downscaled ERA-Interim air temperature data and modeled net shortwave radiation. Accumulation is derived from ERA-Interim precipitation data that are distributed as a function of elevation. Refreezing is estimated using the P_{max} approach [*Reeh*, 1991].

[27] Modeling is done for the 9-year period from September 2000 until August 2009 with a daily resolution on a 250 m grid. Calibration is based on point balance data provided by repeat stake readings and snow pit data.

4.2. Accumulation

[28] Surface accumulation is assumed to be exclusively formed by snowfall. All precipitation occurring at air temperatures below 0°C is assumed to fall as snow, while rain is assumed for all precipitation at temperatures above 2°C. Between 0 and 2°C, a mixture of snow and rain is assumed, and the amount of snowfall is scaled between 100% (0°C) and 0% (2°C) using a hyperbolic function [*Möller et al.*, 2007]. Initial snowfall fields are calculated from daily ERA-Interim total precipitation of a grid point south of Vestfonna (Figure 1) by using the air temperature fields described in section 4.5.

[29] *Möller et al.* [2011] have shown a strong increase of surface accumulation with altitude. Here we approximate surface accumulation (c) from the initial snowfall fields (S_{ERA}) by quadratic scaling according to an index function of altitude (z):

$$c(z) = S_{ERA}\left(mz^2 + nz + 1\right). \quad (1)$$

The coefficients m and n (Table 2) of this index function are determined empirically (Figure 3) from in situ measurements of snow water equivalent in 16 snow pits across the ice cap [*Möller et al.*, 2011]. For each snow pit location, index values are calculated as the ratio of the sum of snow pit-derived surface accumulation close to the end of the winter season and the corresponding snowfall sum obtained from the initial ERA-Interim snowfall fields.

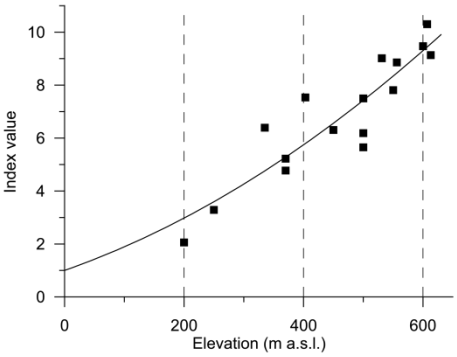

Figure 3. Index function for distribution of accumulation with altitude. Individual index values are marked as black squares. The black line is the fitted index function given in equation (1).

[30] A quadratic accumulation index function defined by m and n is fitted to the set of individual index values (Figure 3). The intercept of the index function is forced to 1.0, as surface accumulation is assumed to be equal to ERA-Interim snowfall at sea level. The relation between index values and elevation holds for all four accumulation seasons included in the data (2006/2007 to 2009/2010).

[31] The fitted index function explains 83% of the variance of the individual index values. Considerable parts of the remaining deviations (RMSE = 0.94) can be attributed to local scale snow depth variability induced by frequent formation of flat, small scale surface roughness (sastrugi). According to the index function, surface accumulation on Vestfonna increases by a factor of more than eight from the margin to the top of the ice cap. Modeled surface accumulation thus resembles magnitudes and gradients previously reported for Austfonna [*Schuler et al.*, 2007; *Taurisano et al.*, 2007].

4.3. Refreezing

[32] Refreezing in snow and firn plays a major role in the mass budget of Arctic glaciers [e.g., *Palosuo*, 1987]. In this study, it is accounted for by applying the well-established $P_{\max}$ modeling approach introduced by *Reeh* [1991]. $P_{\max}$ is calculated as a fraction of winter accumulation. It represents the maximum meltwater amount that can refreeze within the snowpack during the following ablation season before runoff occurs. It thus adds a positive value to glacier mass balance. As done by *Schuler et al.* [2007] for Austfonna, we set $P_{\max}$ = 0.6. Hence, melt and rainwater are retained by refreezing processes until 60% of the current year's winter accumulation is reached. Any excess water is assumed to be lost from the glacier as runoff.

4.4. Ablation

[33] Surface ablation, that is, snow or ice melt, is calculated using a combined temperature-radiation-index approach. Since it only depends on air temperature and surface type as input variables, the temperature-index method [e.g., *Hock*, 2003] is a useful melt modeling approach in regions with limited data availability [e.g., *Braithwaite and Raper*, 2007; *Möller and Schneider*, 2010]. It is justified by the fact that incoming long wave radiation and sensible heat flux, which usually represent the largest energy sources for snow and ice melt, are strongly correlated to air temperature [*Ohmura*, 2001].

[34] We use the temperature-radiation-index model developed by *Pellicciotti et al.* [2005], which parameterizes snow and ice ablation as

$$a = f_T T + f_R(1-\alpha)R_G \text{ for } T > 0^\circ\text{C} \quad (2)$$

$$a = 0 \text{ for } T \leq 0^\circ\text{C},$$

where a is ablation, T is air temperature, and R_G is global radiation. α is albedo, and f_T and f_R are empirical coefficients.

[35] Spatially distributed global radiation is modeled using the radiation model described in section 4.6. The amount of global radiation absorbed at the surface is determined using the MODIS-based albedo fields (see section 3.3).

4.5. Air Temperature

[36] ERA-Interim daily 2 m air temperatures from a grid point south of Vestfonna (Figure 1) were statistically downscaled to match local conditions at Vestfonna using the variance-inflation method [*Karl et al.*, 1990; *Huth*, 1999].

[37] The variance-inflation method was developed for downscaling of global circulation model data, in order to make its variance match the one at local scale. It implicitly assumes local variability to be entirely governed by synoptic scale forcing [*von Storch*, 1999], but was nevertheless considered to be an appropriate tool for reproduction of day-to-day variability in local scale air temperature data [*Huth et al.*, 2001]. Reanalysis data such as those used in this study represent an interpolated local scale and are thus based on measurements and observations. We therefore consider variance inflation to be an appropriate tool for downscaling of ERA-Interim air temperatures to Vestfonna local conditions.

[38] The downscaling follows a two-step approach [*von Storch*, 1999]. It is done separately for each month i in order to account for the strong interannual variability of air-temperature variance at the study site, that is, small variance in summer and high variance in winter. First, the synoptic scale data ($T_{\mathrm{ERA},i}$) are linearly adjusted to local scale conditions at Vestfonna according to

$$\hat{T}_{\mathrm{ERA},i} = o_i + p_i T_{\mathrm{ERA},i}. \quad (3)$$

The coefficients o_i and p_i (Table 2) are determined from linear regression analysis between ERA-Interim and AWS2 data. Then, the variance of the adjusted air temperatures is inflated to match the one observed at AWS2:

$$T_i = \sqrt{\frac{\mathrm{var}(T_{\mathrm{AWS2},i})}{\mathrm{var}(\hat{T}_{\mathrm{ERA},i})}}\,\hat{T}_{\mathrm{ERA},i}. \quad (4)$$

The downscaled air temperature time series (Figure 2) shows RMS errors of 0.7 K (June to August) and 1.2 K (September to May), when compared to measurements at AWS2.

[39] Air temperature fields are created using a constant linear lapse rate (dT/dz, Table 2). This average lapse rate is obtained from daily mean air-temperature data of AWS1–3 during the period June 2008–April 2009. Results suggest a value of 7.0 ± 3.7 K km^{-1}, with the given range indicating one standard deviation.

4.6. Global Radiation

[40] Global radiation (R_G) is calculated as the sum of solar radiation ($R_{S,\mathrm{sol}}$) and multiple scattering and reflection between the glacier and the lowermost cloud layers ($R_{S,\mathrm{msr}}$):

$$R_G = R_{S,\mathrm{sol}} + R_{S,\mathrm{msr}}. \quad (5)$$

[41] All shortwave radiation fluxes are computed with an hourly resolution from which daily means are computed.

4.6.1. Solar Radiation

[42] Potential clear-sky direct solar radiation on an arbitrarily oriented and inclined surface ($R_{0,\mathrm{sol}}$) is estimated according to *Bernhardt and Philipps* [1958] and *Mölg et al.* [2003]:

$$R_{0,\mathrm{sol}} = S_0 E \cos\zeta^* \left[\frac{0.907}{(\cos\zeta)^{0.018}}\right]^{\frac{T_L}{\cos\zeta}}. \quad (6)$$

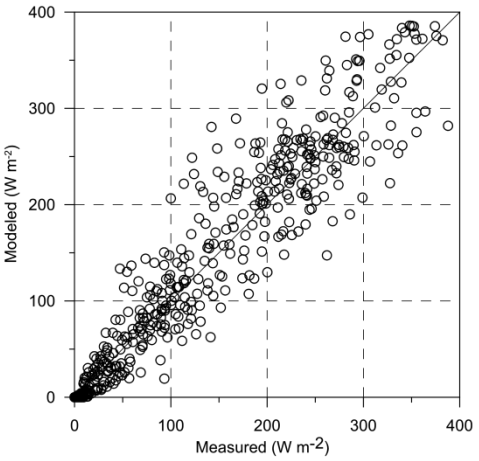

Figure 4. Modeled versus measured daily global radiation at AWS2 in the period May 2008 to April 2010.

S_0 is the solar constant (1368 W m^{-2}). Eccentricity correction factor (E) and zenith angle of the sun with respect to a theoretical, planar surface (ζ) or with respect to an arbitrarily oriented and inclined surface (ζ^*) are calculated according to standard solar geometry [e.g., *Iqbal*, 1983]. Atmospheric turbidity is represented by spatially distributed grids of the Linke turbidity factor (T_L) [*Linke*, 1961]. Terrain shading is taken into account using standard algorithms of solar-radiation geometry [*Corripio*, 2003].

[43] The reduction of clear-sky solar radiation due to actual cloud-cover conditions is determined from $R_{0,\mathrm{sol}}$ using the Savinov-Ångström formula [e.g., *Kondratyev*, 1969]. The portion of clear-sky solar radiation actually reaching the surface ($R_{S,\mathrm{dir}}$) is thus calculated as

$$R_{S,\mathrm{sol}} = R_{0,\mathrm{sol}}\left[1 - (1-\eta')C_{fc}\right]. \quad (7)$$

Cloudiness is incorporated in terms of spatially distributed fractional cloud cover grids (C_{fc}) and η' is an empirical coefficient being 0.58 at 80°N [*Budyko*, 1974]. This implies that under completely overcast conditions (C_{fc} = 1) $R_{S,\mathrm{sol}}$ amounts to 58% of clear-sky solar radiation. Due to the minimal input requirements, the Savinov-Ångström formula (equation (7)) is a feasible method for efficient radiation calculation and has thus been used before in several studies [e.g., *Emelyanov and Konovalov*, 1975; *Dumanskaya*, 2008].

4.6.2. Multiple Scattering and Reflection

[44] Multiple scattering and reflection between the glacier and the lowermost cloud layers is an important component of global radiation at the surface [*Ørbæk et al.*, 1999]. Reflected shortwave radiation from surrounding topography is assumed to be negligible in this study, as the roughly convex shape of the ice body and the resulting lack of surrounding surfaces do not allow for reflections toward the ice cap.

[45] The radiation flux due to multiple scattering and reflection ($R_{S,\mathrm{msr}}$) is calculated from direct radiative forcing according to

$$R_{S,\mathrm{msr}} = R_{S,\mathrm{sol}} s_R. \quad (8)$$

The spatially distributed scaling factor (s_R) that accounts for surface albedo and fractional cloud-cover conditions is empirically calibrated from a comparison of measured and modeled global radiation fluxes at AWS2 in the period from 28 May 2008 to 6 August 2009. It is given by

$$s_R = q + r\alpha C_{fc}\frac{SV}{SV_{\mathrm{AWS2}}}, \quad (9)$$

and depends largely on surface albedo (α) and fractional cloud cover (C_{fc}). Differences in sky-view factors (SV) between any location on the glacier and the calibration site (AWS2) are taken into account by the given quotient ($SV_{\mathrm{AWS2}} = 0.88$). Sky-view factors are computed according to *Corripio* [2003]. The scaling factor s_R is thus a gridded quantity whose spatial distribution depends on daily updated albedo and fractional cloud cover grids and a fixed distribution of sky-view factors. The regression constants (q, r; Table 2) are calibrated from a comparison of measured global radiation (R_{meas}) and modeled ($R_{S,\mathrm{dir}}$) solar radiation at AWS2 using the following equation:

$$\frac{R_{\mathrm{meas,AWS2}} - R_{S,\mathrm{sol,AWS2}}}{R_{S,\mathrm{sol,AWS2}}} = q + r\alpha_{\mathrm{AWS2}} C_{fc,\mathrm{AWS2}}. \quad (10)$$

The difference given in the numerator, that is, the deviation of modeled from measured values, is treated as radiation fluxes originating in multiple scattering and reflection ($R_{S,\mathrm{msr}}$). Hence, the left side of equation (10) represents the ratio between multiple scattering and reflection and direct radiation fluxes at AWS2, and therefore with s_R. The constant r is obtained using linear regression techniques. With the product of albedo and fractional cloud cover ranging between 0 and 1, this means that multiple scattering and reflection at AWS2 might contribute more than one fourth to global radiation. The intercept q is forced to 0 in order to account for the fact that multiple scattering and reflection do not exist where either albedo or fractional cloud cover are zero.

[46] Modeled global radiation fluxes are able to explain 90% of the variance of in situ measurements at AWS2 (Figure 4), and considerable parts of the remaining deviations (RMSE = 36.1 W m^{-2}) can be attributed to intraday changes in cloud cover. This high temporal resolution is not provided in the MODIS-based fractional cloud cover data as it only represents samples at the overpass times of the Terra satellite.

[47] Alternative tests considering a spatially or temporally averaged cloud cover over Vestfonna resulted in a considerably diminished performance of the radiation model. Modeling attempts using the preprocessed 5 km MODIS fractional cloud cover fields led to slightly higher deviations between measured and modeled global radiation fluxes.

4.7. Model Calibration

[48] The calibration of the mass balance model is based on point balances at the stake network. Calibration is done by adjusting the empirical coefficients f_T and f_R of the ablation

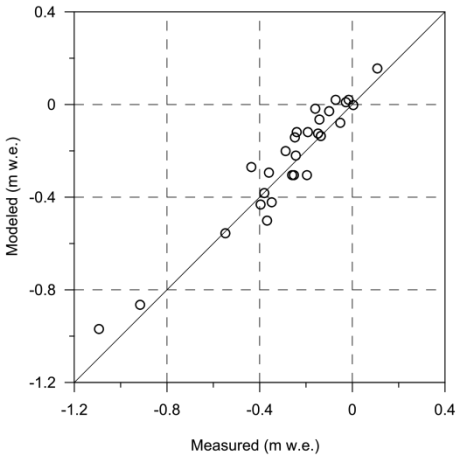

Figure 5. Modeled versus measured point climatic mass balances at the stakes (Figure 1) in the period 2007–2009.

model. Iterative mass balance model runs with continuous changes of f_T and f_R are performed until a best fit approximation between modeled point balances and their measured counterparts is reached, using RMSE minimization (Table 2). The modeled point balances account for an explained variance of 86% of the stake measurements (Figure 5). The RMSE between modeled and measured values is ±0.10 m w.e. Both the spatial and temporal variability in mass balance is reproduced well by the model.

5. Model Uncertainty

[49] The overall uncertainty of the modeled climatic mass balances time series (U_b) is quantified by accounting for errors inherent in the input data and in calibrated model parameters. We include seven individual errors (Table 3) that are assumed to be uncorrelated to each other. The overall uncertainty is thus calculated as

$$U_b = \sqrt{\sum_{i=1}^{7} U_i^2} \tag{11}$$

by applying error propagation rules [*Bevington*, 1969]. U_b is calculated on a monthly basis (Figure 6) by performing additional model runs with input data or model parameters altered according to the individual error ranges (Table 3).

[50] Uncertainty originating from air temperature inputs (U_1) is accounted for by the RMSE between downscaled ERA-Interim data and measurements at AWS2. Different values for ablation and accumulation seasons are given as the distinctly different variances of air temperatures in summer and winter lead to similarly different downscaling accuracies. The uncertainty of the temperature lapse rate (U_2) is accounted for by its measured standard deviation.

[51] Uncertainty originating from global radiation inputs (U_3) is assessed from the RMSE between modeled values and measurements at AWS2. The inaccuracy of the albedo fields (U_4) is incorporated by accounting for the RMSE between measurements at AWS2 and MODIS data of the respective grid cell.

[52] The variability of snow density results in uncertainty ranges of the temperature and radiation factors of the ablation model during calibration (U_5). It is incorporated using the standard deviation of measured bulk snow densities [*Möller et al.*, 2011].

[53] Uncertainties induced by the accumulation model (U_6) are accounted for considering the RMSE of the fitted accumulation-index function (Figure 3). It is incorporated by constant shifts of the function along the intercept according to the RMSE value. The uncertainty within the calculation of refreezing (U_7) is estimated by applying alternative values for the assumed P_{max} fraction, that is, 0.5 and 0.7.

[54] The overall model uncertainty shows distinct differences between summer (June to August) and winter (September to May) seasons (Figure 6). Monthly errors in summer are found to be about nine times higher than in winter. The mean monthly error range in summer is ±0.062 m w.e. and shows high intermonthly variability (standard deviation of ±0.034 m w.e.). Error ranges in the winter months show a mean of only ±0.007 m w.e. with only small intermonthly variability (standard deviation of ±0.005 m w.e.).

[55] This temporal pattern is due to the fact that uncertainty in ablation calculation exceeds that of accumulation and refreezing calculation (Figure 6). The mean annual error range of calculated ablation sums up to ±0.18 m w.e. while that of accumulation and refreezing only amount to ±0.07 m w.e. and ±0.04 m w.e., respectively (Table 4). This is because most of the uncertainties considered predominantly affect ablation. The uncertainties inherent in the albedo fields and the downscaled air temperature data have the greatest impact on overall model uncertainty. Overall, the uncertainty analysis suggests that the model is sufficiently robust to assess the climatic mass balance of Vestfonna.

6. Results and Discussion

[56] In the period 2000–2009, the modeled surface mass balance regime of the ice cap is characterized by long accumulation periods (September to May) and short ablation periods (June to August, Figure 6). Model results reveal a mean climatic mass balance rate of −0.02 ± 0.20 m w.e. yr^{-1}

Table 3. Overview of Uncertainties of Model Parameters[a]

Variable	Parameter	Value
U_1	air temperature	±0.7 K (abl. period) ±1.2 K (acc. period)
U_2	dt/dz	±3.7 K km^{-1}
U_3	global radiation	±36.1 W m^{-2}
U_4	albedo	±0.12
U_5	snow density	±40 kg m^{-3}
U_6	accumulation index	±0.94
U_7	refreezing (P_{max})	±0.1

[a]See equation (11).

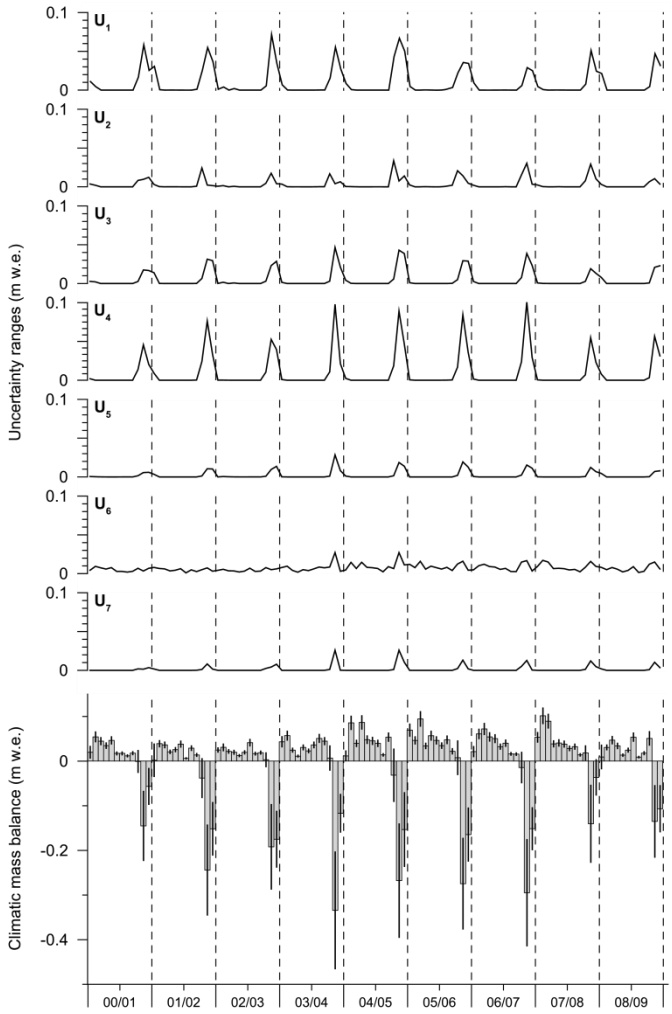

Figure 6. Uncertainties of monthly climatic mass balances. The naming of the individual uncertainty ranges corresponds to Table 3. The black error bars in the bar chart of climatic mass balance represent the overall uncertainty according to equation (11). *x* axis shows mass balance years. Annual subdivisions start September 1.

for the period September 2000 to August 2009 (Figure 7 and Table 4), suggesting roughly balanced conditions. Year-to-year variability is relatively low (<0.5 m) as indicated by the small standard deviation of annual balances (0.15 m w.e.). The mean annual surface ablation rate is -0.58 ± 0.18 m w.e. yr^{-1}, while annual surface accumulation and refreezing rates amount to $+0.40 \pm 0.07$ m w.e. yr^{-1} and $+0.15 \pm 0.04$ m w.e. yr^{-1}, respectively. Hence, on average, approximately one fourth of the surface ablation refreezes. For individual mass balance years, this fraction ranges between 5 and 48% (Figure 7).

[57] The mass balance variability shows a dependency on the North Atlantic Oscillation (NAO, Figure 7). Modeled winter balances correlate significantly ($r = 0.66$, 90% level) with the mean winter NAO (December to February). Posi-

Table 4. Glacier-Wide Modeled Climatic Mass Balance, ELA, and Mass Balance Gradient for the Mass Balance Years 2000/2001 to 2008/2009[a]

Mass Balance Year	Annual Balance (m w.e.)	Winter Balance (m w.e.)	Summer Balance (m w.e.)	Annual Surface Accumulation (m w.e.)	Annual Surface Ablation (m w.e.)	Annual Refreezing (m w.e.)	ELA (m asl)	Gradient (m w.e. km^{-1})
2000/2001	+0.06 ± 0.17	+0.26 ± 0.05	−0.20 ± 0.14	+0.33 ± 0.05	−0.36 ± 0.15	+0.09 ± 0.04	375 ± 18	2.65
2001/2002	−0.22 ± 0.23	+0.21 ± 0.06	−0.43 ± 0.19	+0.29 ± 0.05	−0.55 ± 0.21	+0.03 ± 0.03	457 ± 17	2.91
2002/2003	−0.16 ± 0.18	+0.21 ± 0.04	−0.36 ± 0.17	+0.24 ± 0.04	−0.49 ± 0.16	+0.09 ± 0.04	453 ± 22	2.47
2003/2004	−0.12 ± 0.21	+0.32 ± 0.06	−0.44 ± 0.19	+0.39 ± 0.07	−0.70 ± 0.18	+0.19 ± 0.05	415 ± 19	3.05
2004/2005	−0.03 ± 0.28	+0.42 ± 0.07	−0.45 ± 0.25	+0.51 ± 0.09	−0.78 ± 0.23	+0.24 ± 0.06	383 ± 15	4.16
2005/2006	+0.02 ± 0.22	+0.45 ± 0.08	−0.43 ± 0.19	+0.53 ± 0.09	−0.74 ± 0.22	+0.23 ± 0.06	364 ± 19	3.71
2006/2007	−0.10 ± 0.22	+0.36 ± 0.06	−0.46 ± 0.19	+0.45 ± 0.07	−0.66 ± 0.20	+0.11 ± 0.07	377 ± 18	2.97
2007/2008	+0.28 ± 0.18	+0.44 ± 0.07	−0.16 ± 0.14	+0.51 ± 0.09	−0.45 ± 0.15	+0.21 ± 0.06	283 ± 10	3.19
2008/2009	+0.05 ± 0.18	+0.24 ± 0.05	−0.19 ± 0.14	+0.36 ± 0.06	−0.45 ± 0.16	+0.13 ± 0.03	339 ± 14	2.72
Average	−0.02 ± 0.20	+0.32 ± 0.06	−0.35 ± 0.17	+0.40 ± 0.07	−0.58 ± 0.18	+0.15 ± 0.04	383 ± 17	3.09
Standard Deviation	0.15	0.10	0.13	0.10	0.15	0.08	54	0.54

[a]Annual and seasonal balances are given according to the fixed date system (winter balance, September 1 to May 31; summer balance, June 1 to August 31). Unit is meters water equivalent error ranges are given according to equation (11).

tive NAO conditions have been suggested to coincide with less sea ice in the Barents Sea [*Yamamoto et al.*, 2006], and thus increased precipitation over Svalbard [*Rogers et al.*, 2001], and vice versa. The summer balances in turn anticorrelate significantly ($r = -0.68$, 95% level) with the mean summer NAO (June to August). Sea ice anomalies in the Barents Sea were found to anticorrelate with air temperature anomalies over Svalbard [*Koenigk et al.*, 2009]. Hence, during positive NAO conditions, increased air temperatures are to be expected over Svalbard, and vice versa.

[58] An exceptionally positive annual climatic mass balance (+0.28 ± 0.18 m w.e.) occurred in 2007/2008. This mass balance year is characterized by a highly positive winter NAO (+0.66) and a highly negative summer NAO (−1.27), thus favoring large accumulation and small ablation. However, comparable NAO conditions also occurred during other mass balance years of the study period, and thus other driving forces for the exceptionally positive mass balance have to be considered. *Francis et al.* [2009] found that negative summer sea ice-extent anomalies also coincide with increased precipitation over Svalbard. Hence, the highly positive winter balance (+0.44 ± 0.07 m w.e.) may be attributed to the coincidence of the highly positive winter NAO and the small Arctic sea ice-extent in September 2007. The least negative summer balance (−0.16 ± 0.14 m w.e.) of the entire study period is consistent with the most negative summer NAO (Figure 7), and with transient weather conditions on Nordaustlandet. Several days of heavy snowfall in the first week of August resulted in a deep fresh snow layer (~0.20 m according to own field observations) that effectively increased the surface albedo on the ice cap. Additionally, this led to distinctly reduced ablation sums during the last month of the 2008 ablation season (Figure 6).

[59] The climatic mass balance profiles of Vestfonna show high interannual variability with gradients ranging from 2.47 to 4.16 m w.e. km^{-1} (Figure 8). Modeled annual equilibrium-line altitudes (ELAs) during the nine years range from 283 ± 10 m asl (2007/2008) to 457 ± 17 m asl (2001/2002), with a mean of 383 ± 54 m asl (mean ± one standard deviation). *Hagen et al.* [2003] estimated the ELA of Vestfonna to fluctuate between 400 and 500 m asl during the last decades of the 20th century. However, their estimate refers to surface mass balance and thus does not consider refreezing below the end-of-summer surface. Refreezing has a large impact on the ELA as it tends to shift the ELA

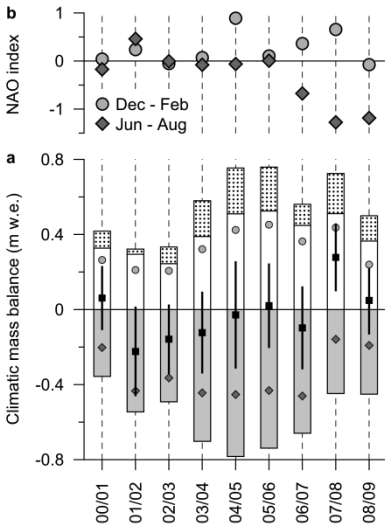

Figure 7. (a) Modeled glacier-wide climatic mass balance of Vestfonna for the mass balance years 2000/2001 to 2008/2009: The bar chart shows annual ablation (gray bars), annual accumulation (white bars), and annual refreezing (dotted). Black squares with error bars represent the annual balances, light gray circles represent the winter balances, and dark gray diamonds represent the summer balances. Each mass balance year lasts from September 1 to August 31. (b) Mean winter (December to February) and mean summer (June to August) NAO (source is the NOAA Climate Prediction Center, http://www.cpc.ncep.noaa.gov).

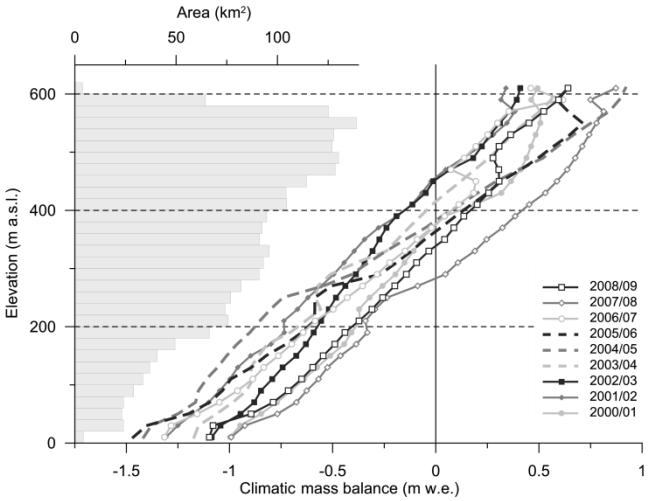

Figure 8. Area-altitude distribution of Vestfonna (bar chart) and mean climatic mass balance profiles for the mass balance years 2000/2001 to 2008/2009. Each mass balance year lasts from September 1 to August 31. Calculations are performed on 20 m altitude bins.

toward higher elevations. As expected, years with more negative climatic balance coincide with lower ELAs, and vice versa.

[60] The spatial variability of climatic mass balance is shown in Figure 9. Mass gain dominated over large parts of the interior of the ice cap, while considerable mass loss occurred throughout the lower marginal areas of the ice cap, in particular on its south facing slopes, as well as Franklinbreen and the northeastern land-terminating parts.

[61] The temporal variability of the modeled climatic mass balances of Vestfonna is in line with findings obtained for Austfonna or the Ny-Ålesund region [*Hagen et al.*, 2003; *Rasmussen and Kohler*, 2007; *Schuler et al.*, 2007]. *Hagen et al.* [2003] suggested Austfonna to be in equilibrium at the beginning of the decade, but for the period from April 2004 to April 2005 *Schuler et al.* [2007] suggested a clearly negative climatic mass balance of −0.32 m w.e. Our results also reveal a quasi-balanced state at the beginning of the decade, but they do not show a distinctly negative mass balance year in the period 2004–2005 (Table 4 and Figure 7). This is likely due to the fact that *Schuler et al.* [2007] modeled accumulation on the basis of the daily precipitation record of the nearest synoptic weather station operated in Ny-Ålesund (180 km southwest of Vestfonna). This record shows a pronounced relative minimum in the period 2004–2005 that is not evident in the ERA-Interim data used in this study. As the ERA-Interim grid point is located much closer to Vestfonna (<50 km SSW), we consider this time series to be distinctly more representative for regional climate on Nordaustlandet than the one from the Ny-Ålesund weather station. The decreasingly negative climatic mass balances of Vestfonna during parts of the decade (Figure 7) are also evident on Austfonna. A comparable pattern was identified in a 5 year surface mass balance time series (2004–2008) of the Eton-/Winsnesbreen basin (northwestern Austfonna) [*Moholdt et al.*, 2010a]. Taken together, it can be concluded that the climatic mass balances of Vestfonna modeled in this study mirror the general mass balance pattern throughout the northern Svalbard archipelago.

7. Conclusion

[62] The climatic mass balance of Vestfonna was calculated for the 9 year period from September 2000 to August 2009 using a temperature-radiation-index mass balance model driven by ERA-Interim air temperature and precipitation data as well as MODIS-based cloud cover and albedo data. Results indicate generally short ablation seasons (3 months) and correspondingly longer accumulation seasons (9 months) over the 9 year period.

[63] Over the nine mass balance years studied Vestfonna shows a mean annual climatic mass balance of −0.02 ± 0.20 m w.e. Mean winter and summer balances amount to +0.32 ± 0.06 and −0.35 ± 0.17 m w.e., respectively, and are found to correlate significantly with NAO conditions. Refreezing plays a major role in the mass budget of the ice cap. On average, roughly one fourth of annual ablation is retained in the firn due to refreezing. However, more measurements and more sophisticated subsurface models are desirable to better ascertain results.

[64] The mean annual ELA is calculated to be 383 ± 54 m asl (mean ± one standard deviation) and thus to a slightly lower altitude than suggested by *Hagen et al.* [2003] for the end of the 20th century. Further studies are needed to

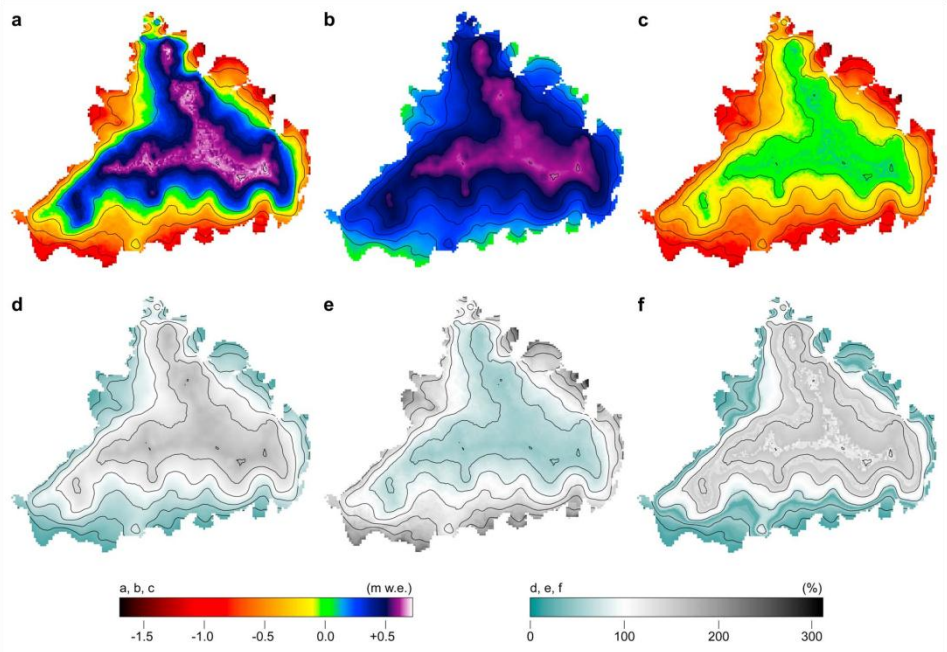

Figure 9. The climatic mass balance of Vestfonna: (a) annual balance, (b) winter balance, and (c) summer balance. (d) Annual accumulation, (e) annual ablation, and (f) annual refreezing presented as deviation from the spatial mean (i.e., as the ratio of specific mass balance components and their glacier-wide means). Each plot shows the averaged pattern of the mass balance years 2000/2001 to 2008/2009. Each mass balance year lasts from September 1 to August 31. Elevation contour spacing is 100 m.

quantify mass loss by calving, in order to arrive at total mass changes of the ice cap.

[65] **Acknowledgments.** This study was carried out under the umbrella of the International Polar Year (IPY) core projects Kinnvika and Glaciodyn and greatly benefited from the logistical sponsorship within IPY Kinnvika in the field. The authors express their gratitude to all people involved in fieldwork during the various field campaigns and acknowledge the Swedish Polar Research Secretariat and R/V *Horyzont II* from the Polish Marine Academy in Gdynia for logistical support. The Nordic Council of Ministers is acknowledged for financial support. The study was funded by grants BR 2105/6–1, SCHE 750/3–1, and SCHN 680/2-1 of the German Research Foundation (DFG). Additional funding was provided by grant 621-2007-3738 of the Swedish Research Council. Comments and suggestions by three anonymous reviewers very much helped to improve the manuscript and are gratefully acknowledged. Bob McNabb is acknowledged for correcting the English.

References

Arendt, A. A., K. A. Echelmeyer, W. D. Harrison, C. S. Lingle, and V. B. Valentine (2002), Rapid wastage of Alaska glaciers and their contribution to rising sea level, *Science*, *297*, 382–386, doi:10.1126/science.1072497.

Bahr, D. B., M. Dyurgerov, and M. F. Meier (2009), Sea-level rise from glaciers and ice caps: A lower bound, *Geophys. Res. Lett.*, *36*, L03501, doi:10.1029/2008GL036309.

Berendes, T. A., D. A. Berendes, R. M. Welch, E. G. Dutton, T. Uttal, and E. E. Clothiaux (2004), Cloud cover comparisons of the MODIS daytime cloud mask with surface instruments at the north slope of Alaska ARM site, *IEEE Trans. Geosci. Remote Sens.*, *42*(11), 2584–2593, doi:10.1109/TGRS.2004.835226.

Bernhardt, F., and H. Philipps (1958), *Die räumliche und zeitliche Verteilung der Einstrahlung, der Ausstrahlung und der Strahlungsbilanz im Meeresniveau, Teil I, Die Einstrahlung*, Akademie Verlag, Berlin.

Berthier, E., E. Schiefer, G. K. C. Clarke, B. Menounos, and F. Rémy (2010), Contribution of Alaskan glaciers to sea-level rise derived from satellite imagery, *Nat. Geosci.*, *3*(2), 92–95, doi:10.1038/ngeo737.

Bevan, S., A. Luckman, T. Murray, H. Sykes, and J. Kohler (2007), Positive mass balance during the late 20th century on Austfonna, Svalbard, revealed using satellite radar interferometry, *Ann. Glaciol.*, *46*, 117–122, doi:10.3189/172756407782871477.

Bevington, R. R. (1969), *Data Reduction and Error Analysis for the Physical Science*, McGraw-Hill, New York.

Braithwaite, R. J., and S. C. B. Raper (2007), Glaciological conditions in seven contrasting regions estimated with the degree-day model, *Ann. Glaciol.*, *46*, 297–302, doi:10.3189/172756407782871206.

Budyko, M. I. (1974), *Climate and Life*, Academic, New York.

Cogley, J. G., et al. (2011), *Glossary of Glacier Mass Balance and Related Terms, IHP-VII Tech. Doc. Hydrol. 86, IACS Contrib. 2*, UNESCO-IHP, Paris.

Corripio, J. G. (2003), Vectorial algebra algorithms for calculating terrain parameters from DEMs and solar radiation modelling in mountainous terrain, *Int. J. Geogr. Inf. Sci.*, *17*(1), 1–23, doi:10.1080/713811744.

Dowdeswell, J. A., and R. L. Collin (1990), Fast-flowing outlet glaciers on Svalbard ice caps, *Geology*, *18*(8), 778–781, doi:10.1130/0091-7613(1990)018<0778:FFOGOS>2.3.CO;2.

Dumanskaya, I. O. (2008), Applying the dynamical-statistical method of calculations of the ice redistribution in the White Sea for the solution

of climatic and prognostic problems, *Oceanology, Engl. Transl.*, *48*(1), 15–22, doi:10.1134/S0001437008010037.
Emelyanov, Y. N., and V. G. Konovalov (1975), Estimation of total ablation on Central Asian glaciers, *IAHS-AISH Publ.*, *104*, 99–105.
Førland, E. J., and I. Hanssen-Bauer (2003), Past and future climate variations in the Norwegian Arctic: Overview and novel analysis, *Polar Res.*, *22*(2), 113–124, doi:10.1111/j.1751-8369.2003.tb00102.x.
Førland, E. J., I. Hanssen-Bauer, and P. Ø. Nordli (1997), Climate statistics and long term series of temperatures and precipitation at Svalbard and Jan Mayen, *DNMI Rep. 21-97*, Det Norske Meteorologisk Institutt, Oslo.
Francis, J. A., W. Chan, D. J. Leathers, J. R. Miller, and D. E. Veron (2009), Winter Northern Hemisphere weather patterns remember summer Arctic sea-ice extent, *Geophys. Res. Lett.*, *36*, L07503, doi:10.1029/2009GL037274.
Goodison, B. E., H. L. Ferguson, and G. A. McKay (1981), Measurement and data analysis, in *Handbook of Snow*, edited by D. M. Gray and D. H. Male, pp. 191–274, Pergamon, Toronto.
Greuell, W., and J. Oerlemans (2005), Validation of AVHRR- and MODIS-derived albedos of snow and ice surfaces by means of helicopter measurements, *J. Glaciol.*, *51*(172), 37–48, doi:10.3189/172756505781829575.
Hagen, J. O., K. Melvold, F. Pinglot, and J. A. Dowdeswell (2003), On the net mass balance of the glaciers and ice caps in Svalbard, Norwegian Arctic, *Arct. Antarct. Alp. Res.*, *35*(2), 264–270, doi:10.1657/1523-0430(2003)035[0264:OTNMBO]2.0.CO;2.
Hall, D. K., and G. A. Riggs (2007), Accuracy assessment of the MODIS snow products, *Hydrol. Processes*, *21*(12), 1534–1547, doi:10.1002/hyp.6715.
Hall, D. K., G. A. Riggs, V. V. Salomonson, N. E. DiGirolamo, and K. J. Bayr (2002), MODIS snow-cover products, *Remote Sens. Environ.*, *83*(1–2), 181–194, doi:10.1016/S0034-4257(02)00095-0.
Hanssen-Bauer, I., and E. J. Førland (1998), Long-term trends in precipitation and temperature in the Norwegian Arctic: Can they be explained by changes in atmospheric circulation patterns?, *Clim. Res.*, *10*(2), 143–153, doi:10.3354/cr010143.
Hock, R. (2003), Temperature index melt modelling in mountain areas, *J. Hydrol.*, *282*(1–4), 104–115, doi:10.1016/S0022-1694(03)00257-9.
Huth, R. (1999), Statistical downscaling in central Europe: Evaluation of methods and potential predictors, *Clim. Res.*, *13*, 91–101, doi:10.3354/cr013091.
Huth, R., J. Kyselý, and M. Dubrovský (2001), Time structure of observed, GCM-simulated, downscaled, and stochastically generated daily temperature series, *J. Clim.*, *14*(20), 4047–4061, doi:10.1175/1520-0442(2001)014<4047:TSOOGS>2.0.CO;2.
Iqbal, M. (1983), *An Introduction to Solar Radiation*, Academic, New York.
Kääb, A. (2008), Glacier volume changes using ASTER satellite stereo and ICESat GLAS laser altimetry. A test study on Edgeøya, eastern Svalbard, *IEEE Trans. Geosci. Remote Sens.*, *46*(10), 2823–2830, doi:10.1109/TGRS.2008.2000627.
Karl, T. R., W. C. Wang, M. E. Schlesinger, R. W. Knight, and D. Portman (1990), A method of relating general circulation model simulated climate to observed local climate. Part I: Seasonal statistics, *J. Clim.*, *3*(10), 1053–1079, doi:10.1175/1520-0442(1990)003<1053:AMORGC>2.0.CO;2.
Kaser, G., J. G. Cogley, M. B. Dyurgerov, M. F. Meier, and A. Ohmura (2006), Mass balance of glaciers and ice caps: Consensus estimates for 1961–2004, *Geophys. Res. Lett.*, *33*, L19501, doi:10.1029/2006GL027511.
Koenigk, T., U. Mikolajewicz, J. H. Jungclaus, and A. Kroll (2009), Sea ice in the Barents Sea: Seasonal to interannual variability and climate feedbacks in a global coupled model, *Clim. Dyn.*, *32*, 1119–1138, doi:10.1007/s00382-008-0450-2.
Kohler, J., T. D. James, T. Murray, C. Nuth, O. Brandt, N. E. Barrand, H. F. Aas, and A. Luckman (2007), Acceleration in thinning rate on western Svalbard glaciers, *Geophys. Res. Lett.*, *34*, L18502, doi:10.1029/2007GL030681.
Kondratyev, K. Y. (1969), *Radiation in the Atmosphere*, Academic, San Diego, Calif.
Linke, F. (1961), Die Sonnenstrahlung und ihre Schwächung in der Atmosphäre, in *Handbuch Geophysik*, vol. 8, edited by F. Linke and F. Möller, pp. 239–338, Borntraeger, Berlin.
Meier, M. F., et al. (2007), Glaciers dominate eustatic sea-level rise in the 21st century, *Science*, *317*, 1064–1067, doi:10.1126/science.1143906.
Moholdt, G., J. O. Hagen, T. Eiken, and T. V. Schuler (2010a), Geometric changes and mass balance of the Austfonna ice cap, Svalbard, *Cryosphere*, *4*(1), 21–34, doi:10.5194/tc-4-21-2010.
Moholdt, G., C. Nuth, J. O. Hagen, and J. Kohler (2010b), Recent elevation changes of Svalbard glaciers derived from ICESat laser altimetry, *Remote Sens. Environ.*, *114*(11), 2756–2767, doi:10.1016/j.rse.2010.06.008.
Mölg, T., C. Georges, and G. Kaser (2003), The contribution of increased incoming shortwave radiation to the retreat of the Rwenzori Glaciers, East Africa, during the 20th century, *Int. J. Climatol.*, *23*(3), 291–303, doi:10.1002/joc.877.
Möller, M., and C. Schneider (2010), Calibration of glacier volume-area relations from surface extent fluctuations and application to future glacier change, *J. Glaciol.*, *56*(195), 33–40, doi:10.3189/002214310791190866.
Möller, M., C. Schneider, and R. Kilian (2007), Glacier change and climate forcing in recent decades at Gran Campo Nevado, southernmost Patagonia, *Ann. Glaciol.*, *46*, 136–144, doi:10.3189/172756407782871530.
Möller, M., R. Möller, É. Beaudon, O.-P. Mattila, R. Finkelnburg, M. Braun, B. Luks, U. Jonsell, D. Scherer, and C. Schneider (2011), Snowpack characteristics of Vestfonna and De Geerfonna (Nordaustlandet, Svalbard)–A spatiotemporal analysis based on multiyear snow pit data, *Geogr. Ann.*, in press.
Moritz, R. E., C. M. Bitz, and E. J. Steig (2002), Dynamics of recent climate change in the Arctic, *Science*, *297*, 1497–1502, doi:10.1126/science.1076522.
Nuth, C., G. Moholdt, J. Kohler, J. O. Hagen, and A. Kääb (2010), Svalbard glacier elevation changes and contribution to sea level rise, *J. Geophys. Res.*, *115*, F01008, doi:10.1029/2008JF001223.
Ohmura, A. (2001), Physical basis for the temperature-based melt-index method, *J. Appl. Meteorol.*, *40*(4), 753–761, doi:10.1175/1520-0450(2001)040<0753:PBFTTB>2.0.CO;2.
Ørbæk, J. B., V. Hisdal, and L. E. Svaasand (1999), Radiation climate variability in Svalbard: Surface and satellite observations, *Polar Res.*, *18*(2), 127–134, doi:10.1111/j.1751-8369.1999.tb00284.x.
Palosuo, E. (1987), Ice layers and superimposition of ice on the summit and slope of Vestfonna, Svalbard, *Geogr. Ann. Ser. A*, *69*(2), 289–296, doi:10.2307/521189.
Paterson, W. S. B. (1994), *The Physics of Glaciers*, Elsevier, Oxford, U. K.
Pellicciotti, F., B. Brock, U. Strasser, P. Burlando, M. Funk, and J. Corripio (2005), An enhanced temperature-index glacier melt model including the shortwave radiation balance: Development and testing for Haut Glacier d'Arolla, Switzerland, *J. Glaciol.*, *51*(175), 573–587, doi:10.3189/172756505781829124.
Przybylak, R. (2000), Temporal and spatial variation of surface air temperature over the period of instrumental observations in the Arctic, *Int. J. Climatol.*, *20*(6), 587–614, doi:10.1002/(SICI)1097-0088(200005)20:6<587::AID-JOC480>3.0.CO;2-H.
Przybylak, R. (2007), Recent air temperature changes in the Arctic, *Ann. Glaciol.*, *46*, 316–324, doi:10.3189/172756407782871666.
Raper, S. C. B., and R. J. Braithwaite (2006), Low sea level rise projections from mountain glaciers and ice caps under global warming, *Nature*, *439*, 311–313, doi:10.1038/nature04448.
Rasmussen, L. A., and J. Kohler (2007), Mass balance of three Svalbard glaciers reconstructed back to 1948, *Polar Res.*, *26*, 168–174, doi:10.1111/j.1751-8369.2007.00023.x.
Reeh, N. (1991), Parameterization of melt rate and surface temperature on the Greenland ice sheet, *Polarforschung*, *59*(3), 113–128.
Rigor, I. G., R. L. Colony, and S. Martin (2000), Variations in surface air temperature observations in the Arctic, 1979–97, *J. Clim.*, *13*(5), 896–914, doi:10.1175/1520-0442(2000)013<0896:VISATO>2.0.CO;2.
Rinke, A., and K. Dethloff (2008), Simulated circum-Arctic climate changes by the end of the 21st century, *Global Planet. Change*, *62*(1–2), 173–186, doi:10.1016/j.gloplacha.2008.01.004.
Rogers, A. N., D. H. Bromwich, E. N. Sinclair, and R. I. Cullather (2001), The atmospheric hydrologic cycle over the Arctic Basin from reanalysis. Part II: Interannual variability, *J. Clim.*, *14*(11), 2414–2429, doi:10.1175/1520-0442(2001)014<2414:TAHCOT>2.0.CO;2.
Schuler, T. V., E. Loe, A. Taurisano, T. Eiken, J. O. Hagen, and J. Kohler (2007), Calibrating a surface mass-balance model for Austfonna ice cap, Svalbard, *Ann. Glaciol.*, *46*, 241–248, doi:10.3189/172756407782871783.
Schüttemeyer, D., C. Schillings, A. F. Moene, and H. A. R. de Bruin (2007), Satellite-Based Actual Evapotranspiration over Drying Semiarid Terrain in West Africa, *J. Appl. Meteorol. Climatol.*, *46*(1), 97–111, doi:10.1175/JAM2444.1.
Stroeve, J. C., J. E. Box, and T. Haran (2006a), Evaluation of the MODIS (MOD10A1) daily snow albedo product over the Greenland ice sheet, *Remote Sens. Environ.*, *105*(2), 155–171, doi:10.1016/j.rse.2006.06.009.
Stroeve, J., T. Markus, W. N. Meier, and J. Miller (2006b), Recent changes in the Arctic melt season, *Ann. Glaciol.*, *44*, 367–374, doi:10.3189/172756406781811583.
Strozzi, T., A. Kouraev, A. Wiesmann, U. Wegmüller, A. Sharov, and C. Werner (2008), Estimation of Arctic glacier motion with satellite L-band SAR data, *Remote Sens. Environ.*, *112*(3), 636–645, doi:10.1016/j.rse.2007.06.007.
Taurisano, A., T. V. Schuler, J. O. Hagen, T. Eiken, E. Loe, K. Melvold, and J. Kohler (2007), The distribution of snow accumulation across the Austfonna ice cap, Svalbard: Direct measurements and modelling, *Polar Res.*, *26*(1), 7–13, doi:10.1111/j.1751-8369.2007.00004.x.

Uppala, S. M., et al. (2005), The ERA-40 re-analysis, *Q. J. R. Meteorol. Soc.*, *131*, 2961–3012, doi:10.1256/qj.04.176.

von Storch, H. (1999), On the use of "inflation" in statistical downscaling, *J. Clim.*, *12*(12), 3505–3506, doi:10.1175/1520-0442(1999)012<3505:OTUOII>2.0.CO;2.

Wald, L., et al. (2002), SoDa: A project for the integration and exploitation of networked solar radiation databases, in *Environmental Communication in the Information Society*, edited by W. Pillmann and K. Tochtermann, pp. 713–720, Int. Soc. for Environ. Prot., Vienna.

Wang, X., and C. S. Zender (2010), MODIS snow albedo bias at high solar zenith angles relative to theory and to in situ observations in Greenland, *Remote Sens. Environ.*, *114*(3), 563–575, doi:10.1016/j.rse.2009.10.014.

Wang, X., H. Xie, and T. Liang (2008), Evaluation of MODIS snow cover and cloud mask and its application in Northern Xinjiang, China, *Remote Sens. Environ.*, *112*(4), 1497–1513, doi:10.1016/j.rse.2007.05.016.

Wu, X., M. B. Heflin, H. Schotman, B. L. A. Vermeersen, D. Dong, R. S. Gross, E. R. Ivins, A. W. Moore, and S. E. Owen (2010), Simultaneous estimation of global present-day water transport and glacial isostatic adjustment, *Nat. Geosci.*, *3*(9), 642–646, doi:10.1038/ngeo938.

Yamamoto, K., Y. Tachibana, M. Honda, and J. Ukita (2006), Intra-seasonal relationship between the Northern Hemisphere sea ice variability and the North Atlantic Oscillation, *Geophys. Res. Lett.*, *33*, L14711, doi:10.1029/2006GL026286.

M. Braun and R. Hock, Geophysical Institute, University of Alaska Fairbanks, 903 Koyukuk Dr., Fairbanks, AK 99775, USA.

R. Finkelnburg and D. Scherer, Department of Ecology, Technische Universität Berlin, Rothenburgstr. 12, D-12165 Berlin, Germany.

U. Jonsell, Swedish Polar Research Secretariat, PO Box 50003, SE-104 05 Stockholm, Sweden.

M. Möller and C. Schneider, Department of Geography, RWTH Aachen University, D-52062 Aachen, Germany. (marco.moeller@geo.rwth-aachen.de)

V. A. Pohjola, Department of Earth Sciences, Uppsala University, Villavägen 16, SE-752 36, Uppsala, Sweden.

Appendix C: Seasonality and variability of the climate in Svalbard as resolved by the European Arctic Reanalysis (EAR) for the glacier mass-balance years 2001 to 2011

Finkelnburg, R., Maussion, F. and Scherer, D., 2013. Seasonality and variability of the climate in Svalbard as resolved by the European Arctic Reanalysis (EAR) for the glacier mass-balance years 2001 to 2011. To be Submitted to the *Journal of Climate*.

Status: Manuscript prepared for submission

Own contribution:

- Preparation, conduction and leading of field campaigns
- Design and implementation of measurement concepts
- Acquisition of field observational data and from online data bases
- Software and hardware design and implementation of the reanalysis framework
- Production of the EAR data sets
- Processing, analysis and interpretation of data from field observation, AWS, NPI, UNIS, remote sensing systems, global tropospheric analyses and the EAR
- Literature review on atmospheric modeling and observational studies
- Preparation of the manuscript including all figures and tables
- Revision of the manuscript after comments and improvements of the co-authors

Seasonality and variability of the climate in Svalbard as resolved by the European Arctic Reanalysis (EAR) for the glacier mass-balance years 2001 to 2011

R. Finkelnburg[1], F. Maussion[1] and D. Scherer[1]

[1]Department of Ecology, Technische Universität Berlin, Berlin, Germany.

Abstract. The European Arctic Reanalysis (EAR) was carried out using the numerical weather prediction model for polar conditions (Polar WRF) to provide an atmospheric data set with focus on Svalbard and selected regions, to overcome the limitations arising from data scarcity in the Arctic. Data from NCEP Final Analyses were reprocessed together with high resolution geographical fields and remotely sensed sea surface temperature and fractional sea ice cover to obtain data for 30, 10 and 2 km grids for the glacier mass-balance years 2001 to 2011. We analyzed air temperature, precipitation and wind with respect to seasonality and variability. Generally, seasonal courses of the climate elements are consistent with observations from other studies. The EAR shows mean cold biases for air temperature at coastal locations, while no biases were detected at inland locations that are reasonably represented by the digital elevation models used in the EAR. No detectable bias was found for precipitation. Wind speed is slightly higher in the EAR than field observations. Variability of air temperature and wind speed is higher during winter than during other seasons. We found that air-temperature anomalies correlate with precipitation anomalies and are stronger over sea ice. Four winter seasons were analyzed with respect to the driving processes. The results indicate that cyclone activity is a key factor of climate variability in the European Arctic during winter. The EAR has shown to be a suitable data set for studying climate at monthly to annual time scales.

1 Introduction

Our understanding of the Arctic climate system seriously suffers from a lack of data from field observations compared to other regions (e.g. New et al., 2002; Førland and Hanssen-Bauer, 2003; Kristjánsson et al., 2011). Thus, remote sensing (e.g. Frei et al., 2012), general circulation models (GCMs) (e.g. Shaffrey et al., 2009), global operational analyses (e.g. Kanamitsu, 1989; Kalnay et al., 1990; Kanamitsu et al., 1991) and reanalyses (e.g. Kalnay et al., 1996; Uppala et al., 2005; Onogi et al., 2007; Dee et al., 2011) became data sources for studies of Arctic weather and climate (e.g. Bitz et al., 2002; Eneroth et al., 2003; Serreze et al., 2011). However, data sets of large-scale climate dynamics are of coarse resolution. Reprocessing these global data sets using limited area models (LAM) links the large-scale controls to small-scale processes. Regional reanalyses like the U.S. National Centers for Environmental Prediction (NCEP) North American Regional Reanalysis (NARR) or the Arctic System Reanalysis (ASR) with horizontal resolutions of about 30 km are adequate data sets for process analyses on the meso-beta scale (Orlanski, 1975, Mesinger et al., 2006; Wilson et al., 2012). Nevertheless, other studies (e.g. Orlanski, 1975; Sandvik and Furevik, 2002; Barstad and Adakudlu, 2011; Kilpelainen et al., 2011; McInnes et al., 2011; Wagner et al., 2011) indicate that horizontal resolutions of about 2 km are necessary to solve the whole mesoscale and completely downscale synoptic signals to the local scale. A dynamical downscaling at such high resolutions generates data sets of adequate spatio-temporal resolution for energy and mass balance

modelling (e.g. Mölg and Kaser, 2011) and provides the ability to physically link energy and mass exchange at the glacier-atmosphere interface to large-scale climate dynamics. Furthermore, such methods can give a better understanding of cascaded process chains.

We present the European Arctic Reanalysis (EAR) that has been carried out to provide a data set especially for the glaciological community investigating regions located in Svalbard. A state-of-the-art numerical weather prediction model for polar conditions, Polar WRF (Hines and Bromwich, 2008), was used to reprocess meteorological data together with geographical fields and remote sensing data of sea surface temperature and fractional sea ice cover. The resulting regional reanalysis data comprise horizontal resolutions of 30 km, 10 km and 2 km of the glacier mass-balance years 2001 to 2011.

We hypothesise that the EAR can give better insight into the spatial variability of processes and therefore improve our understanding of how large-scale climate change can affect glacier behaviour locally. In this study we want to examine the nature of the mesoscale processes in Svalbard and Nordaustlandet rather than to quantitatively link our results to a glacier energy and mass balance model (e.g. Ettema et al., 2010; Claremar et al., 2012; van Pelt et al., 2012). We want to illustrate the potential of the EAR to enhance our understanding of climate-glacier relations in the mesoscale process space. Therefore we concentrate our analysis on interseasonal and interannual variability of climate elements like air temperature, precipitation and wind. For simplification we will use the terms air temperature for the 2 m air temperature derived from EAR, precipitation for the sum of all surface precipitation variables derived from EAR and wind for the resulting vector obtained from the sum of 10 m u and v vectors derived from EAR. Furthermore, we mean monthly mean values if temporal resolution is not further specified.

A description of the EAR is presented in Section 2, followed by a comparison of the EAR with field observations in Section 3, where we only analyzed the variables which are central to this study. In Section 4 we show how the EAR resolves seasonality and variability of air temperature, precipitation and wind using monthly aggregated values for the time period from 1st September 2000 to 31st August 2011. In addition, we show for a set of cases how anomalous climate conditions are developing in the study region. The results are then discussed in Section 5, and conclusions are drawn in Section 6.

2 The European Arctic Reanalysis (EAR)

This regional reanalysis was made using the Polar WRF model version 3.1.1 (Hines and Bromwich, 2008). Three two-way nesting levels of 30 km, 10 km and 2 km horizontal resolution are defined with a polar stereographic projection. The first-level EAR domain called the European Arctic domain (99 x 99 grid points, 30 km) is centered at 80.0 °N, 20.0 °E (see Fig. 1). The second-level Svalbard domain (49 x 52 grid points, 10 km) covers the archipelago of Svalbard. Five third-level domains of 2 km horizontal resolution cover areas of Svalbard of special interest. These are areas where we have access to data of field observations like automatic weather station (AWS) observations or synoptic observations by the Norwegian Meteorological Institute, i.e. Nordaustlandet domain (106 x 86 grid points, 2 km), North-West Spitsbergen domain (46 x 66 grid points, 2 km), Longyearbyen domain (26 x 26 grid points, 2 km), Hornsund domain (46 x 31 grid points, 2 km) and Hopen domain (21 x 26 grid points, 2 km) (see Fig. 2 and 3). Besides the identification of the regions Fig. 1, 2 and 3 show the topography of each domain.

All domains are resolved by 28 vertical levels with the top set to 50 hPa. The first nine levels approximately represent the bottom 1500 m of the boundary layer. Static geographical fields are initialized by the USGS geographical data sets. We set the surface parameterization options to use time-varying sea surface

temperature and fractional sea ice cover. The Runge-Kutta time step is set to 120 s for the European Arctic domain, to 40 s for the Svalbard domain and to 8 s for the third-level domains.

A cascading approach was used for the reanalysis of the different domain levels. In a first step all three domain levels were processed using a two-way telescope nesting obtaining reanalysis data for the third-level domains. In a second step the reanalysis of the Svalbard domain was processed by discarding all third-level domains from the recalculation to obtain unaffected results, i.e. we found out the two-way nesting produces artifacts in the region of nesting in the data of the parent domain (Maussion et al., 2011). In a last step the reanalysis of the European Arctic domain was done without any nesting of other domains.

The reanalysis was initialized by data from the Operational Model Global Tropospheric Analyses (Final Analyses, FNL; data set ds083.2), published by the CISL Data Support Section at the U.S. National Center for Atmospheric Research, Boulder, CO; performed by the U.S. National Centers for Environmental Prediction (NCEP)) (1°, 6 h) and NCEP's Real-time, global, sea surface temperature (RTG_SST) analysis (0.5°, daily). Additionally we used daily sea ice concentrations from Advanced Microwave Scanning Radiometer for Earth Observing System (AMSR-E) observations at 12.5 km horizontal resolution. Since data of daily sea surface temperature are not available before 12.02.2001 and daily sea ice concentration are not available before 20.06.2002 we did the reanalysis before these dates without the respective data set. We filled missing values in the sea ice dataset with values of the nearest valid neighbor and generated 6 h data sets from the daily data of SST and sea ice by linear interpolation. Thus, the reanalysis was driven providing data of lateral boundary conditions at 6 h intervals. Individual simulation runs comprising 36 h were produced by daily reinitialization (simulation started at 1200 UTC daily). A continuous time series comprising a period of 01.09.2000 to 31.08.2011 for each domain analog to the strategy of Maussion et al. (2011) was produced by assembling individual simulation runs comprising 36 h each, whereof the first 12 h were discarded to avoid spin-up effects and the next 24 h were stored. Output was written at 3-hourly resolution for the European Arctic domain and hourly for all other domains.

The choice for the physical parameterization schemes as summarized in Table 1 is based on the studies of Hines and Bromwich (2008), Hines et al. (2011) and diverse sensitivity studies.

3 Comparison with field observations

3.1 Methods

The results are compared on a monthly basis against field observation data to assess the accuracy of EAR. Discrepancies of EAR to observations are expected to be smaller inland where the surface is more homogenous and the climate gradients less steep than in coastal areas. Therefore, we distinguish between coastal and inland stations in this analysis (see Table 2 and 3). For coastal stations, it was checked for the model land surface category, and the closest non water-covered grid point was selected. The elevation bias is defined as positive if the elevation of the reanalysis grid point is above the station's elevation. If the resulting elevation bias exceeds 10 % of the horizontal model resolution, the station was discarded from the analysis. No further adjustments (e.g. bias correction for 2 m temperature or 10 m wind) were applied, since the bias value is rather the result of complex interactions of different influences (e.g. different measurement heights and stability of stratification) than a simple offset. Furthermore, we want to analyse the general performance of EAR including all error sources.
We applied a strict data filtering, i.e. only monthly means with 100 % valid data are considered, to obtain most complete

observational data for the analysis. Two different data sources were employed, i.e. synoptic observations of the Norwegian Meteorological Institute provided by the National Climate Data Center (NCDC) and field observations of AWS measurements in the region of Vestfonna (see Fig. 2). No data on wind direction were available in the NCDC data sets and no precipitation was measured by the AWS located in the region of Vestfonna.
The Pearson's correlation coefficient, mean bias and bias corrected root mean square deviation (rmsd) are calculated for the assessment.

3.2 Field observations

3.2.1 Coastal regions

Synoptic observations of the Norwegian Meteorological Institute were downloaded from the NCDC database (ftp://ftp.ncdc.noaa.gov/pub/data/gsod/) comprising daily means of air temperature, precipitation and wind speed measured for the period 2000 to 2011 at Ny-Ålesund (WMO-Nr. 010070, 11.9333°E 78.9167°N), Svalbard-Lufthavn, Longyearbyen (WMO-Nr. 010080, 15.4667°E 78.2500°N), Hornsund (WMO-Nr. 010030, 15.5000°E 77.0000°N) and Hopen (WMO-Nr. 010620, 25.0133°E 76.5097°N) (see Fig. 2). An additional data set provided by The University Center in Svalbard (UNIS) of AWS measurements at the coast line of Rijpfjorden at Nordaustlandet (RF-AWS, Fig. 3) was used. At this station no precipitation was measured. Further information and data can be found on the UNIS website (http://met.unis.no).

3.2.2 Inland regions

Monthly means of air temperature, wind speed and wind direction were calculated from field observations of AWS located in the region of Vestfonna (see Fig. 3). The AWS network had no precipitation sensors installed. A detailed description of the different locations and time series used in this study is given in Table 3. We discarded data of VF-AWS335 from the analysis of the 2 km resolution results due to a very large elevation bias compared to the horizontal resolution (see Table 2).

3.3 Air temperature

The very high correlations indicate that the variability of air temperature is well captured by EAR (see Fig. 4 and Table 4). All correlations were significant on a 0.01 significance level. Correlations for inland regions show slightly better performance than for coastal regions. The mean bias at coastal sites exceeds the range of the rmsd, i.e. the systematic error exceeds the variance of error. In contrast the mean bias at inland sites is always within the range of the rmsd. Results of higher resolution reanalysis indicate generally smaller deviation since both mean bias and rmsd values are smaller.
The data population used for coastal regions differs from the data population used for inland regions due to general availability and covered periods of field observations (see Fig. 4 and Table 4), i.e. 264 pairs (eleven years) of data at coastal sites and 67 pairs (five years) of data at inland sites. However, this cannot cause the range of the mentioned differences in statistical measures found at coastal sites and inland sites (e.g. mean bias). We rather assume the elevation bias (see Table 2) to be the main source of error besides the fact that surface types and reanalysis physics were optimized for glacial sites and all inland AWS are located on glaciers. Nevertheless, a general under-estimation of the near-surface air temperature (i.e. cold bias) is mentioned for polar regions as result of an unsolved problem in the land surface model used in Polar WRF (e.g. Wilson et al., 2012). This problem is also observable in this study while the cold bias is generally larger during summer and at lower altitudes.

3.4 Precipitation

Field observations of precipitation were only available at coastal sites, i.e. synoptic observations of the Norwegian Meteorological Institute. Thus, the vertical distribution of field observational data is very small due to the lack

of inland observations. Our strict data filtering strongly reduced the precipitation data since only monthly means consisting of 100 % valid data were considered in this study. We applied a correction factor of 1.6 to the measurement data to take account of snow undercatch as suggested by Førland and Hanssen-Bauer (2003). The results of our analysis are presented in Fig. 5 and Table 5. Herein field observations and reanalysis show very good correlations in consideration of the very high spatio-temporal variability of precipitation. All correlations were significant on a 0.01 significance level. Generally, mean biases are very small. The variance of deviation exceeds the systematic error since the rmsd value exceeds the mean bias. We could only find slight improvement of reanalysis results using higher horizontal resolutions. The fact that 57 % of the variance of precipitation is already captured at a horizontal resolution of 30 km indicates that advective precipitation processes dominate in the region of Svalbard. This is consistent with observations of other studies (e.g. Wada and Konoshi, 1998) that precipitating clouds are associated with deeply occluded fronts and extratropical cyclones in the study region. We will discuss general precipitation distribution in respect to findings of other studies in Svalbard in Section 5.

3.5 Wind

All correlations except for inland regions at a 30 km resolution were significant on a 0.01 significance level (see Fig. 6 and Table 6). Mean bias values were always smaller than rmsd values indicating the variance of deviation exceeds the systematic error. A strong improvement of the captured wind speed variability with higher resolutions is observable due to better representation of orography. Very high correlation (r^2 = 0.84) was only found for inland regions at 2 km resolution. All other correlations showed low to medium performance. Results at inland regions again showed generally better accordance with field observations than results at coastal regions. This further indicates that the mismatch of surface types and/or reanalysis physics is greater for coastal regions. Reanalysis results of 2 km resolution showed a prominent improvement compared to results of 10 km and 30 km resolution since reanalyzing at the lower limit of meso-gamma scale enables the closure of complex terrain flows.

We produced monthly vector means of field observations and compared the data to 2 km EAR results in Fig. 7. The wind rose plots show that low and high wind speeds as well as main wind directions are well represented by the EAR. This suggests that surface friction and terrain is adequately accounted for in the reanalysis using 2 km horizontal resolution, especially at glacial sites.

3.6 Further variables

Correlation analyses (not shown in this paper) between the EAR and air pressure, specific humidity, down-welling short- and long-wave radiation from field observations are statistically significant (p = 0.01), showing r^2 values greater than 0.97. The results for specific humidity are analog to those for air temperature. Highest r^2 values are reached for air pressure at coastal stations independent of the horizontal resolution, while largest mean bias values were found for the same variable due to elevation biases. Down-welling short-wave radiation is overestimated while down-welling long-wave radiation is underestimated by about 10 W m^{-2} each, and thus total down-welling radiation does not show a mean bias.

4 Seasonality and climate variability

4.1 Annual means and seasonal courses

4.1.1 Air temperature

Air temperature shows a very stable spatial distribution strongly formed by orography. However, the absolute range of air temperature within the orographic pattern varies by season

(see Fig. 8, 9 and 10). Fig. 8 shows eleven-year mean values of air temperature and identifies Nordaustlandet as coldest region of Svalbard (see also Fig. 14 and Table 7). A pronounced south-west to north-east gradient is observable. The warmest regions with an annual mean air temperature of about -0.5 °C are located in the south-west and the coldest regions with an annual mean air temperature of about -12.8 °C are located in the north-east (see Fig. 8). Thereby the range between highest and lowest air temperature within the Svalbard domain is about 12.3 K and about 5.5 K within the Nordaustlandet domain. The Nordaustlandet domain shows nearly the same minimum air temperature of -12.5 °C as found in the Svalbard domain whereas the maximum air temperature with about -7.0 °C differs. The air-temperature ranges are smaller on land areas than over sea areas as indicated by Table 7 and Fig. 10.

Considering the seasonality of air temperature, DJF is the coldest and JJA the warmest season. The range of air temperatures is the largest in DJF and the smallest in JJA (see Fig. 9, 10 and 14 and Table 7). The intermediate SON season shows very similar values and spatial distribution compared to the annual mean air-temperature fields in Fig. 8. The air-temperature range of SON and MAM within the Svalbard domain is nearly identical but smaller than the range of DJF and larger than JJA (see Fig. 10 and Table 7), and air temperatures in MAM are generally lower than in SON. Considering the Nordaustlandet domain MAM is also colder than SON but shows a range more similar to JJA. The SON range is in the dimension of DJF. Air temperatures at coastal land areas partly exceed air temperatures over neighboring sea areas in JJA (see Fig. 10). During the other seasons air temperatures at sea areas especially in the south-west exceed air temperatures over land areas due to warm currents from the Atlantic Ocean (e.g. Walczowski and Piechura, 2011).

4.1.2 Precipitation

A distinct orographic dependency of precipitation is observable in Fig. 8 and 11 whereas the absolute amount decreases with latitude and maxima tend to be located eastwards. Fig. 8 shows eleven-year mean values of accumulated annual precipitation and identifies south Spitsbergen as wettest region of Svalbard with the highest values of about 1139 mm/year (see Fig. 14 and Table 8) since moisture is transported into the region of Svalbard mainly from the south-west (e.g. Sorteberg and Walsh, 2008). Precipitation over sea areas is small compared to land areas due to the lack of orography. Within the Nordaustlandet domain the eleven-year mean values of accumulated annual precipitation reach a maximum of about 844 mm/year (see Fig. 14 and Table 8). Mean values of the eleven-year mean values of accumulated annual precipitation of all land based grid points reach 602 mm/year within the Svalbard domain and 545 mm/year within the Nordaustlandet domain. This is due to large dry regions in the center and north-west of Spitsbergen. Comparing values of the Nordaustlandet domain (2 km grid) to values in the Svalbard domain (10 km grid) in the overlapping region (not shown) we found that mean precipitation is 13 mm/year (approx. 2 %) higher in the higher-resolution data set. The difference in the maxima of the eleven-year mean values of accumulated annual precipitation between the Nordaustlandet domain and the Svalbard domain was even higher; 70 mm/year (approx. 8 %) higher maxima are present in the high-resolution data set.

SON is the wettest and JJA the driest season. A distinct decrease of precipitation is observable between SON and JJA. In the region of Nordaustlandet no significant difference were found between JJA and MAM (see Fig. 11, Fig. 14 and Table 8). The seasonal decrease in precipitation is more pronounced in the northern parts of Svalbard, i.e. accumulated precipitation in MAM exceeds still 3 mm/d in the south-east of Spitsbergen. Mean and

maximum values derived for the Svalbard domain were always larger than for the Nordaustlandet domain, i.e. Svalbard is in average wetter than the Nordaustlandet region.

4.1.3 Wind

The eleven-year mean wind field shows a strong south-west component on meso-beta scale with wind speeds of about 6 m/s (see Fig. 8). Over sea areas the wind field is generally very uniform due to the lack of disturbing land masses. In valleys and areas surrounded by high mountains or ice caps wind speed is lower due to sheltering effects and reaches values of 3-4 m/s. In contrast highest wind speeds of about 8 m/s are reached at high elevations (ridges). Especially areas at the lee side (south-west) of the ridges in respect of the subordinated wind direction (south-west) show the highest wind speeds. This dislocation is probably produced by the combination of frequent katabatic winds adding to a channeling effect at the ridges caused by low Arctic boundary layer heights. Prevalent katabatic wind fields are observable especially at large ice caps like Vestfonna or Austfonna on Nordaustlandet. At slopes directed windward (north-east) to the mean wind direction (south-west) katabatic winds counteract and windward slopes show weaker winds than leeward slopes. Further, analyses of the vertical wind field (not shown) revealed strong down winds (often exceed 0.4 m/s in the eleven-year mean) especially over tops of mountains and ice caps having strong katabatic wind systems. In contrast to that the surrounding sheltered areas which showed the low wind speeds in Fig. 8 experience pronounced updraft winds. The up and down wind columns reach heights of about 1500 m above ground while the horizontal extend between the opposed columns is in the scale of 50 km. This is consistent with observations of Sandvik and Furevik (2002) or Barstad and Adakudlu (2011). They further documented a strong gap flow (Hinlopen jet) at the northern exit of the Hinlopen Strait as the result of the local wind systems and the mechanical disturbance of the subordinated wind field also observable in Fig. 8.

Fig. 12 shows that DJF is the windiest season at most places reaching values of 10 m/s and JJA is the calmest season. Synoptic wind fields tend to have a more pronounced east-to-west direction component in seasons of higher wind speeds and a more pronounced north -to-south direction component in seasons of lower wind speed. This is probably due to the increased Coriolis effect (e.g. Skeie and Grønås, 2000). SON and MAM are intermediate seasons. Katabatic patterns are strongest in DJF, probably due to excessive radiative cooling, and weakest in JJA.

4.2 Seasonal and interannual anomalies

4.2.1 Air-temperautre anomalies

Fig. 13 shows that the standard deviation of annual mean air temperature is larger for lower altitudes and in the eastern parts of Svalbard. Largest standard deviation is found over sea areas in the east exceeding 3 K and lowest standard deviation at sea areas in the south-west or at the highest points of Spitsbergen. The same pattern is observable in the Nordaustlandet domain but the range of differences is lower. Land areas show a generally lower standard deviation than sea areas. This is due to strong year-to-year variability of sea ice cover and the West Spitsbergen Current. Considering only larger islands we see standard deviation is larger on Nordaustlandet, Barentsøya and Edgeøya than on Spitsbergen. A clear seasonality of standard deviation is observable for Nordaustlandet and whole Svalbard (see Fig. 14). Values of the Nordaustlandet domain are slightly larger. Largest differences are found in SON and DJF. In general the DJF season shows the largest standard deviation of about 4 to 5 K. JJA shows the lowest standard deviation of about 1 K. Standard deviations of SON and MAM are about 3 K.

4.2.2 Precipitation anomalies

Largest relative standard deviation of annual mean precipitation of about 37 % is found in the eastern parts on land with a prominent decrease from north to south (see Fig. 13) since cyclones from southern directions generate most of the precipitation variability (not shown). The spatial distribution of relative standard deviation of precipitation (Fig. 11) is not similar to the spatial distribution of precipitation (Fig. 8). E.g. Vestfonna and Austfonna in the Nordaustlandet domain show areas of same annual precipitation amount but the relative standard deviation of the north-eastern areas on Austfonna is nearly doubled compared to the other areas. Also areas of high precipitation amounts in the west and south of Spitsbergen and on Edgeøya show very little relative standard deviation. A clear seasonality of standard deviation of precipitation is observable for Nordaustlandet and whole Svalbard (see Fig. 14). Both regions show the same pattern with a maximum of about 1.0 mm/d in SON and DJF, values of about 0.8 mm/d in MAM and a minimum of about 0.6 mm/d in JJA. Values for the Nordaustlandet domain are slightly higher for SON whereas a distinct increase to 1.5 mm/d during November causes the main difference. Except SON and JJA, values for the whole Svalbard domain are slightly higher. In contrast to that the relative standard deviation is largest (smallest) in MAM (SON) indicating that the seasonal coefficient of variation of year-to-year variability is greatest (smallest) in MAM (SON).

4.2.3 Wind anomalies

Areas of higher relative standard deviations of about 16 % are mainly limited to areas of generally low wind speed in average (see Fig. 8, 12 and 13). These areas are orographically sheltered from the north-east which is the main wind direction and showed strong updraft winds. In contrast the relative standard deviation is lower at ridges where the highest wind speeds and strong down winds are present. A clear seasonality of standard deviation is observable in Fig. 14. Largest values of about 1.5 m/s are found in DJF in the Nordaustlandet domain. Lowest values for the Nordaustlandet domain of about 1.0 m/s are found in JJA. Values for SON are about 1.3 m/s and for MAM are about 1.4 m/s. The standard deviation of the Svalbard domain shows the same seasonal course but is approximately 0.2 m/s lower due to effects of coarser horizontal resolution discussed in Section 3. The seasonal course of standard deviation of wind speed is consistent with seasonal courses of cyclone activity in the region of Svalbard (e.g. Sorteberg and Walsh, 2008). Nevertheless, as well as found for precipitation the relative standard deviation of wind speed is largest (smallest) in MAM (SON) indicating that the seasonal coefficient of variation of year-to-year variability is greatest (smallest) in MAM (SON).

4.3 Examples of anomalies

In the following we will analyze four examples comprising extremes in precipitation and air temperature during seasons of the highest absolute variability, i.e. DJF. We picked two of the driest and two of the wettest winters of the eleven-year time series, i.e. 2003 and 2004 were cold and dry, 2005 and 2006 were warm and wet.

The frequency of cyclones reaching Svalbard over the North Atlantic cyclone track (e.g. Tsukernik et al., 2007) is higher during 2005 and 2006 compared to 2003 and 2004 while the frequency is lowest during 2003 (not shown). We will use the 850-300 hPa thickness (also termed relative topography) as an indicator for the movement of meso-beta scale convective elements following Corfidi et al. (1996) who showed that the motion of convective systems can be considered the sum of an advective component, given by the mean motion of the cells composing the system, and a propagation component, defined by the rate and location of new cell formation relative to existing cells. Furthermore, they showed the 850-300 hPa thickness is an indicator of the differences between the mean flow in the cloud layer and

the low-level jet. Shifts in seasonal mean 850-300 hPa thickness, sea level pressure and surface wind field between the examples are observable in Fig. 15. The thickness indicates that cyclones could hardly reach Svalbard in 2003 and 2004. Nevertheless, in 2004 eastward propagation south of Svalbard was possible. In 2005 and 2006 the thickness indicates strong northward cyclone propagation mainly transported over the Greenland Sea. The low sea level pressures switch from eastern locations in 2003 and 2004 to western locations in 2005 and 2006 in respect to Svalbard. Respectively, air masses are frequently transported to Svalbard from northern directions in 2003, north-eastern directions in 2004, south-eastern directions in 2005 and to southern directions in 2006, i.e. air masses were mainly transported over the Arctic Ocean in 2003, the Barents Sea and Arctic Ocean in 2004, the Norwegian and Barents Sea in 2005 and the Norwegian Sea in 2006.

These synoptic circulation patterns generate differences in the spatial distribution of air-temperature and precipitation anomalies as shown in Fig. 16 and 17. Colder and drier (wetter and warmer) conditions than normal are connected with a decreased (increased) impact of the North Atlantic cyclone track to the Arctic Ocean, i.e. air mass transport from northern directions is increased (decreased) in 2003 and 2004 (2005 and 2006). The anomalies are more pronounced over sea ice and land masses than over open water and are mostly limited to areas of about 500 – 700 km to the sea ice margin. Comparing this feature in 2003 and 2004 with 2005 and 2006 (see Fig. 16) cold anomalies show sharper boundaries. Especially in the south a clear gradient in the region of the sea ice margin is observable during cold anomalies in 2003 and 2004. This gradient is more diffuse during warm anomalies in 2005 and 2006. Fig. 18 indicates that the very strong gradients observed at the southern edge of cold anomalies are mainly produced by a positive sea ice anomaly covering the normally exposed warm sea surface. This is further backed by observable strong cold anomalies in SST fields in these regions (not shown). Nevertheless, great parts of cold and warm air-temperature anomalies are located further north where no anomalies in sea ice could be observed. In general areas of maximum anomalies in DJF 2003 to 2006 are mostly located to the sea ice region east of Svalbard while warm anomalies show the tendency to reach far north and cold anomalies show the distinct cut at the sea ice margin.

Strong precipitation gradients are observable at the ice margin in Fig. 17 whereas the region of positive (negative) air-temperature anomalies in Fig. 16 show more (less) precipitation than normal. Strong negative (positive) precipitation anomalies on Svalbard were experienced during 2003 and 2004 (2005 and 2006). During negative (positive) precipitation anomalies in the north (over sea ice) a positive (negative) precipitation anomaly in the south (over open water) is observable (see Fig. 17). However, distinct differences are also observable. The transport of air masses in 2003 and 2004 from the Atlantic Ocean was strongly suppressed (see Fig. 15). Large differences in precipitation over the Norwegian Sea are observable between these years. Compared to normal amounts, precipitation was reduced in the Norwegian Sea in 2003 and increased in 2004 (see Fig. 17). Similar differences in this sector can be found between 2005 and 2006. Precipitation was increased in the Norwegian Sea in 2005 and reduced in 2006 compared to normal amounts. Comparing 2003 and 2005 as well as 2004 and 2006 we observe opposite patterns in precipitation and wind field anomalies.

As indicated in Section 4.2.1 the air-temperature anomalies in the Svalbard domain in Fig. 19 are stronger over sea areas than over land areas showing an east-west gradient. Nevertheless, Svalbard is entirely within the area influenced by the anomalies. The years 2003 and 2004 show strong negative and 2005 and 2006 strong positive air-temperature anomalies in Svalbard. The wind field anomaly shows stronger eastern directions in 2003, southern directions in 2004, north-western directions in 2005 and north-eastern directions

in 2006. Precipitation anomaly distribution in Fig. 20 show more connection with wind field anomalies than the air-temperature anomalies in Fig. 19 do. Negative (positive) precipitation anomalies in 2003 (2005) are mainly limited to the eastern parts of Svalbard which are the regions of the highest precipitation amounts (see Fig. 8 and 11). The wind field anomalies show strong south-eastern (north-western) directions during 2003 (2005). Precipitation anomalies in 2004 and 2006 are shifted to the west compared to 2003 and 2005 while the wind field anomalies show south-western (north-eastern) directions during 2004 (2006). Therefore, positive (negative) precipitation anomalies seem to increase windward (leeward).

Summarizing these examples a positive (negative) precipitation anomaly on Svalbard correlates with a positive (negative) air-temperature anomaly (see Fig. 19 and 20). Positive (negative) precipitation and air-temperature anomalies are connected with increased (decreased) influence of the North Atlantic cyclone track (see Fig. 15). Averaging the sea level pressure results in central to western (eastern) positions of lows in respect to Svalbard for increased (decreased) influence of the North Atlantic cyclone track.

5 Discussion

A pronounced air-temperature gradient between south-west and north-east Svalbard was observed in the EAR data (see Fig. 8, 9 and 10). This is consistent with observations of other studies (e.g. Hisdal, 1976; Walczowski and Piechura, 2011) which discuss the interaction of warm Atlantic water (West Spitsbergen Current) and sea ice as origin of the strong air-temperature gradient in the region of Svalbard. Nevertheless, examples of air-temperature and precipitation anomalies show beside connections to sea ice and sea surface temperature also strong connections to the influence of advected air masses since Svalbard lies in the border zone of cold Arctic air from the Polar Basin and mild maritime air over the oceans towards the south.

Sorteberg and Walsh (2008) showed the major moisture transport and therefore precipitation in the region of Svalbard is strongly correlated with the cyclone activity of the North Atlantic cyclone track. They identified two different paths by a cluster analysis. One is taking course northward along the Greenland Sea strongly affecting Svalbard and terminates in the Arctic Ocean and the other is taking course eastward along the Barents Sea and terminates in Siberia. This is consistent with patterns of 850-300 hPa thickness and precipitation found in Fig. 15 and 17. First analyses suppose the cyclone activity was generally low in 2003 resulting in strong negative precipitation anomalies all over the European Arctic. In 2004 cyclones mainly traveled along the path south of Svalbard resulting in a negative precipitation anomaly in Svalbard and the Arctic Ocean and a positive precipitation anomaly in the Norwegian and Barents Sea. During 2005 and 2006 the cyclone activity seems to have increased, resulting in positive precipitation anomalies in Svalbard and the Arctic Ocean. Precipitation patterns in Fig. 17 show that the other path along the Greenland Sea was more active during these years, causing a negative precipitation anomaly in the Barents Sea. Nevertheless, this needs further investigation to show a robust relation.

Seasonal maxima in wind speed and precipitation were found in autumn and winter (see Fig. 11 and 12). A seasonal maximum of precipitation in autumn and increased winds during winter were also mentioned by Hisdal (1976). Also the variability of air-temperature, precipitation and wind speed was the largest during these seasons (see Fig. 14). This is furthermore consistent with the increased activity of the North Atlantic cyclone track during winter (e.g. Tsukernik et al., 2007; Sorteberg and Walsh, 2008), transporting moisture and moist static energy (sensible heat, latent heat and geopotential) into the Arctic and also agrees with the observed connection between positive (negative) air-temperature

and precipitation anomalies (see Fig. 16 and 17).

In respect to air-temperature we assume two aspects mainly caused the observed anomalies. The exposure (cover) of warm sea water causes positive (negative) air-temperature anomalies especially at the sea ice margin due to sea ice anomalies (see Fig. 16 and 18). This aspect is further supported by studies of Serreze et al. (2011) and Day et al. (2012). Nevertheless, Vihma and Pirazzini (2005) indicate that positive air-temperature changes over sea ice are strongly connected to an increase in cloud cover and warm air advection. Furthermore, Hisdal (1976) describes northerly to easterly winds on Svalbard to be associated with clear skies and radiative heat loss from the ground, while southerly winds are generally associated with overcast skies reducing heat loss from the surface. In this study a connection of southerlies (northerlies) and positive (negative) air-temperature anomalies on sea ice far north from the sea ice margin and over land is observed. A considerable heat gain due to increase (decrease) in cloudiness related with southerlies (northerlies) as pointed out by Hisdal (1976) could explain this feature. This would furthermore match to the feature of orographic variability observed for air temperature (see Fig. 13) and the higher potential temperature at high land areas (see Fig. 9) since surface temperatures and therefore thermal radiation has to be larger at lower altitudes. The south-west to north-east air-temperature gradient and the variability are decreased during summer (see Fig. 10 and 14). That is consistent with described decreases in cyclone activity during summer, concurring effects of increased solar input and warm air advection reducing the heating effect of the solar rays due to related overcast skies and dampening effects due to melt and refreezing processes (e.g. Hisdal, 1976; Ohmura, 2001; Tsukernik et al., 2007).

Studies of Winther et al. (1998) discussed elevation, south-north and west-east precipitation gradients on Spitsbergen consistent with the precipitation distribution in Fig. 8. The accumulation observations in Winther et al. (1998) indicate precipitation amounts of about 1200 mm/year in the region of Torell Land (south Spitsbergen), 1000 mm/year in the region of Sabine Land (central-east Spitsbergen) and 800 mm/year in the region Olav V Land (north-east Spitsbergen). Values resolved by EAR are of equal dimension in these areas. Furthermore, west-east transects showed a prominent accumulation minimum in the center parts for northern regions which is also observable in Fig. 8. Möller et al. (2011) showed strong orographic dependencies of precipitation and accumulation on Vestfonna consistent with results of this study. Solid ground and orography act generally as a precipitation trigger by forcing rising atmospheric motions. We further assume cold surfaces like sea ice, glaciers or ice caps may additionally activate condensation and precipitation due to increased radiative cooling of the clouds from the bottom as Curry and Herman (1985) have shown for the Arctic.

Strong katabatic wind systems are observable (see Fig. 8) able to generate distinct mass loss due to snow drift as discussed in Sauter et al. (2013). Furthermore, the general existence of differences in precipitation distribution and its variability over very short distances is an important result (see Fig. 13). From a glaciological perspective the tremendous differences in precipitation variability on Vestfonna and Austfonna observable in Fig. 13 in regions of similar precipitation amounts (see Fig. 8) are valuable facts for the interpretation of differences in surface mass balances in these regions.

6 Conclusions

We analyzed climate variability of Svalbard and Nordaustlandet using a regional reanalysis of the European Arctic produced with Polar WRF for an eleven-year period. The regional reanalysis was in good accordance with observations on Svalbard. Based on the reanalysis some of the regional processes have

been documented and analyzed. The results were discussed with the synoptic features in the region of Svalbard. Spatial distribution, seasonality and variability of air temperature, precipitation and wind were presented, analyzed and were consistent with results of other studies. Four examples of precipitation and air-temperature anomalies were analyzed and their coupling to cyclone activity was discussed. Air-temperature anomalies correlate with precipitation anomalies and are more pronounced on sea ice whereas areas of cold dry anomalies show better correlation with sea ice anomalies and sea surface temperature. We assume strong connections of clouds and air temperature due to complex radiation climate feedbacks. Nevertheless, ways of impacts and interactions in the Arctic system are complex and we have only touched on some of the major issues. The results indicate that cyclone activity is a key factor of climate variability in the European Arctic.

Our analyses showed that the interaction of the West Spitsbergen Current, sea ice, radiative cooling/warming and advection processes produces large gradients and therefore increases variability of air-temperature, precipitation and wind especially during winter. Observed precipitation patterns strongly correlate with orography. Greatest precipitation amounts were observed in SON and smallest precipitation amount were observed in JJA. Regions of high precipitation amounts are located to the east while a latitudinal gradient exists in general. We could identify that maximum variability of precipitation is dislocated to northeastern directions. From a glaciological perspective the heterogeneous distribution of precipitation variability is a valuable fact, comparing the variability of mass input in different regions such as the Vestfonna and Austfonna ice caps on Nordaustlandet. Pronounced katabatic wind systems were observed in glaciated areas of Svalbard and are prevalent in all seasons while regions of highest wind speed show the smallest variability. A considerable mass loss due to snow drift at large ice caps caused by the katabatic wind systems is assumed. DJF is the season of highest wind speeds and wind speed absolute variability whereas JJA is the calmest season. The warmest season is JJA while the coldest season DJF shows the largest variability of air temperatures with the greatest gradients between sea and land.

The orographic influences were clearly captured by the regional reanalysis. Nevertheless, inaccuracy of the used elevation data set is one of the most prominent flaws. We could even observe strong influence of orography and a large elevation bias at Vestfonna, an ice cap of very simple shape. The errors surely increase for more complex topographies. Larger deviations between field observations and the reanalysis are related to the elevation bias: the less the elevation bias the less the deviation. Especially results for air temperature and wind show a large sensitivity to topography mismatch. Besides this the study showed how important a high horizontal domain resolution is to properly resolve the local wind field. Providing an elevation data set of better accuracy is therefore fundamental for further improvements.

Acknowledgments. This work was funded by grants no. BR 2105/6-1, SCHE 750/3-1, SCHN 680/2-1 of the German Research Foundation (DFG). Additional funding was provided by grants no. 03F0623A and 03F0623B of the German Federal Ministry of Education and Research (BMBF). We gratefully acknowledge the efforts of Matthias Braun, Regine Hock, Ulf Jonsell, Hartmut Küster, Bob McNabb, Fred Meier, Marco and Rebecca Möller, Albert Polze, Tobias Sauter, Christoph Schneider, Lars Schneider and Ingo Suchland for their assistance with setting up and maintaining the sensor networks. We also thank the International Polar Year (IPY) and European Science Foundation (ESF) project frameworks “GlacioDyn”, “IPY - Kinnvika” and “SvalGlac” for all scientific and logistical support.

References

Barstad, I. and Adakudlu, M., 2011. Observation and modelling of gap flow and wake formation on Svalbard. *Quarterly Journal of the Royal Meteorological Society*, 137, 1731-1738.

Bitz, C., Fyfe, J. and Flato, G., 2002. Sea ice response to wind forcing from AMIP models. *Journal of Climate*, 15, 522-536.

Claremar, B., Obleitner, F., Reijmer, C., Pohjola, V., Waxegard, A., Karner, F. and Rutgersson, A., 2012. Applying a Mesoscale Atmospheric Model to Svalbard Glaciers. *Advances in Meteorology*.

Corfidi, S., Merritt, J. and Fritsch, J., 1996. Predicting the movement of mesoscale convective complexes. *Weather and Forcasting*, 11, 41-46.

Curry, J. and Herman, G., 1985. Relationships between Large-scale Heat and Moisture Budgets and the occurrence of Arctic Stratus Clouds. *Monthly Weather Review*, 113, 1441-1457.

Day, J. J., Bamber, J. L., Valdes, P. J. and Kohler, J., 2012. The impact of a seasonally ice free Arctic Ocean on the temperature, precipitation and surface mass balance of Svalbard. *The Cryosphere*, 6, 35-50.

Dee, D. P., Uppala, S. M., Simmons, A. J., Berrisford, P., Poli, P., Kobayashi, S., Andrae, U., Balmaseda, M. A., Balsamo, G., Bauer, P., Bechtold, P., Beljaars, A. C. M., van de Berg, L., Bidlot, J., Bormann, N., Delsol, C., Dragani, R., Fuentes, M., Geer, A. J., Haimberger, L., Healy, S. B., Hersbach, H., Holm, E. V., Isaksen, L., Kallberg, P., Koehler, M., Matricardi, M., McNally, A. P., Monge-Sanz, B. M., Morcrette, J. J., Park, B. K., Peubey, C., de Rosnay, P., Tavolato, C., Thepaut, J. N. and Vitart, F., 2011. The ERA-Interim reanalysis: configuration and performance of the data assimilation system. *Quarterly Journal of the Royal Meteorological Society*, 137, 553-597.

Eneroth, K., Kjellstrom, E. and Holmen, K., 2003. A trajectory climatology for Svalbard; investigating how atmospheric flow patterns influence observed tracer concentrations. *Physics and Chemistry of the Earth*, 28, 1191-1203.

Ettema, J., van den Broeke, M. R., van Meijgaard, E. and van de Berg, W. J., 2011. Climate of the Greenland ice sheet using a high-resolution climate model - Part 2: Near-surface climate and energy balance. *The Cryosphere*, 4, 529-544.

Førland, E. and Hanssen-Bauer, I., 2003. Past and future climate variations in the Norwegian Arctic: overview and novel analyses. *Polar Research*, 22, 113-124.

Frei, A., Tedesco, M., Lee, S., Foster, J., Hall, D. K., Kelly, R. and Robinson, D. A., 2012. A review of global satellite-derived snow products. *Advances in Space Research*, 50, 1007-1029.

Hines, K. M. and Bromwich, D. H., 2008. Development and testing of Polar Weather Research and Forecasting (WRF) Model. Part I: Greenland ice sheet meteorology. *Monthly Weather Review*, 136, 1971-1989.

Hines, K. M., Bromwich, D. H., Bai, L.-S., Barlage, M. and Slater, A. G., 2011. Development and Testing of Polar WRF. Part III: Arctic Land. *Journal of Climate*, 24, 26-48.

Hisdal, V., 1976. Geography of Svalbard: a short survey. Norsk Polarinstitutt, 75.

Kalnay, E., Kanamitsu, M. and Baker, W., 1990. Global Numerical Weather Prediction at the National-Meteorological-Center. *Bulletin of the American Meteorological Society*, 71, 1410-1428.

Kalnay, E., Kanamitsu, M., Kistler, R., Collins, W., Deaven, D., Gandin, L., Iredell, M., Saha, S., White, G., Woollen, J., Zhu, Y., Chelliah, M., Ebisuzaki, W., Higgins, W., Janowiak, J., Mo, K., Ropelewski, C., Wang, J., Leetmaa, A., Reynolds, R., Jenne, R. and Joseph, D., 1996. The NCEP/NCAR 40-year reanalysis project. *Bulletin of the American Meteorological Society*, 77, 437-471.

Kanamitsu, M., 1989. Description of the NMC global data assimilation and forecast system. *Weather and Forecasting*, 4, 335-342.

Kanamitsu, M., Alpert, J., Campana, K., Caplan, P., Deaven, D., Iredell, M., Katz, B., Pan, H.,

Sela, J. and White, G., 1991. Recent Changes Implemented into the Global Forecast Stystem at NMC. *Weather and Forecasting*, 6, 425-435.

Kilpelainen, T., Vihma, T. and Olafsson, H., 2011. Modelling of spatial variability and topographic effects over Arctic fjords in Svalbard. *Tellus Series A - Dynamic Meteorology and Oceanography*, 63, 223-237.

Kristjánsson, J. E., Barstad, I., Aspelien, T., Fore, I., Godoy, O., Hov, O., Irvine, E., Iversen, T., Kolstad, E., Nordeng, T. E., McInnes, H., Randriamampianina, R., Reuder, J., Saetra, O., Shapiro, M., Spengler, T. and Olafsson, H., 2011. The Norwegian IPY-THORPEX Polar Lows and Arctic Fronts during the 2008 Ancloya Campaign. *Bulletin of the American Meteorological Society*, 92, 1443-1466.

Maussion, F., Scherer, D., Finkelnburg, R., Richters, J., Yang, W. and Yao, T., 2011. WRF simulation of a precipitation event over the Tibetan Plateau, China - an assessment using remote sensing and ground observations. *Hydrology and Earth System Science*, 15, 1795-1817.

McInnes, H., Kristiansen, J., Kristjansson, J. E. and Schyberg, H., 2011. The role of horizontal resolution for polar low simulations. *Quarterly Journal of the Royal Meteorological Society*, 137, 1674-1687.

Mesinger, F., DiMego, G., Kalnay, E., Mitchell, K., Shafran, P., Ebisuzaki, W., Jovic, D., Woollen, J., Rogers, E., Berbery, E., Ek, M., Fan, Y., Grumbine, R., Higgins, W., Li, H., Lin, Y., Manikin, G., Parrish, D. and Shi, W., 2006. North American regional reanalysis. *Bulletin of the American Meteorological Society*, 87, 343-360.

Mölg, T. and Kaser, G., 2011. A new approach to resolving climate-cryosphere relations: Downscaling climate dynamics to glacier-scale mass and energy balance without statistical scale linking. *Journal of Geophysical Research – Atmospheres*, 116.

Möller, M., Möller, R., Beaudon, E., Mattila, O.-P. , Finkelnburg, R., Braun, M., Grabiec, M. Jonsell, U., Luks, B., Puczko, D., Scherer, D. and Schneider C. (2011): Snowpack characteristics of Vestfonna and De Geerfonna (Nordaustlandet, Svalbard) – a spatiotemporal analysis based on multiyear snow-pit data. *Geografiska Annaler: Series* A, 93 (4), 273-285.

New, M., Lister, D., Hulme, M. and Makin, I., 2002. A high-resolution data set of surface climate over global land areas. *Climate Research*, 21, 1-25.

Ohmura, A., 2001. Physical basis for the temperature-based melt-index method. *Journal of Applied Meteorology*, 40, 753-761.

Onogi, K., Tslttsui, J., Koide, H., Sakamoto, M., Kobayashi, S., Hatsushika, H., Matsumoto, T., Yamazaki, N., Kaalhori, H., Takahashi, K., Kadokura, S., Wada, K., Kato, K., Oyama, R., Ose, T., Mannoji, N. and Taira, R., 2007. The JRA-25 reanalysis. *Journal of the Meteorological Society of Japan*, 85, 369-432.

Orlanski, I., 1975. A rational subdivision of scales for atmospheric processes. *Bulletin of the American Meteorological Society*, 56, 527-530.

van Pelt, W. J. J., Oerlemans, J., Reijmer, C. H., Pohjola, V. A., Pettersson, R. and van Angelen, J. H., 2012. Simulating melt, runoff and refreezing on Nordenskioldbreen, Svalbard, using a coupled snow and energy balance model. *The Cryophere*, 6, 641-659.

Sandvik, A. and Furevik, B., 2002. Case study of a coastal jet at Spitsbergen - Comparison of SAR- and model-estimated wind. *Monthly Weather Review*, 130, 1040-1051.

Sauter, T., Möller, M., Finkelnburg, R., Grabiecz, M., Scherer, D. and Schneider, C., 2013. Snowdrift modelling for Vestfonna ice cap, northeastern Svalbard. *The Cryosphere Discuss.*, 7, 709-741.

Serreze, M. C., Barrett, A. P. and Cassano, J. J., 2011. Circulation and surface controls on the lower tropospheric air temperature field of the Arctic. *Journal of Geophysical Research - Atmospheres*, 116.

Shaffrey, L. C., Stevens, I., Norton, W. A., Roberts, M. J., Vidale, P. L., Harle, J. D., Jrrar, A., Stevens, D. P., Woodage, M. J., Demory,

M. E., Donners, J., Clark, D. B., Clayton, A., Cole, J. W., Wilson, S. S., Connolley, W. M., Davies, T. M., Iwi, A. M., Johns, T. C., King, J. C., New, A. L., Slingo, J. M., Slingo, A., Steenman-Clark, L. and Martin, G. M., 2009. UK HiGEM: The New UK High-Resolution Global Environment Model-Model Description and Basic Evaluation. *Journal of Climate*, 22, 1861-1896.

Skeie, P. and Grønås, S., 2000. Strongly stratified easterly flows across Spitsbergen. *Tellus Series A - Dynamic Meteorology and Oceanography*, 52, 473-486

Sorteberg, A. and Walsh, J. E., 2008. Seasonal cyclone variability at 70 degrees N and its impact on moisture transport into the Arctic. *Tellus Series A - Dynamic Meteorology and Oceanography*, 60, 570-586.

Tsukernik, M., Kindig, D. N. and Serreze, M. C., 2007. Characteristics of winter cyclone activity in the northern North Atlantic: Insights from observations and regional modeling. *Journal of Geophysical Research – Atmospheres*, 112.

Uppala, S., Kallberg, P., Simmons, A., Andrae, U., Bechtold, V., Fiorino, M., Gibson, J., Haseler, J., Hernandez, A., Kelly, G., Li, X., Onogi, K., Saarinen, S., Sokka, N., Allan, R., Andersson, E., Arpe, K., Balmaseda, M., Beljaars, A., Van De Berg, L., Bidlot, J., Bormann, N., Caires, S., Chevallier, F., Dethof, A., Dragosavac, M., Fisher, M., Fuentes, M., Hagemann, S., Holm, E., Hoskins, B., Isaksen, L., Janssen, P., Jenne, R., McNally, A., Mahfouf, J., Morcrette, J., Rayner, N., Saunders, R., Simon, P., Sterl, A., Trenberth, K., Untch, A., Vasiljevic, D., Viterbo, P. and Woollen, J., 2005. The ERA-40 re-analysis. *Quarterly Journal of the Royal Meteorological Society*, 131, 2961-3012.

Vihma, T. and Pirazzini, R., 2005. On the factors controlling the snow surface and 2-m air temperatures over the Arctic sea ice in winter. *Boundary-Layer Meteorology*, 117, 73-90.

Wada, M. and Konishi, H., 1998. A study of precipitating clouds close to fronts using microwave radiometry and radar in Svalbard, Arctic. *Atmospheric Research*, 49, 253-265.

Wagner, J. S., Gohm, A., Doernbrack, A. and Schaefler, A., 2011. The mesoscale structure of a polar low: airborne lidar measurements and simulations. *Quarterly Journal of Royal Meteorological Society*, 137, 1516-1531.

Wilson, A. B., Bromwich, D. H. and Hines, K. M., 2012. Evaluation of Polar WRF forecasts on the Arctic System Reanalysis Domain: 2. Atmospheric hydrologic cycle. *Journal of Geophysical Research - Atmospheres*, 117.

Winther, J., Bruland, O., Sand, K., Killingtveit, A. and Marechal, D., 1998. Snow accumulation distribution on Spitsbergen, Svalbard, in 1997. *Polar Research*, 17, 155-164.

Table 1. Physical parameterization.

Microphysics	Morrison 2-moment scheme
Boundary layer parameterization	Mellor-Yamada-Janjic (Eta) TKE scheme
Cumulus parameterization	Grell 3d ensemble cumulus scheme; no scheme for 2 km domains
Land-surface model	Noah Land-surface Model (LSM)
Long-wave radiation	Rapid Radiative Transfer Model (RRTM) scheme
Short-wave radiation	Goddard scheme

Table 2. Elevation bias at domain resolution and region type (see Fig. 2 and 3). A positive elevation bias indicates model elevation is greater than the measured elevation.

	Coastal region			**Inland region**			
	30 km (m)	**10 km (m)**	**2 km (m)**	**30 km (m)**	**10 km (m)**	**2 km (m)**	
Hopen	-6	-6	-6	-70	-50	6	**DG-AWS**
Hornsund	314	178	118	-36	-50	82	**VF-AWS240**
Svalbard-Lufthavn	164	254	128	-131	140	*325**	**VF-AWS335**
Ny-Ålesund	293	212	122	-166	-38	-48	**VF-AWS370**
RF-AWS	224	81	48	-296	-25	-39	**VF-AWS500**
				-393	-122	63	**VF-T597**
Average Abs. Bias	200	146	84	182	71	48	**Average Abs. Bias**

*discarded due to elevation bias exceeding 10 % of horizontal resolution

Table 3. Coordinates, altitude and period of operation of the Automatic Weather Stations (AWS) in western Nordaustlandet (Fig. 3).

AWS Name	**Latitude (°N)**	**Longitude (°E)**	**Altitude (m a.s.l.)**	**Start Date**	**End Date**
DG-AWS	80.0163	19.1855	240	26-May-08	20-May-12
VF-AWS240	79.9995	19.4442	240	22-May-08	20-May-09
VF-AWS335	79.9342	19.1823	335	22-Apr-07	2-Dec-09
VF-AWS370	79.9847	19.4738	370	28-May-08	15-Sep-11
VF-AWS500	79.965	19.532	500	21-May-08	21-May-09
VF-T597	79.987	20.1299	597	28-Apr-07	11-May-08
RF-AWS	80.2183	22.4783	10	25-Jan-07	In operation

Table 4. Results of air-temperature analysis at domain resolution and region type (see Fig. 4). A negative bias indicates that reanalysis is colder than the observation. N is the number of pairs available for the analysis.

	30 km		10 km		2 km	
	Coastal	Inland	Coastal	Inland	Coastal	Inland
r^2	0.96	0.97	0.96	0.99	0.96	0.99
rmsd (K)	1.51	1.33	1.38	0.87	1.39	0.93
Mean bias (K)	-4.02	-0.71	-3.31	-0.8	-2.28	-0.56
N	268	108	268	108	268	108

Table 5. Results of precipitation analysis at domain resolution and region type (see Fig. 5). A negative bias indicates that reanalysis precipitation is less than observed. N is the number of pairs available for the analysis.

	30 km	10 km	2 km
	Coastal	Coastal	Coastal
r^2	0.57	0.6	0.61
rmse (mm/d)	1.08	1.07	1.05
Mean bias (mm/d)	-0.01	-0.05	-0.06
N	54	54	54

Table 6. Results of wind-speed analysis at domain resolution and region type (see Fig. 6 and 7). A negative bias indicates that reanalysis wind speed is lower than observed. N is the number of pairs available for the analysis.

	30 km		10 km		2 km	
	Coastal	Inland	Coastal	Inland	Coastal	Inland
r^2	0.18	*0.03**	0.33	0.36	0.48	0.83
rmse (m/s)	1.73	1.99	1.41	1.57	1.13	0.9
Mean bias (m/s)	1	-0.56	0.99	-0.24	0.47	0.53
N	264	67	264	67	264	41

*not statistically significant (p = 0.01)

Table 7. Averaged air temperature of all land based grid points as resolved in the Nordaustlandet and the Svalbard domain (see Fig. 8 and 10).

	Nordaustlandet domain				Svalbard domain			
	Mean (°C)	Min (°C)	Max (°C)	Range (K)	Mean (°C)	Min (°C)	Max (°C)	Range (K)
SON	-9.3	-12.3	-5.5	5.7	-8.2	-12.6	-3	9.6
DJF	-17.2	-19.2	-13.6	5.6	-15.9	-21.3	-11.1	10.1
MAM	-14.2	-16.2	-11.6	4.5	-12.8	-16.6	-8.2	8.4
JJA	-0.7	-2.8	1.3	4.1	-0.3	-3	3.3	6.3
Annual	-10.3	-12.5	-7.9	4.6	-9.3	-12.8	-5.4	7.4

Table 8. Averaged accumulated precipitation of all land based grid points as resolved in the Nordaustlandet and the Svalbard domain (see Fig. 8 and 11).

	Nordaustlandet domain		Svalbard domain	
	Mean (mm/d)	Max (mm/d)	Mean (mm/d)	Max (mm/d)
SON	2.1	3.2	2.2	3.9
DJF	1.6	2.7	1.9	3.7
MAM	1.1	1.8	1.4	3.1
JJA	1.1	2	1.1	1.7
Annual	1.5	2.3	1.6	3.1

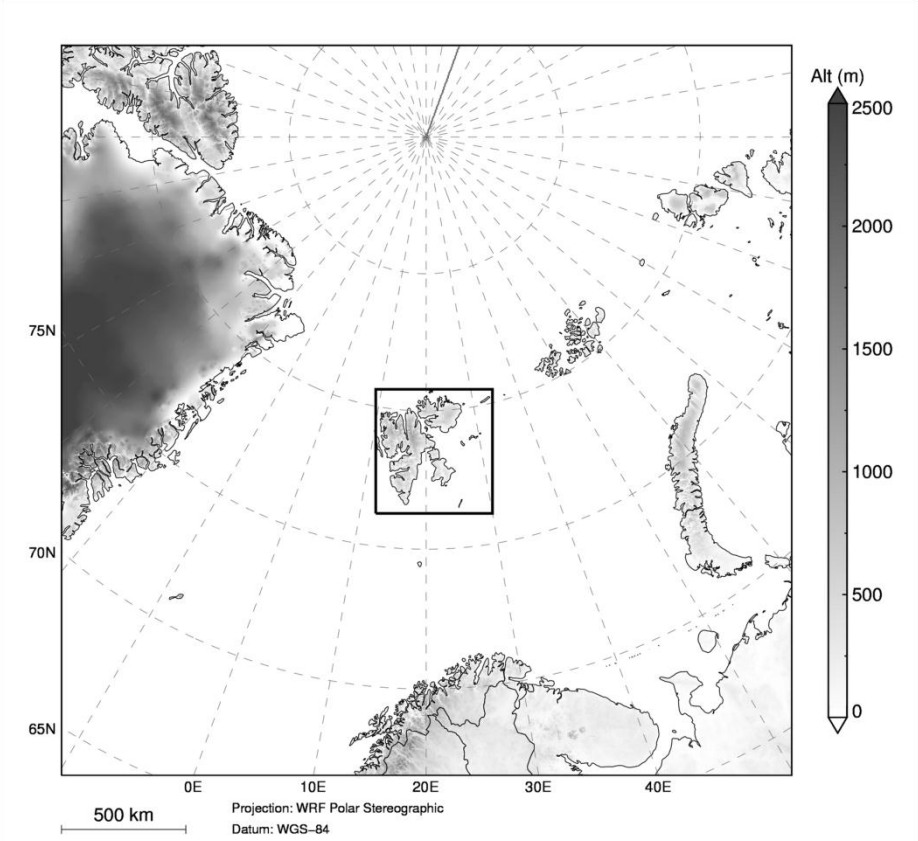

Fig. 1. Terrain height and location of the parent domain (30 km) part of the European Arctic Reanalysis (EAR). Black square shows the location of the nested Svalbard domain (10 km).

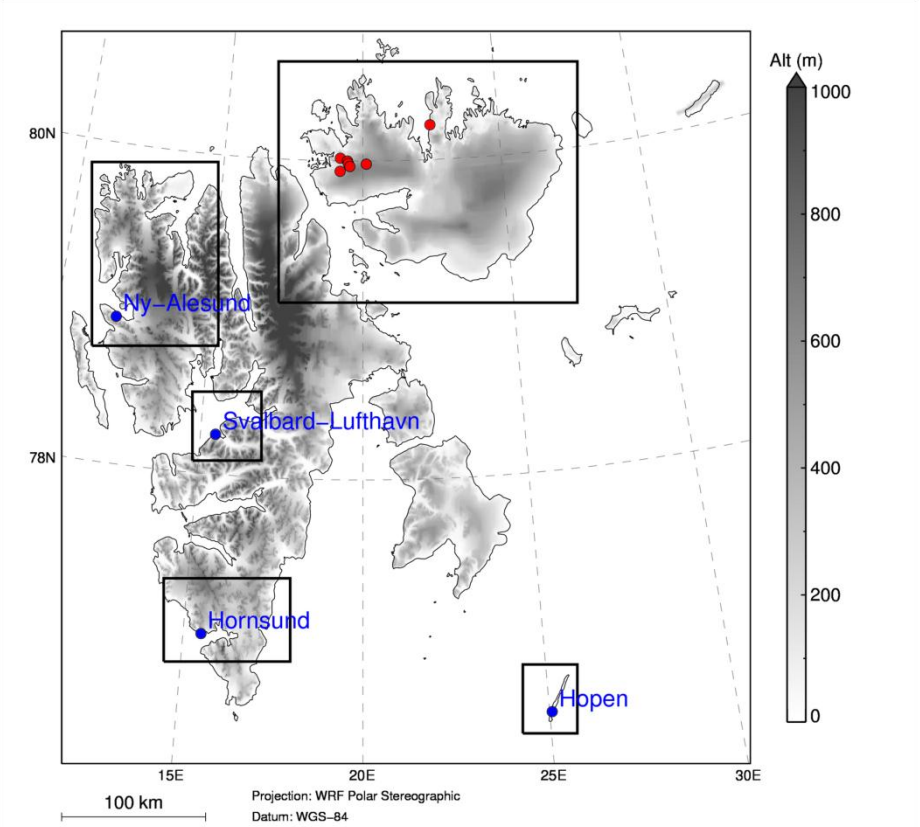

Fig. 2. Terrain height of the second-level Svalbard domain (10 km) part of the European Arctic Reanalysis (EAR). Black squares display the regions of the five third-level domains (2 km): a) Northwest Spitsbergen, b) Nordaustlandet, c) Longyearbyen, d) Hornsund and e) Hopen. Blue points mark synoptic stations of the Norwegian Meteorological Institute, while red points mark the automatic weather stations (AWS) used in this study.

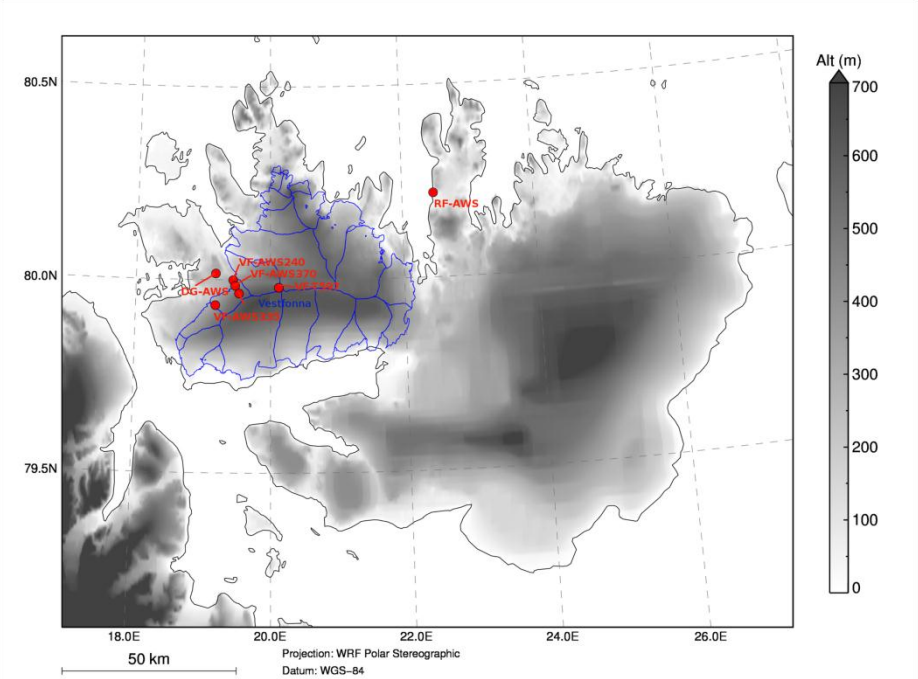

Fig. 3. Terrain height and location of the Nordaustlandet domain (2 km) part of the European Arctic Reanalysis (EAR). Red points are locations of automatic weather stations (AWS) and blue outlines define the region of Vestfonna derived from Randolph Glacier Inventory used in this study.

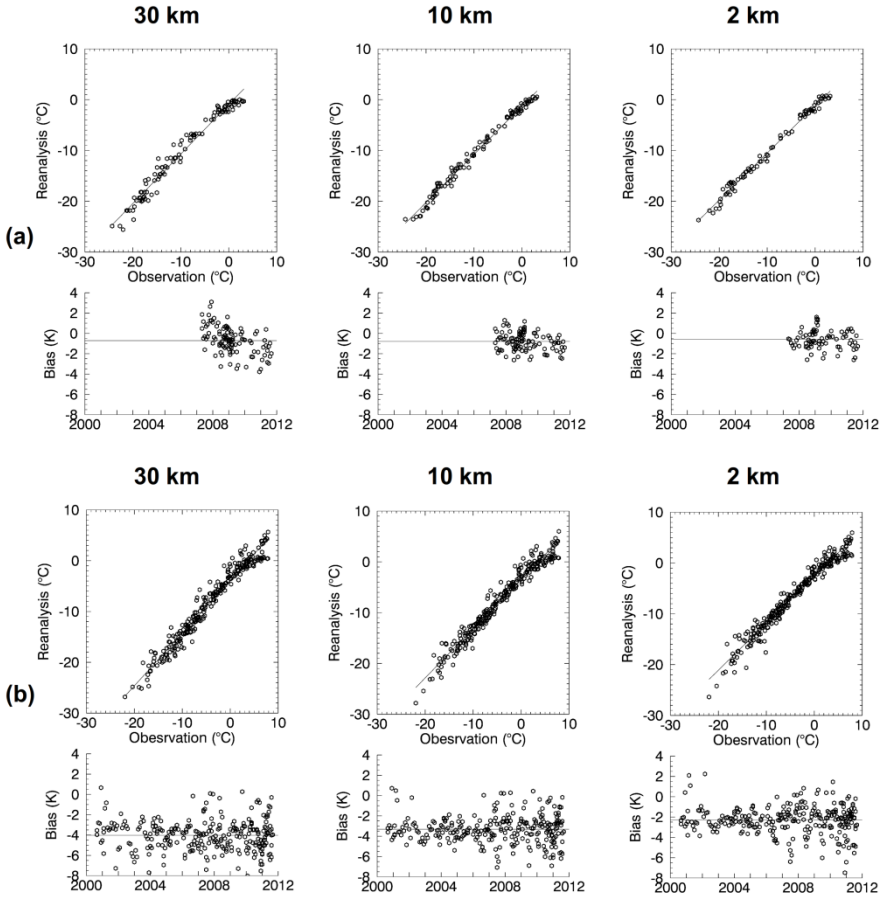

Fig. 4. Analysis results of monthly mean air temperature for (a) coastal regions (Hopen, Hornsund, Svalbard-Lufthavn, Ny-Ålesund and RF-AWS) and (b) inland regions (DG-AWS, VF-AWS240, VF-AWS335, VF-AWS370, VF-AWS500 and VF-T597). The results are presented for each domain resolution by scatter plot (upper part) and time series of bias (middle part). Solid lines show the linear regression function in the scatter plot and the mean bias in the bias time series plot. A negative bias indicates that reanalysis is colder than the observation. Statistical measures of the regression analysis are presented in Table 4.

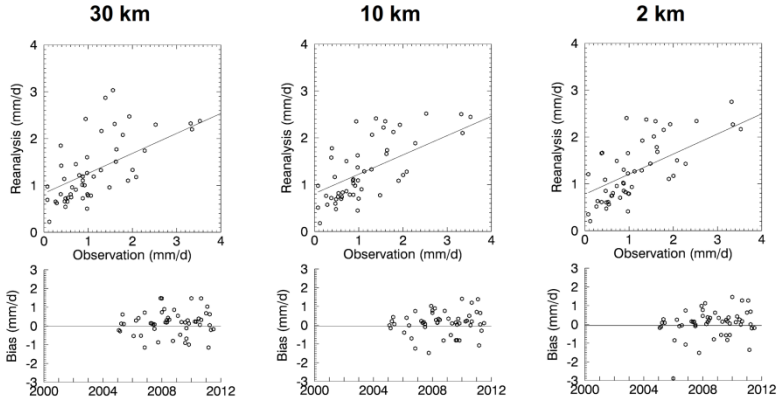

Fig. 5. Analysis results of monthly mean precipitation for coastal regions (Hopen, Hornsund, Svalbard-Lufthavn and Ny-Ålesund). The results are presented for each domain resolution by scatter plot (upper part) and time series of bias (middle part). Solid lines show the linear regression function in the scatter plot and the mean bias in the bias time series plot. A negative bias indicates that reanalysis precipitation is less than observed. Statistical measures of the regression analysis are presented in Table 5.

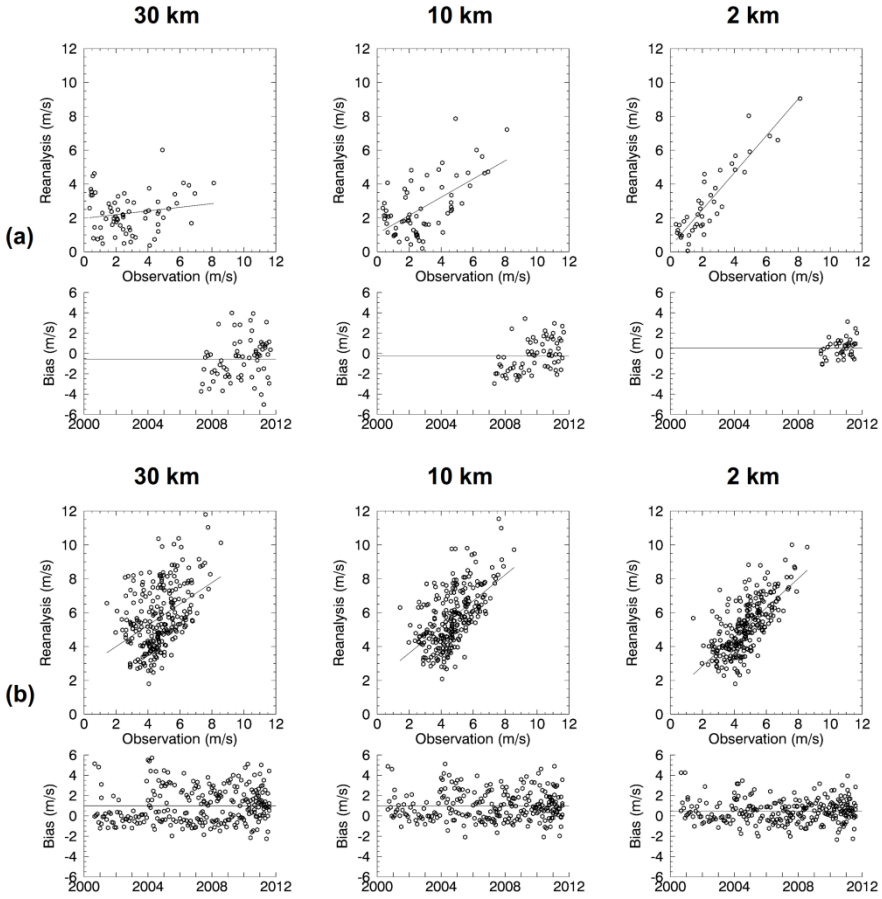

Fig. 6. Analysis results of monthly mean near surface wind speed for (a) coastal regions (Hopen, Hornsund, Svalbard-Lufthavn, Ny-Ålesund and RF-AWS) and (b) inland regions (DG-AWS, VF- VF-AWS335, VF-AWS370). The results are presented for each domain resolution by scatter plot (upper part) and time series of bias (middle part). Solid lines show the linear regression function in the scatter plot and the mean bias in the bias time series plot. A negative bias indicates that reanalysis wind speed is lower than observed. Statistical measures of the regression analysis are presented in Table 6.

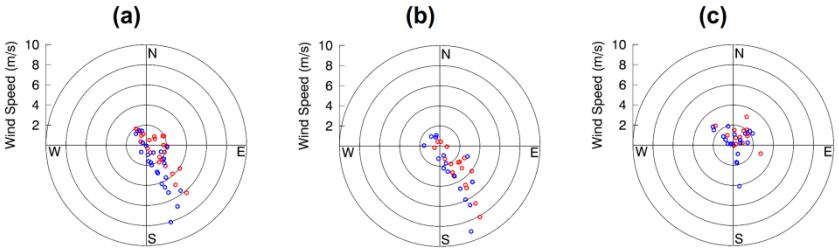

Fig. 7. Comparison of monthly mean near surface wind speed and wind direction in the Nordaustlandet domain at (a) DG-AWS, (b) VF-AWS370 and (c) RF-AWS (see Fig. 3). Observations are displayed in red and reanalysis data are displayed in blue.

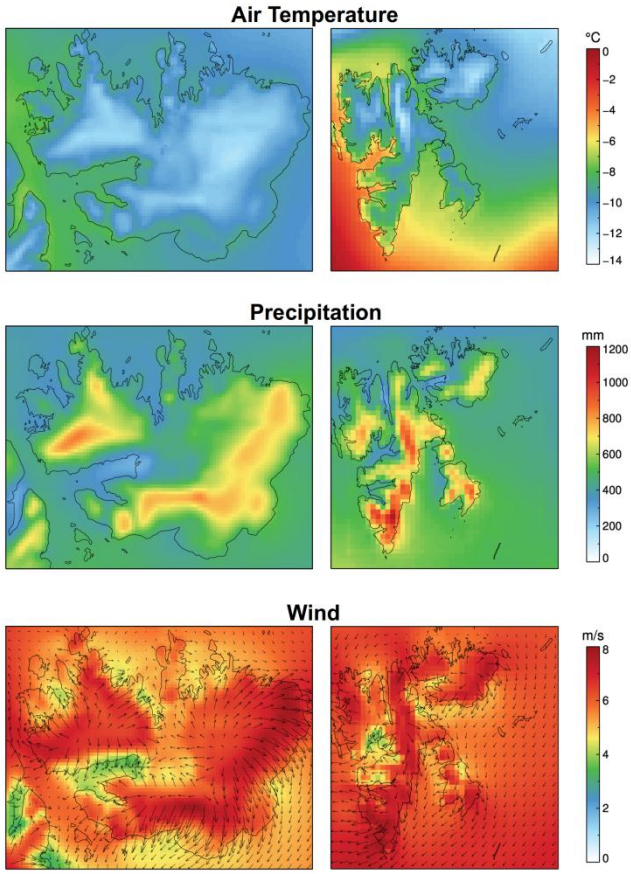

Fig. 8. Eleven-year annual mean of air temperature, accumulated precipitation and wind as resolved by the reanalysis. Each variable is plotted for the Nordaustlandet domain (left) and the Svalbard domain (right). Arrows in the wind plot are vector averages while colours present the scalar average of wind speed.

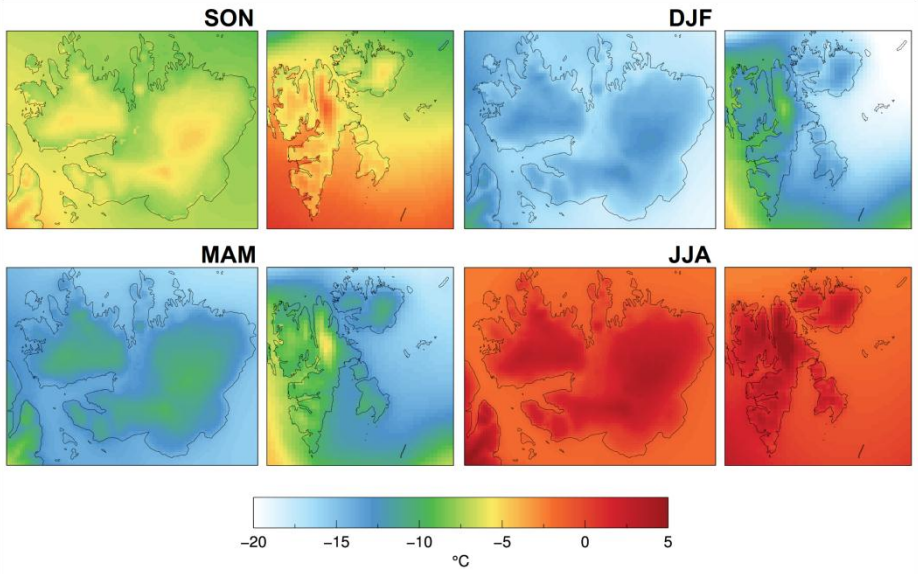

Fig. 9. Eleven-year seasonal mean of potential temperature at 1013 hPa level derived from reanalysis air temperature. Each season is plotted for the Nordaustlandet domain (left) and the Svalbard domain (right).

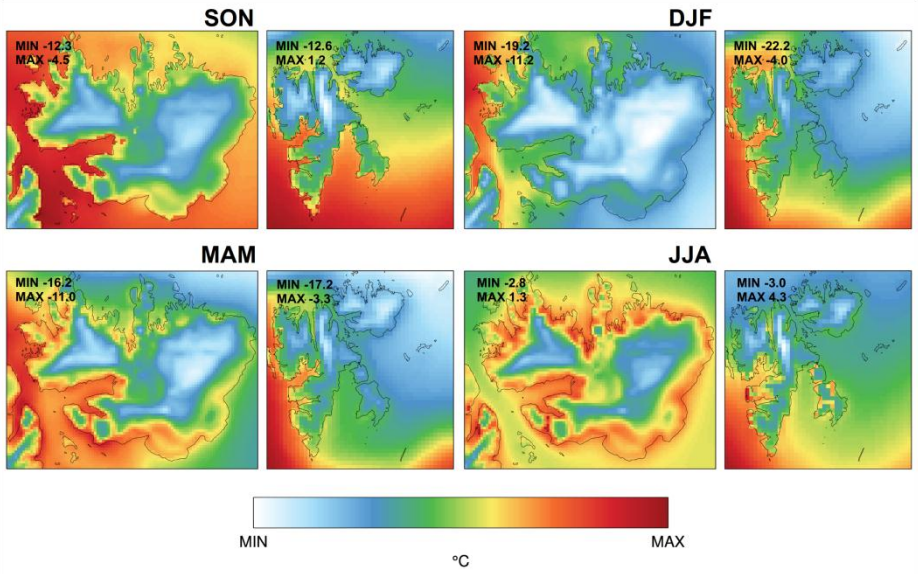

Fig. 10. Eleven-year seasonal mean of air temperature as resolved by the reanalysis. Color table ranges from minimum to maximum air temperature as indicated in each plot. Each season is plotted for the Nordaustlandet domain (left) and the Svalbard domain (right).

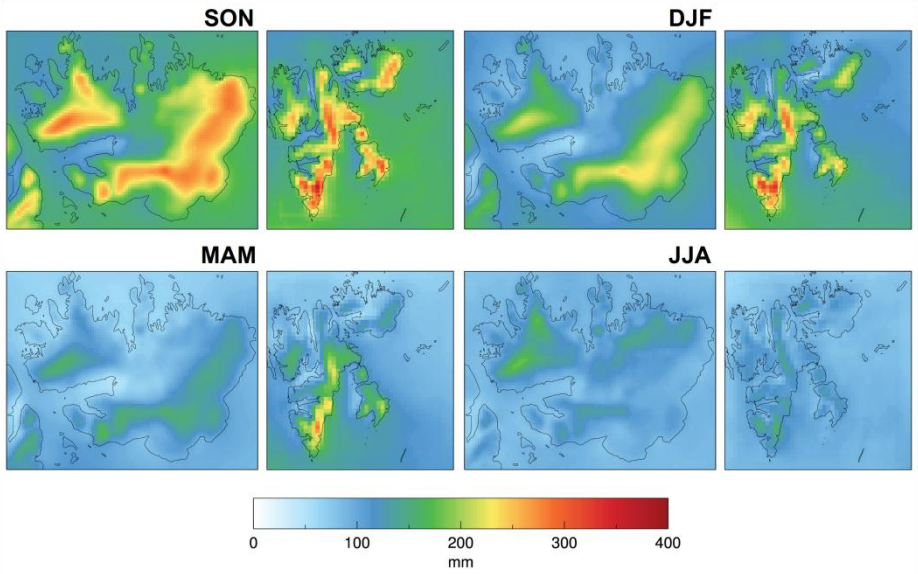

Fig. 11. Eleven-year seasonal mean of accumulated precipitation as resolved by the reanalysis. Each season is plotted for the Nordaustlandet domain (left) and the Svalbard domain (right).

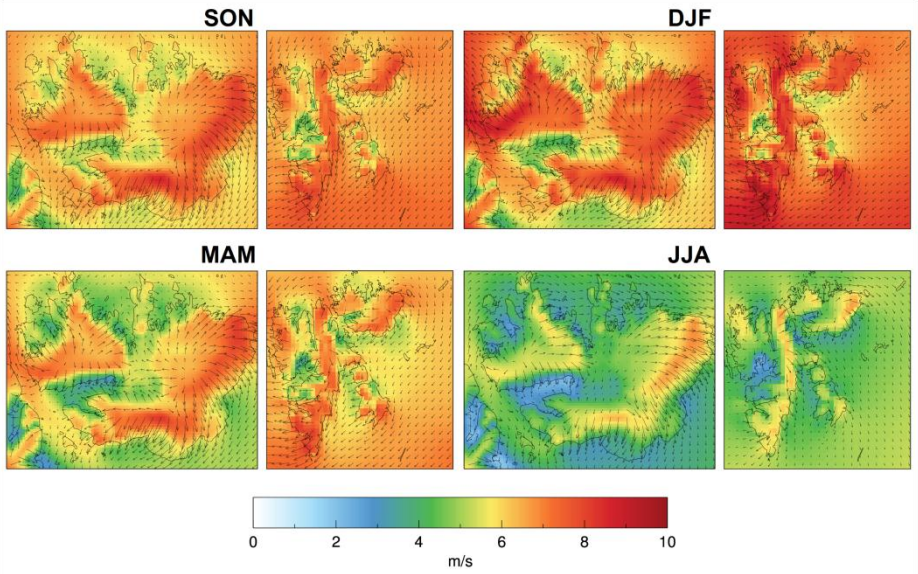

Fig. 12. Eleven-year seasonal mean of 10 m wind as resolved by the reanalysis. Each season is plotted for the Nordaustlandet domain (left) and the Svalbard domain (right). Arrows in the wind plot are vector averages while colours present the scalar average of wind speed.

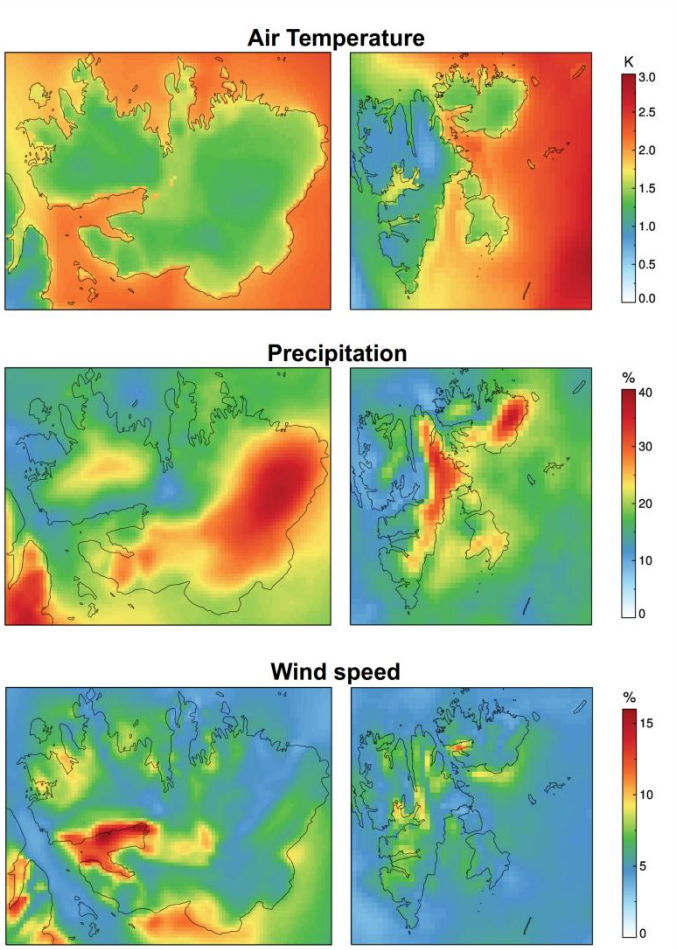

Fig. 13. Variability of annual means derived from eleven-year reanalysis data. Values for air temperature are displayed as standard deviation. Values for precipitation and wind speed are displayed as relative standard deviation. Each variable is plotted for the Nordaustlandet domain (left) and the Svalbard domain (right).

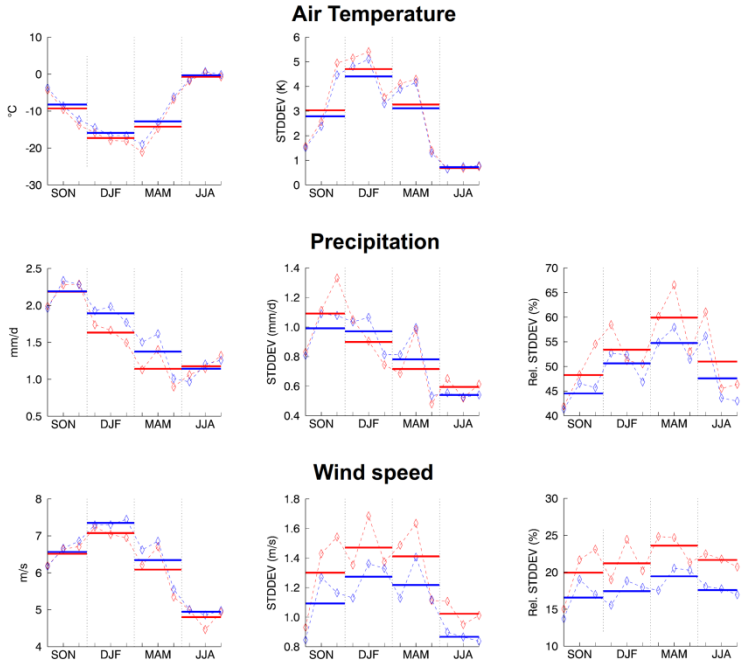

Fig. 14. Seasonal means (bold line) of air temperature, precipitation and wind speed (left), their standard deviation (middle) and relative standard deviation (right) as derived from eleven-year reanalysis data. Only land-based grid points of the Nordaustlandet domain (red) and the Svalbard domain (blue) are included.

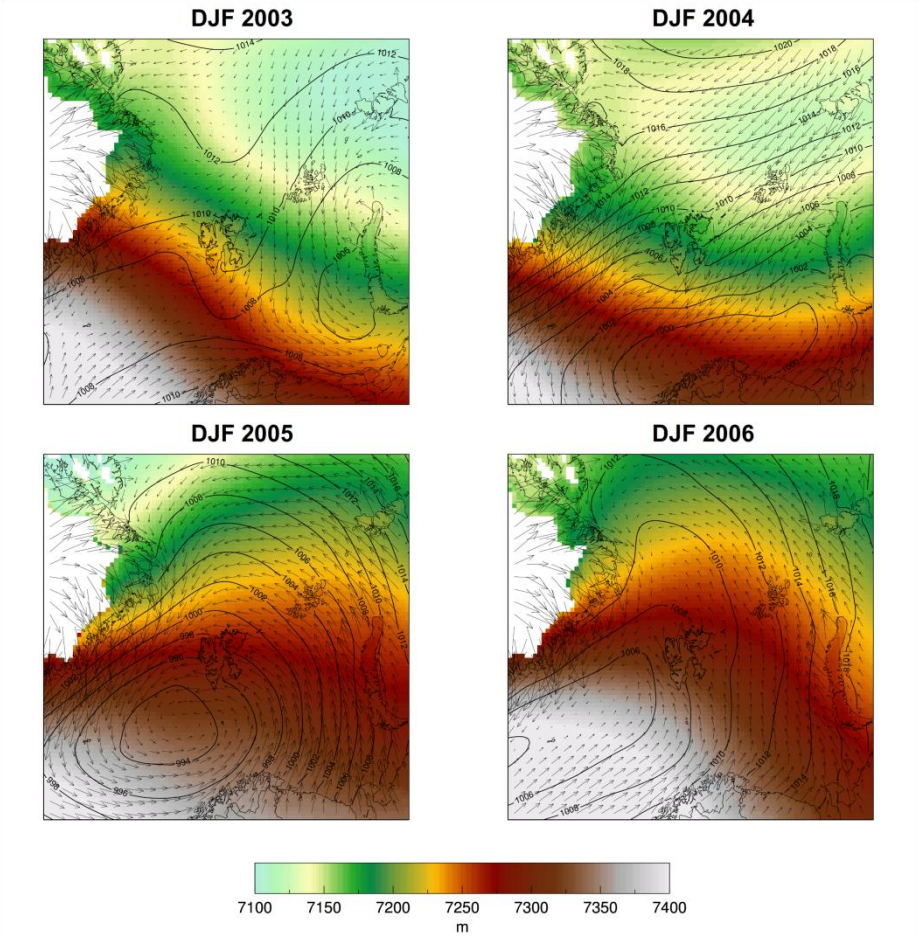

Fig. 15. Seasonal mean thickness (also termed relative topography), sea level pressure and wind field of the EAR domain as resolved by the reanalysis. Thickness is calculated from 300 and 850 hPa level heights.

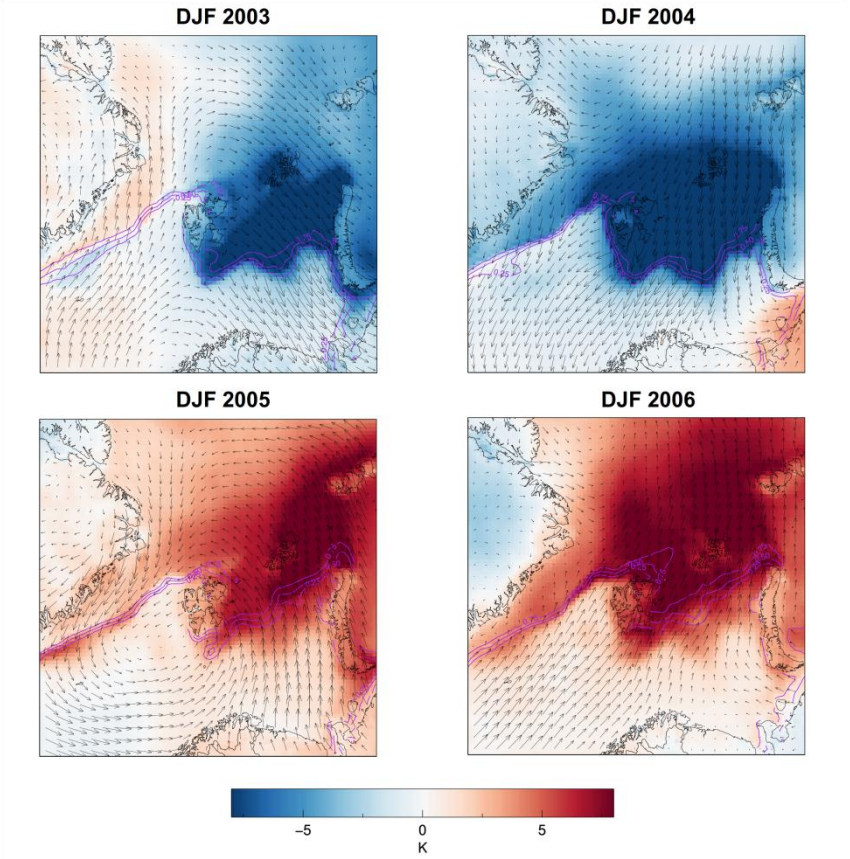

Fig. 16. Seasonal air-temperature and wind field anomaly of the European Arctic domain (30 km) as resolved by the European Arctic Reanalysis (EAR). Purple contours indicate seasonal sea ice margin.

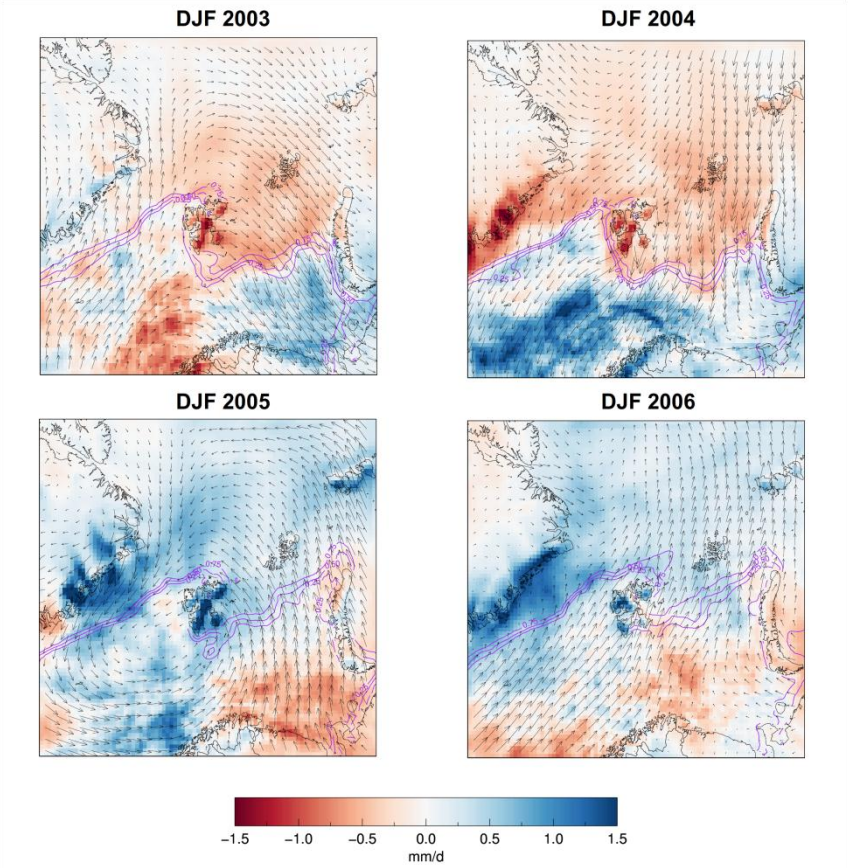

Fig. 17. Seasonal precipitation and wind field anomaly of the EAR domain as resolved by the reanalysis. Purple contours indicate seasonal sea ice margin.

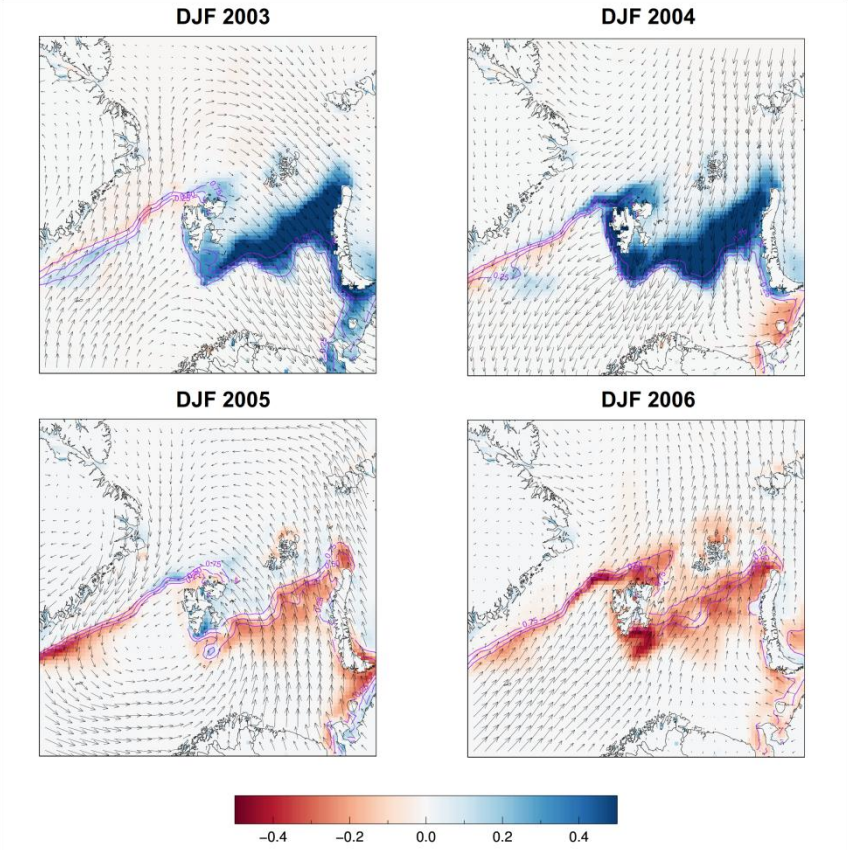

Fig. 18. Seasonal sea ice and wind field anomaly of the EAR domain as resolved by the reanalysis. Displayed is the fractional sea ice. 0.5 indicates 50 % more and -0.5 indicates 50 % less sea ice than normal. Purple contours indicate seasonal sea ice margin.

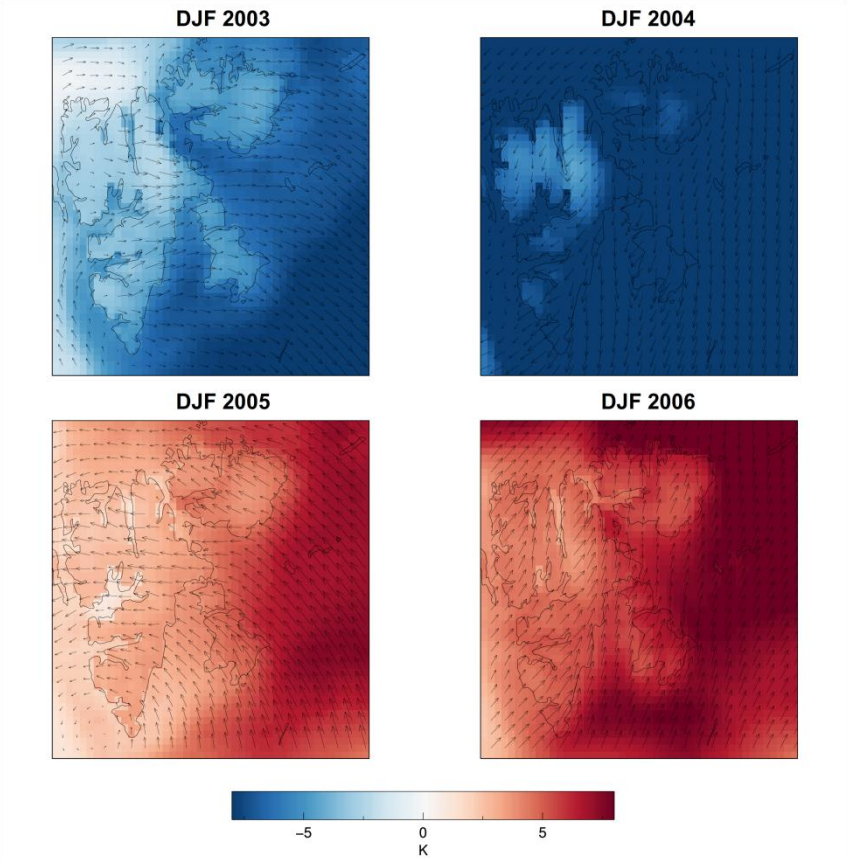

Fig. 19. Seasonal air-temperature and wind field anomaly of the Svalbard domain as resolved by the reanalysis.

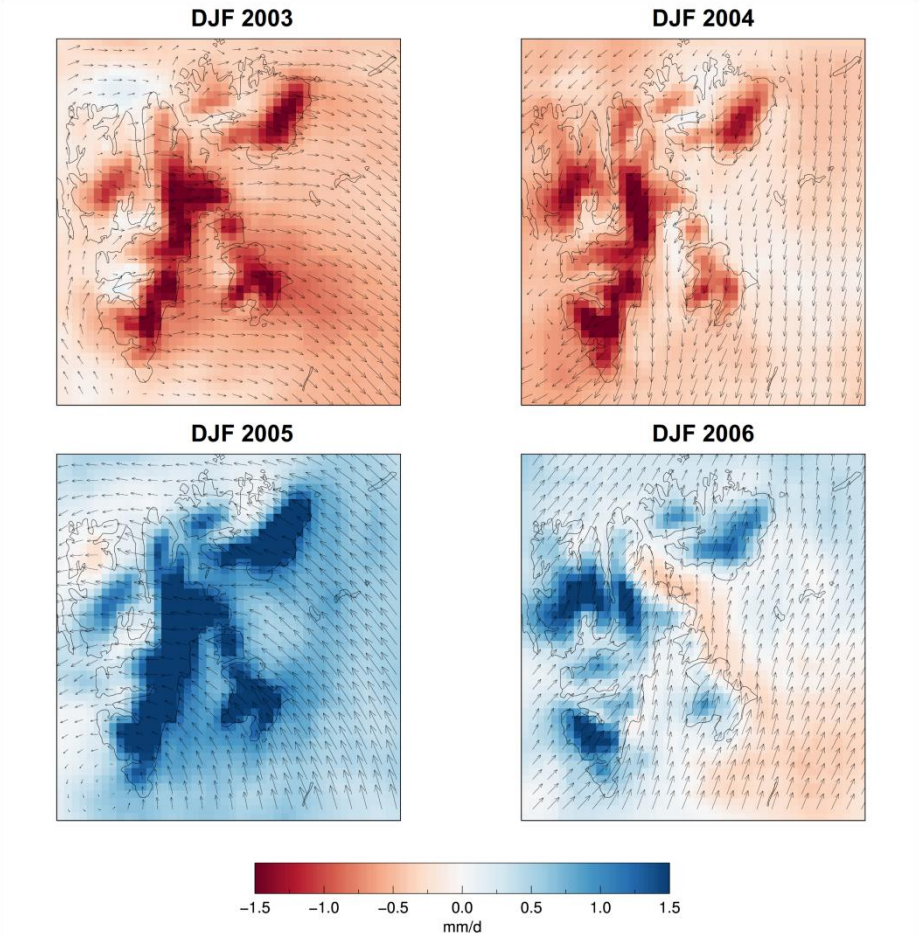

Fig. 20. Seasonal precipitation and wind field anomaly of the Svalbard domain as resolved by the reanalysis.

Appendix D: Snowdrift modelling for Vestfonna ice cap, northeastern Svalbard

Sauter, T., Möller, M., Finkelnburg, R., Grabiecz, M., Scherer, D. and Schneider, C., 2013. Snowdrift modelling for Vestfonna ice cap, northeastern Svalbard. *The Cryosphere Discuss.*, 7, 709-741, doi: 10.5194/tcd-7-709-2013.

Status: Published

Own contribution:

- Preparation, conduction and leading of field campaigns
- Design and implementation of measurement concepts
- Acquisition of field observational data and from online data bases
- Software and hardware design and implementation of the reanalysis framework
- Production of the EAR data sets
- Processing, interpretation and analysis of AWS data and the EAR
- Preparation of manuscript parts concerning AWS data and the EAR
- Review, comments and improvements of the manuscript

The Cryosphere Discuss., 7, 709–741, 2013
www.the-cryosphere-discuss.net/7/709/2013/
doi:10.5194/tcd-7-709-2013

The Cryosphere Discussions
Open Access

Snowdrift modelling for Vestfonna ice cap, north-eastern Svalbard

T. Sauter[1], M. Möller[1], R. Finkelnburg[2], M. Grabiec[3], D. Scherer[2], and C. Schneider[1]

[1]Department of Geography, RWTH Aachen University, Germany
[2]Department of Ecology, Technische Universität Berlin, Germany
[3]Department of Geomorphology, University of Silesia, Poland

Received: 5 February 2013 – Accepted: 14 February 2013 – Published: 28 February 2013

Correspondence to: T. Sauter (tobias.sauter@geo.rwth-aachen.de)

Published by Copernicus Publications on behalf of the European Geosciences Union.

Abstract

The redistribution of snow by drifting and blowing snow frequently leads to an inhomogeneous snow mass distribution on larger ice caps. Together with the thermodynamic impact of drifting snow sublimation on the lower atmospheric boundary layer, these processes affect the glacier surface mass balance. This study provides a first quantification of snowdrift and sublimation of blowing and drifting snow on Vestfonna ice cap (Svalbard) by using the specifically designed "snow2blow" snowdrift model. The model is forced by atmospheric fields from the Weather Research and Forecasting model and resolves processes on a spatial resolution of 250 m. Comparison with radio-echo soundings and snow-pit measurements show that important local scale processes are resolved by the model and the overall snow accumulation pattern is reproduced. The findings indicate that there is a significant redistribution of snow mass from the interior of the ice cap to the surrounding areas and ice slopes. Drifting snow sublimation of suspended snow is found to be stronger during winter. It is concluded that both processes are strong enough to have a significant impact on glacier mass balance.

1 Introduction

In high arctic regions, redistribution of snow mass by wind drift has an important impact on the balance of glaciers. The intensity of the redistribution process is essentially given by the interaction of the inherent erosional capacity of the wind flow and the snow pack characteristics. Particularly along the margin of larger ice caps, persistent katabatic winds become often strong enough to effectively remove snow from the surface and re-accumulate the eroded snow mass within the surrounding areas (e.g. Boon et al., 2010; Mernild et al., 2006). Once snow particles become mobile, they can be advected over long distances by the mean flow, while influencing the turbulent structure of the atmospheric boundary layer. Snow particles, which are entrained far upwards (above 2 m) by turbulent eddies are generally refered to as blowing snow, whereas

the advection of snow mass within the surface layer is termed drifting snow. During transport part of the snow mass is removed by sublimation which modifies the vertical temperature and moisture profiles of the near-surface layer. The cooler and more humid air masses, then have a non-neglectable impact on the surface energy fluxes. Since the effect on mass balance can be strong, bridging the gap between drifting and blowing snow and the local scale impact on glacier mass balance in polar regions has been addressed by several glaciological studies (e.g. Jaedicke, 2002; Bintanja, 1998; Lenaerts et al., 2010, 2012).

The importance of drifting and blowing snow in the European Arctic has early been postulated by Ahlmann (1933). Based on point field measurements in Nordaustlandet, he estimated that at least 1/8 of the total snow accumulation is redistributed by wind. The first detailed accumulation map of Nordaustlandet (Spitsbergen) has been provided by Schytt (1964), based on point measurements collected during the Swedish Glaciological Expedition in 1957/58. Later, better insights along several transects have been gained by extensive repeated ground penetrating radar measurements carried out by Taurisano et al. (2007) and Grabiec et al. (2011). Both studies substantially contributed to a better understanding and a consistent idea of the spatial snow cover pattern on the two large ice caps on Nordaustlandet, Austfonna and Vestfonna. Their findings have been recently affirmed by on-site snow measurements from Möller et al. (2011b) and Beaudon et al. (2011). Unfortunately, due to the heterogeneity of the complex snowdrift processes a comprehensive, glacier wide spatio-temporal quantification by measurements, however, proof to be a challenging task.

This study presents the first spatio-temporal estimate of snowdrift in the southwest part of Vestfonna ice cap. We discuss the processes involved and describe the mathematical framework of the specifically designed three-dimensional *snow2blow* model. The model is then applied to Vestfonna ice for the accumulation period 2008/2009. Model results are compared with radio-echo sounding measurements and on-site snow-pitdata. Finally, the contribution and influence of individual component on the snow distribution is discussed in detail.

2 Study area

The ice cap Vestfonna covers a surface area of 2340 km^2 in 2005 (Braun et al., 2011) and is thus the second largest single ice mass of the Svalbard archipelago and among the largest ice caps of the Eurasian Arctic (see Fig. 1). Its star-shaped ice dome is formed by an east-west oriented ridge that extends over the main summit, Ahlmann Summit. From the eastern summit, which is the highest point of the ice cap (647 m over WGS84 ellipsoid, Braun et al., 2011), a secondary ridge extends towards the north. Apart from these main ridges the morphology of Vestfonna is dominated by several land-terminating ice lobes and extensive outlet glacier basins that form marine terminating, calving glacier fronts.

The strongly maritime climate of Svalbard is characterized by the contrasting influences of warm and humid North Atlantic air masses to the south and cold and dry Arctic air masses to the northeast (Svendsen et al., 2002). The warm West Spitsbergen Current (Walczowski and Piechura, 2011) frequently causes sea ice-free conditions along the western part of the archipelago while the eastern areas are directly influenced by cold Arctic ocean currents (Loeng, 1991) with closed sea-ice cover during most winters. Extratropical cyclones mainly control the synoptic-scale variability in the southern parts of the archipelago while the Arctic high pressure system forms the strongest influencing factor for the northern parts (Skeie, 2000). The synoptic forcing markedly imprints on the surface climate especially during the winter months (Bednorz and Fortuniak, 2011). The synoptic-scale airflow across the archipelago is dominated by southerly directions during the summer season while during winter northeasterly directions prevail (Käsmacher and Schneider, 2011).

Due to its location within the archipelago, Nordaustlandet is less directly influenced by the warmer Atlantic air and water masses. Its climatic setting is mainly governed by easterly weather systems originating in the Barents Sea region (Taurisano et al., 2007). These provide the major moisture source for precipitation during the winter season (Førland et al., 1997) with the absolute amounts partly depending on sea-ice coverage

(Rogers et al., 2001). During conditions of easterly air flow, Vestfonna is located in the lee of its larger and higher neighbour Austfonna which makes precipitation sums being generally smaller here (Hagen, 1993).

Snow accumulation throughout the slopes of Vestfonna was found to be mainly governed by terrain elevation (Möller et al., 2011a,b). Along the main ridges the pattern of accumulated winter snow shows substantial zonal variability that differs between individual years (Beaudon et al., 2011). The prevalence of katabatic wind directions throughout the slopes of the ice cap (Claremar et al., 2012) promotes radial drifting snow trajectories while synoptic winds and thus less consistent drifting snow directions dominate on the ridges (Möller, 2012; Möller et al., 2013). Overall, the magnitude of snow accumulation across the ice cap shows high interannual variability and therewith reflects the synoptic forcing (Beaudon et al., 2011).

3 Field observations

The here presented study requires different types of field data for validation purposes, i.e. snow-depth information from radio-echo sounding and snow-pit analysis as well as in situ meteorological measurements at automatic weather stations.

A snow-depth profile that is acquired from radio-echo sounding carried out in spring 2009 by Grabiec et al. (2011) serves as a basis for the validation of the modelled snow accumulation pattern (Fig. 1). The first part of this profile that is used in this study extends over 14 km and reaches from the forefield of the northwestern land-terminating parts of Vestfonna up to the main ridge of the ice cap and further on to Ahlmann Summit. The second used part of the profile covers 32 km of the western part of the main ridge. The original snow-depth soundings provide point data that are unevenly distributed along the profile line. For application in model validation we smoothed the original data using a 21-point moving-window filter in order to eliminate local outliers. Afterwards the smoothed profile data were averaged to fit the 250 m pixel resolution of the modelling domain. Snow depth along the profile ranges between 0 and 2.24 m.

According to the measurements three different types of altitude dependent accumulation patterns are observable, i.e. inversion, precipitation and redistribution. At elevations below 350 m the snow accumulates in a permanent aggregation wedge (Grabiec et al., 2011; Ahlmann, 1933) and forms a surrounding snow band that is clearly visible on satellite images throughout the entire year. Within a small zone of this snow band snow depth gradually decreases with increasing altitude. In contrast, snow depth above an altitude of 350 m tends to increase with altitude. Throughout the uppermost parts of the ice cap the spatial distribution of snow depth is mainly determined by snowdrift that result in frequent sastrugi formation and thus in a high local-scale variability of snow accumulation. The radar measurements shown in Figs. 2 and 3 indicate both low and high frequency fluctuations of snow depth that can be attributed to short and longwave sastrugi formation as it is especially visible between markers D and E.

Point related, multi-year snow-cover data from an extensive snow-pit study (Möller et al., 2011b) provide information on snow depth and density for 21 points on Vestfonna and nearby De Geerfonna for the period 2007–2010. According to this study, the mean density of the snow pack lies in the range 300–400 $kg\,m^{-3}$. The snow-pit data are integrated in the discussion of qualitative model performance with respect to interannual persistence of the ice cap-wide snow-depth pattern.

Meteorological data from an automatic weather station operated on the northwestern slope of Vestfonna (VF-AWS, Fig. 1) since spring 2008 is used for validation of WRF derived fields of wind speed and direction, air temperature and relative humidity. The records used here comprise the period September 2008 to May 2009.

4 Physical processes in two-phase flow

The redistribution of snow strongly depends on the available turbulent kinetic energy of the atmospheric boundary layer, and thus from the momentum flux and the surface shear effects (Liston and Sturm, 1998; Lehning et al., 2008; Bintanja, 2000). Once the surface shear stress exceeds the inertia and the cohesive bonds of the snow particles,

transport takes place. Within a thin surface layer the ejected particles follow a ballistic trajectory under the influence of gravity. The rebounds of these particles on the snow surface, again, are able to eject more grains. This near-surface layer is barely influenced by turbulence so that the prevailing particle transport mechanism is pure saltation. Depending on the momentum flux some of the particles within the saltation layer may be entrained further upwards against their gravitative force by turbulent diffusion and further suspended by the mean flow. Once the particle is in suspension the particle velocity is assumed to be equivalent to the fluid velocity.

Blowing and drifting of snow is considered to be a dilute two-phase flow consisting of solid snow particles in a fluid phase. Transport- and exchange processes in such two-phase flows are given by turbulent fluid motion, which in turn is affected by the presence of the particles. Thus, snow particle can either enhance or damp turbulent velocity fluctuations depending on the different characteristic time and length scales of the flow. It appears that, if snow particles are small compared to the turbulent length scale they tend to absorb turbulent kinetic energy (Gore and Crowe, 1989). The evolution of turbulence in the presence of snow particles is a function of the Stokes number St, which is given by the ratio of the particle relaxation time and the characteristic time scale of energy containing eddies (Kolmogorov time scale $\tau = (\nu/\epsilon)^{1/2}$). Assuming that the particle diameters of drifting snow is typically in the range 10–400 µm and the Kolmogorov length scale of the atmosphere is $(\eta = (\nu^3/\epsilon)^{1/4})$ $\eta \approx 1$ mm leads to a St < 1. Such a small Stokes number implies that the particles enhance the dissipation of turbulent energy in order to keep the particles in suspension. This reduces the available turbulent energy for further entrainment.

Elgobashi (1994) likewise described interaction effects of particle-laden flows by the Stokes number St and the average volumetric particle concentration. Since the average volumetric snow particle concentration of suspended snow is usually below 10^{-3} (Bintanja, 2000; Gauer, 2001; Schneiderbauer et al., 2008), and thus the average distance between the particles is large compared to their size, it is feasible to neglect interaction effects (Crowe et al., 1996; Elgobashi, 1994). As shown by Bintanja (2000)

the presence of particles also modifies the mean wind velocity profile. Snow particles in suspension are balanced by the particle-fluid drag force and the counteracting gravity force. If this equilibrium is perturbed by turbulent motion the air parcel experience an anomalous buoyancy, which is similar to a thermally stable turbulent layer. As a consequence of the stable stratification the density of the fluid-particle mixture increases towards the surface. Therefore, friction velocity u_* is not constant with height according to $u_* = \sqrt{\tau_0/\rho}$, leading to a reduction of the turbulent exchange coefficient $K_M = \kappa u_* z$. Due to the change of the turbulent exchange coefficient the wind speed gradient, and thus the wind speed increases.

5 Model description

5.1 General comments and model setup

Snow erosion and transport processes are inherently linked to the characteristics of the air flow and snow properties. Therefore, the quantitative assessment of snow redistribution requires an approximation of the buoyant, turbulent surface wind field. Similar to previous studies (e.g. Liston and Sturm, 1998; Naaim et al., 1998; Schneiderbauer et al., 2008; Bintanja, 2000; Pomeroy and Gray, 1990; Gauer, 2001; Durand et al., 2005), the interactions between particles are neglected and snow particles are treated as a continuous phase solely interacting with the background flow. The proposed model solves the Reynolds averaged Navier–Stokes equation using the k-ω turbulence model. The model is implemented within the open source C++ library OpenFOAM and is freely downloadable at the author's webpage.

5.2 Governing equations

The turbulent flow is assumed to be incompressible, so that the continuous continuity equation reduces to

$$\frac{\partial u_i}{\partial x_i} = 0 \tag{1}$$

Taken the particle buoyancy and Boussinesq approximation into account while neglecting the Coriolis force, the extended momentum equation can be written using Einstein's summation notation as

$$\frac{\mathrm{d}u_i}{\mathrm{d}t} = -\frac{1}{\rho}\frac{\partial p}{\partial x_i} - \delta_{i3}g + \nu_t \frac{\partial^2 u_i}{\partial x_j^2} - g\delta_{i3}\frac{\phi_s}{\rho} + \delta_{i3}g\left[1 - \beta(\bar{\theta} - \theta_0)\right] \tag{2}$$

where x_i ($i = 1,2,3$) are the Cartesian coordinates and u_i are the Cartesian components of the velocity vector. The fourth term on the right side describes the particle buoyancy. The Boussinesq approximation $g[1 - \beta(\bar{\theta} - \theta_0)]$ considers density changes due to temperature variations in the lower atmosphere and primarily forces the katabatic surface winds. The β is the coefficient of thermal expansion. All remaining terms are similar to the common Navier–Stokes equation (e.g. Stull, 1988). Proceeding from the instantaneous internal energy equation the conservation equation of the potential temperature can be derived, and finally becomes

$$\frac{\partial \bar{\theta}}{\partial t} + \frac{\partial(\bar{\theta}u_i)}{\partial x_i} - \frac{\partial}{\partial x_j}\left(\kappa_{\mathrm{eff}}\frac{\partial \bar{\theta}}{\partial x_j}\right) = 0 \tag{3}$$

whereas temperature changes by radiative forcing and phase change of water are neglected in this study. The Reynolds averaged momentum equation is closed using the k-ω turbulence model. The equation for the turbulent kinetic energy, k, reads as

$$\frac{\partial k}{\partial t} + \frac{\partial u_j k}{\partial x_j} = P_k - \beta_k^* k\omega + \frac{\partial}{\partial x_j}\left[\left(\nu + \frac{\nu_t}{\sigma_k^*}\right)\frac{\partial \omega}{\partial x_j}\right] \tag{4}$$

with the production rate of kinetic energy by the mean velocity field, P_k, given by

$$P_k = \nu_t\left(\frac{\partial u_i}{\partial x_j} + \frac{\partial u_j}{\partial x_i}\right)\frac{\partial u_i}{\partial x_j} \tag{5}$$

The equation for dissipation uses the inverse time scale ω that determines the scale of turbulence

$$\frac{\partial \omega}{\partial t} + \frac{\partial u_j \omega}{\partial x_j} = \alpha\frac{\omega}{k}P_k - \beta_k\omega^2 + \frac{\partial}{\partial x_j}\left[\left(\nu + \frac{\nu_t}{\sigma_\omega^*}\right)\frac{\partial \omega}{\partial x_j}\right] \tag{6}$$

Based on these equations the turbulent viscosity is defined as

$$\nu_t = \frac{k}{\omega} \tag{7}$$

While the particle effect on turbulence stability is taken into account (see Eq. 2) we neglect the enhanced dissipation of turbulent kinetic energy by snow particles, even though this effect is present.

The rate of snow mass change $\partial\phi_\mathrm{s}/\partial t$ is described by the continuum equation for conservation of mass

$$\underbrace{\frac{\partial \phi_\mathrm{s}}{\partial t}}_{\text{(I)}} + \underbrace{\frac{\partial(\phi_\mathrm{s}u_i)}{\partial x_i}}_{\text{(II)}} = \underbrace{\frac{\partial}{\partial x_3}\left(K_\mathrm{M}\frac{\partial \phi_\mathrm{s}}{\partial x_3} - V\phi\right)}_{\text{(III)}} + \underbrace{\left(\frac{\partial \phi_\mathrm{s}}{\partial t}\right)_{\mathrm{sub}}}_{\text{(IV)}} \tag{8}$$

Since we make the simplifying assumption that the relative velocity between the two phases is always zero there is no need to use a combined phase continuity equation as it reduces to the equivalent single phase flow equation. The drifting snow flux in the i direction is $\phi_\mathrm{s}u_i$ and therefore the net flux due to the fluid motion is given by the divergence of the mass flux (Term II). Term IV gives the mass loss of suspended snow

by sublimation. Besides the vertical entrainment of snow particles by turbulent diffusion, there is a downward flux $-V\phi$ due to gravity (Term III). For the sake of simplicity the terminal fallout velocity V is assumed to be constant. The total amount of drifting and blowing snow mass depends on the erosion flux and accumulation flux, respectively, which are discussed in detail in the next section.

5.3 Erosion and accumulation flux

The snow mass within the saltation layer primarily gains by the aerodynamic entrainment of snow particles from the underlying snowpack. According to Anderson and Haff (1991) the erosional mass flux q_e is assumed to be proportional to the excess surface shear stress

$$q_e = e_{salt}\left(\rho u_*^2 - \rho_a\, u_{th}^2\right) \tag{9}$$

Once the surface shear stress u_*^2 exceeds the friction threshold velocity u_{th} particles are ejected from the snowpack. The efficiency of the erosional process is described by the e_{salt}. The friction threshold velocity strongly depends on the physical properties of the snowpack. Through the process of kinetic and melt-freeze metamorphosis the snowpack is in a constant state of change. Both processes modify the snow density and hence the kinetic resistance of the snowpack. The friction threshold velocity is therefore assumed to be proportional to the snow density,

$$u_{th} = 0.0195 + \left(0.021\sqrt{\rho_s}\right) \tag{10}$$

Typical values for u_{th} are in the range of $0.3\,m\,s^{-1}$ for loose fresh snow to $0.6\,m\,s^{-1}$ for consolidated firn. Based on these values saltation starts at wind speed u_{10} of about 7–$14\,m\,s^{-1}$ for consolidated snow and of about 4–$11\,m\,s^{-1}$ for fresh snow (cf. Pomeroy and Gray, 1990). However, the ejected particles do have a strong impact on the prevailing flow which affects the mass exchange process. The force exerted by the particles on

the wind field lowers the wind shear stress and consequently reduces the capacity to eject further particles. To allow for such effect the friction velocity is corrected by the particle-saturation ratio (Naaim et al., 1998). Taking into account the particle-saturation ratio the corrected friction velocity u_*^{corr} can be written as

$$u_*^{corr} = u_* + (u_{th} - u_*)\left(\frac{\phi_s}{\phi_{max}}\right)^2 \tag{11}$$

If the drifting snow density reaches saturation ϕ_{max} the friction velocity reduces to the friction threshold velocity and entrainment is suppressed. In case the saltation layer contains no particles both, the corrected and uncorrected, friction velocity are equal. The maximum concentration ϕ_{max} is estimated by the following semi-empirical relationship (Pomeroy and Male, 1992),

$$\phi_{max} = \frac{\rho}{3.29u_*}\left(1 - \frac{u_{th}^2}{u_*^2}\right) \tag{12}$$

By replacing u_* by u_*^{corr} in Eq. (9), the final erosion flux

$$q_e = e_{salt}\left(\rho\left[(u_{th} - u_*)\left(\frac{\phi_s}{\phi_{max}}\right)^2 + u_*\right]^2 - \rho u_{th}^2\right) \tag{13}$$

is obtained. Once the threshold velocity exceeds the friction velocity deposition is possible. Similar to Beyers et al. (2004) the deposition flux is simply related to the downward flux (Eq. 8) and the shear stress ratio.

$$q_d = V\phi \cdot \max\left(\frac{u_{th}^2 - u_*^2}{u_{th}^2}, 0\right) \tag{14}$$

5.4 Sublimation

Sublimation of suspended snow particles is an important process, particularly in arctic regions where saturation deficits are usually large. The used approach approximates the sublimation loss rates by

$$q_s = \psi_s \phi_s h_* + \int_{h_*}^{z} \psi_t(z)\phi_t(z)\mathrm{d}z \tag{15}$$

where the subscripts s and t indicate the saltation (with height h_*) and suspension layer, respectively. The sublimation-loss-rate coefficients, ψ_s and ψ_t, represent the time rate of change of snow particle mass as a function of the mean particle size, solar radiation, saturation deficit and conductive and advective energy and moisture transfer. For a detailed description see Schmidt (1972, 1991), Pomeroy and Gray (1995), Pomeroy et al. (1993), Bintanja (2000) and Naaim et al. (1998). The effect of sublimation on the vertical profiles of temperature and humidity is not included in this work. This simplified assumption ignores the fact that sublimation of drifting snow is a self-limiting process, in the sense that the intensity depends on the saturation deficit of the environment. Neglecting the feedback mechanism on the atmospheric profiles can therefore lead to an overestimation of snow drift sublimation.

6 Numerical setup

The snow2blow model is applied to the southwestern part of Vestfonna (79°41′49.029″ N to 80°04′09.647″ N and 18°12′33.253″ W to 19°58′17.844″ E) with an horizontal resolution of 250 m. For this study the domain top is set to 3000 m consisting of 5 vertical layers within in the near surface layer (5 m), and further 40 vertical layers above. This setup allows for a better representation of the turbulent near-surface

wind field and the derived fluxes therefrom. The decision to highly resolve the surface layer was done at the expense of the horizontal domain size, because any additional vertical layer increases the computational cost exponentially. The daily atmospheric fields from the WRF with a horizontal resolution of 2 km are mapped onto the snow2blow grid. It is then forced by the lateral boundaries of the WRF, so that an independent internal turbulent wind field can evolve. The snow mass flux at the boundaries for the saltation layer is given by the formulation of Pomeroy and Gray (1990)

$$q_{\mathrm{salt}} = \frac{0.68\rho}{u_* g} u_{\mathrm{th}} \left(u_*^2 - u_{\mathrm{th}}^2\right) \tag{16}$$

The inlet snow density profile for the suspension layer is given by Pomeroy and Male (1992)

$$\phi_s(u_*, z) = 0.8 \cdot \exp\left[-1.55\left(4.784 u_*^{-0.544} - z^{-0.544}\right)\right] \tag{17}$$

Up to now, no parametrization scheme for the snow cover evolution is included, which might account for the snow densification processes. However, in order to prevent that the entire snow cover is eroded at once only the present day fresh snow is allowed to redistribute. This is an acceptable assumption given the fact, that the high wind velocities lead to a rapid densification of the upper snow cover (Möller et al., 2011b) and formation of sastrugi. Snowdrift model parameters used for the simulations are given in Table 2.

The daily atmospheric fields employed by the WRF are based on the six hourly Global Forecast System (GSF) global gridded analysis of the National Centers for Environmental Prediction (NCEP) with a spatial resolution of 1.0°. The original fields of this product are reprocessed and dynamically downscaled to one day temporal and 2 km spatial resolution using a polar-optimized version of the WRF model (PWRF 3.1.1). Lateral boundary conditions for the downscaling are given by NCEP low resolution Real Time Global sea-surface temperature analysis (NCEP RTG SST) with a spatial resolution of 0.5° and Advanced Microwave Scanning Radiometer EOS (AMSR-E) daily sea

ice concentrations with a spatial resolution of 12.5 km. The static geographical fields of the WRF model are initialized using the United States Geological Survey (USGS) standard data sets. The applied downscaling procedure features a telescope two-way nesting of three polar stereographic domains (30, 10 and 2 km horizontal resolution). The inner domain of this nesting is used as input to the snow2blow model. All three domains are resolved in 28 vertical layers reaching up to the 50 hPa level. The temporal reprocessing from the original six hourly to the final daily datasets is done using the method presented by Maussion et al. (2010). The setup of the physical parameterizations of the WRF model is motivated by Hines et al. (2011) and Hines and Bromwich (2008).

7 Results and discussion

7.1 WRF model evaluation

The performance of the WRF generated atmospheric fields was evaluated with data from the VF-AWS. Figure 4 shows the observed wind conditions at the VF-AWS and the closest WRF grid point, respectively. Frequent strong winds of up to 15 $m s^{-1}$ are observed from the south-easterly direction, clearly indicating the persistent katabatic wind flows. In contrast, the more fluctuating north-westerly flows are weak during the entire observation period. For validation the best out of the four closest WRF model grids points was chosen and compared with the observations (Claremar et al., 2012). The WRF wind speed at 10 m height was corrected to the corresponding sensor height at 2.4 m using Monin-Obukhov theory for stable boundary layer (Stull, 1988), while the Obukhov length has been derived from the WRF output variables. The model slightly overestimates the katabatic wind speeds and tends to have a more southerly wind component (Fig. 4). Air temperatures at 2 m height varied at the VF-AWS between −37.9 and +5.8 °C during this period. Observed and modelled air temperatures significantly correlate with an r^2 = 0.98, but show a neglectable cold bias of −0.05 K, which is

a problem of the WRF model that was previously reported for the study region (Claremar et al., 2012).

Figure 5 shows the spatial distribution of the uncorrected snow water equivalent (SWE) field for the accumulation period September 2008 to May 2009 obtained from the WRF model run. Snow distribution is predominantly controlled by altitude ranging from 0.2 m w.e. in coastal areas to 0.6 m w.e. in higher regions along the ice cap ridge. The general increase of SWE with altitude is consistent with studies carried out by Grabiec et al. (2011) and Möller et al. (2011b). However, these studies also emphasize that drifting and blowing snow often lead to local scale deviation from this dominant pattern.

7.2 Snowdrift

The modelled distribution of SWE on Vestfonna ice cap for the period September 2008 to May 2009 is shown in Fig. 6. Snow is heterogeneously distributed across the domain ranging between 0.11 m w.e. in the southeast and 0.49 m w.e. in higher regions. This corresponds to a total snow loss of ∼ 10–20 % along the ridge by blowing snow. At the ice cap slopes the total snow loss is about 5–15 %. Parts of the eroded and suspended snow mass is later accumulated in the undulating northwestern forefield of the ice cap. In regions of disturbed flow, re-accumulation can be more than 0.1 m w.e. for this period. In this way, the De Geerfonna ice body receives between 15 and 20 % of its total snow mass by drifting snow which therefore is an important term for the local mass balance. Snow mass blowing away from the ice cap to the open sea was not quantified in this study. Jaedicke (2002) estimated that snow mass loss to the open sea only accounts for 0.2 % of the precipitated mass in Svalbard. In most areas near the ice fringe and the western forefield accumulation and erosion are widely balanced. In contrary, largest snow mass losses of 0.10–0.25 m w.e. (30–50 %) are found south-easterly of the main ridge. A comparison of modelled snow depths with radio-echo soundings and snow pits shows that there is a bias of +0.07 m w.e. along the ridge, while at the De Geerfonna snow is underestimated by about −0.08 m w.e. by the model.

However, these errors are insignificant in the light of the spatial variability of snow depth, which sometimes may vary between ±0.13 m w.e. within very short distances of less than 50 m caused by sastrugi formation. Due to the limited information on the spatial distribution it, however, remains uncertain, whether the deviations represent a systematic pattern or are purely random.

The occurrence of drifting and blowing snow events follow a pattern similar to the SWE distribution (see Fig. 7). Blowing and drifting of snow occur most frequently (38–40 %) at wind exposed region, such as the higher elevated regions along the ridge. In the range of the isolated upstream ice bodies (including De Geerfonna) and the ice cap slopes snow erosion occurs of 30–34 %. Lower frequencies (20–24 %) are generally found in the forefield of the ice cap and on the south-eastern slope. These pattern imply that drifting snow events are triggered by the superposition of the paramount flow and katabatic winds, whereas the latter one is according to amount less efficient. This result is similar to observations of Grabiec et al. (2011), who found that air circulation patterns over Nordaustlandet and the mesoscale surface roughness play a major role in snow redistribution on the interior of Vestfonna. The magnitude of the modelled katabatic wind component along the slopes vary between 1–2 $m s^{-1}$ at 2 m height during the winter months, and thus leading to $u_* \leq 0.1\,m s{-}1$. The glacier wind components may be underestimated as a consequence of the assumption of homogeneous surface temperatures, which affects the buoyancy term and subsequently the occurrence of drifting snow events at the slopes.

Indeed it is observed, that katabatic glacier winds redistribute snow from the slopes to the ice edge forming a persistent surrounding snow band (see arrows in Fig. 6). Since the snow band exists all year, it is very likely that more accumulation takes place at these zones. Although katabatic winds might be underestimated, the distribution of the snow band along the Vestfonna margin and the nearby Backabreen and De Geerfona are clearly reproduced by the snowdrift model. Together with the radar-echo sounding (Figs. 2 and 6) it appears that after the 2–3 km wide snow band SWE decreases rapidly within a short distance of 2 km (marker B in Figs. 6 and 2). This

decrease in SWE with altitude in the vicinity of the ice edge is also observed in most years by the snow pit measurements at location V2 and V4 (Möller et al., 2011b). The general spatial distribution along the slopes and the higher regions is reproduced by the model, as indicated by Fig. 2. Discrepancies are found in the region of the snow band and in the section between kilometer 54 and 58 along the radar-echo sounding path. The former one is most likely due to the limitations of the 250 m grid cell resolution in reproducing the complex small scale topography and its curvature pattern along the ice cap margin. Furthermore, the sudden change in mesoscale terrain roughness at the glacier fringe increases the turbulent kinetic energy and decreases the vertical wind shear. This process weakens the katabatic wind at the glacier slope, and thus the suspension capacity of the flow. Snow accumulated by this process is not captured by the model. To account for this process a Large Eddy Simulation model is required, rather than a Reynolds Averaged Models, in order to resolve the small scale flow pattern in detail. The overestimation of erosion between kilometer 54 and 58, however, can be probably attributed to boundary effects.

For the sake of clarity, drifting snow sublimation is discussed for the location VF-AWS, and has been integrated over the lower atmospheric boundary layer (10 m). Drifting and blowing snow sublimation shows a seasonal cycle with maximum values up to 8–12 % in April/May (see Fig. 8). During the winter months drifting snow sublimation rarely removes more than 6–8 % of the suspended snow. The seasonal variability can be attributed to the interplay between saturation deficit, temperature and wind speed. Particularly in spring conditions are favourable when high saturation deficits occur simultaneously with strong winds and moderate temperatures. The absorbed heat due to the sublimation process leads to a cooling and moistening of the near-surface airmass. As the moisture gradient decreases at the snow-atmosphere surface, surface sublimation gradually ceases. Since in the Arctic surface sublimation significantly contribute to the glacier surface mass balance, it is recommended to include drifting snow sublimation in such studies.

8 Conclusions

This paper presents a high-resolution (250 m) spatial estimation of snowdrift over Vestfonna ice cap during the accumulation season 2008/2009. Blowing and drifting snow are frequent processes (10–25 %), which significantly modify snow accumulation distribution of the entire ice cap. In particular, along the wind exposed zones about 10–20 % of the primarily accumulated snow is redistributed to peripheral zones and must be considered a loss term for the ice cap mass balance. In this way, ice bodies such as the De Geerfonna receive up to 20 % additional snow mass. Based on the results, three characteric erosion zones can be identified on Vestfonna ice cap: (1) *inversion zone*, increase of SWE with altitude, (2) *precipitation zone*, decrease of SWE similar to the precipitation gradient and (3) *redistribution zone*, where the spatial distribution of snow is characterized by blowing and drifting of snow triggered by the paramount flow. These zones correspond to snow radar observations of Grabiec et al. (2011). Whether blowing snow from sea ice surfaces provide additional snow mass is still an open question. There is a pronounced variation in drifting and blowing snow sublimation during the simulation period with a maximum in April/May of 8–12 % and a minimum in winter with about 6–8 %. A detailed analysis of the effect of drifting snow sublimation on surface sublimation was not performed in this study, but will be covered in the future. Further work will also include drifting and blowing snow processes into the calculation of glacier mass balance and a more detailed description of snow pack processes.

Acknowledgements. This study was co-funded by grants no. BR 2105/6-1, SCHE 750/3-1 and SCHN 680/2-1 of the German Research Foundation (DFG). The Polish Ministry of Science and Higher Education funded the radar field work by grant no. IPY/279/2006. Additional funding was provided by the International SvalGlac-Project of the European Science Foundation through the German Federal Ministry of Education and Research (BMBF, grants no. 03F0623A and 03F0623B) and NCBiR/PolarCLIMATE-2009/2-1/2010. The authors acknowledge the logistical assistance of the Swedish Polar Research Secretariat in the field that was provided in the framework of the 3rd International Polar Year (IPY) core project "IPY Kinnvika" and of the Norsk Polar Institute for provision of logistical support at Oxford Halfoya field camp.

References

Ahlmann, H.: Scientific results of the Swedish–Norwegian Artic Expedition in the summer of 1931, Part 8, Geogr. Ann., 15, 161–216, 1933. 711, 714

Anderson, R. and Haff, P.: Wind modification and bed response during saltation of sand in air, supplementum 1. Aoelian Grain Transport, 1: Mechanics, Acta Mech., 1, 21–52, 1991. 719

Beaudon, E., Arppe, L., Jonsell, U., Martma, T., Möller, M., Pohjola, V., Scherer, D., and Moore, J.: Spatial and temporal variability of net accumulation from shallow cores from Vestfonna ice cap (Nordaustlandet, Svalbard), Geogr. Ann., 93, 287–299, 2011. 711, 713

Bednorz, E. and Fortuniak, K.: The occurrence of coreless winters in central Spitsbergen and their synoptic conditions, Polar Res., 30, 12218, doi:10.3402/polar.v30i0.12218, 2011. 712

Beyers, J., Sundsbø, P., and Harms, T.: Numerical simulation of three-dimensional, transient snow drifting around a cube, J. Wind Eng. Ind. Aerod., 92, 725–747, 2004. 720

Bintanja, R.: The contribution of drifting snow sublimation to the surface mass balance of Antarctica, Ann. Glaciol., 27, 251–259, 1998. 711

Bintanja, R.: Snowdrift suspension and atmospheric turbulence, Part 1: Theoretical background and model description, Bound.-Lay. Meteorol., 95, 343–368, 2000. 714, 715, 716, 721

Boon, S., Burgess, D., Koerner, R., and Sharp, M.: Forty-seven years of research on the Devon Island ice cap, Arctic Canada, Arctic, 63, 13–29, 2010. 710

Braun, M., Pohjola, V., Pettersson, R., Möller, M., Finkelnburg, R., Falk, U., Scherer, D., and Schneider, C.: Changes of glacier frontal positions of Vestfonna (Nordaustlandet, Svalbard), Geogr. Ann., 93, 301–310, 2011. 712

Claremar, B., Obleitner, F., Reijmer, C., Pohjola, V., Waxegård, A., Karner, F., and Rutgersson, A.: Applying a mesoscale atmospheric model to Svalbard glaciers, Adv. Meteorol., 2012, 321649, doi:10.1155/2012/321649, 2012. 713, 723, 724

Crowe, C., Troutt, T., and Chung, J.: Numerical models for two-phase turbulent flows, Ann. Rev. Fluid Mech., 28, 11–43, 1996. 715

Durand, Y., Gyomarc'h, G., Mérindol, L., and Corripio, J.: Improvement of a numerical snow drift model and field validation, Cold Reg. Sci. Technol., 43, 93–103, 2005. 716

Elgobashi, S.: On predicting particle-laden turbulent flows, Appl. Sci. Res., 52, 309–329, 1994. 715

Førland, E., Hanssen-Bauer, I., and Nordli, P.: Climate statistics and longterm series of temperature and precipitation at Svalbard and Jan Mayen, Det Norske Meteorologiske Institutt Klima Report, 21, 97, 1997. 712
Gauer, P.: Numerical modeling of blowing and drifting snow in Alpine terrain, J. Glaciol., 47, 97–110, 2001. 715, 716
Gore, R. and Crowe, C.: Effect of particle size on modulating turbulent intensity, Int. J. Multiphas. Flow, 15, 278–285, 1989. 715
Grabiec, M., Puczko, D., Budzik, T., and Gajek, G.: Snow distribution patterns on Svalbard glaciers derived from radio-echo soundings, Pol. Polar Res., 32, 393–421, 2011. 711, 713, 714, 724, 725, 727, 734, 738, 740
Hagen, J.: Glacier atlas of Svalbard and Jan Mayen, 129, Norsk polarinstitutt, 1993. 713
Hines, K. and Bromwich, D.: Development and testing of polar Weather Research and Forecasting (WRF) model, Part 1: Greenland ice sheet meteorology, Mon. Weather Rev., 136, 1971–1989, 2008. 723
Hines, K., Bromwich, D., Bai, L., Barlage, M., and Slater, A.: Development and testing of polar WRF, Part 3: Arctic land, J. Climate, 24, 26–48, 2011. 723
Jaedicke, C.: Snow drift losses from an Arctic catchment on Spitsbergen: an additional process in the water balance, Cold Reg. Sci. Technol., 34, 1–10, 2002. 711, 724
Käsmacher, O. and Schneider, C.: An objective circulation pattern classification for the region of Svalbard, Geogr. Ann. A, 93, 259–271, 2011. 712
Lehning, M., Löwe, H., Ryser, M., and Raderschall, N.: Inhomogeneous precipitation distribution and snow transport in steep terrain, Water Resour. Res., 44, W07404, doi:10.1029/2007WR006545, 2008. 714
Lenaerts, J. T. M., van den Broeke, M. R., Déry, S. J., König-Langlo, G., Ettema, J., and Munneke, P. K.: Modelling snowdrift sublimation on an Antarctic ice shelf, The Cryosphere, 4, 179–190, doi:10.5194/tc-4-179-2010, 2010. 711
Lenaerts, J. T. M., van den Broeke, M. R., van Angelen, J. H., van Meijgaard, E., and Déry, S. J.: Drifting snow climate of the Greenland ice sheet: a study with a regional climate model, The Cryosphere, 6, 891–899, doi:10.5194/tc-6-891-2012, 2012. 711
Liston, G. and Sturm, M.: A snow-transport model for complex terrain, J. Glaciol., 44, 498–516, 1998. 714, 716
Loeng, H.: Features of the physical oceanographic conditions of the Barents Sea, Polar Res., 10, 5–18, 1991. 712

Maussion, F., Scherer, D., Finkelnburg, R., Richters, J., Yang, W., and Yao, T.: WRF simulation of a precipitation event over the Tibetan Plateau, China – an assessment using remote sensing and ground observations, Hydrol. Earth Syst. Sci., 15, 1795–1817, doi:10.5194/hess-15-1795-2011, 2011. 723
Mernild, S., Liston, G., Hasholt, B., and Knudsen, N.: Snow distribution and melt modeling for Mittivakkat Glacier, Ammassalik Island, southeast Greenland, J. Hydrometeorol., 7, 808–824, 2006. 710
Möller, M.: A minimal, statistical model for the surface albedo of Vestfonna ice cap, Svalbard, The Cryosphere, 6, 1049–1061, doi:10.5194/tc-6-1049-2012, 2012. 713
Möller, M., Finkelnburg, R., Braun, M., Hock, R., Jonsell, U., Pohjola, V., Scherer, D., and Schneider, C.: Climatic mass balance of Vestfonna ice cap, Svalbard: a spatially distributed assessment using ERA-Interim and MODIS data, J. Geophys. Res., 116, F03009, doi:10.1029/2010JF001905, 2011a. 713
Möller, M., Möller, R., Beaudon, E., Mattila, O.-P., Finkelnburg, R., Braun, M., Grabiec, M., Jonsell, U., Luks, B., Puczko, D., Scherer, D., and Schneider, C.: Snowpack characteristics of Vestfonna and DeGeerfonna (Nordaustlandet, Svalbard) – a spatiotemporal analysis based on multiyear snow-pit data, Geogr. Ann., 93, 273–285, 2011b. 711, 713, 714, 722, 724, 726
Möller, M., Finkelnburg, R., Braun, M., Scherer, D., and Schneider, C.: Variability of the climatic mass balance of Vestfonna ice cap (northeastern Svalbard), Ann. Glaciol., 54, 1979–2011, 2013. 713
Naaim, M., Naaim-Bouvet, F., and Martinez, H.: Numerical simulation of drifting snow: erosion and deposition models, Ann. Glaciol., 26, 191–196, 1998. 716, 720, 721
Pomeroy, J. and Gray, D.: Saltation of snow, Water Resour. Res., 26, 1583–1594, 1990. 716, 719, 722
Pomeroy, J. and Gray, D.: Snowcover accumulation, relocation and management., B. Int. Soc. Soil Sci., 88, 422–423, doi:10.1080/02626669609491514, 1995. 721
Pomeroy, J. and Male, D.: Steady-state suspension of snow, J. Hydrol., 136, 275–301, 1992. 720, 722
Pomeroy, J., Gray, D., and Landine, P.: The prairie blowing snow model: characteristics, validation, operation, J. Hydrol., 144, 165–192, 1993. 721
Rogers, A., Bromwich, D., Sinclair, E., and Cullather, R.: The atmospheric hydrologic cycle over the Arctic Basin from reanalyses, Part 2: Interannual variability, J. Climate, 14, 2414–2429, 2001. 713

Schmidt, R.: Sublimation of Wind-Transported Snow: a Model, Rocky Mountain Forest and Range Experiment Station, Forest Service, US Department of Agriculture, 1972. 721
Schmidt, R.: Sublimation of snow intercepted by an artificial conifer, Agr. Forest Meteorol., 54, 1–27, 1991. 721
Schneiderbauer, S., Tschachler, T., Fischbacher, J., Hinterberger, W., and Fischer, P.: Computational fluid dynamic (CFD) simulation of snowdrift in alpine environments, including a local weather model, for operational avalanche warning, Ann. Glaciol., 48, 150–158, 2008. 715, 716
Schytt, V.: Scientific results of the Swedish glaciological expedition to Nordaustlandet, Spitsbergen, Geogr. Ann., 46, 242–281, 1964. 711
Skeie, P.: Meridional flow variability over the Nordic seas in the, Geophys. Res. Lett., 27, 2569–2572, 2000. 712
Stull, R.: An Introduction to Boundary Layer Meteorology, vol. 13, Springer, Kluver Academic, Dordrecht, the Netherlands, 1988. 717, 723
Svendsen, H., Beszczynska-Møller, A., Hagen, J., Lefauconnier, B., Tverberg, V., Gerland, S., Ørbæk, J., Bischof, K., Papucci, C., Zajaczkowski, M., Azzolini, R., Bruland, O., Wiencke, C., Winther, J.-G., and Dallmann, W.: The physical environment of Kongsfjorden-Krossfjorden, an Arctic fjord system in Svalbard, Polar Res., 21, 133–166, 2002. 712
Taurisano, A., Schuler, T., Hagen, J., Eiken, T., Loe, E., Melvold, K., and Kohler, J.: The distribution of snow accumulation across the Austfonna ice cap, Svalbard: direct measurements and modelling, Polar Res., 26, 7–13, 2007. 711, 712
Walczowski, W. and Piechura, J.: Influence of the West Spitsbergen Current on the local climate, Int. J. Climatol., 31, 1088–1093, 2011. 712

Table 1. Notation.

u_*	friction velocity [$\mathrm{m\,s^{-1}}$]
τ_0	surface shear stress [$\mathrm{kg\,m^{-1}\,s^{-2}}$]
z	height above surface [m]
κ	von Kármán constant
ϕ_s	snow mass in saltation layer [$\mathrm{kg\,m^{-3}}$]
ϕ_max	max. particle concentration (steady-state) [$\mathrm{kg\,m^{-3}}$]
β	coefficient of expansion [$\mathrm{K^{-1}}$]
θ	potential temperature [K]
K_M	eddy diffusivity [$\mathrm{m^2\,s}$]
κ_eff	heat transfer coefficient [$\mathrm{m^2\,s}$]
ν	kinematic viscosity [$\mathrm{m^2\,s}$]
ν_t	turbulent viscosity [$\mathrm{m^2\,s}$]
δ_{ij}	Kronecker delta
ρ	air density [$\mathrm{kg\,m^{-3}}$]
k	turbulent kinetic energy [$\mathrm{m^2\,s^{-2}}$]
ω	turbulent dissipation [$\mathrm{s^{-1}}$]
α	$k-\omega$ model coefficient
β_k, β_k^*	$k-\omega$ model coefficients
$\sigma_k^*, \sigma_\omega^*$	$k-\omega$ model coefficients
ρ_s	snow density [$\mathrm{kg\,m^{-3}}$]
e_salt	efficiency of saltation [$0 \le e_\mathrm{salt} \le 1$]
h_salt	saltation layer height [m]
g	gravity acceleration [$\mathrm{m\,s^{-2}}$]
u_salt	horizontal saltation particle velocity [$\mathrm{m\,s^{-1}}$]
V	mean particle settling velocity [$\mathrm{m\,s^{-1}}$]
u_th	friction velocity threshold [$\mathrm{m\,s^{-1}}$]
q_e	erosion flux [$\mathrm{kg\,m^{-2}\,s^{-1}}$]
q_d	vertical turbulent diffusion flux [$\mathrm{kg\,m^{-2}\,s^{-1}}$]
q_s	horizontal flux in saltation layer [$\mathrm{kg\,m^{-2}\,s^{-1}}$]
q_salt	snow mass flux in the saltation layer [$\mathrm{kg\,m^{-2}\,s^{-1}}$]
$\psi_\mathrm{s}, \psi_\mathrm{t}$	sublimation-loss-rate coefficients [–]

Table 2. Model parameters.

Parameter	Symbol	Value	Unit
Erosion efficiency	e_{salt}	5×10^{-4}	–
Fallout velocity	V	0.02	ms^{-1}
Fresh snow density	ρ_s	250	kgm^{-3}

733

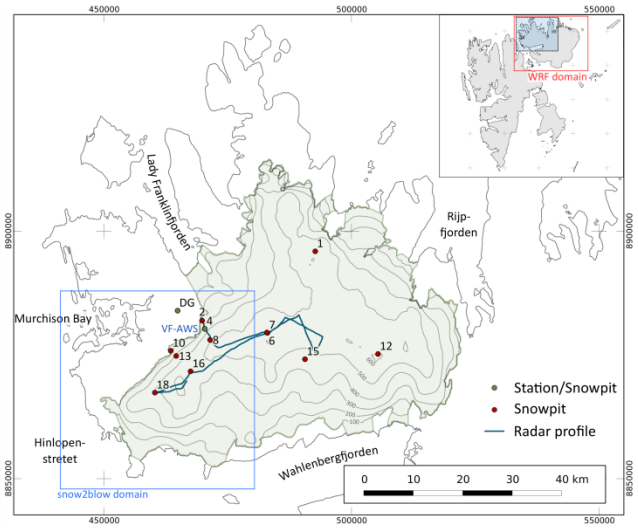

Fig. 1. Detailed map of Vestfonna ice cap (UTM 34N, WGS84). The grey shading shows the approximately edge of the ice cap. The locations of the Automatic Weather Stations VF-AWS (accompanied by snowpit measurement) are denoted as green dots, single snowpit measurements as red dots. The radio-echo sounding profile of Grabiec et al. (2011) is indicated as a blue line.

734

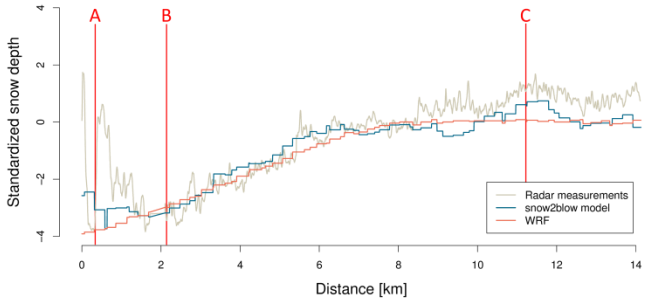

Fig. 2. The standardized anomalies (by subtracting the sample mean, and dividing by the sample standard deviation) of the radio-echo sounding, modelled snow depths and WRF along the profile shown in Fig. 1. Capital letters correspond to the markers given in Fig. 6.

735

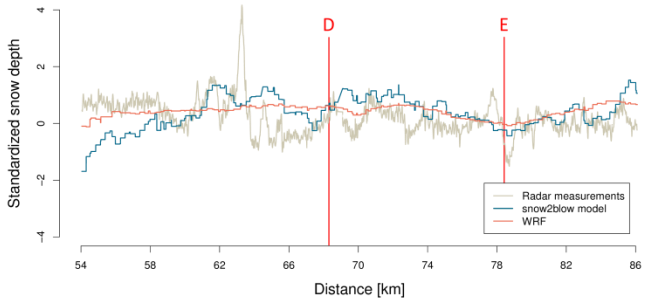

Fig. 3. The standardized anomalies (by subtracting the sample mean, and dividing by the sample standard deviation) of the radio-echo sounding, modelled snow depths and WRF along the profile shown in Fig. 1. Note that the mean SWE of the radio-sounding, snow2blow model and WRF model is approximately 0.34 m, 0.47 m and 0.56 m. Capital letters correspond to the markers given in Fig. 6.

736

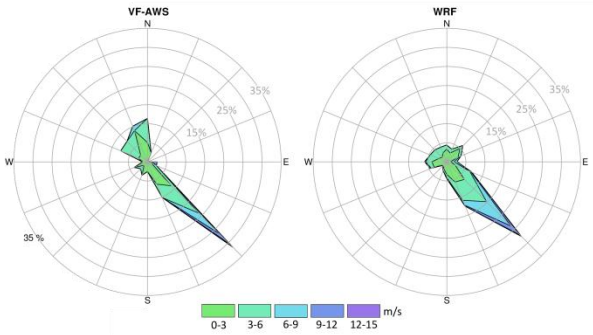

Fig. 4. Wind direction and speed measured at the VF-AWS (left) and modelled by the WRF (right).

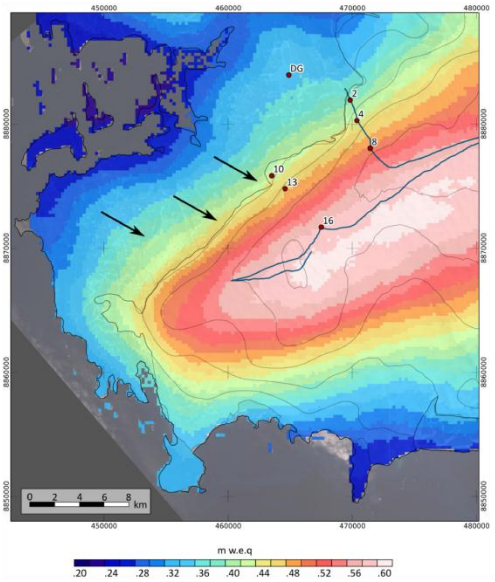

Fig. 5. Snow accumulation in m w.e. from the WRF model runs over the period September 2008 to May 2009. The arrows mask regions of special interest which are discussed in detail in the text. The blue line shows the radio-echo sounding profile of Grabiec et al. (2011) in May 2009.

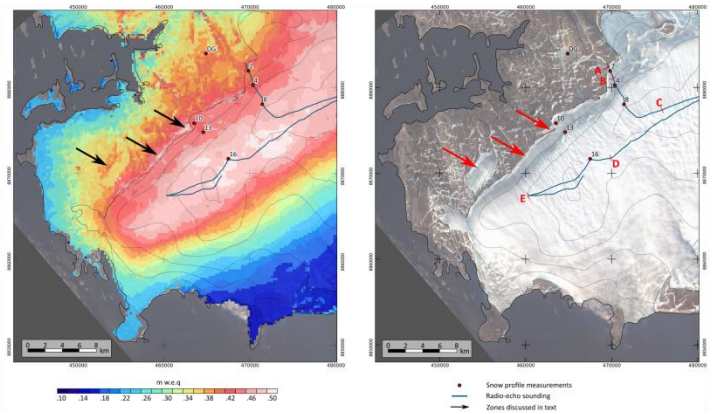

Fig. 6. Modelled snow depths in m w.e. after the accumulation season 2008/2009 (left) and ASTER satellite image from 17 August 2000 (right, UTM 34N, WGS84). The arrows mark regions of special interest which are discussed in detail in the text. The blue line shows the path of the radio-echo sounding measurements in May 2009.

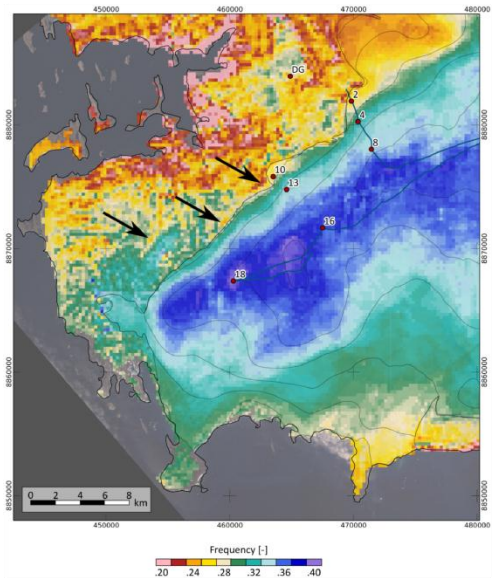

Fig. 7. Drifting snow frequency in the period September 2008 to May 2009, defined as the ratio of days with non-zero erosion flux and the total number of days. The blue line shows the radio-echo sounding profile of Grabiec et al. (2011) in May 2009.

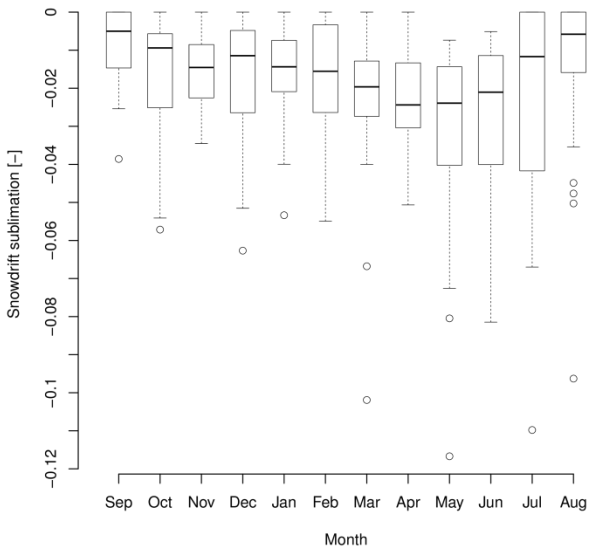

Fig. 8. Interseasonal variability of the mean drifting snow sublimation within the near-surface layer (below 10 m) at the location VF-AWS. The boxes spread between lower and upper quartiles of the values with the median shown as the thick line in between, the whiskers extend the boxes by 1.5 times the inter quartile range. Values outside this range are considered as outliers.

Appendix E: On elevational gradients of air temperature on Vestfonna, Svalbard

Finkelnburg, R., Scherer, D., Möller, M., Hock, R., Jonsell, U., Braun, M. and Schneider, C., 2013. On elevational gradients of air temperature on Vestfonna, Svalbard. To be submitted to *The Cryosphere*.

Status: Manuscript prepared for submission

Own contribution:

- Preparation, conduction and leading of field campaigns
- Design and implementation of measurement concepts
- Acquisition of field observational data and from online data bases
- Software and hardware design and implementation of the reanalysis framework
- Production of the EAR data sets
- Processing, analysis and interpretation of data from field observation, AWS, NPI, UNIS, remote sensing systems, global tropospheric analyses and the EAR
- Literature review on atmospheric modeling and observational studies
- Preparation of the manuscript including all figures and tables
- Revision of the manuscript after comments and improvements of the co-authors

On elevational gradients of air temperature on Vestfonna, Svalbard

R. Finkelnburg[1], D. Scherer[1], M. Möller[2], R. Hock[3], U. Jonsell[4] ,M. Braun[5] and C. Schneider[2]

[1]Department of Ecology, Technische Universität Berlin, Berlin, Germany.
[2]Department of Geography, RWTH Aachen University, Aachen, Germany.
[3]Geophysical Institute, University of Alaska Fairbanks, Fairbanks, Alaska, USA.
[4]The Swedish Research Council for Environment, Agricultural Sciences and Spatial Planning, Stockholm, Sweden.
[5]Institute of Geography, University of Erlangen-Nuremberg, Erlangen, Germany.

Abstract. Many glaciers and ice caps in Svalbard show a negative surface mass balance. In contrast, modelling studies of Vest- and Austfonna ice caps in northeastern Svalbard indicate near-zero surface budgets during recent decades. However, uncertainty remains about the present state of the balance of these ice masses. Most of the used numerical modelling approaches employ elevational gradients of near-surface air temperature ($\frac{\partial T}{\partial h}$), often also referred to as lapse rates, combined with digital elevation models for generating the required temperature input fields. Studies on other glaciers show considerable seasonal or even daily variations in $\frac{\partial T}{\partial h}$. Additionally results of surface mass balance modelling have shown to be sensitive to the assumptions on $\frac{\partial T}{\partial h}$. The aim of this study is to investigate $\frac{\partial T}{\partial h}$ and its temporal variability on Vestfonna with the ultimate goal to improve the spatial representation of temperature in mass balance models. We use data obtained from weather stations on and around Vestfonna, reconstructed time series derived from statistical transfer of temperature measured at Svalbard-Lufhavn and gridded data sets from the European Arctic Reanalysis (EAR) for the glacier mass-balance years 2001 to 2011. Annual mean values (-5.4 ± 2.9 K/km) are found to be higher than the often used standard moist adiabatic values. Furthermore, the existence of a two-phase annual course of $\frac{\partial T}{\partial h}$ is revealed. The general course of $\frac{\partial T}{\partial h}$ seems to be determined by the progression of radiative cooling, advection and sea ice variations during Polar night and melt and refreezing during Polar day. We further found coherences with courses and features published for the Arctic PBL in general.

1 Introduction

Many glaciers and ice caps in Svalbard have shown a negative surface mass balance during recent decades (e.g. Rasmussen and Kohler, 2007; Rye et al., 2010; Grabiec et al., 2012; van Pelt et al., 2012) consistent with glaciers in many regions of the world (e.g. Kaser et al., 2006; Cogley, 2009). In contrast, observations and modelling studies indicated that on average the ice caps Vest- and Austfonna in northeastern Svalbard have experienced a near-zero surface budget in recent years (Schuler et al., 2007; Möller et al., 2011; Möller et al., 2013). However, uncertainty remains about the present state of balance of these ice masses and its possible response to climate change.

Spatially distributed numerical models are a valuable tool to obtain information on the current state and to better understand the past and future of glacier mass changes. These models require spatially distributed time series of meteorological data as input. Observations at one or several automatic weather stations (AWS) or various gridded climate products have been used to generate distributed temperature

series by inter-/extrapolation using various approximation techniques. One of the key variables is near-surface air temperature (usually at 2 m above ground), which largely controls ice and snow melt (e.g. Ohmura, 2001; Hock, 2003, 2005). Elevation generally exerts a strong control on near-surface air temperature whereas horizontal differences are often less pronounced. Thus, elevational gradients of near-surface air temperature, often referred to as lapse rates, combined with digital elevation models provide a widely used method for generating temperature input fields.

In the glaciological community lapse rates refer sometimes to a decrease (e.g. Gardner et al., 2009) and sometimes to an increase (e.g. Braun and Hock 2004) in near-surface air temperature with elevation following the glacier surface. On the other hand in atmospheric science air temperature lapse rates are defined as decrease (e.g. Stull, 1991) or increase (e.g. Rennick, 1977) of air temperature with vertical height. Thus, in this study we use the term vertical gradient of air temperature, henceforth referred to as $\frac{\partial T}{\partial z}$, defined as increase of air temperature with vertical height and the term elevational gradient of air temperature, henceforth referred to as $\frac{\partial T}{\partial h}$, defined as increase in near-surface air temperature with elevation along the glacier surface to avoid any confusion.

Based on a digital elevation model, $\frac{\partial T}{\partial h}$ may be used to extrapolate temperature measurements across an entire glacier. In the simplest form, the standard moist adiabatic lapse rate of −6.5 K/km is used as time-constant value (e.g. Michlmayr et al., 2008; Nolin et al., 2010). Other authors keep $\frac{\partial T}{\partial h}$ constant in time, but determine $\frac{\partial T}{\partial h}$ from measurements (e.g. Schuler et al., 2007; Möller et al., 2011). However, previous studies have shown considerable seasonal or even daily variations in $\frac{\partial T}{\partial h}$ (e.g. Braun and Hock, 2004; Marshall et al. 2007; Gardner and Sharp, 2009; Gardner et al., 2009; Petersen and Pellicciotti, 2011) indicating that modeling results may be sensitive to the assumptions on $\frac{\partial T}{\partial h}$. Marshall et al. (2007) suggested that temporal variations in $\frac{\partial T}{\partial h}$ are primarily driven by variations in the local energy balance.

The aim of this study is to investigate $\frac{\partial T}{\partial h}$ and its temporal variability on Vestfonna with the ultimate goal to improve the spatial representation of air temperature in mass balance models. We use discontinuous daily mean temperature measurements obtained from several weather stations on and around Vestfonna, and data from Svalbard-Lufhavn to reconstruct continuous daily time series for the period 2001 to 2011 by statistical transfer functions. In addition we use daily mean temperature time series for the Vestfonna region from the European Arctic Reanalysis (EAR) (Finkelnburg et al., 2013) for the glacier mass-balance years 2001 to 2011. Daily $\frac{\partial T}{\partial h}$ are computed from linear regression analysis, and effects of net radiation, melt, refreezing and sea ice variations on seasonal progression of $\frac{\partial T}{\partial h}$ are explored.

2 Study region

Vestfonna is located on Nordaustlandet, the second largest island of the Svalbard archipelago, separated from Spitsbergen by the Hinlopenstrait (Fig. 1). Two large ice caps (Vestfonna and Austfonna) and several smaller ice masses are located on Nordaustlandet. Vestfonna covers an area of approximately 2,340 km^2 (Braun et al., 2011) and has a dome-like shape with altitudes up to 647 m a.s.l.. Two large ridges form the highest points of Vestfonna stretching across the central parts in east-west and north-south directions. Vestfonna drains through several outlet glaciers most of them terminating in the ocean.

Generally, the winter season is warmer and summer season is colder in Svalbard than at comparable latitudes due to strong maritime conditions. Cold arctic air masses and warm ocean currents (West Spitsbergen Current)

generate a strong air temperature gradient from south-west to north-east across Svalbard (Loeng, 1991 and Schuler et al., 2007). Thus, Nordaustlandet is among the coldest regions in Svalbard (Hisdal, 1976).

Near-surface air temperature at Vestfonna shows a distinct seasonal pattern with large day-to-day variability (Fig. 2) especially in winter. We observe some asymmetry in this seasonal course since the period of continuously increasing monthly mean air temperatures comprises four months (March to July) while the period of continuously decreasing monthly mean air temperatures comprises eight months (July to March). An annual mean air temperature of −10 °C at 370 m a.s.l., i.e. approximately the equilibrium line altitude (ELA) of 380 m a.s.l. (Möller et al. 2011), for the region of Vestfonna was calculated from data of VF-AWS370 (see Fig. 1) for the period 2008 to 2011.

3 Data

3.1 Overview of atmospheric measurement data on Nordaustlandet

As part of several expeditions atmospheric variables have been measured on Nordaustlandet since the 1930s. Most of the datasets before 2004 cover only a few weeks up to a few months (e.g. Tymms, 1925; Sandford, 1926; Ahlmann, 1933; Angström, 1933; Eriksson., 1933; Thompson, 1953; Arkhipov,1987; Watanabe et al. 2000; Motoyama et al., 2001 and Blake, 2006). Only three datasets (1935-36, 1944-45 and 1957-58) provide continuous observations for nearly a whole year (e.g. Glen, 1937 and 1939; Liljequist, 1959; Dege, 1960; Schytt, 1964, Ekman, 1971 and Palosuo, 1987).

Continuous AWS measurements started on Nordaustlandet in April 2004, when two AWS were installed on Austfonna (Schuler et al. 2007). In January 2007 an additional AWS (RF-AWS, Fig. 1.) was set up by The University Center in Svalbard (UNIS) at the coast line of Rijpfjorden. During the Third International Polar Year (IPY) the measurement network was extended by one additional AWS on Austfonna and eight AWS near Kinnvika (KV-AWS) on De Geerfonna (DG-AWS) and on various locations on Vestfonna. While all stations recorded air temperature, some stations also included measurements of relative humidity, short- and long-wave radiation fluxes, wind speed and direction, atmospheric CO_2 and water vapour concentration, three-dimensional wind components and virtual acoustic air temperature, vertical profiles of soil and ice temperature, soil and ice heat flux, water content and surface displacement.

3.2 Air temperature

We use four different data sets of air temperature in this study: (1) AWS data series directly measured on and around Vestfonna between 2007 and 2011, (2) reconstructed data series at all station locations, (3) gridded air temperature data obtained from the European Arctic Reanalysis (EAR) and (4) air temperature measurements at Haudegen station in 1944/1945. The datasets are described in detail in the following sections.

3.2.1 AWS data

We use the daily mean near-surface air temperature data from seven AWS (Fig. 1) operated on and around Vestfonna between 2007 and 2011. Details about the AWS and available datasets are provided in Tables 1 and 2. Sensor height differs between the installations. No height correction of air temperature is applied. All data were quality-controlled and temperatures exceeding plausible ranges ($T < -50$ °C and $T > 30$ °C) as well as unrealistic outliers were eliminated. Daily means based on data covering less than 80 % of the day and all days of any month covering less than 80 % of the days of that month were eliminated from the analysis.

Different sensor systems and installation variants were used at the weather stations used in this study (Table 2). Thus, systematic and statistical errors can vary within the network.

Considering the statistical errors a mean air temperature of −10 °C was calculated from all valid temperature readings of the measurement network. Thus, we consider the contribution of sensor accuracy to the statistical error in the individual temperature reading to be equal to the sensor accuracy at −10 °C. We have a statistical error reduction by almost a factor of five in the daily means, since daily temperatures are always based on at least 20 individual readings (80 % of at least hourly readings, on average the number of readings per day is much higher). Therefore the statistical error on daily mean values is estimated to be less than 0.1 K considering the accuracies in Table 2. Addressing systematic errors we carried out reference measurements between sensors. These measurements showed sensor offsets were less than 0.2 K. Radiation errors were reduced by installing radiation shields at all sensors. In addition some sensors were artificially ventilated. Considering studies on the influence of ventilation on air temperature measurements for glacier-climate studies (e.g. Georges and Kaser, 2002) we estimate the systematic error caused by radiation on daily means to be less than 0.5 K for ventilated sensors and less than 1 K for unventilated sensors in the region of Vestfonna. Therefore, we estimate the mean error being not higher than 1 K for daily means considering all contributing errors.

3.2.2 Reconstructed data

Due to instrument failure all time series described in section 3.2.1 show considerable data gaps (Fig. 3). Daily mean air temperature data from Svalbard-Lufthavn, Longyearbyen (WMO-Nr. 010080, 15.4667°E 78.2500°N, 28 m a.s.l.) operated by the Norwegian Meteorological Institute (http://eklima.met.no) were used to reconstruct continuous data series at all station locations by the method described in section 4.1. For consistency we chose to use the reconstructed data series also for the periods of available measurements.

3.2.3 European Arctic Reanalysis (EAR) data

In addition, we used gridded 2 m air temperature data of 2 km horizontal resolution obtained from the European Arctic Reanalysis (EAR). The EAR set up is described and analysed in detail in Finkelnburg et al. (2013). The data set used in this study comprises hourly data on 2 m air temperature of 2 km horizontal resolution for the Nordaustlandet domain of the glacier mass-balance years 2001 to 2011.

Outlines of Vestfonna were derived from the Randolph Glacier Inventory (http://www.glims.org/RGI/randolph.html) to define the region of interest and generate the subset of gridded 2 m air temperature data of 2 km horizontal resolution obtained from the EAR. Finally, daily mean values were generated for this subset.

3.2.4 Measurements at Haudegen station in 1944/1945

We used daily mean near-surface air temperature measurements and daily vertical profiles of air temperature measured by radio soundings in 1944/1945 at Haudegen station (Dege, 1960; Fig. 1) to investigate causes of seasonality in $\frac{\partial T}{\partial h}$. We discarded all data of a month if less than 25 % of the month's daily vertical air temperature profiles were available.

3.3 Surface net radiation data

We used radiation measurement data from VF-AWS335 (Fig. 1) between 1st June 2007 and 13th May 2009 to explore the effect of surface net radiation on the seasonal variations of $\frac{\partial T}{\partial h}$. A Kipp&Zonen CNR-1 sensor mounted 1.2 m above the snow surface measured all four (short-wave and long-wave) radiation fluxes. All data was quality-controlled analogue to the procedure used for the air temperatures applying plausible ranges of $R > -300$ W/m^2 and $R < 800$ W/m^2. Surface net solar radiation (down-welling minus up-welling short wave radiation), surface net thermal radiation (down-

welling minus up-welling long wave radiation), and surface net radiation (surface net thermal radiation plus surface net solar radiation) were calculated from the filtered data.

3.5 Sea ice data

Additionally we used daily sea ice concentrations from Advanced Microwave Scanning Radiometer for Earth Observing System (AMSR-E) observations at 12.5 km horizontal resolution to explore the effect of sea ice variation on the seasonal variations of $\frac{\partial T}{\partial h}$. Missing values in the sea ice dataset were filled with values of the nearest valid neighbor. Since sea ice data was analysed with EAR data the region of interest was defined by the Nordaustlandet domain of the EAR. Domain-wide daily mean sea ice concentration was calculated from the subset and used for the analysis.

4 Methods

4.1 Reconstruction of daily mean air temperature time series

Due to large data gaps we reconstructed continuous data series at the AWS using temperature data from Longyearbyen. Daily temperatures of each AWS have been regressed against those from Longyearbyen. The resulting linear relations in Table 3 were used to reconstruct continuous data series for the entire study period 2001 to 2011. Thus reconstructed data series were used to compute $\frac{\partial T}{\partial h}$. For consistency we chose to use the reconstructed data series also for the periods of available measurements. Using data from Ny-Ålesund (WMO-Nr. 010070, 11.9333°E 78.9167°N, 8 m a.s.l.) instead of Longyearbyen produced no statistically significant differences in the correlations.

The distances between measurement site and reference station vary between 203 and 263 km., which is below the correlation length of approximately 1,000 km during the winter season and 300 km during the summer season for monthly mean near-surface air temperatures in the Arctic as determined by Rigor et al. (2000).

We used linear regressions as reconstruction method which reduces the total variance and simultaneously filters extreme values out of the data. Unmatched variance and extremes are therefore internalized into the root mean squared errors (rmse).

Correlations between the mean daily temperature at each sensor and the reference station are very high (r^2 values range between 0.85 and 0.93), and are statistically significant on the 0.01 significance level. Table 3 shows the results of the regressions used for the reconstruction of daily mean air temperature by each sensor. The average rmse of all sensor regressions is 2.7 K on a daily basis and 0.9 K on a monthly basis (not shown in Table 3). Table 3 also presents rmse values for all days with mean near-surface air temperatures above 0 °C for which we find a 15 % lower value in average. Probably, snow and ice melting and refreezing dampens the amplitude in near-surface air temperatures, and therefore slightly lowers the rmse in the summer season.

4.2 Gradients of air temperature

In this study two kinds of gradients of air temperature are calculated, i.e. $\frac{\partial T}{\partial h}$ from AWS measurements, reconstructed data and EAR data and $\frac{\partial T}{\partial z}$ from Haudegen data. The gradients are computed day by day by linear regression where altitude is used as predictor and air temperature is used as predictand. The slope of the resulting regression function defines the gradient.

Calculation of $\frac{\partial T}{\partial h}$ from AWS measurements consists of two steps. First, we determine the lowest and highest elevation with valid data within our AWS network day by day. If this elevation difference is less than 150 m $\frac{\partial T}{\partial h}$ is not calculated. We estimated this limit from the maximum mean measurement error of about 1 K for daily means (see above) and the

expected magnitude of −6.5 K/km (standard moist adiabatic lapse rate) for $\frac{\partial T}{\partial h}$, i.e.

$$ABS\left(\frac{1K}{-6.5\frac{K}{km}}\right) \approx 150\ m$$

This means data of an elevation differences less than 150 m are problematic since the difference in the near-surface air temperatures at two different elevations may be smaller than the measurement error. In a second step daily $\frac{\partial T}{\partial h}$ are computed by the regression method described above.

For the calculation of $\frac{\partial T}{\partial z}$ of the lower boundary layer we use all valid air temperature values below 1000 m a.s.l. at Haudegen station including daily mean near-surface air temperatures and the radiosonde profiles. $\frac{\partial T}{\partial z}$ is discarded if less than three valid records are available for the linear regression or months have less than 25 % of days with valid data (see Table 4).

5 Results

5.1 Elevational gradients derived from measurement data

Values of $\frac{\partial T}{\partial h}$ derived from measurement data have a mean value of −5.7 ± 5.4 K/km and a median value of −6.3 K/km (Fig. 4). The large standard deviation of 5.4 K/km is produced by the large day-to-day variability. The mean and median values of $\frac{\partial T}{\partial h}$ are above the moist adiabatic lapse rate (0 °C and 1013 hPa: −6.5 K/km, −20 °C and 1013 hPa: −8.7 K/km) indicating that stable atmospheric conditions are generally prevailing near the surface on Vestfonna. We observe a clear seasonality in monthly mean and median of $\frac{\partial T}{\partial h}$. The values of $\frac{\partial T}{\partial h}$ are generally higher in winter and summer while lower in spring and autumn. Therefore, conditions seem less stable during spring and autumn (i.e. −7.5 ± 4.4 K/km, February, March and August to October) than during winter and summer (i.e. −4.7 ± 5.5 K/km, November to January and April to July). The seasonal course of $\frac{\partial T}{\partial h}$ shows minima in February, May and October and maxima in January, April and June.

5.2 Elevational gradients derived from reconstructed data and the EAR

Values of $\frac{\partial T}{\partial h}$ derived from the reconstructed data and from EAR are of the same magnitude like $\frac{\partial T}{\partial h}$ derived from measurements (see Fig. 5). The interannual and intra annual variability of $\frac{\partial T}{\partial h}$ is well captured by the EAR while underestimated by the reconstructed data. A prominent difference is observable especially during summer wherein the reconstructed data indicate very unstable conditions whereas the EAR and measurement data indicate stable conditions. We therefore assume the process of melt and its influence on near-surface air temperatures are not well captured by the reconstruction. Also periods of strong stability during winter (e.g. 2011 in Fig. 5) are not well captured by the reconstruction while the EAR performs better under these conditions. Thus, we only analyze $\frac{\partial T}{\partial h}$ derived from measured data and the EAR in the following paragraphs.

A correlation analysis of the 30-day means of $\frac{\partial T}{\partial h}$ derived from measured data and the EAR is shown in Fig. 6. It is significant on the 0.01 significance level with a r^2 of 0.45, rmsd of 1.7 K/km and a mean bias of 0.2 K/km. $\frac{\partial T}{\partial h}$ derived from the EAR. The EAR comprises data of the whole Vestfonna region whereas the measurement data comprises point measurements with a strong bias to western regions and lacks in the times series. We assume that these factors partly generate the differences indicated by r^2, rmsd and bias in the correlation.

$\frac{\partial T}{\partial h}$ derived from the EAR has a mean value of −5.4 ± 2.9 K/km and a median value of −6.1 K/km (Fig. 7). The standard deviation of

2.9 K/km is nearly half of the standard deviation of $\frac{\partial T}{\partial h}$ derived from the measurements (see above). Mean and median values are in good accordance with results derived from measurements (Fig. 4) if the bias of 0.2 K/km is considered. This indicates a good accuracy of the method. Nevertheless, differences between values in Fig. 4 and 7 are observable during periods of $\frac{\partial T}{\partial h}$ maxima in Fig. 7, i.e. January, March and July. The April maximum of Fig. 4 is shifted to March in Fig. 7 while the June maximum in Fig. 4 is shifted to July in Fig. 7. As mentioned before we strongly assume that these differences are caused by temporal changes in elevations represented by the measurements data (see Fig. 3 and Fig. 5). During the period May 2007 to April 2008 measurements above 335 m a.s.l. mainly provide data for $\frac{\partial T}{\partial h}$ calculations. We observe a retarded increase in $\frac{\partial T}{\partial h}$ derived from measurements compared to $\frac{\partial T}{\partial h}$ derived from the EAR during this period. We suppose the later increase during summer is caused by later onset of melt and the later decrease in winter is caused by better mixing due to higher wind speeds at higher altitudes. This also explains the decrease in amplitude of the variation in $\frac{\partial T}{\partial h}$ derived from measurements since climate conditions are assumed to be more homogeneous in the interior than at the edge of the ice cap. During the period May 2008 to July 2008 only measurements located in the ablation zone, i.e. below the ELA of 380 m a.s.l., are available. $\frac{\partial T}{\partial h}$ derived from measurement data shows higher values and an earlier increase than $\frac{\partial T}{\partial h}$ derived from the EAR. The same holds true for the period November 2010 to September 2011.

During the period September 2008 to April 2009 measurement data located in the ablation zone and the accumulation zone is available. During this period $\frac{\partial T}{\partial h}$ derived from measurement data show the best consistency with $\frac{\partial T}{\partial h}$ derived from the EAR (see Fig. 5). Nevertheless, during February and March a systematic deviation, i.e. $\frac{\partial T}{\partial h}$ derived from measurement data are lower than $\frac{\partial T}{\partial h}$ derived from the EAR, is observable. We argue these differences are mainly caused by the fact that measurement data represents only parts of the whole ice cap in contrast to gridded EAR data.

Thus, the EAR dataset seems the best suitable for the analysis of the seasonal course, inter- and intra-annual variability of $\frac{\partial T}{\partial h}$ on Vestfonna since it comprises an eleven-year period without gaps or distribution biases and is capable of reproducing measured seasonality in general.

6 Discussion

Schytt (1964) published a value of −6.9 K/km of $\frac{\partial T}{\partial h}$ obtained from field measurements on Vestfonna carried out during July and August 1958. For these months we calculated a mean of −5.3 K/km of $\frac{\partial T}{\partial h}$ from the measurements and −3.7 K/km of $\frac{\partial T}{\partial h}$ from the EAR. Both values are considerably higher. Schytt (1964) derived his values by comparing two records from Vestfonna with a record from Murchison Bay. He mentioned that the temperature variations are much smaller on the ice cap and that air temperatures at Murchison Bay are generally larger than at the glacial sites. We therefore argue that the usage of Murchison Bay temperature measurements not located on the ice cap could have generated too small $\frac{\partial T}{\partial h}$ values.

In Möller et al. (2011) measurements of VF-AWS240, VF-AWS370 and VF-AWS500 during the period of June 2008 to April 2009 were used to obtain a mean value of $\frac{\partial T}{\partial h}$ of −7.0 ± 3.7 K/km. We calculated a mean value of $\frac{\partial T}{\partial h}$ of −5.6 K/km from the EAR for this period. The difference between these results is probably caused by two reasons. Fig. 3 indicates that only using VF-AWS240, VF-AWS370 and VF-AWS500 in the

period of June to September 2008 is error-prone since the elevational difference of the used data is small enough that measurement errors can have considerable impact on $\frac{\partial T}{\partial h}$ calculations. Furthermore, we see in Fig. 5 that the winter 2008 experienced very low $\frac{\partial T}{\partial h}$ values compared to other winters. Also a temporal difference between $\frac{\partial T}{\partial h}$ derived from measurements (red line) and from the EAR (black line) exists in spring 2009 whereas $\frac{\partial T}{\partial h}$ from measurements is lower than from the EAR. Therefore data in Möller et al. (2011) strongly reflect the conditions of the unstable winter and spring period 2009. However, the values derived from the EAR in this study (-5.4 ± 2.9 K/km) and in Möller et al. (2011) (-7.0 ± 3.7 K/km) are consistent since they are within the 1-sigma ranges.

Schuler et al. (2007) reported a value of $\frac{\partial T}{\partial h}$ of –4.4 K/km obtained from field measurements on Austfonna. Austfonna is also located on Nordaustlandet but in the east of Vestfonna. We found the same value on Vestfonna for the ablation period (July to August) using the eleven-year EAR data. Therefore, we assume a $\frac{\partial T}{\partial h}$ value of –4.4 K/km to correctly reflect conditions on Vestfonna during ablation periods whereas the annual mean has to be slightly larger (see above).

The values reported for Vestfonna so far seem to be rather low whereas the value for Austfonna is of the same magnitude as values found during ablation seasons in this study. All reported values are constants. But there are strong indications (e.g. Gardner and Sharp, 2009; Petersen and Pellicciotti, 2011) that large differences in the results of melt modelling can be caused by not considering a seasonal course of $\frac{\partial T}{\partial h}$ during the ablation season.

Marshall et al. (2007) and Gardner et al. (2009) pointed out seasonal courses of $\frac{\partial T}{\partial h}$ in the Canadian high Arctic. We found a similar two-phase seasonal course of $\frac{\partial T}{\partial h}$ (i.e., values of $\frac{\partial T}{\partial h}$ are generally higher during winter and summer than during spring and autumn) on Vestfonna as indicated by the results of Marshall et al. (2007) and Gardner et al. (2009). Their seasonal courses also show minima in $\frac{\partial T}{\partial h}$ before and after the ablation season. However, maximum values of $\frac{\partial T}{\partial h}$ during summer are less pronounced compared to values found for Vestfonna whereas maxima during winter are of the same magnitude. Furthermore, Rolland (2003) showed for Alpine regions a prominent lack of a summer maximum. On the other hand the seasonality presented in Rolland (2003) is very similar to results obtained from the reconstructed data (see Fig. 5). Since we assume melt processes are not correctly captured in the reconstructed data and therefore cause the lack of the summer maximum we argue that differences in melt processes in the Canadian high Arctic and in the Alps probably also cause the smaller to absent summer maxima. The signal of melt is probably more existent on an Arctic ice cap than in the Alpine region during the ablation season since the Polar day certainly strongly amplifies it. Schytt (1964) also obtained very low values of $\frac{\partial T}{\partial h}$ during the ablation season by using measurements of a non-glacial site which probably lack on melt compared to locations on Vestfonna what further supports this thesis.

As origin of the seasonal course Marshall et al. (2007) assume differences in the local energy balance (i.e. net radiative and turbulent heat flux) as a primary determinant of the differences in the local near-surface air temperature (i.e. $\frac{\partial T}{\partial h}$). We follow this estimation by assuming complex interactions of radiation, melt/refreezing, sea ice and advection creating the variability and seasonal course observed for $\frac{\partial T}{\partial h}$ on Vestfonna. Therefore, we want to examine a conceptual model by discussion the idealized seasonal course of $\frac{\partial T}{\partial h}$ in Fig. 7 obtained by averaging the eleven-year EAR data. Doing this we will keep our focus mainly on general features and try to put them into the context of other data and publication.

Various publications (e.g. Curry et al., 1996, Busch et al., 1982; Overland and Guest, 1991; Kahl et al., 1992; Serreze et al., 1992; Serreze and Barry, 2009) discussed radiation-climate feedback mechanisms in the Arctic strongly control the thermal structure of the lower planetary boundary layer (PBL). One feature is the frequently produced surface based low-level tropospheric inversion especially during Arctic winter. Furthermore, Wang et al. (2001) and Vihma and Pirazzini (2005) showed that the near-surface temperature strongly depends on processes of advection and radiative cooling controlled by cloudiness during the Polar night. The strong interconnection of $\frac{\partial T}{\partial h}$ and $\frac{\partial T}{\partial z}$ is further indicated by very similar winter courses of $\frac{\partial T}{\partial h}$ in Fig. 7 and $\frac{\partial T}{\partial z}$ of the lower planetary boundary layer (PBL) in Fig. 8 derived from radio soundings at Haudegen station in 1944/1945. Also further analyzes of the EAR (not shown) revealed that winter seasons experiencing low $\frac{\partial T}{\partial h}$ values (e.g. winter 2008 in Fig. 5) coincide with periods of increased advection of warm moist air and low sea ice concentration. Winter seasons experiencing high $\frac{\partial T}{\partial h}$ values (e.g. winter 2011 in Fig. 5) coincide with periods of increased cold dry air advection and high sea ice concentration. Inter-annual variation of seasonal mean values of $\frac{\partial T}{\partial h}$ and sea ice concentration showed a high correlation (r^2 = 0.8) significant on 0.01 significance level for the winter seasos (December to February). We therefore suppose increased (decreased) cloud formation during periods of warm (cold) air advection and low (high) sea ice concentration combined with the general character and thermal structure of the advected air to control $\frac{\partial T}{\partial h}$ during the winter through radiation-climate feedback mechanisms broadly discussed in context of $\frac{\partial T}{\partial z}$ by the former mentioned publications.

The first solar radiation is detectable mid of March (Fig. 9). We observe a coinciding start of decrease of $\frac{\partial T}{\partial h}$ in Fig. 7. The decreasing process starts in March and ends in May when the surface net radiation starts to become positive (Fig. 9). We assume the increasing solar radiation input to cause labialization of the PBL during the spring period before the net radiation surplus and the ambient air temperature are high enough for ablation processes. A formation of a mixed convective boundary layer on Vestfonna causing the decrease of $\frac{\partial T}{\partial h}$ would be consistent with Kahl et al. (1992) and Serreze et al. (1992) who indicated a formation of a mixed convective boundary layer beneath an elevated low-level inversions during periods of sufficient solar input. Further studies confirmed the development of convective boundary layers in the Arctic and Antarctic during summer (e.g. Mastrantonia et al., 1999; Argentini et al., 2005; Cullen et al., 2007; Di Liberto et al., 2012 and Pietroni et al., 2012). Van den Broeke et al. (2005) showed that near-surface air temperatures below 0 °C limit sublimation, and, in the absence of other heat sinks, skin temperatures rise rapidly during periods of high insolation resulting in convective conditions.

We observe an increase of $\frac{\partial T}{\partial h}$ in Fig. 7 between May and July which coincides with the period of increasing surface net radiation surplus in Fig. 9. Möller et al. (2011) determined that the ablation starts in average not before June on Vestfonna. As soon as melt and refreezing processes become important components in the local surface energy budget near-surface air temperature is close to 0 °C while variability is dampened (Fig. 2). Other studies (e.g. Busch et al., 1982; Serreze and Barry, 2009) described that the constrained surface temperature is often associated with the formation of shallow surface-based inversions. Furthermore, melt and refreezing processes are supposed to unify near-surface air temperatures within the ablation zone and elevational differences also to near-surface air temperatures in the accumulation zone decrease. Thus, $\frac{\partial T}{\partial h}$ increases during this period sometimes reaching values close to 0 K/km

(Fig. 7) and dampening effects of melt and refreezing combined with a decrease in cyclone activity during summer (e.g. Tsukernik et al., 2007) dampen day-to-day variability of $\frac{\partial T}{\partial h}$.

Solar radiation inputs start to decrease the end of June. But ongoing decrease in surface albedo counteracts and keeps the surface net solar radiation constant or even increasing until mid of July (Fig. 9). With the start of decreasing surface net solar radiation and therefore surface net radiation melt processes become less dominant and $\frac{\partial T}{\partial h}$ decreases. Snow events in August and September may accelerate the decrease. Surface-based inversions vanish and turbulent mixing may establish $\frac{\partial T}{\partial h}$ similar to the conditions in spring. The decrease of $\frac{\partial T}{\partial h}$ ends in October (Fig. 7) when the surface net radiation turns negative again (Fig. 9). Radiative cooling builds up strong surface based low-level tropospheric inversions reaching the maximum frequency in March. As described above the courses of $\frac{\partial T}{\partial h}$ and $\frac{\partial T}{\partial z}$ are linked again.

7 Summary and Conclusions

So far no extensive analysis of $\frac{\partial T}{\partial h}$ on Vestfonna was available. Considering the calculation of $\frac{\partial T}{\partial h}$ we found a high sensitivity to spatio-temporal distribution of the used measurement data. We completely reconstructed daily mean near-surface air temperature on Vestfonna to address the problem of generating unrealistic values caused by inhomogeneity and/or lacks in the data set. Two strategies were applied. A statistical transfer function used to reconstruct daily mean air temperature measurements from a weather station of the Norwegian Meteorological Institute closest to our measurement sites showed major problems especially during ablation season or cold air advection form northern directions. In contrast the EAR was capable of reproducing the general course found in the measurement data providing an eleven-year period used for further analyses in this study. Furthermore we validated the applicability of the EAR by statistical analysis.

Annual mean values were found to be higher than the often used standard moist adiabatic values (-5.4 ± 2.9 K/km). Furthermore, this analysis revealed the existence of a considerably two-phase annual course of $\frac{\partial T}{\partial h}$ on Vestfonna which was also observed in other regions. Our results during summer (-4.4 K/km) are consistent with values published for Austfonna by Schuler et al. (2007) but show differences to values published by Schytt (1964) and Möller et al. (2011) for Vestfonna. We point out that these differences can be caused by using data of different spatio-temporal distribution such as using different seasons, different number and/or distances of measurement sites or that measurement sites are not located on the glacier. In general, using $\frac{\partial T}{\partial h}$ to generate annual mean temperature distribution on Vestfonna standard moist adiabatic values seem not to be a proper approximation. Large differences in the results of melt modelling can be expected by not considering a seasonal or daily variation.

The general course of $\frac{\partial T}{\partial h}$ seems to be determined by the progression of radiative cooling, advection and sea ice conditions during Polar night and melt and refreezing during Polar day. Large inter-annual variability of the seasonal course was found especially during winter. We assume general changes in sea ice cover and evaporation (clouds, precipitation), synoptic circulation (wind regime and advection of air and moisture) or mean air temperature (melt) would have an impact on annual mean values, amplitude and shape of the annual course and day-to-day variance of $\frac{\partial T}{\partial h}$. Furthermore, depending on the sort of study using even a seasonal course of $\frac{\partial T}{\partial h}$ for generating input fields could be unsuitable since processes exist in parallel on Vestfonna and differ by time and region. Therefore, regional reanalyzes could be a valuable alternative providing input fields for these studies.

Acknowledgments. This work was funded by grants no. BR 2105/6-1, SCHE 750/3-1, SCHN 680/2-1 of the German Research Foundation (DFG). Additional funding was provided by grants no. 03F0623A and 03F0623B of the German Federal Ministry of Education and Research (BMBF). We gratefully acknowledge the efforts of Hartmut Küster, Bob McNabb, Fred Meier, Rebecca Möller, Albert Polze, Tobias Sauter, Lars Schneider and Ingo Suchland for their assistance with setting up and maintaining the sensor networks. We also thank the International Polar Year (IPY) and European Science Foundation (ESF) project frameworks "GlacioDyn", "IPY - Kinnvika" and "SvalGlac" for all scientific and logistical support.

References

Ahlmann, H.W., 1933. Scientific results of the Swedish-Norwegian Arctic Expedition in the summer of 1931. *Geografiska Annaler*, 15, 47-68 and 261-295.

Angström, A., 1933. Scientific results of the Swedish-Norwegian Arctic Expedition in the summer of 1931. Part VII - On the total Radiation from Sun and Sky at Sveanor (79°56.5'N, 18°18'E). *Geografiska Annaler*, 15, 151-159.

Argentini, S., Viola, A., Sempreviva, A. and Petenko, I., 2005. Summer boundary-layer height at the plateau site of Dome C, Antarctica. *Boundary-Layer Meteorology*, 115, 409-422.

Arkhipov, S.M., Vaykmyae, R.A., Vasilenko, Ye.V., Zagorodnov, V.S., Zinger, Ye.M., Martma, T.A., Macheret, Yu.Ya., Punning, Y.-M.K., Samoylov, O.Yu., Sin'kevich, S.A., Toots, M.D. and Troitskiy, L.S., 1987. Soviet glaciological investigations on Austfonna , Nordaustlandet, Svalbard in 1984-1985. *Polar Geography and Geology*, 11(1), 25-49.

Blake, W., 2006. Occurrence of the Mytilus edulis complex on Nordaustlandet, Svalbard: radiocarbon ages and climatic implications. *Polar Reasearch*, 25(2), 123-137.

Braun, M. and Hock, R. 2004. Spatially distributed surface energy balance and ablation modelling on the ice cap of King George Island, Antarctica. *Global and Planetary Change*, 42(1–4), 45–58.

Braun, M., Pohjola, V. A., Pettersson, R., Möller, M., Finkelnburg, R., Falk, U., Scherer, D. and Schneider, C., 2011. Changes of Glacier Frontal Positions of Vestfonna(Nordaustlandet, Svalbard). *Geografiska Annaler, Series A: Physical Geography*, 93, 301-310.

Busch, N., Ebel, U. Kraus, H. and Schaller, E., 1982. The Structure of the Subpolar Inverion-Capped ABL. *Archives for Meteorology, Geophysics, and Bioclimatology*, 31A, 1-18.

Cogley, J. G., 2009. Geodetic and direct mass-balance measurements: comparison and joint analysis. *Annals of Glaciology*, 50, 96-100.

Cullen, N.J., Steffen, K. and Blanken, P.D., 2007. Nonstationarity of turbulent heat fluxes at Summit, Greenland. *Boundary-Layer Meteorology*, 122, 439-455.

Curry, J., Rossow, W., Randall, D. and Schramm, J., 1996. Overview of Arctic cloud and radiation characteristics. *Journal of Climate*, 9, 1731-1764.

Dege, W., 1960. Wissenschaftliche Beobachtungen auf dem Nordostland von Spitzbergen 1944-1945. *Berichte des Deutschen Wetterdienstes*, 72, 99 p.

Di Liberto, L., Angelini, F., Pietroni, I., Cairo, F., Di Donfrancesco, G., Viola, A., Argentini, S., Fierli, F., Gobbi, G., Maturilli, M., Neuber, R. and Snels, M., 2012. Estimate of the Arctic Convective Boundary Layer Height from Lidar Observations: A Case Study. *Advances in Meteorolgy*.

Ekman, S.R., 1971. Seismic investigations on the Nordaustlandet ice caps. *Geografiska Annaler, Series A: Physical Geography*, 53, 1-13.

Eriksson, B.E., 1933. Scientific results of the Swedish-Norwegian Arctic Expedition in the summer of 1931. Part VI - Climatology and

Meteorology. *Geografiska Annaler*, 15, 117-150.

Finkelnburg, R., Maussion, F. and Scherer, D., 2013. Seasonality and variability of the climate in Svalbard as resolved by the European Arctic Reanalysis (EAR) for the glacier mass-balance years 2001 to 2011. *To be submitted to Journal of Climate*.

Gardner, A. S. and Sharp, M., 2009. Sensitivity of net mass-balance estimates to near-surface temperature lapse rates when employing the degree-day method to estimate glacier melt. *Annals of Glaciology*, 50, 80-86.

Gardner, A. S., Sharp, M. J., Koerner, R. M., Labine, C., Boon, S., Marshall, S. J., Burgess, D. O. and Lewis, D., 2009. Near-Surface Temperature Lapse Rates over Arctic Glaciers and Their Implications for Temperature Downscaling. *Journal of Climate*, 22, 4281-4298.

Georges, C. and Kaser, G., 2002. Ventilated and unventilated air temperature measurements for glacier-climate studies on a tropical high mountain site. *Journal of Geophysical Research - Atmosphere*, 107.

Glen, A.R., 1937. The Oxford University Arctic Expedition, North East Land, 1935-36. *The Geographical Journal*, 90(3), 193-222.

Glen, A.R., 1939. The glaciology of North East Land. Geografiska Annaler, 21, 1-38.

Grabiec, M., Budzik, T. and Glowacki, P., 2012. Modeling and Hindcasting of the Mass Balance of Werenskioldbreen (Southern Svalbard). *Arctic Antarctic and Alpine Research*, 44, 164-179.

Hisdal, V., 1976. Geography of Svalbard: a short survey. *Norsk Polarinstitutt*, 75.

Hock, R., 2003. Temperature index melt modelling in mountain areas. *Journal of Hydrology*, 282, 104-115.

Hock, R., 2005. Glacier melt: a review of processes and their modelling. *Progress in Physical Geography*, 29, 362-391.

Kahl, J., Serreze, M. and Schnell, R., 1992. Troposheric Low-Level Temperature Inversions in the Canadian Arctic. *Atmosphere-Ocean*, 30, 511-529.

Kaser, G., Cogley, J. G., Dyurgerov, M. B., Meier, M. F. and Ohmura, A., 2006. Mass balance of glaciers and ice caps: Consensus estimates for 1961-2004. *Geophysical Research Letters*, 33, L19501.

Liljequist, G.H., 1959. Murchison Bay. Den svensk-finsk-schweiziska expedition till Nordaustlandet 1957-58. *Ymer*, 79, 81-139.

Loeng, H., 1991. Features of the physical oceanographic conditions of the Barents Sea. *Polar Research*, 10(1), 5-18.

Marshall, S. J., Sharp, M. J., Burgess, D. O. and Anslow, F. S., 2007. Near-surface-temperature lapse rates on the Prince of Wales Icefield, Ellesmere Island, Canada: implications for regional downscaling of temperature. *International Journal of Climatology*, 27, 385-398.

Möller, M., Finkelnburg, R., Braun, M., Hock, R., Jonsell, U., Pohjola, V. A., Scherer, D. and Schneider, C., 2011. Climatic mass balance of the ice cap Vestfonna, Svalbard: A spatially distributed assessment using ERA-Interim and MODIS data. Journal of Geophysical Research - Earth Surface, 116.

Möller, M., Finkelnburg, R., Braun, M., Scherer, D. and Schneider, C., 2013. Variability of the climatic mass balance of Vestfonna ice cap, northeastern Svalbard, 1979–2011. *Annals of Glaciology*, 54 (63), accepted.

Motoyama, H., Watanabe, O., Goto-Azuma, K., Igarashi, M., Miyahara, H., Nagasaki, T., Karlof, L. and Isaksson, E., 2001. Activities of the Japanese Arctic Glaciological Expedition in 1999 (JAGE 1999). *Memoirs of National Institute of Polar Research*, 54, 253-60.

Ohmura, A., 2001. Physical basis for the temperature-based melt-index method. *Journal of Applied Meteorology*, 40, 753-761.

Overland, J. and Guest, P., 1991. The Arctic Snow and Air-Temperature Budget over Sea Ice during Winter. *Journal of Geophysical Research - Oceans*, 96.

Palosuo, E., 1987. A Study of Snow and Ice Temperatures on Vestfonna, Svalbard, 1956, 1957 and 1958. *Geografiska Annaler, Series A: Physical Geography*, 69, 431–437.

Petersen, L. and Pellicciotti, F., 2011. Spatial and temporal variability of air temperature on a melting glacier: Atmospheric controls, extrapolation methods and their effect on melt modeling, Juncal Norte Glacier, Chile. *Journal of Geophysical Research - Atmosphere*, 116.

Pietroni, I., Argentini, S., Petenko, I. and Sozzi, R., 2012. Measurements and Parametrizations of the Atmospheric Boundary-Layer Height at Dome C, Antarctica. *Boundary-Layer Meteorology*, 143, 189-206.

Rennick, M., 1977. Parameterization of Tropospheric Lapse rates in Terms of Surface-Temperature. *Journal of the Atmospheric Sciences*, 34, 854-862.

Rigor, I.G., Colony, R.L. and Martin, S., 2000. Variations in Surface Air Temperature Observations in the Arctic, 1979-97. *Journal of Climate*, 13, 896-914.

Rolland, C., 2003. Spatial and seasonal variations of air temperature lapse rates in Alpine regions. *Journal of Climate*, 16, 1032-1046.

Rye, C. J., Arnold, N. S., Willis, I. C. and Kohler, J., 2010. Modeling the surface mass balance of a high Arctic glacier using the ERA-40 reanalysis. *Journal of Geophysical Research - Earth Surface*, 115, F02014.

Sandford, K.S., 1926. Summer in North-East Land, 1924: The climate and surface changes. *The Geographical Journal*, 68(3), 200-225.

Schuler, T.V., Loe, E., Taurisano, A., Eiken, T., Hagen, J.O. and Kohler, J., 2007. Calibrating a surface mass-balance model for Austfonna ice cap, Svalbard. *Annals of Glaciology*, 46, 241-248.

Schytt, V., 1964. Scientific results of the Swedish Glaciological Expedition to Nordaustlandet, Spitsbergen, 1957 and 1958. *Geografiska Annaler, Series A: Physical Geography*, 46(3), 243-281.

Serreze, M., Kahl, J. and Schnell, R., 1992. Low-Level Temperature Inversions of the Eurasian Arctic and Comparisons with Soviet Drifting Station Data. *Journal of Climate*, 5, 615-629.

Serreze, M. and Barry, R., 2009. The Arctic Climate System. *Cambridge University Press*,385 p.

Stull, R., 1991. Static Stability - An Update. *Bulletin of the American Meteorological Society*, 72, 1521-1529.

Thompson, H.R., 1953. Geology and Geomorphology in Southern Nordaustlandet (Nort-East Land), Spitsbergen. *Proceedings of Geologists' Association*,64(4), 293-312.

Tsukernik, M., Kindig, D. N. and Serreze, M. C., 2007. Characteristics of winter cyclone activity in the northern North Atlantic: Insights from observations and regional modeling. *Journal of Geophysical Research - Atmospheres*, 112.

Tymms, F., 1925. The Oxford University Expedition, 1924. III – Meteorology. *The Geographical Journal*, 66(2), 120-126.

Van den Broeke, M., van As, D., Reijmer, C. and van de Wal, R., 2004. Assessing and improving the quality of unattended radiation observations in Antarctica. *Journal of Atmospheric and Oceanic Technology*, 21, 1417-1431.

Van den Broeke, M., Van As, D., Reijmer, C. and Van De Wal, R., 2005. Sensible heat exchange at the antarctic snow surface: A study with automatic weather stations. *International Journal of Climatology*, 25, 1081-1101.

Van Pelt, W. J. J., Oerlemans, J., Reijmer, C. H., Pohjola, V. A., Pettersson, R. and van Angelen, J. H., 2012. Simulating melt, runoff and refreezing on Nordenskioldbreen, Svalbard, using a coupled snow and energy balance model. *The Cryosphere*, 6, 641-659.

Vihma, T. and Pirazzini, R., 2005. On the factors controlling the snow surface and 2-m air temperatures over the Arctic sea ice in winter. *Boundary-Layer Meteorology*, 117, 73-90.

Wang, S., Wang, Q., Jordan, R. and Persson, P., 2001. Interactions among longwave radiation of clouds, turbulence, and snow surface temperature in the Arctic: A model

sensitivity study. *Journal of Geophysical Research - Atmospheres*, 106, 15323-15333.

Watanabe, O., Kamiyama, K., Kameda, T., Takahashi, S., and Isaksson, E., 2000. Activities of the Japanese Arctic Glaciological Expedition in 1998 (JAGE 1998). *Bulletin of Glaciological Research*, 17, 31–35.

Table 1. Coordinates, altitude and period of operation of the Automatic Weather Stations (AWS) in western Nordaustlandet (Fig. 1).

AWS Name	Latitude	Longitude	Altitude [m a.s.l.]	Start Date	End Date
DG-AWS	80.0163 N	19.1855 E	240	26-May-08	20-May-12
VF-AWS240	79.9995 N	19.4442 E	240	22-May-08	20-May-09
VF-AWS335	79.9342 N	19.1823 E	335	22-Apr-07	2-Dec-09
VF-AWS370	79.9847 N	19.4738 E	370	28-May-08	15-Sep-11
VF-AWS500	79.9650 N	19.5320 E	500	21-May-08	21-May-09
VF-T597	79.9870 N	20.1299 E	597	28-Apr-07	11-May-08
RF-AWS	80.2183 N	22.4783 E	10	25-Jan-07	In operation

Table 2. Characteristics of air-temperature sensors used in this study.

AWS Name	Sensor height *[m]*	Sensor type	Accuracy at -10 °C *[K]*	Artificially ventilated	Sampling interval *[min]*	Storage interval *[min]*	Aggregation
DG-AWS	2.1	Campbell Sci., CS215	±0.6	Yes	10,30,60	10,30,60	Sample value
VF-AWS240	2.3	Campbell Sci., CS215	±0.6	Yes	10	10	Sample value
VF-AWS335	1.8	Vaisala, HMP45A	±0.4	No	1	60, 120	Mean value
VF-AWS370	1.9	Campbell Sci., CS215	±0.6	Yes	1,10,30,60	1,10,30,60	Sample value
VF-AWS500	1.1	Campbell Sci., CS215	±0.6	Yes	10	10	Sample value
VF-T597	0.6	Campbell Sci, Model 107 Temperature Probe	±0.1	No	5	60	Mean value
RF-AWS	4.5	Rotronic, Hygroclip	±0.2	No	0.25	60	Mean value

Table 3. Linear regression factors and statistics for correlations between daily mean air temperatures measured at our Automatic Weather Station (AWS) sites and the reference WMO station located at Svalbard-Lufthavn, Longyearbyen (WMO-Nr. 010080, 15.4667°E 78.2500°N, 28 m a.s.l.). n: Number of data pairs used to calculate the linear regression factors c_0 and c_1 ($AWS_T = LYR_T * c_1 + c_0$). For c1 also the 1σ-level (±σ) is displayed. The root mean square error (rmse) and the coefficient of determination (r^2) refer to the correlation with n data pairs. n* is the number of days in n with a daily mean air temperature above 0 °C. rmse* is the root mean square error considering only the n* data pairs.

AWS Name	Sensor	c0	c1	r^2	n	rmse *[K]*	n*	rmse* *[K]*
RF-AWS	AIR_T_4.5m	-3.83	1.04 ± 0.016	0.85	754	3.56	*223*	*2.66*
DG-AWS	AIR_T_2.1m	-4.59	1.08 ± 0.010	0.93	902	2.38	*273*	*2.13*
VF-AWS240	AIR_T_2.3m	-4.61	1.03 ± 0.022	0.91	242	2.66	*11*	*2.24*
VF-AWS335	AIR_T_1.8m	-5.8	1.01 ± 0.010	0.92	817	2.36	*104*	*2.1*
VF-AWS370	AIR_T_1.9m	-5.64	1.03 ± 0.010	0.93	852	2.68	*193*	*2.09*
VF-AWS500	AIR_T_1.1m	-6.68	1.02 ± 0.022	0.89	242	2.8	*6*	*2.19*
VF-T597	AIR_T_0.6m	-7.66	1.00 ± 0.016	0.91	366	2.47	*24*	*1.92*

Table 4. Percentage of monthly data coverage of measurement data at Haudegen station used in the discussion.

Jan	Feb	Mar	Apr	May	Jun	Jul	Aug	Sep	Oct	Nov	Dec
71	89	42	30	26	0	0	0	0	0	0	77

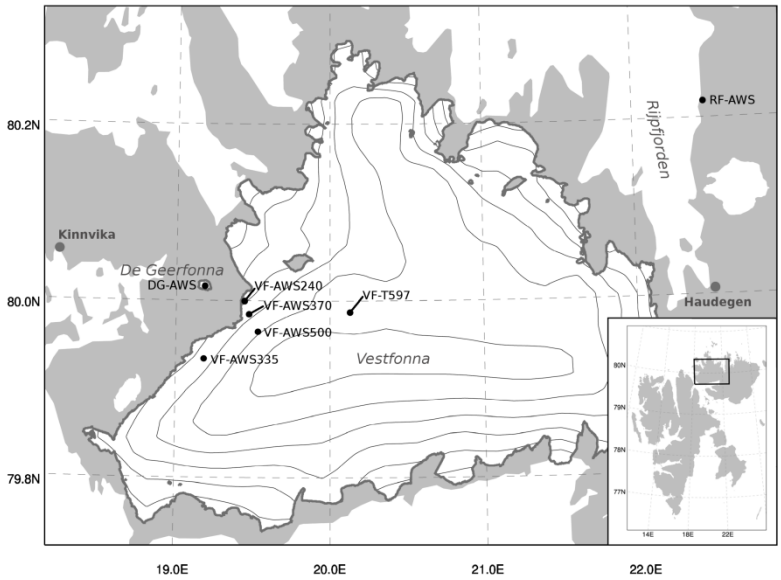

Fig. 1. Locations of Automatic Weather Stations (AWS) in western Nordaustlandet used in this study. The numbers in some of the station names refer to the AWS elevation in m a.s.l.

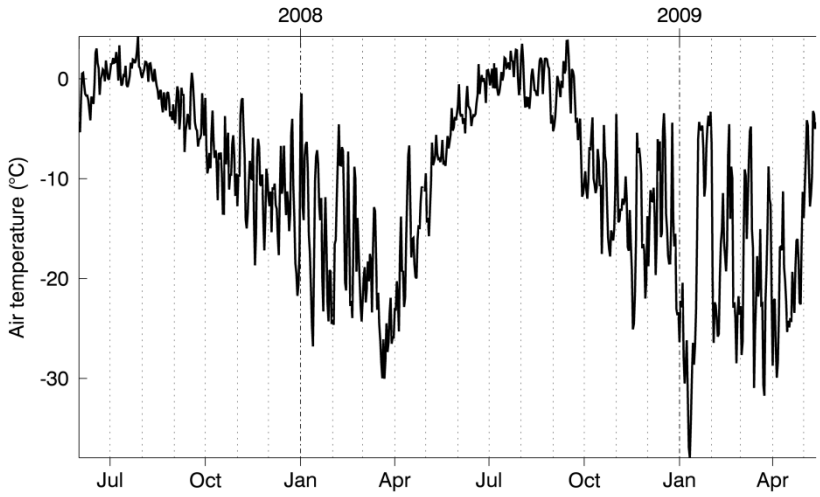

Fig. 2. Daily mean air temperature measured at VF-AWS335 (Fig. 1) between 1 January 2007 and 31 December 2009. Labels refer to the beginning of the month.

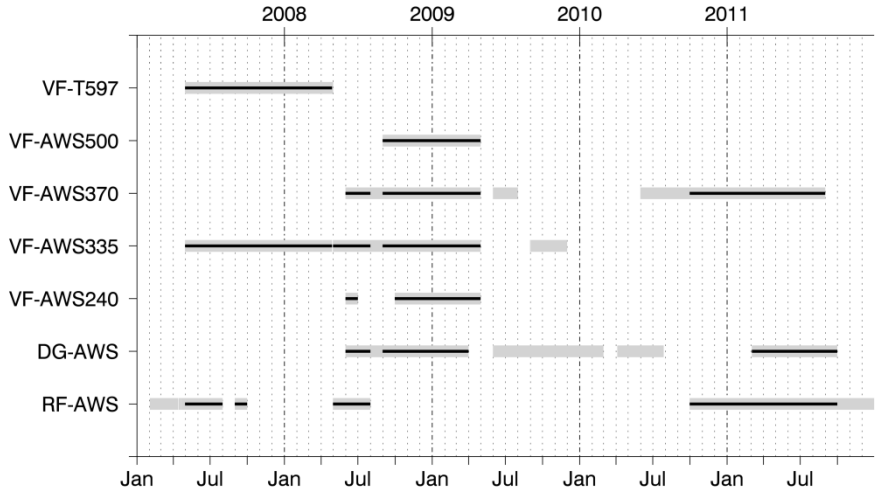

Fig. 3. Periods for which AWS temperature data are available (grey lines) and periods used to compute daily elevational gradients (black lines), i.e. elevation difference of at least 150 m. See Fig. 1 for location of AWS and Table 1 for their altitudes.

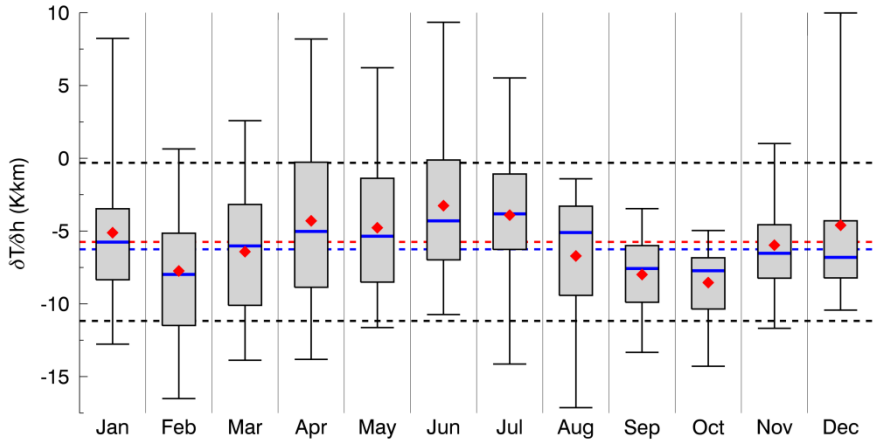

Fig. 4. Annual cycle of daily elevational gradients derived from measured near-surface air temperature series between 1 January 2007 and 31 December 2011. Minimum: 5 % percentile, maximum: 95 % percentile, box bottom: 25 % percentile, box top: 75 % percentile, blue bold line: median, red diamond: mean, dashed red line: overall mean, dashed back lines: overall mean ± 1-sigma, dashed blue line: overall median.

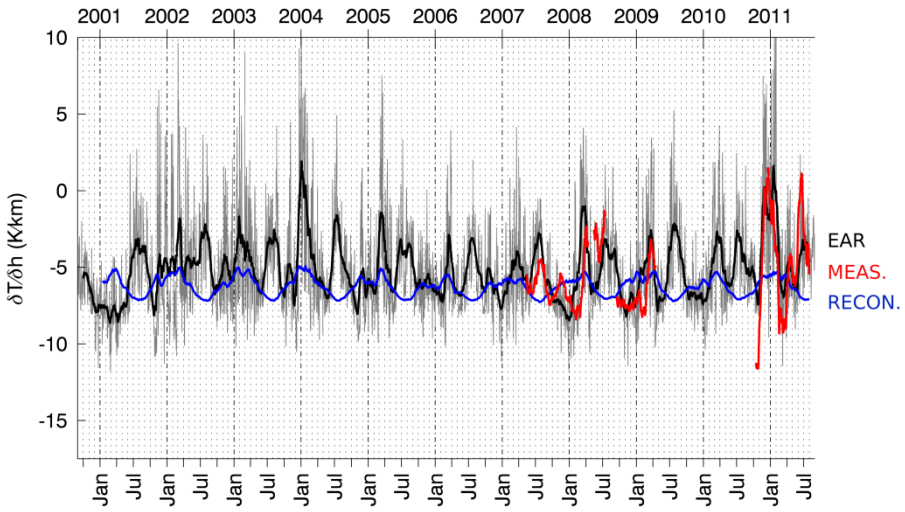

Fig. 5. Annual cycle of elevational gradients of air temperature on Vestfonna. Grey line: daily values derived from reanalysis, black line: moving 30-day mean of daily values derived from European Arctic Reanalysis (EAR), blue line: moving 30-day mean of daily values derived from reconstructed data (RECON), red line: moving 30-day mean of daily values derived from measurements (MEAS).

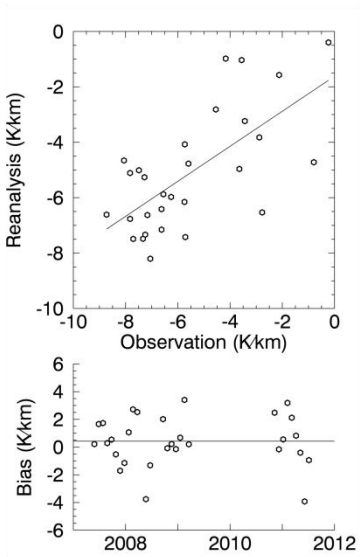

Fig. 6. Correlation analysis between 30-day mean values of elevational gradients derived from measurements and from European Arctic Reanalysis (EAR) data in the region of Vestfonna.

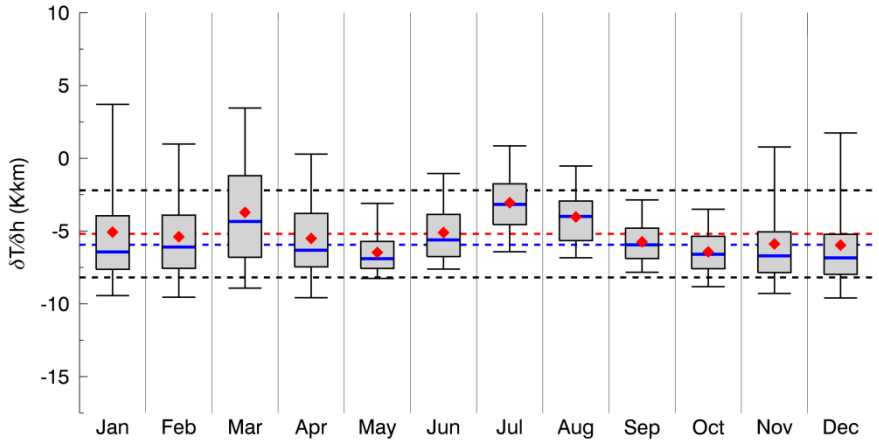

Fig. 7. Annual cycle of daily elevational gradients derived from European Arctic Reanalysis (EAR) 2 m air temperature series between 1 September 2000 and 31 August 2011. Minimum: 5 % percentile, maximum: 95 % percentile, box bottom: 25 % percentile, box top: 75 % percentile, blue bold line: median, red diamond: mean, dashed red line: overall mean, dashed back lines: overall mean ± 1-sigma, dashed blue line: overall median.

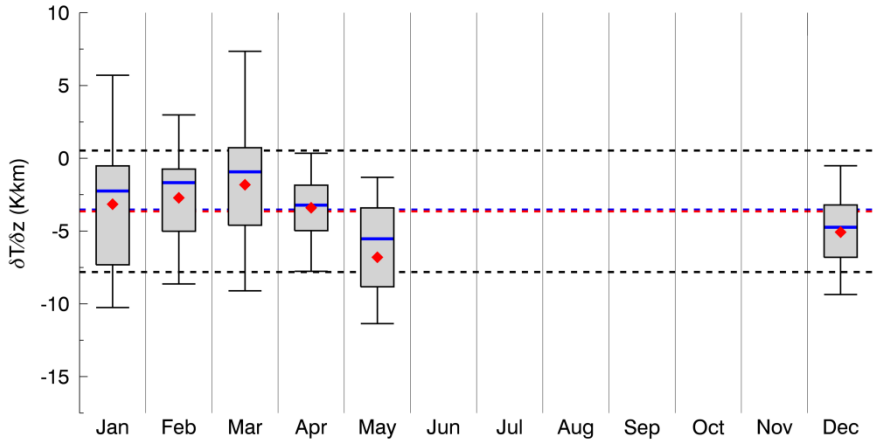

Fig. 8. Annual cycle of daily vertical gradients of air temperature derived from daily mean surface air temperature and values below 1000 m a.s.l. of vertical profiles (radio soundings) of air temperature measurements at Haudegen station in 1944/1945. Minimum: 5 % percentile, maximum: 95 % percentile, box bottom: 25 % percentile, box top: 75 % percentile, blue bold line: median, red diamond: mean, dashed red line: overall mean, dashed back lines: overall mean ± 1-sigma, dashed blue line: overall median.

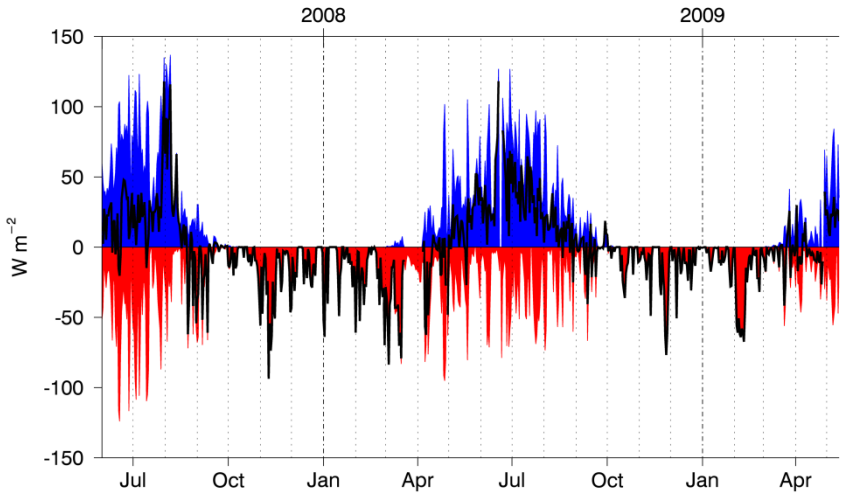

Fig. 9. Daily mean surface net radiation (black line), daily mean surface net solar radiation (blue) and daily mean surface net thermal radiation measured at VF-AWS335 (Fig. 1) between 1 June 2007 and 13 May 2009.

Appendix F: Photos of field work logistics and equipment

Snowmobile transport

By foot operation

Helicopter transport

Ship transport

Figure F.1 *Means of transport: snow mobile, hiking, helicopter, ship transport.*

Kinnvika research station *Camp at Oxfordhalvøya*

Figure F.2 *Logistical bases: Kinnvika research station and camp at Oxfordhalvøya.*

Kitchen tents and equipment *Sleeping tents*

Figure F.3 *Temporal tent camp set up.*

Satellite phones, GPS, etc. *Rifle and signal pistol*

Figure F.4 *Various equipment.*

Appendix G: Metadata of automatic weather station (AWS) measurements

Table G.1 *Locations, measurement periods and physical setup of automatic weather stations (AWS). Examples for a small and a large setup are given in Figure 3.2.*

AWS Name	Latitude (°N)	Longitude (°E)	Altitude (m a.s.l.)	Start Date	End Date	Grounding	Setup
KV-AWS	80.0514	18.2163	6	15.05.2008	04.08.2009	Soil	Large
DG-AWS	80.0163	19.1855	240	26.05.2008	20.05.2012	Ice	Small
VF-AWS240	79.9995	19.4442	240	22.05.2008	20.05.2009	Ice	Large
VF-AWS370	79.9847	19.4738	370	28.05.2008	15.09.2011	Ice	Large
VF-AWS500	79.9650	19.5320	500	21.05.2008	21.05.2009	Ice	Large
VF-AWS605	79.9801	20.1242	605	18.05.2008	19.05.2009	Snow	Small

Table G.2 *Logger setup of automatic weather stations (AWS).*

AWS Name	Loggers
KV-AWS	Campbell Sci., CR1000
DG-AWS	Campbell Sci., CR1000
VF-AWS240	2 x Campbell Sci., CR800
VF-AWS370	2 x Campbell Sci., CR800. Campbell Sci., CR1000 and CR800 since May 2010
VF-AWS500	2 x Campbell Sci., CR800
VF-AWS605	Campbell Sci., CR1000

Table G.3 *Sensor setup of automatic weather station (AWS) measurements. Ground type, locations, measurement periods, physical setup, logger setup and storage intervals are summarized in Tables G.1 and G.2.*

	SID	Measured variable	Sensor	Initial height above Ground (m)
DG-AWS	TH	Air Temperature, Relative Humidity	Campbell Sci., CS215	2.1, 3.6
	SD	Solar iradiation	Campbell Sci. (Apogee), CS300 (PYR-P)	2.6
	SU	Reflected shortwave radiation	Campbell Sci. (Apogee), CS300 (PYR-P)	2.6
	LU	Surface thermal radiation	Kipp&Zonen, CGR3	2.6
	N	Net radiation	Campbell Sci., NR-LITE	2.6
	W	Wind speed, Wind direction	Young, 05103-45	4.2
	P	Air pressure	T. Friedrichs & Co, 5004.000 BG	1.5
	D	Snow depth	Campbell Sci., SR50A	2.5
	IT	Snow and ice temperature	Campbell Sci., Model 107 Temperature Probe	0.1, 0.0, -2.0, -8.0
VF-AWS240	TH	Air Temperature, Relative Humidity	Campbell Sci., CS215	2.3, 4.0
	SD	Solar iradiation	Campbell Sci. (Apogee), CS300 (PYR-P)	2.8
	SU	Reflected shortwave radiation	Campbell Sci. (Apogee), CS300 (PYR-P)	2.8
	N	Net radiation	Campbell Sci., NR-LITE	2.8
	D	Snow depth	Campbell Sci., SR50A	2.7
	IT	Snow and ice temperature	Campbell Sci., Model 107 Temperature Probe	0.5, 0.2, 0.1, 0.0, -0.2, -2.0, -5.0, -8.0
VF-AWS370	TH	Air Temperature, Relative Humidity	Campbell Sci., CS215	1.9, 3.9
	SD	Solar iradiation	Campbell Sci. (Apogee), CS300 (PYR-P)	2.1
	SU	Reflected shortwave radiation	Campbell Sci. (Apogee), CS300 (PYR-P)	2.1
	LD	Thermal	Kipp&Zonen, CGR3	2.1
	N	Net radiation	Campbell Sci., NR-LITE	2.1
	N2	Net radiation	Kipp&Zonen, CNR-1	2.1
	W	Wind speed, Wind direction	Young, 05103-45	2.4
	U	Eddy covariance	Gill Inst., WindMaster Ultrasonic Anemometer	4.3
	P	Air pressure	T. Friedrichs & Co, 5004.000 BG	1.5
	D	Snow depth	Campbell Sci., SR50A	2.0
	IT	Snow and ice temperature	Campbell Sci., Model 107 Temperature Probe	0.5, 0.2, 0.1, 0.0, -0.2, -2.0, -5.0, -8.0
VF-AWS500	TH	Air Temperature, Relative Humidity	Campbell Sci., CS215	2.5, 4.0
	SD	Solar iradiation	Campbell Sci. (Apogee), CS300 (PYR-P)	3.0
	SU	Reflected shortwave radiation	Campbell Sci. (Apogee), CS300 (PYR-P)	3.0
	N	Net radiation	Campbell Sci., NR-LITE	3.0
	D	Snow depth	Campbell Sci., SR50A	2.9
	IT	Snow and ice temperature	Campbell Sci., Model 107 Temperature Probe	0.5, 0.2, 0.1, 0.0, -0.2, -2.0, -5.0, -8.0
VF-AWS605	TH	Air Temperature, Relative Humidity	Campbell Sci., CS215	2.6, 3.9
	SD	Solar iradiation	Campbell Sci. (Apogee), CS300 (PYR-P)	3.0
	SU	Reflected shortwave radiation	Campbell Sci. (Apogee), CS300 (PYR-P)	3.0
	N	Net radiation	Campbell Sci., NR-LITE	3.0
	P	Air pressure	T. Friedrichs & Co, 5004.000 BG	1.5
	D	Snow depth	Campbell Sci., SR50A	2.9
	IT	Snow temperature	Campbell Sci., Model 107 Temperature Probe	-2.0, -10.0
KV-AWS	TH	Air Temperature, Relative Humidity	Campbell Sci., CS215	2.5, 4.0
	SD	Solar iradiation	Campbell Sci. (Apogee), CS300 (PYR-P)	3.0
	SU	Reflected shortwave radiation	Campbell Sci. (Apogee), CS300 (PYR-P)	3.0
	N	Net radiation	Kipp&Zonen, CNR-1	3.0
	U	Eddy covariance	Metek, USA-1 CHNS + LICOR	4.4
	P	Air pressure	T. Friedrichs & Co, 5004.000 BG	1.5
	D	Snow depth	Campbell Sci., SR50A	2.9
	IT	Soil temperature	Campbell Sci., Model 107 Temperature Probe	-0.025, -0.075, -0.125, -0.175
	HF	Soil heat flux	Carter-Scott Design, CN3 Heat Flux Plate	-0.05, -0.10, -0.15
	WC	Soil water content	Campbell Sci., CS616-L	-0.05, -0.15

Table G.4 *Storage intervals in minutes of sensors at DG-AWS. SIDs are described in Table G.3. Both intervals are presented in months of storage intervals changes.*

		2008												2009											
	SID	J	F	M	A	M	J	J	A	S	O	N	D	J	F	M	A	M	J	J	A	S	O	N	D
DG-AWS	TH (2.1m)					10	10	10	10	10	10	10	10	10	10	10	10	10,30	30	30	30,60	60	60	60	60
	TH (3.6m)					10	10	10	10	10	10	10	10	10	10	10	10	10,30	30	30	30,60	60	60	60	60
	SD					10	10	10	10	10	10	10	10	10	10	10	10	10,30	30	30	30,60	60	60	60	60
	SU					10	10	10	10	10	10	10	10	10	10	10	10	10,30	30	30	30,60	60	60	60	60
	N																	30	30	30	30,60	60	60	60	60
	W																	30	30	30	30,60	60	60	60	60
	P																	30	30	30	30,60	60	60	60	60
	D					10	10	10	10	10	10	10	10	10	10	10	10	10,30	30	30	30,60	60	60	60	60
	IT (0.1m)					10	10	10	10	10	10	10	10	10	10	10	10	10,30	30	30	30,60	60	60	60	60
	IT (0.0m)					10	10	10	10	10	10	10	10	10	10	10	10	10,30	30	30	30,60	60	60	60	60
	IT (-2.0m)					10	10	10	10	10	10	10	10	10	10	10	10	10,30	30	30	30,60	60	60	60	60
	IT (-8.0m)					10	10	10	10	10	10	10	10	10	10	10	10	10,30	30	30	30,60	60	60	60	60

		2010												2011											
	SID	J	F	M	A	M	J	J	A	S	O	N	D	J	F	M	A	M	J	J	A	S	O	N	D
DG-AWS	TH (2.1m)	60	60	60	60	10,60	10	10	10	10	10	10	10	10	10	10	10	10	10	10	10,60	60	60	60	60
	TH (3.6m)	60	60	60	60	10,60	10	10	10	10	10	10	10	10	10	10	10	10	10	10	10,60	60	60	60	60
	SD	60	60	60	60	10,60	10	10	10	10	10	10	10	10	10	10	10	10	10	10	10,60	60	60	60	60
	SU	60	60	60	60	10,60	10	10	10	10	10	10	10	10	10	10	10	10	10	10	10,60	60	60	60	60
	LU								10	10	10	10	10	10	10	10	10	10	10	10	10,60	60	60	60	60
	N	60	60	60	60	10,60	10	10	10	10	10	10	10	10	10	10	10	10	10	10	10,60	60	60	60	60
	W	60	60	60	60	10,60	10	10	10	10	10	10	10	10	10	10	10	10	10	10	10,60	60	60	60	60
	P	60	60	60	60	10,60	10	10	10	10	10	10	10	10	10	10	10	10	10	10	10,60	60	60	60	60
	D	60	60	60	60	10,60	10	10	10	10	10	10	10	10	10	10	10	10	10	10	10,60	60	60	60	60
	IT (0.1m)	60	60	60	60	10,60	10	10	10,60	60	60	60	60	60	60	60	60								
	IT (0.0m)	60	60	60	60	10,60	10	10	10,60	60	60	60	60	60	60	60	60								
	IT (-2.0m)	60	60	60	60	10,60	10	10	10,60	60	60	60	60	60	60	60	60	60	60	60	60	60	60	60	60
	IT (-8.0m)	60	60	60	60	10,60	10	10	10,60	60	60	60	60	60	60	60	60	60	60	60	60	60	60	60	60

		2012											
	SID	J	F	M	A	M	J	J	A	S	O	N	D
DG-AWS	TH (2.1m)	60	60	60	60	60							
	TH (3.6m)	60	60	60	60	60							
	SD	60	60	60	60	60							
	SU	60	60	60	60	60							
	LU	60	60	60	60	60							
	N	60	60	60	60	60							
	W	60	60	60	60	60							
	P	60	60	60	60	60							
	D	60	60	60	60	60							
	IT (-2.0m)	60	60	60	60	60							
	IT (-8.0m)	60	60	60	60	60							

Table G.5 *Storage intervals in minutes of sensors at VF-AWS370. SIDs are described in Table G.3. Both intervals are presented in months of storage intervals changes.*

		2008												2009											
	SID	J	F	M	A	M	J	J	A	S	O	N	D	J	F	M	A	M	J	J	A	S	O	N	D
VF-AWS370	TH (1.9m)					10	10	10	10	10	10	10	10	10	10	10	10	10,30	30	30	30,60	60	60	60	60
	TH (3.9m)					10	10	10	10	10	10	10	10	10	10	10	10	10,30	30	30	30,60	60	60	60	60
	SD					10	10	10	10	10	10	10	10	10	10	10	10	10,30	30	30	30,60	60	60	60	60
	SU					10	10	10	10	10	10	10	10	10	10	10	10	10,30	30	30	30,60	60	60	60	60
	N					10	10	10	10	10	10	10	10	10	10	10	10	10,30	30	30	30,60	60	60	60	60
	W																	30	30	30	30,60	60	60	60	60
	D					10	10	10	10	10	10	10	10	10	10	10	10	10,30	30	30	30,60	60	60	60	60
	IT (0.5m)					10	10	10	10	10	10	10	10	10	10	10	10	10,30	30	30	30,60	60	60	60	60
	IT (0.2m)					10	10	10	10	10	10	10	10	10	10	10	10	10,30	30	30	30,60	60	60	60	60
	IT (0.1m)					10	10	10	10	10	10	10	10	10	10	10	10	10,30	30	30	30,60	60	60	60	60
	IT (0.0m)					10	10	10	10	10	10	10	10	10	10	10	10	10,30	30	30	30,60	60	60	60	60
	IT (-0.2m)					10	10	10	10	10	10	10	10	10	10	10	10	10,30	30	30	30,60	60	60	60	60
	IT (-2.0m)					10	10	10	10	10	10	10	10	10	10	10	10	10,30	30	30	30,60	60	60	60	60
	IT (-5.0m)					10	10	10	10	10	10	10	10	10	10	10	10	10,30	30	30	30,60	60	60	60	60
	IT (-8.0m)					10	10	10	10	10	10	10	10	10	10	10	10	10,30	30	30	30,60	60	60	60	60

		2010												2011											
	SID	J	F	M	A	M	J	J	A	S	O	N	D	J	F	M	A	M	J	J	A	S	O	N	D
VF-AWS370	TH (1.9m)	60	60	60	60	1,60	1	1	1,10	10	10	10	10	10	10	10	10	10	10	10	10,60	60	60	60	60
	TH (3.9m)	60	60	60	60	1,60	1	1	1,10	10	10	10	10	10	10	10	10	10	10	10	10,60	60	60	60	60
	SD	60	60	60	60	1,60	1	1	1,10	10	10	10	10	10	10	10	10	10	10	10	10,60	60	60	60	60
	SU	60	60	60	60	1,60	1	1	1,10	10	10	10	10	10	10	10	10	10	10	10	10,60	60	60	60	60
	LD					1	1	1	1,10	10	10	10	10	10	10	10	10	10	10	10	10,60	60	60	60	60
	N (CNR-1)																	10	10	10	10,60	60	60	60	60
	N	60	60	60	60	1,60	1	1	1,10	10	10	10	10	10	10	10	10	10	10	10	10,60	60	60	60	60
	W	60	60	60	60	1,60	1	1	1,10	10	10	10	10	10	10	10	10	10	10	10	10,60	60	60	60	60
	U																	1	1	1	1				
	P	60	60	60	60	1,60	1	1	1,10	10	10	10	10	10	10	10	10	10	10	10	10,60	60	60	60	60
	D	60	60	60	60	1,60	1	1	1,10	10	10	10	10	10	10	10	10	10	10	10	10,60	60	60	60	60
	IT (0.5m)	60	60	60	60																				
	IT (0.2m)	60	60	60	60																				
	IT (0.1m)	60	60	60	60	60	60	60	60	60	60	60	60	60	60	60	60	60	60	60	60	60	60	60	60
	IT (0.0m)	60	60	60	60	60	60	60	60	60	60	60	60	60	60	60	60	60	60	60	60	60	60	60	60
	IT (-0.2m)	60	60	60	60	60	60	60	60	60	60	60	60	60	60	60	60	60	60	60	60	60	60	60	60
	IT (-2.0m)	60	60	60	60	60	60	60	60	60	60	60	60	60	60	60	60	60	60	60	60	60	60	60	60
	IT (-5.0m)	60	60	60	60	60	60	60	60	60	60	60	60	60	60	60	60	60	60	60	60	60	60	60	60
	IT (-8.0m)	60	60	60	60	60	60	60	60	60	60	60	60	60	60	60	60	60	60	60	60	60	60	60	60

		2012											
	SID	J	F	M	A	M	J	J	A	S	O	N	D
VF-AWS370	TH (1.9m)	60	60	60	60	60							
	TH (3.9m)	60	60	60	60	60							
	SD	60	60	60	60	60							
	SU	60	60	60	60	60							
	LD	60	60	60	60	60							
	N (CNR-1)	60	60	60	60	60							
	N	60	60	60	60	60							
	W	60	60	60	60	60							
	P	60	60	60	60	60							
	D	60	60	60	60	60							
	IT (0.1m)	60	60	60	60	60							
	IT (0.0m)	60	60	60	60	60							
	IT (-0.2m)	60	60	60	60	60							
	IT (-2.0m)	60	60	60	60	60							
	IT (-5.0m)	60	60	60	60	60							
	IT (-8.0m)	60	60	60	60	60							

Table G.6 *Storage intervals in minutes of sensors at VF-AWS240. SIDs are described in Table G.3. Both intervals are presented in months of storage intervals changes.*

		2008												2009										
	SID	J	F	M	A	M	J	J	A	S	O	N	D	J	F	M	A	M	J	J	A	S	O	N	D
VF-AWS240	TH (2.3m)					10	10	10	10	10	10	10	10	10	10	10	10	10							
	TH (4.0m)					10	10	10	10	10	10	10	10	10	10	10	10	10							
	SD					10	10	10	10	10	10	10	10	10	10	10	10	10							
	SU					10	10	10	10	10	10	10	10	10	10	10	10	10							
	N					10	10	10	10	10	10	10	10	10	10	10	10	10							
	D					10	10	10	10	10	10	10	10	10	10	10	10	10							
	IT (0.5m)					10	10	10	10	10	10	10	10	10	10	10	10	10							
	IT (0.2m)					10	10	10	10	10	10	10	10	10	10	10	10	10							
	IT (0.1m)					10	10	10	10	10	10	10	10	10	10	10	10	10							
	IT (0.0m)					10	10	10	10	10	10	10	10	10	10	10	10	10							
	IT (-0.2m)					10	10	10	10	10	10	10	10	10	10	10	10	10							
	IT (-2.0m)					10	10	10	10	10	10	10	10	10	10	10	10	10							
	IT (-5.0m)					10	10	10	10	10	10	10	10	10	10	10	10	10							
	IT (-8.0m)					10	10	10	10	10	10	10	10	10	10	10	10	10							

Table G.7 *Storage intervals in minutes of sensors at VF-AWS500. SIDs are described in Table G.3. Both intervals are presented in months of storage intervals changes.*

		2008												2009										
	SID	J	F	M	A	M	J	J	A	S	O	N	D	J	F	M	A	M	J	J	A	S	O	N	D
VF-AWS500	TH (2.5m)					10	10	10	10	10	10	10	10	10	10	10	10	10							
	TH (4.0m)					10	10	10	10	10	10	10	10	10	10	10	10	10							
	SD					10	10	10	10	10	10	10	10	10	10	10	10	10							
	SU					10	10	10	10	10	10	10	10	10	10	10	10	10							
	N					10	10	10	10	10	10	10	10	10	10	10	10	10							
	D					10	10	10	10	10	10	10	10	10	10	10	10	10							
	IT (0.5m)					10	10	10	10	10	10	10	10	10	10	10	10	10							
	IT (0.2m)					10	10	10	10	10	10	10	10	10	10	10	10	10							
	IT (0.1m)					10	10	10	10	10	10	10	10	10	10	10	10	10							
	IT (0.0m)					10	10	10	10	10	10	10	10	10	10	10	10	10							
	IT (-0.2m)					10	10	10	10	10	10	10	10	10	10	10	10	10							
	IT (-2.0m)					10	10	10	10	10	10	10	10	10	10	10	10	10							
	IT (-5.0m)					10	10	10	10	10	10	10	10	10	10	10	10	10							
	IT (-8.0m)					10	10	10	10	10	10	10	10	10	10	10	10	10							

Table G.8 *Storage intervals in minutes of sensors at VF-AWS605. SIDs are described in Table G.3. Both intervals are presented in months of storage intervals changes.*

		2008												2009										
	SID	J	F	M	A	M	J	J	A	S	O	N	D	J	F	M	A	M	J	J	A	S	O	N	D
VF-AWS605	TH (2.6m)					10	10	10	10	10	10	10	10	10	10	10	10	10							
	TH (3.9m)					10	10	10	10	10	10	10	10	10	10	10	10	10							
	SD					10	10	10	10	10	10	10	10	10	10	10	10	10							
	SU					10	10	10	10	10	10	10	10	10	10	10	10	10							
	N					10	10	10	10	10	10	10	10	10	10	10	10	10							
	P					10	10	10	10	10	10	10	10	10	10	10	10	10							
	D					10	10	10	10	10	10	10	10	10	10	10	10	10							
	IT (-2.0m)					10	10	10	10	10	10	10	10	10	10	10	10	10							
	IT (-10.0m)					10	10	10	10	10	10	10	10	10	10	10	10	10							

Table G.9 *Storage intervals in minutes of sensors at KV-AWS. SIDs are described in Table G.3. Both intervals are presented in months of storage intervals changes.*

		2008												2009										
	SID	J	F	M	A	M	J	J	A	S	O	N	D	J	F	M	A	M	J	J	A	S	O	N	D
KV-AWS	TH (2.5m)					1	1	1	1,10	10	10	10	10	10	10	10	10	10	10	10	10				
	TH (4.0m)					1	1	1	1,10	10	10	10	10	10	10	10	10	10	10	10	10				
	SD					1	1	1	1,10	10	10	10	10	10	10	10	10	10	10	10	10				
	SU					1	1	1	1,10	10	10	10	10	10	10	10	10	10	10	10	10				
	N					1	1	1	1,10	10	10	10	10	10	10	10	10	10	10	10	10				
	U					1	1	1	1,10	10	10	10	10	10	10	10	10	10	10	10	10				
	P					1	1	1	1,10	10	10	10	10	10	10	10	10	10	10	10	10				
	D					1	1	1	1,10	10	10	10	10	10	10	10	10	10	10	10	10				
	IT (-0.025m)					1	1	1	1,10	10	10	10	10	10	10	10	10	10	10	10	10				
	IT (-0.075m)					1	1	1	1,10	10	10	10	10	10	10	10	10	10	10	10	10				
	IT (-0.125m)					1	1	1	1,10	10	10	10	10	10	10	10	10	10	10	10	10				
	IT (-0.175m)					1	1	1	1,10	10	10	10	10	10	10	10	10	10	10	10	10				
	HF(-0.05m)					1	1	1	1,10	10	10	10	10	10	10	10	10	10	10	10	10				
	HF(-0.10m)					1	1	1	1,10	10	10	10	10	10	10	10	10	10	10	10	10				
	HF(-0.15m)					1	1	1	1,10	10	10	10	10	10	10	10	10	10	10	10	10				
	WC (-0.05m)					1	1	1	1,10	10	10	10	10	10	10	10	10	10	10	10	10				
	WC (-0.15m)					1	1	1	1,10	10	10	10	10	10	10	10	10	10	10	10	10				

Appendix H: Metadata of hardware within the modeling and analysis framework

Table H.1 *Specifications of the hardware in the reanalysis framework.*

#	Task	Mainboard	Arch.	RAM [GB]	Disk space [GB]	Processor type	Processors per node	Threads per node	appr. GigaFlops per node	appr. GigaFlops total
1	Controling	Intel S3210SH	x86_64	2	7240	Intel Core 2 Duo CPU E8400 (2x3GHz)				
6	Computing	Tyan S7002	x86_64	16	220	Intel Xeon CPU L5520 (4x2.26GHz)	2	16	43	257
17	Computing	Intel S5520HC	x86_64	16	220	Intel Xeon CPU E5620 (4x2.4GHz)	2	16	46	774
										1032

Table H.2 *Specifications of the hardware used for analyses.*

#	Task	Mainboard	Arch.	RAM [GB]	Disk space [GB]	Processor types	Processors per node	Threads per node	appr. GigaFlops per node	appr. GigaFlops total
1	Controling	Gigabyte EG41MF-US2H	x86_64	2	70	Intel Pentium Dual-Core CPU E6500 (2x2.93GHz)				
3	Computing	Intel S5400SF	x86_64	16	220	Intel Xeon CPU L5420 (4x2.5GHz)	2	8	47	141
										141

Table H.3 *Specifications of the network attached storage (NAS).*

#	Name	Network	Disk Slots	Used Disks type	RAID Level	Storage [TB]	Total Storage [TB]
7	ReadyNAS Ultra 4 Plus	2x1Gbit	4	Western Digital WD RE4-GP (2TB)	5	6	42
6	ReadyNAS Pro 6	2x1Gbit	6	Hitachi HDS723030ALA640 (3TB)	5	15	90
1	QNAP Turbo NAS	2x1Gbit	4	Western Digital WD RE4-GP (2TB)	5	6	6
							138

Appendix J: Results of conducted field work and measurement quality assessment

Table J.1 *Overview of conducted field work.*

Date	Used logistics	Team members	Conducted work
01.05.-01.06.2008	Helicopter and snowmobiles	Roman Finkelnburg, Marco Möller, Dieter Scherer and Christoph Schneider	Setting up five AWS and 24 ablation/ice velocity stakes. Digging of five snow pits. Differential GPS measurements at nine ablation stakes. Eight kinematic profiles.
01.08.-22.08.2008	Helicopter/ Ship and by foot operations	Matthias Braun, Roman Finkelnburg, Fred Meier and Marco Möller	Gathering data from AWS. Fixing and maintaining AWS. Metering and maintaining of ablation stake network. Digging of two snow pits. Differential GPS measurements at four ablation stakes.
10.05.-29.05.2009	Helicopter and snowmobiles	Roman Finkelnburg, Marco Möller, Tobias Sauter and Dieter Scherer	Gathering data from AWS. Fixing and maintaining AWS. Dismounting three AWS and nine ablation stakes. Metering and maintaining of ablation stake network. Digging one snow pit. Differential GPS measurements at four ablation stakes.
31.07.-19.08.2009	Helicopter/Ship and by foot operations	Matthias Braun, Roman Finkelnburg, Bob McNabb and Marco Möller	Gathering data from AWS. Fixing and maintaining AWS. Dismounting one AWS. Metering and maintaining of ablation stake network.
06.05.-26.05.2010	Helicopter and by foot operations	Roman Finkelnburg, Alber Polze, Rebecca Möller and Marco Möller	Gathering data from AWS. Fixing and maintaining AWS. Metering and maintaining of ablation stake network. Digging two snow pits.
12.08.-28.08.2010	Ship and by foot operations	Roman Finkelnburg, Marco Möller and Christoph Schneider	Gathering data from AWS. Fixing and maintaining AWS. Metering and maintaining of ablation stake network. Digging two snow pits.
10.05.-29.05.2011	Helicopter and snowmobiles	Roman Finkelnburg, Marco Möller, Dieter Scherer and Christoph Schneider	Gathering data from AWS. Fixing and maintaining AWS. Metering and maintaining of ablation staknetwork. Digging seven snow pits.
27.07.-11.08.2011	Ship and by foot operations	Roman Finkelnburg, Fabien Maussion and Marco Möller	Gathering data from AWS. Fixing and maintaining AWS. Metering and maintaining of ablation stake network.
09.05.-02.06.2012	Helicopter and snowmobiles	Roman Finkelnburg, Albert Polze, Marco Möller and Lars Schneider	Gathering data from AWS. Fixing and maintaining AWS. Metering and maintaining of ablation stake network. Digging two snow pits. Dismounting two AWS and 15 ablation stakes.

Table J.2 *Quality assessment of measurements of DG-AWS. SIDs are described in Table G.3. Categories are described in Table 3.2.*

		2008												2009											
	SID	J	F	M	A	M	J	J	A	S	O	N	D	J	F	M	A	M	J	J	A	S	O	N	D
DG-AWS	TH (2.1m)					N	N	N	N	N	N	N	N	N	N	N	E	E	N	N	N	N	N	N	N
	TH (3.6m)					N	N	N	N	N	E	E	E	N	N	N	E	E	N	N	N	N	N	N	N
	SD					N	N	N	N	N	E	E	E	N	N	N	E	E	N	N	N	N	N	N	N
	SU					N	N	N	N	N	E	E	E	N	N	N	E	E	N	N	N	N	N	N	N
	N																	N	N	N	N	N	N	N	N
	W																	N	N	N	N	N	N	N	N
	P																	N	N	N	N	N	N	N	N
	D					N	E	N	N	N	N	N	N	N	E	E	E	E	N	N	N	N	S	S	S
	IT (0.1m)					N	N	N	N	N	E	E	E	E	E	E	E	E	N	N	N	N	N	N	N
	IT (0.0m)					N	N	N	N	N	N	N	E	E	E	E	E	E	N	N	N	N	N	N	N
	IT (-2.0m)					N	N	N	N	N	N	N	N	N	N	N	E	E	N	N	N	N	N	N	N
	IT (-8.0m)					N	N	N	E	E	N	N	N	N	N	N	E	E	N	N	N	N	N	N	N

		2010												2011											
	SID	J	F	M	A	M	J	J	A	S	O	N	D	J	F	M	A	M	J	J	A	S	O	N	D
DG-AWS	TH (2.1m)	N	N	E	N	N	N	N	E	N	E	E	E	E	E	N	N	N	N	N	N	N	C	C	C
	TH (3.6m)	N	N	E	N	N	N	N	E	N	E	E	E	E	E	N	N	N	N	N	N	N	C	C	C
	SD	N	N	E	N	N	N	N	E	N	N	N	N	N	N	N	N	N	N	N	N	N	C	C	C
	SU	N	N	E	N	N	N	N	N	N	N	N	N	N	N	N	N	N	N	N	N	N	C	C	C
	LU								N	N	N	N	N	N	N	N	N	N	N	N	N	N	C	C	C
	N	N	N	E	N	N	N	N	E	N	N	N	N	N	N	N	N	N	N	N	N	N	C	C	C
	W	N	N	E	N	N	N	N	N	N	N	N	N	N	N	N	N	N	N	N	N	N	C	C	C
	P	N	N	E	N	N	N	N	N	N	N	N	N	N	N	N	N	N	N	N	N	N	C	C	C
	D	N	S	S	S	S	S	S	S	S	S	S	S	S	S	S	S	S	N	N	N	U	C	C	C
	IT (0.1m)	N	N	E	N	N	N	E	E	E	E	E	E	E	E	E	E								
	IT (0.0m)	N	N	E	N	N	N	E	E	E	E	E	E	E	E	E	E								
	IT (-2.0m)	N	N	E	N	N	N	N	N	N	N	N	N	N	N	N	N	N	N	N	N	N	N	N	N
	IT (-8.0m)	N	N	E	N	N	N	N	E	E	N	N	N	N	N	N	N	N	U	U	U	N	N	N	N

		2012											
	SID	J	F	M	A	M	J	J	A	S	O	N	D
DG-AWS	TH (2.1m)	C	C	C	C	C							
	TH (3.6m)	C	C	C	C	C							
	SD	C	C	C	C	C							
	SU	C	C	C	C	C							
	LU	C	C	C	C	C							
	N	C	C	C	C	C							
	W	C	C	C	C	C							
	P	C	C	C	C	C							
	D	C	C	C	C	C							
	IT (-2.0m)	N	N	N	N	N							
	IT (-8.0m)	N	N	N	N	N							

Table J.3 *Quality assessment of measurements of VF-AWS370. SIDs are described in Table G.3. Categories are described in Table 3.2.*

		2008												2009											
	SID	J	F	M	A	M	J	J	A	S	O	N	D	J	F	M	A	M	J	J	A	S	O	N	D
VF-AWS370	TH (1.9m)					N	N	N	N	N	N	N	N	N	N	N	N	N	N	N	A	A	A	A	A
	TH (3.9m)					N	N	N	N	N	N	N	N	N	N	N	N	N	N	N	A	A	A	A	A
	SD					N	N	N	N	N	N	N	N	N	N	N	N	N	N	N	A	A	A	A	A
	SU					N	N	N	N	N	N	N	N	E	E	E	E	E	N	N	A	A	A	A	A
	N					N	N	N	N	N	N	N	N	E	E	E	E	E	N	N	A	A	A	A	A
	W																	N	N	N	A	A	A	A	A
	D					N	N	N	N	N	N	N	N	N	N	N	N	E	N	N	A	A	A	A	A
	IT (0.5m)					N	N	N	N	N	N	N	N	E	E	E	E	E	N	N	N	N	N	N	N
	IT (0.2m)					N	N	N	N	N	N	N	N	E	E	E	E	E	N	N	N	N	N	N	N
	IT (0.1m)					N	N	N	N	U	U	U	U	E	E	E	E	E	N	N	N	N	N	N	N
	IT (0.0m)					N	N	N	N	N	U	U	U	E	E	E	E	E	N	N	N	N	N	N	N
	IT (-0.2m)					N	N	N	N	N	U	U	U	E	E	E	E	E	N	U	U	N	N	N	N
	IT (-2.0m)					N	N	N	N	N	N	N	N	E	E	E	E	E	N	U	N	N	N	N	N
	IT (-5.0m)					N	U	U	U	U	U	U	U	E	E	E	E	E	N	U	N	N	N	N	N
	IT (-8.0m)					N	U	N	N	N	N	N	N	E	E	E	E	E	U	U	N	N	N	N	N

		2010												2011											
	SID	J	F	M	A	M	J	J	A	S	O	N	D	J	F	M	A	M	J	J	A	S	O	N	D
VF-AWS370	TH (1.9m)	A	A	A	A	N	N	N	N	N	N	N	N	N	N	N	N	N	N	N	N	N	C	C	C
	TH (3.9m)	A	A	A	A	N	N	N	N	N	N	N	N	N	N	N	N	N	N	N	N	N	C	C	C
	SD	A	A	A	A	N	N	N	N	N	N	N	N	N	N	N	N	N	N	N	N	N	C	C	C
	SU	A	A	A	A	N	N	N	N	N	N	N	N	N	N	N	N	N	N	N	N	N	C	C	C
	LD					N	N	N	N	N	N	N	N	N	N	N	N	N	N	N	N	N	C	C	C
	N (CNR-1)																	N	N	N	N	U	C	C	C
	N	A	A	A	A	N	N	N	N	N	N	N	N	N	N	N	N	N	N	N	N	N	C	C	C
	W	A	A	A	A	N	N	N	N	N	N	N	N	N	N	N	N	N	N	N	N	N	C	C	C
	U																	N	N	S	S				
	P					N	N	N	N	N	N	N	N	N	N	N	N	N	N	N	N	N	C	C	C
	D	A	A	A	A	S	S	S	S	S	S	S	S	S	S	S	S	N	N	N	N	U	C	C	C
	IT (0.5m)	N	N	N	N																				
	IT (0.2m)	N	N	N	N																				
	IT (0.1m)	N	N	N	N	N	N	N	N	N	N	N	N	N	N	N	N	N	N	N	N	N	C	C	C
	IT (0.0m)	N	N	N	N	N	N	N	N	N	N	N	N	N	N	N	N	N	N	N	N	N	C	C	C
	IT (-0.2m)	N	N	N	N	N	N	U	N	N	N	N	N	N	N	N	N	N	N	N	N	N	C	C	C
	IT (-2.0m)	N	N	N	N	N	N	N	N	N	N	N	N	N	N	N	N	N	N	N	N	N	C	C	C
	IT (-5.0m)	N	N	N	N	N	N	N	N	N	N	N	N	N	N	N	N	N	N	N	N	N	C	C	C
	IT (-8.0m)	N	N	N	N	N	N	N	N	N	N	N	N	N	N	N	N	N	N	N	N	N	C	C	C

		2012											
	SID	J	F	M	A	M	J	J	A	S	O	N	D
VF-AWS370	TH (1.9m)	C	C	C	C	C							
	TH (3.9m)	C	C	C	C	C							
	SD	C	C	C	C	C							
	SU	C	C	C	C	C							
	LD	C	C	C	C	C							
	N (CNR-1)	C	C	C	C	C							
	N	C	C	C	C	C							
	W	C	C	C	C	C							
	P	C	C	C	C	C							
	D	C	C	C	C	C							
	IT (0.1m)	C	C	C	C	C							
	IT (0.0m)	C	C	C	C	C							
	IT (-0.2m)	C	C	C	C	C							
	IT (-2.0m)	C	C	C	C	C							
	IT (-5.0m)	C	C	C	C	C							
	IT (-8.0m)	C	C	C	C	C							

Table J.4 *Quality assessment of measurements of VF-AWS240. SIDs are described in Table G.3. Categories are described in Table 3.2.*

		2008												2009									
	SID	J	F	M	A	M	J	J	A	S	O	N	D	J	F	M	A	M	J	J	A	S	O	N	D
VF-AWS240	TH (2.3m)					N	N	U	U	N	N	N	N	N	N	N	N	E							
	TH (4.0m)					N	N	U	U	N	N	N	N	N	N	N	N	E							
	SD					N	N	N	N	N	N	N	N	E	E	E	E	E							
	SU					N	N	N	N	N	N	N	N	E	E	E	E	E							
	N					N	N	N	N	N	N	N	N	E	E	E	E	E							
	D					N	N	U	U	N	N	N	N	N	N	N	N	E							
	IT (0.5m)					N	N	U	U	U	N	N	N	E	E	E	E	E							
	IT (0.2m)					N	N	U	U	U	N	N	N	E	E	E	E	E							
	IT (0.1m)					N	N	U	U	U	N	N	N	E	E	E	E	E							
	IT (0.0m)					N	N	U	U	U	N	N	N	E	E	E	E	E							
	IT (-0.2m)					N	N	U	U	U	N	N	N	E	E	E	E	E							
	IT (-2.0m)					N	N	U	U	U	N	N	N	E	E	E	E	E							
	IT (-5.0m)					N	N	U	U	U	N	N	N	E	E	E	E	E							
	IT (-8.0m)					N	N	U	U	U	N	N	N	E	E	E	E	E							

Table J.5 *Quality assessment of measurements of VF-AWS500. SIDs are described in Table G.3. Categories are described in Table 3.2.*

		2008												2009									
	SID	J	F	M	A	M	J	J	A	S	O	N	D	J	F	M	A	M	J	J	A	S	O	N	D
VF-AWS500	TH (2.5m)					N	N	C	N	N	N	N	N	N	N	N	N	E							
	TH (4.0m)					N	N	C	N	N	N	N	N	N	N	N	N	E							
	SD					N	N	C	S	S	S	S	S	S	S	S	S	S							
	SU					N	N	C	N	N	N	N	N	E	E	E	E	E							
	N					N	N	C	N	N	N	N	N	E	E	E	E	E							
	D					N	N	C	N	N	S	S	S	S	S	S	S	S							
	IT (0.5m)					N	N	N	N	N	N	N	N	E	E	E	E	E							
	IT (0.2m)					N	N	N	N	N	N	N	N	E	E	E	E	E							
	IT (0.1m)					N	N	N	N	N	N	N	N	E	E	E	E	E							
	IT (0.0m)					N	N	N	N	N	N	N	N	E	E	E	E	E							
	IT (-0.2m)					N	N	N	N	N	N	N	N	E	E	E	E	E							
	IT (-2.0m)					N	N	N	N	N	N	N	N	E	E	E	E	E							
	IT (-5.0m)					N	N	N	N	N	N	N	N	E	E	E	E	E							
	IT (-8.0m)					N	N	N	N	N	N	N	N	E	E	E	E	E							

Table J.6 *Quality assessment of measurements of VF-AWS605. SIDs are described in Table G.3. Categories are described in Table 3.2.*

		2008												2009											
	SID	J	F	M	A	M	J	J	A	S	O	N	D	J	F	M	A	M	J	J	A	S	O	N	D
VF-AWS605	TH (2.6m)					N	C	C	C	C	C	C	C	C	C	C	C	C							
	TH (3.9m)					N	C	C	C	C	C	C	C	C	C	C	C	C							
	SD					N	C	C	C	C	C	C	C	C	C	C	C	C							
	SU					N	C	C	C	C	C	C	C	C	C	C	C	C							
	N					N	C	C	C	C	C	C	C	C	C	C	C	C							
	P					N	C	C	C	C	C	C	C	C	C	C	C	C							
	D					N	C	C	C	C	C	C	C	C	C	C	C	C							
	IT (-2.0m)					N	P	P	P	P	N	N	N	N	N	N	N	N							
	IT (-10.0m)					N	P	P	P	P	N	N	N	N	N	N	N	N							

Table J.7 *Quality assessment of measurements of KV-AWS. SIDs are described in Table G.3. Categories are described in Table 3.2.*

		2008												2009											
	SID	J	F	M	A	M	J	J	A	S	O	N	D	J	F	M	A	M	J	J	A	S	O	N	D
KV-AWS	TH (2.5m)					N	N	P	N	N	N	N	A	A	A	A	A	A	A	A	A				
	TH (4.0m)					N	N	P	N	N	N	N	A	A	A	A	A	A	A	A	A				
	SD					N	N	P	N	N	N	N	A	A	A	A	A	A	A	A	A				
	SU					N	N	P	N	N	N	N	A	A	A	A	A	A	A	A	A				
	N					N	N	P	N	N	N	N	A	A	A	A	A	A	A	A	A				
	U					N	N	P	N	N	N	N	A	A	A	A	A	A	A	A	A				
	P					N	N	P	N	N	N	N	A	A	A	A	A	A	A	A	A				
	D					N	N	P	N	N	N	N	A	A	A	A	A	A	A	A	A				
	IT (-0.025m)					N	N	P	N	N	N	N	A	A	A	A	A	A	A	A	A				
	IT (-0.075m)					N	N	P	N	N	N	N	A	A	A	A	A	A	A	A	A				
	IT (-0.125m)					N	N	P	N	N	N	N	A	A	A	A	A	A	A	A	A				
	IT (-0.175m)					N	N	P	N	N	N	N	A	A	A	A	A	A	A	A	A				
	HF(-0.05m)					N	N	P	N	N	N	N	A	A	A	A	A	A	A	A	A				
	HF(-0.10m)					N	N	P	N	N	N	N	A	A	A	A	A	A	A	A	A				
	HF(-0.15m)					N	N	P	N	N	N	N	A	A	A	A	A	A	A	A	A				
	WC (-0.05m)					N	N	P	N	N	N	N	A	A	A	A	A	A	A	A	A				
	WC (-0.15m)					N	N	P	N	N	N	N	A	A	A	A	A	A	A	A	A				

Table J.8 *Metering of ablation/accumulation stake network. A cross marks campaigns when stake was metered. Spring campaigns are indicated by ‚Sp' and summer campaigns are indicated by ‚Su'. Grayed periods indicate that the ablation/accumulation stake has been removed.*

Name	Lat	Long	Alt	2008		2009		2010		2011		2012	Repeat
	[° N]	[° E]	[m a.s.l]	Sp	Su	Sp	Su	Sp	Su	Sp	Su	Sp	readings
VF1	80.00287	19.43709	197	x									**0**
DG2	80.01375	19.19085	210	x	**x**	**x**	**x**		**x**	**x**	**x**	**x**	**7**
DG3	80.01227	19.19513	225	x	**x**	**x**	**x**		**x**	**x**	**x**	**x**	**7**
DG-AWS-1	80.01632	19.18440	240	x	**x**		**x**		**x**	**x**	**x**	**x**	**6**
DG-AWS-2	80.01630	19.18660	240	x	**x**		**x**		**x**	**x**	**x**	**x**	**6**
VF-AWS240-1	79.99952	19.44525	240	x	**x**	**x**		**x**	**x**		**x**	**x**	**6**
VF-AWS240-2	79.99914	19.44303	240	x	**x**	**x**		**x**	**x**	**x**	**x**		**6**
VF-AWS240-3	79.99908	19.44149	240	x	**x**	**x**		**x**	**x**	**x**	**x**		**6**
DG4	80.01942	19.18938	252	x	**x**		**x**		**x**	**x**	**x**	**x**	**6**
DG5	80.02163	19.19505	266	x	**x**		**x**		**x**	**x**	**x**		**5**
VF2	79.99616	19.45360	285	x	**x**	**x**		**x**	**x**	**x**	**x**		**6**
VF3	79.99050	19.46205	329	x	**x**	**x**		**x**	**x**	**x**	**x**		**6**
VF-AWS370-1	79.98516	19.47517	370	x	**x**	**x**		**x**	**x**				**4**
VF-AWS370-2	79.98484	19.47424	370	x	**x**	**x**		**x**	**x**		**x**		**5**
VF-AWS370-3	79.98444	19.47286	370	x	**x**				**x**		**x**	**x**	**4**
VF4	79.97724	19.49016	413	x	**x**	**x**							**2**
VF5	79.97150	19.50872	458	x	**x**							**x**	**2**
VF-AWS500-1	79.96510	19.53296	500	x	**x**								**1**
VF-AWS500-2	79.96489	19.53150	500	x	**x**								**1**
VF-AWS500-3	79.96484	19.53078	500	x	**x**								**1**
VF6	79.95482	19.57353	550	x									**0**
VF-AWS605-1	79.97996	20.12621	605	x		**x**							**1**
VF-AWS605-2	79.98011	20.12254	605	x									**0**
VF-AWS605-3	79.98060	20.12549	605	x									**0**
			Repeat readings		**19**	**11**	**6**	**7**	**14**	**10**	**13**	**8**	

Table J.9 *Dates and locations of snow pits measurements.*

#	Date	Lat [° N]	Long [° E]	Alt [m a.s.l]
1	18.05.2008	79.98015	20.12419	600
2	19.05.2008	79.99951	19.44416	240
3	20.05.2008	79.96506	19.53199	500
4	26.05.2008	80.01630	19.18551	240
5	28.05.2008	79.98473	19.47380	370
6	05.08.2008	79.99951	19.44416	240
7	08.08.2008	79.96506	19.53199	500
8	23.05.2009	80.01630	19.18551	240
9	16.05.2010	79.98473	19.47380	370
10	19.05.2010	80.01630	19.18551	240
11	20.08.2010	79.98473	19.47380	370
12	21.08.2010	80.01630	19.18551	240
13	14.05.2011	79.83705	21.81320	240
14	14.05.2011	79.86085	21.83096	378
15	14.05.2011	79.91669	21.85447	518
16	15.05.2011	80.13345	20.63861	550
17	17.05.2011	79.98473	19.47380	370
18	18.05.2011	80.01630	19.18551	240
19	19.05.2011	79.96254	19.69312	562
20	19.05.2012	79.98473	19.47380	370
21	21.05.2012	80.01630	19.18551	240

Table J.10 *Number of snow pit measurements per field campaign. Spring campaigns are indicated by ‚Sp' and summer campaigns are indicated by ‚Su'.*

2008		2009		2010		2011		2012
Sp	Su	Sp	Su	Sp	Su	Sp	Su	Sp
5	2	1	0	2	2	7	0	2

Appendix K: Results of surface energy and mass balance analyses of Vestfonna ice cap

Table K.1 *Annual surface accumulation on Vestfonna as resolved by the regional reanalysis assuming different mass loss rates due to snow drift.*

Mass loss (%)	Accumulation (m w.e. yr−1)
0 %	0.51
7 %	0.47
12 %	0.45
15 %	0.43
20 %	0.41

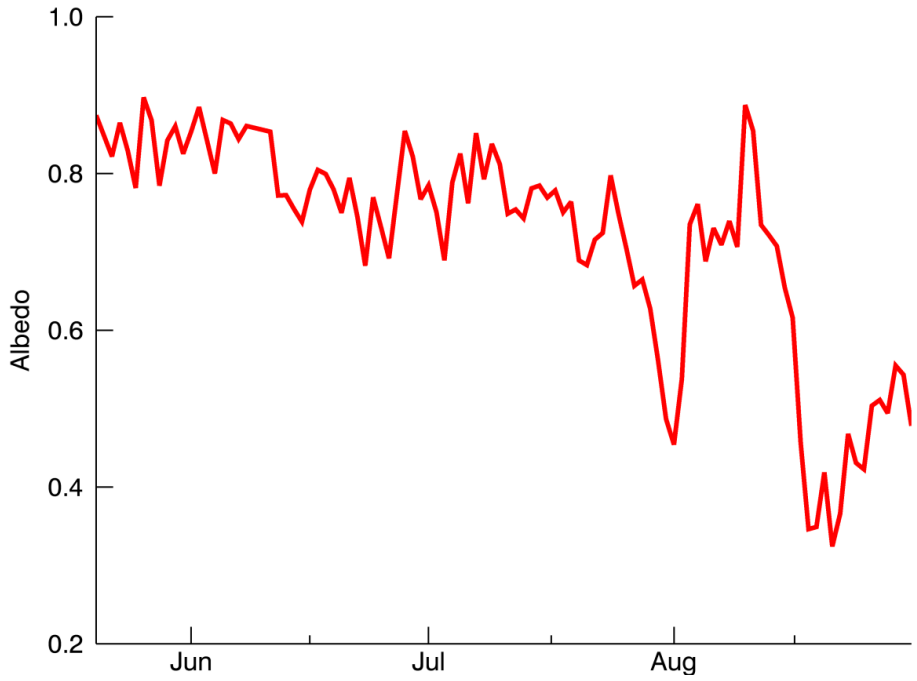

Figure K.1 *Shortwave albedo measured at VF-AWS370 (see Figure 3.1) for the period 20th May – 31st August 2011.*

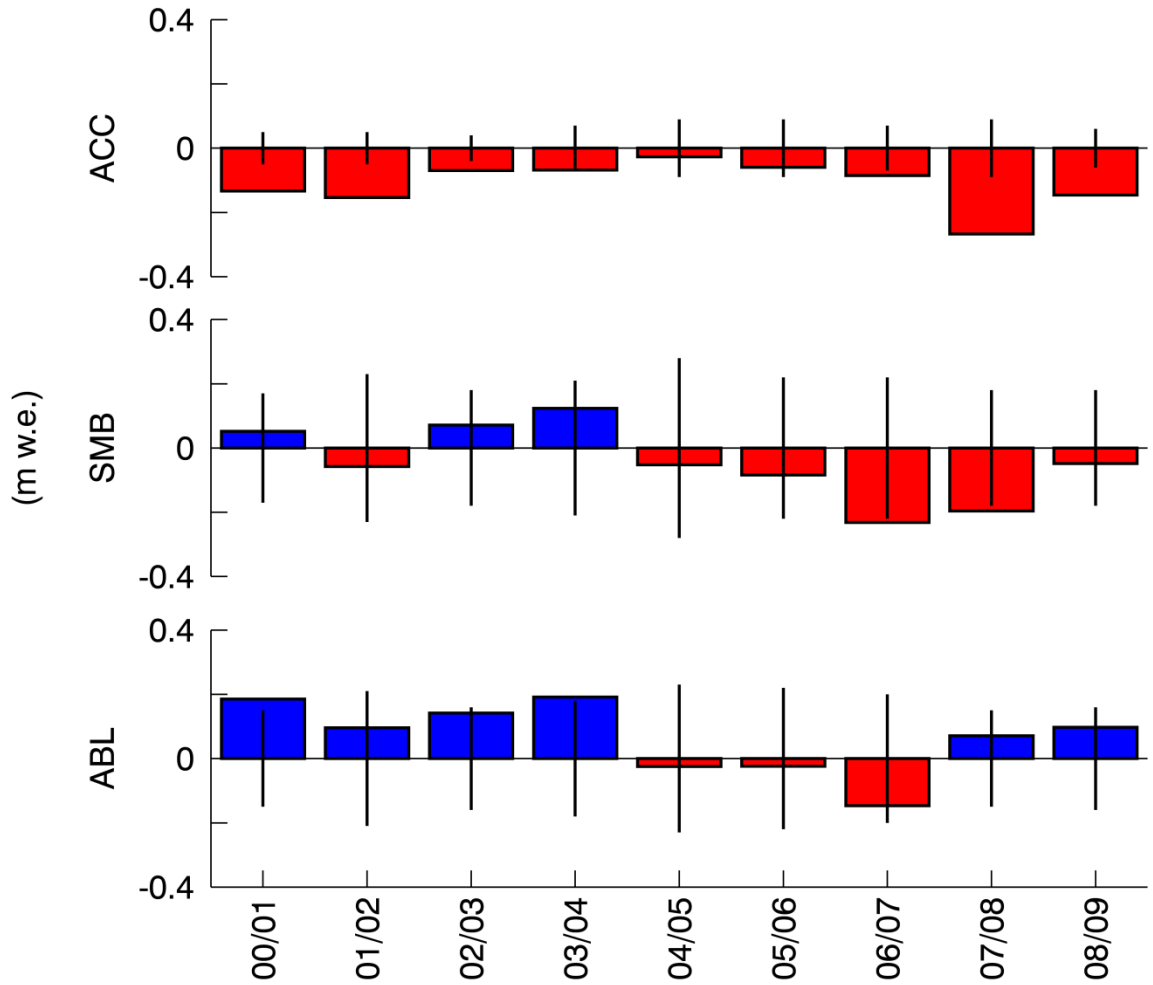

Figure K.2 *Annual difference of accumulation (ACC), surface mass balance (SMB) and ablation (ABL) rates from mass balance modeling in Paper II and surface energy and mass balance as resolved by the regional reanalysis for the mass balance years 2001 to 2009. Rates of refreezing have been subtracted from ablation rates of Paper II to obtain SMB values. A zero value represents the value obtained from analysis in Paper II with the respective error bar (black line). Bar charts show the difference of the respective rates derived from the regional reanalysis. A positive difference indicates the value of respective rate is larger in Paper II than derived from the regional reanalysis.*

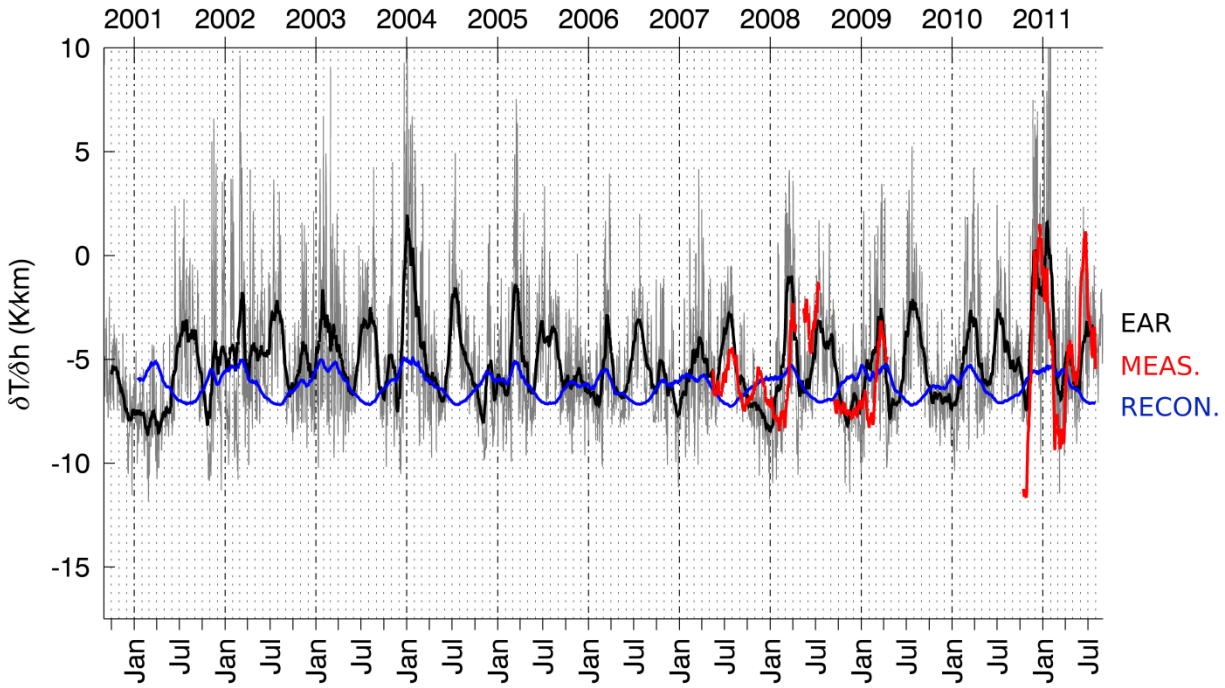

Figure K.3 *Annual cycle of elevational gradients of air temperature on Vestfonna. Grey line: daily values derived from reanalysis, black line: moving 30-day mean of daily values derived from regional reanalysis (EAR), blue line: moving 30-day mean of daily values derived from reconstructed data, red line: moving 30-day mean of daily values derived from measurements.*

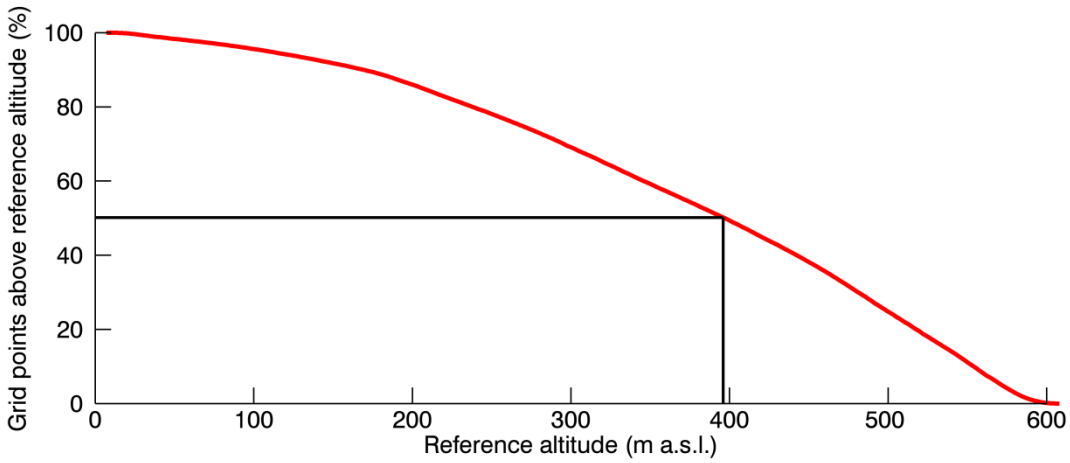

Figure K.4 *Altitudinal distribution of Vestfonna grid points within the ASTER ASTER Global Digital Elevation Model (GDEM) in respect to a reference altitude. The values present the percentage of grid points above the respective reference altitude (red line). The altitude of equilibrium, i.e. amounts of grid points above and below this altitude are equal, is indicated by black lines.*

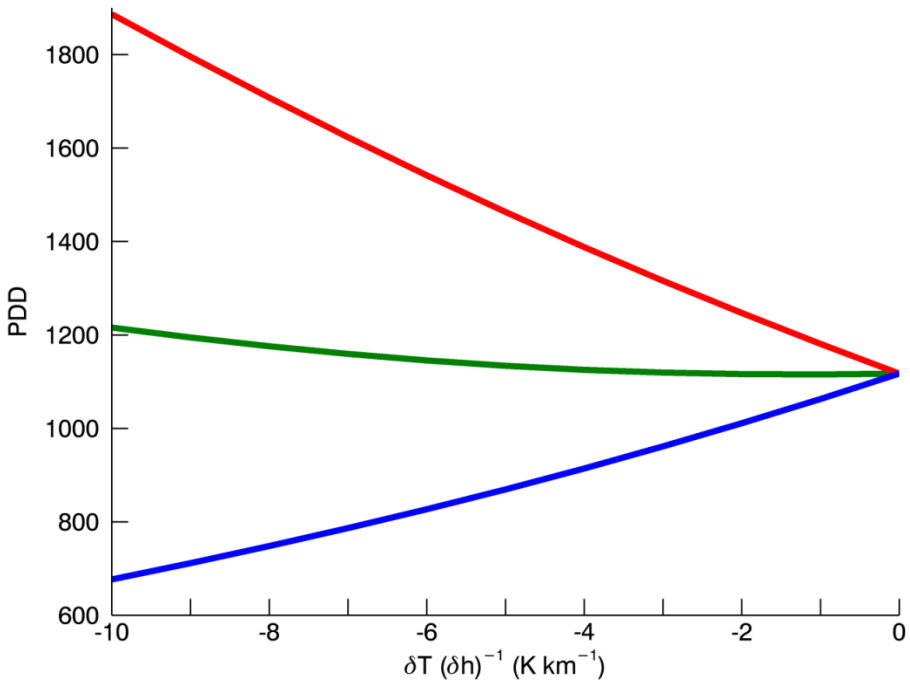

Figure K.5 *Spatial means of accumulated positive degree days (PDD) for the mass balance years 2001 to 2009 presented as glacier-wide mean PPDs (green), mean PPDs above 370 m a.s.l. (blue) and mean PPDs below 370 m a.s.l. (red). Different elevational gradients ($\frac{\partial T}{\partial h}$) have been used for the extrapolation of air temperature on Vestfonna using the ASTER Global Digital Elevation Model (GDEM). As input the reconstructed air-temperature time series of VF-AWS370 located at 370 m a.s.l. of Paper II is used.*

Appendix L: Results of large-scale process analyses

Table L.1 *Correlation of seasonal anomalies of glacier-wide mean air-temperature, solid precipitation, wind speed and rain-snow ratio at Vestfonna for September to November (SON), December to February (DJF), March to May (MAM) and June to August (JJA) of the mass balance years 2001 to 2011 as resolved by the EAR at 2 km horizontal resolution. Results are presented as squared Pearson product-moment correlation coefficient (r^2) and significance is indicated by the Student's t probability (p). The type of correlation is indicated, i.e. positive (C) and negative (A). Correlations significant on 0.05 significance level are highlighted, i.e. positive correlation (green) and negative correlations (orange).*

	Predictor	Predictand	r^2	p (%)	Type
SON	Wind speed	Precipitation	**0.63**	**100**	**C**
	Wind speed	Air-temperature	0.01	19	C
	Air-temperature	Precipitation	0.22	86	C
	Ait-temperature	Rain-snow ratio	0.01	19	C
DJF	Wind speed	Precipitation	**0.68**	**100**	**C**
	Wind speed	Air-temperature	**0.57**	**99**	**C**
	Air-temperature	Precipitation	**0.68**	**100**	**C**
	Ait-temperature	Rain-snow ratio	0.02	31	C
MAM	Wind speed	Precipitation	0.23	86	C
	Wind speed	Air-temperature	0.19	82	C
	Air-temperature	Precipitation	0.05	48	C
	Ait-temperature	Rain-snow ratio	**0.44**	**97**	**C**
JJA	Wind speed	Precipitation	**0.55**	**99**	**C**
	Wind speed	Air-temperature	0.00	6	C
	Air-temperature	Precipitation	0.15	77	A
	Ait-temperature	Rain-snow ratio	**0.42**	**97**	**C**

Table L.2 *Correlation of seasonal anomalies of glacier-wide mean air-temperature, solid precipitation and elevational gradients of air temperature at Vestfonna as resolved by the EAR at 2 km horizontal resolution with indices of the sea ice coverage of the Nordaustlandet domain for September to November (SON), December to February (DJF), March to May (MAM) and June to August (JJA) of the mass balance years 2001 to 2011 . Results are presented as squared Pearson product-moment correlation coefficient (r^2) and significance is indicated by the Student's t probability (p). The type of correlation is indicated, i.e. positive (C) and negative (A). Correlations significant on 0.05 significance level are highlighted, i.e. positive correlation (green) and negative correlations (orange).*

		r^2	p (%)	Type
SON	Precipitation	0.14	71	A
	Air temperature	0.01	25	A
	dT/dH	0.14	72	C
DJF	Precipitation	**0.52**	**98**	**A**
	Air temperature	**0.76**	**100**	**A**
	dT/dH	**0.80**	**100**	**C**
MAM	Precipitation	0.04	41	A
	Air temperature	**0.68**	**100**	**A**
	dT/dH	0.34	92	C
JJA	Precipitation	0.27	88	C
	Air temperature	0.00	10	C
	dT/dH	0.13	69	C

Table L.3 *Correlation of the frequency and origin of cyclones (see Section 3.3.6) with seasonal anomalies of glacier-wide mean air-temperature, solid precipitation and wind speed at Vestfonna as resolved by the EAR at 2 km horizontal resolution, sea ice anomalies within the Nordaustlandet domain and the North Atlantic Oscillation (NAO) Index for September to November (SON), December to February (DJF), March to May (MAM) and June to August (JJA) of the mass balance years 2001 to 2008 (source is the National Snow and Ice Data Center (sources are http://nsidc.org/data/docs/daac/nsidc0423_cyclone/ and the NOAA Climate Prediction Center, http://www.cpc.ncep.noaa.gov). Results are presented as squared Pearson product-moment correlation coefficient (r^2) and significance is indicated by the Student's t probability (p). The type of correlation is indicated, i.e. positive (C) and negative (A). Correlations significant on 0.05 significance level are highlighted, i.e. positive correlation (green) and negative correlations (orange).*

		South-West			Local		
		r^2	p (%)	Type	r^2	p (%)	Type
SON	Precipitation	**0.54**	**96**	**C**	0.14	64	C
	Air temperature	0.15	67	C	0.00	13	A
	Wind speed	0.19	72	C	0.21	75	C
	Sea ice	0.09	49	C	0.25	75	C
	NAO	0.16	67	C	0.02	27	C
DJF	Precipitation	**0.57**	**97**	**C**	**0.83**	**100**	**A**
	Air temperature	**0.60**	**98**	**C**	0.40	91	A
	Wind speed	**0.68**	**99**	**C**	0.36	89	A
	Sea ice	0.20	68	A	0.30	80	C
	NAO	**0.65**	**98**	**C**	**0.67**	**99**	**A**
MAM	Precipitation	0.11	58	A	0.18	71	C
	Air temperature	0.06	45	A	0.08	52	C
	Wind speed	0.02	29	C	**0.66**	**99**	**C**
	Sea ice	0.00	3	C	0.39	87	A
	NAO	0.03	30	C	0.12	61	A
JJA	Precipitation	0.08	50	A	**0.54**	**96**	**C**
	Air temperature	0.07	46	A	0.28	82	A
	Wind speed	**0.59**	**97**	**A**	0.24	79	C
	Sea ice	**0.74**	**99**	**A**	0.18	65	C
	NAO	0.00	7	C	**0.53**	**96**	**A**

Table L.4 *Correlation of seasonal anomalies of glacier-wide mean air-temperature, solid precipitation and wind speed at Vestfonna as resolved by the EAR at 2 km horizontal resolution and sea ice anomalies within the Nordaustlandet domain with indices of the North Atlantic Oscillation (NAO) and the Arctic Oscillation (AO) for September to November (SON), December to February (DJF), March to May (MAM) and June to August (JJA) of the mass balance years 2001 to 2011 (source is the NOAA Climate Prediction Center, http://www.cpc.ncep.noaa.gov). Results are presented as squared Pearson product-moment correlation coefficient (r^2) and significance is indicated by the Student's t probability (p). The type of correlation is indicated, i.e. positive (C) and negative (A). Correlations significant on 0.05 significance level are highlighted, i.e. positive correlation (green) and negative correlations (orange).*

			r^2	p (%)	Type
NAO	SON	Precipitaton	0.28	91	C
		Air-temperature	0.14	74	C
		Wind speed	**0.38**	**96**	**C**
		Sea ice	0.06	52	A
	DJF	Precipitaton	**0.52**	**99**	**C**
		Air-temperature	0.13	72	C
		Wind speed	**0.45**	**98**	**C**
		Sea ice	0.07	53	A
	MAM	Precipitaton	0.16	78	C
		Air-temperature	0.06	52	C
		Wind speed	0.11	69	C
		Sea ice	0.00	2	C
	JJA	Precipitaton	0.24	88	A
		Air-temperature	**0.38**	**96**	**C**
		Wind speed	0.14	74	A
		Sea ice	0.09	60	A
AO	SON	Precipitaton	0.12	71	C
		Air-temperature	0.08	60	C
		Wind speed	0.07	57	C
		Sea ice	0.02	31	C
	DJF	Precipitaton	0.01	20	C
		Air-temperature	0.00	5	A
		Wind speed	0.00	12	C
		Sea ice	0.03	37	C
	MAM	Precipitaton	0.27	90	C
		Air-temperature	0.03	37	C
		Wind speed	0.04	43	C
		Sea ice	0.00	9	C
	JJA	Precipitaton	0.16	78	A
		Air-temperature	0.12	69	C
		Wind speed	0.13	72	A
		Sea ice	0.00	8	A

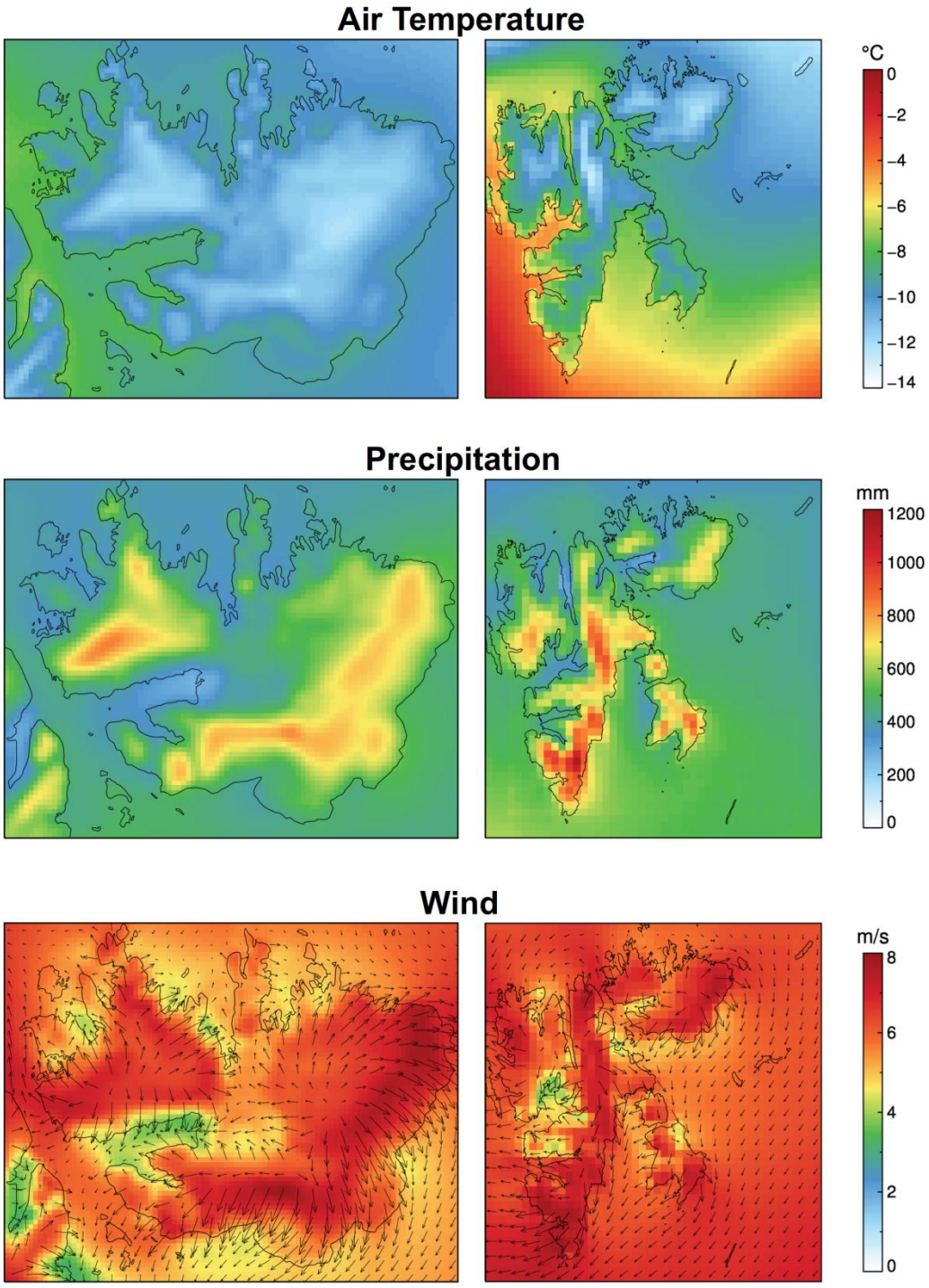

Figure L.1 *Eleven-year annual mean of air-temperature, accumulated precipitation and wind as resolved by the EAR. Each variable is plotted for the Nordaustlandet domain (left) and the Svalbard domain (right). Arrows in the wind plot are vector averages while colours present the scalar average of wind speed.*

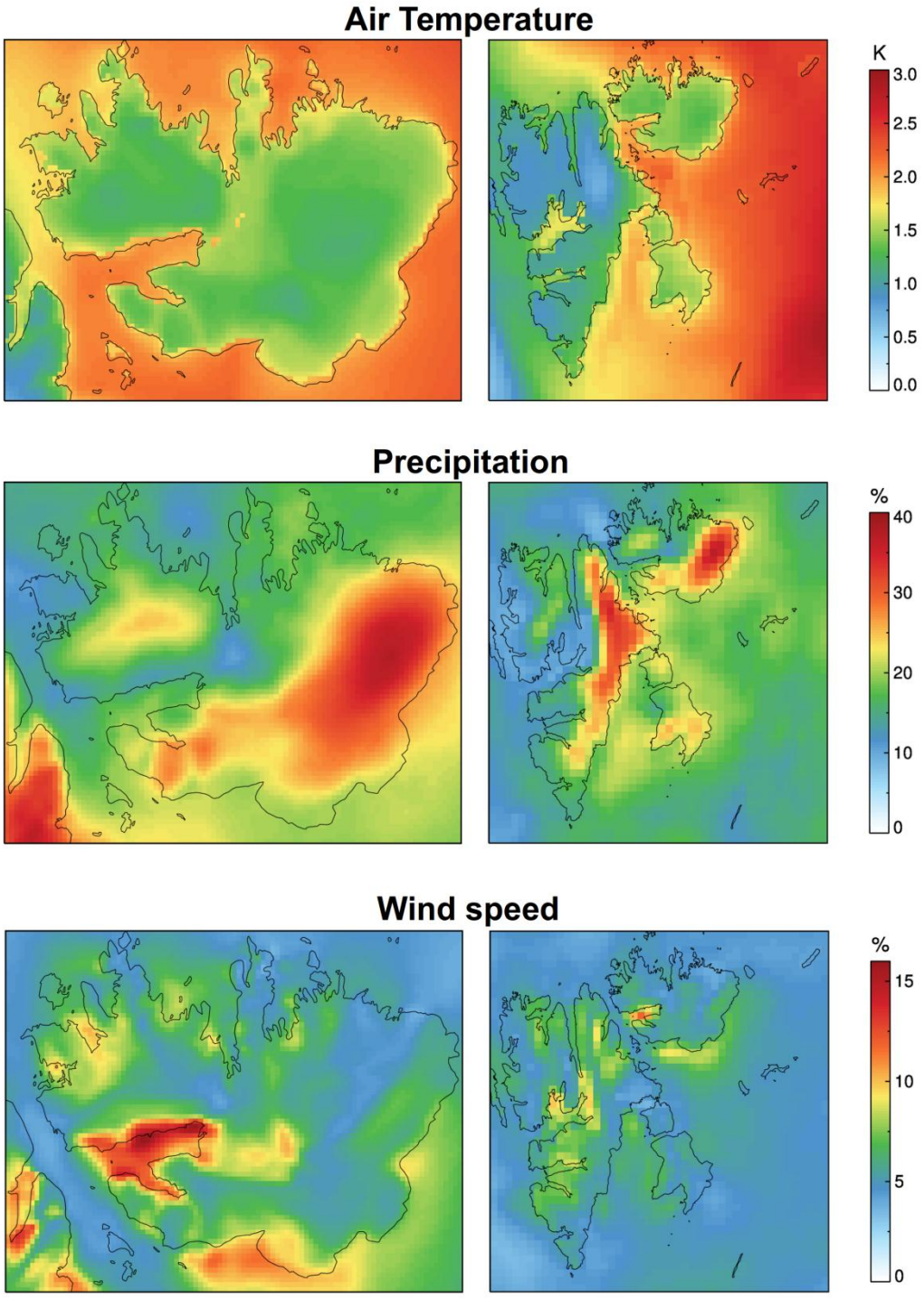

Figure L.2 *Variability of annual means derived from eleven-year EAR data. Values for air-temperature are displayed as standard deviation. Values for precipitation and wind speed are displayed as relative standard deviation. Each variable is plotted for the Nordaustlandet domain (left) and the Svalbard domain (right).*

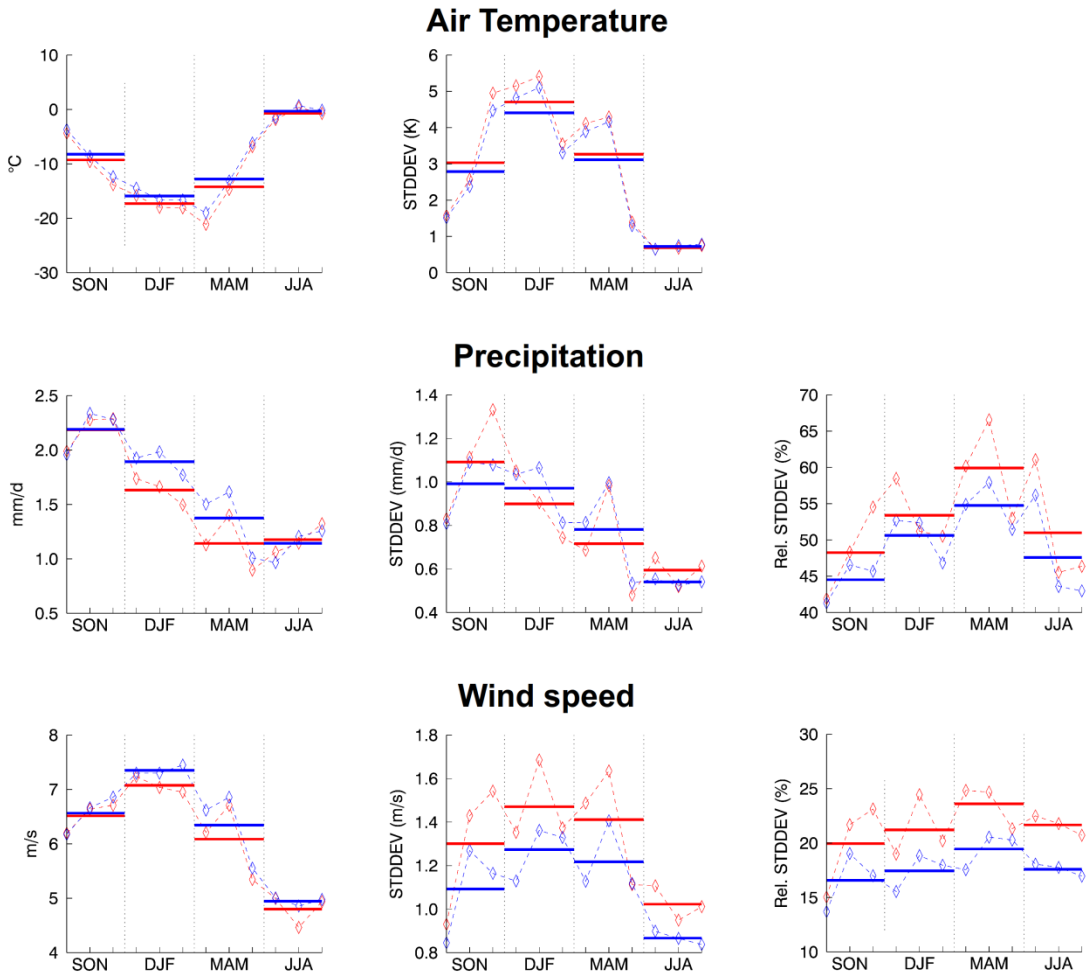

Figure L.3 *Seasonal means (bold line) of air-temperature, precipitation and wind speed (left), their standard deviation (middle) and relative standard deviation (right) as derived from eleven-year EAR data. Only land-based grid points of the Nordaustlandet domain (red) and the Svalbard domain (blue) are included.*

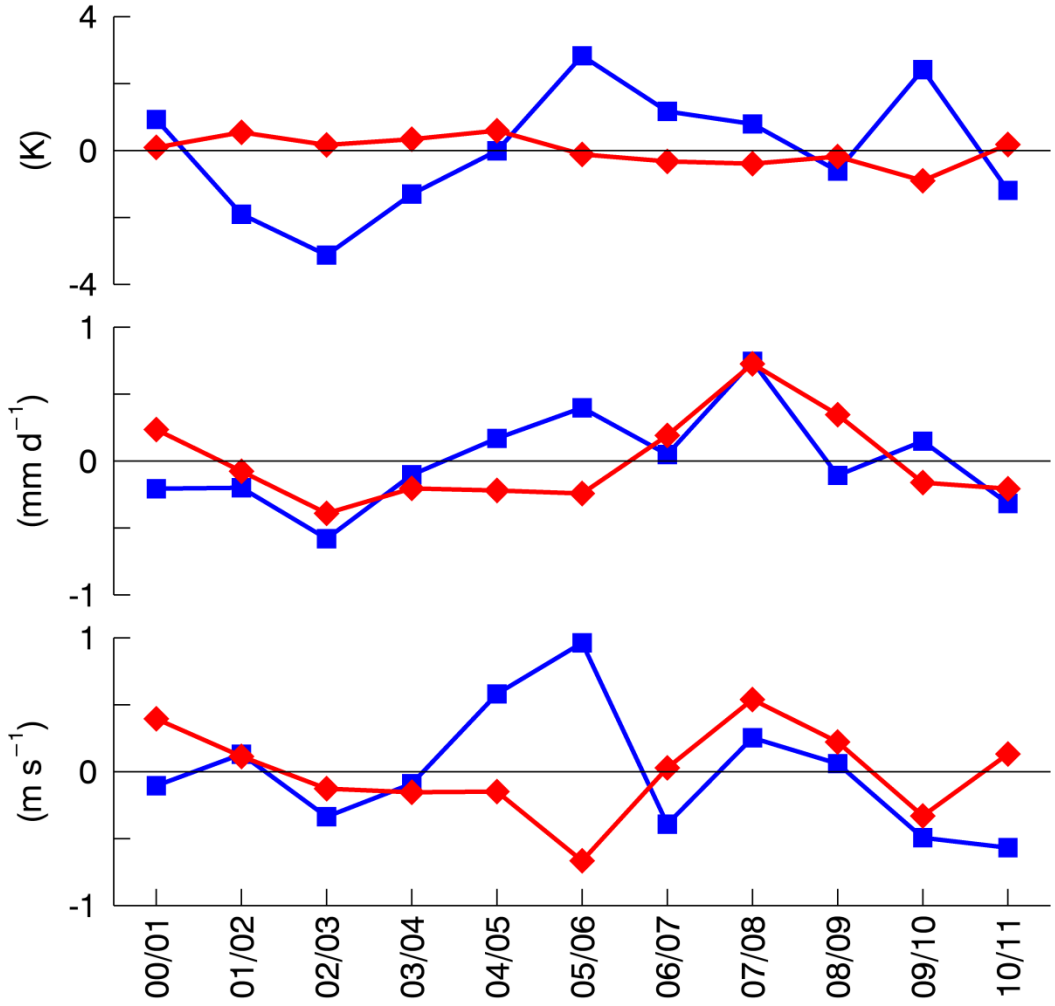

Figure L.4 *Seasonal anomalies of glacier-wide mean air-temperature (top), solid precipitation (middle) and wind speed (bottom) as resolved by the EAR. Accumulation season (blue) comprises values of the period September to May and ablation season (red) comprises values of the period June to August of the mass balance years 2001 to 2011.*

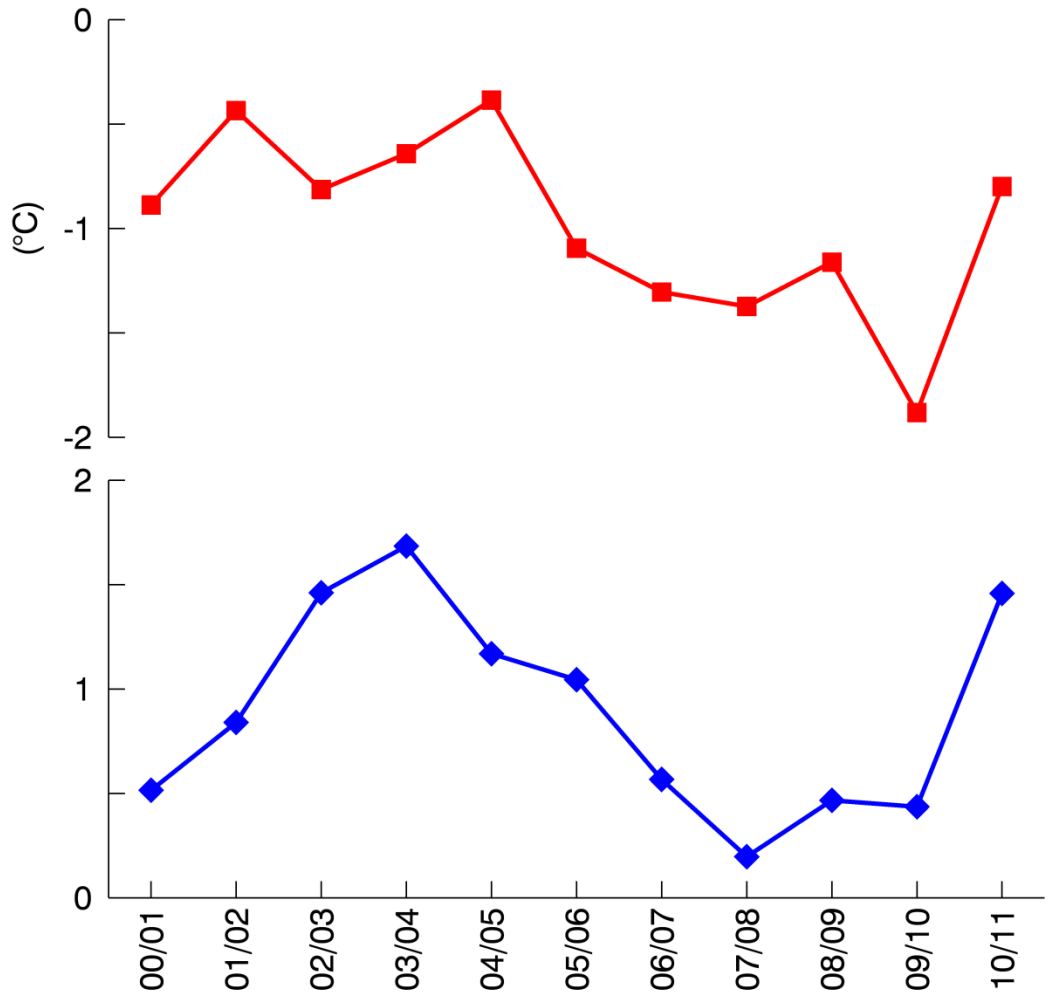

Figure L.5 *Glacier-wide mean air-temperature (red, top) and rain-snow ratio (blue, bottom) during ablation season (June to August) of the mass balance year 2001 to 2011 as resolved by the EAR.*

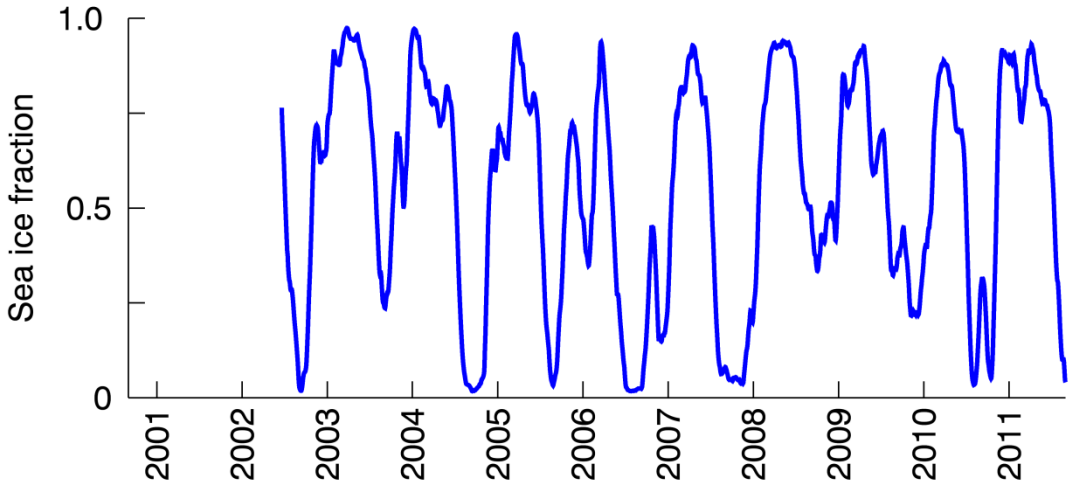

Figure L.6 *Mean sea ice concentrations from Advanced Microwave Scanning Radiometer for Earth Observing System (AMSR-E) observations at 12.5 km horizontal resolution within the Nordaustlandet domain for the period September 2000 to August 2011. A 30-day moving window was used to smooth the curves.*